Fall 2019

Multi-body dynamic and finite element modeling of ultra-large dump truck - haul road interactions for machine health and haul road structural integrity

Bruno Ayaga Kansake

Department: Mining and Nuclear Engineering

MULTI-BODY DYNAMIC AND FINITE ELEMENT MODELING OF ULTRA-LARGE DUMP TRUCK – HAUL ROAD INTERACTIONS FOR MACHINE HEALTH AND HAUL ROAD STRUCTURAL INTEGRITY

by

BRUNO AYAGA KANSAKE

A DISSERTATION

Presented to the Faculty of the Graduate School of the

MISSOURI UNIVERSITY OF SCIENCE AND TECHNOLOGY

In Partial Fulfillment of the Requirements for the Degree

DOCTOR OF PHILOSOPHY

in

MINING ENGINEERING

2019

Approved by:

Samuel Frimpong, Advisor
Grzegorz Galecki
Nassib Aouad
Taghi Sherizadeh
K. Chandrashekhera

ABSTRACT

Haul truck capacities have increased due to their economies of scale in large-scale surface mine production systems. Ultra-large trucks impose high dynamic loads on haul roads. The dynamic loads are exacerbated by road surface roughness and truck over-loading. The dynamic forces also subject trucks to high torsional stresses, which affect truck health. Current haul road response models are 2D and use static truckloads for low capacity trucks. Existing 3D models consider the road as a two-layer system. No models capture the truck dynamic effects on haul roads and predict strut pressures during haulage.

Lagrangian mechanics was used to formulate the governing equations of the truck-haul road system. The equations were solved in MSC.ADAMS, based on multi-body dynamics, to generate the truck dynamic forces, which were verified and validated using data obtained from an open-pit mine. These forces were used in an FE model developed, verified and validated in ABAQUS to model the response of the haul road to the truck dynamic forces. The road was modeled using an elastoplastic Mohr-Coulomb model.

The results showed that the maximum truck tire dynamic forces were 2.86 and 3.02 times the static force at rated payload and 20% over-loading, respectively. The trucks were exposed to torsional stresses that were up to 2.9 times the recommended threshold. Road deformation decreased with increasing layer modulus and increased with increasing payload. This study proposed novel multivariate models for predicting dynamic truck strut pressures. The novel 3D FE model and empirical relations for calculating truck dynamic forces incorporate truck dynamic forces into haul road design. This study forms a basis for designing structurally competent haul roads and improving truck health.

ACKNOWLEDGMENTS

I am grateful to God for seeing me through the Ph.D. program successfully. I am indebted to my advisor, Dr. Samuel Frimpong, for his patience, inspiration, and guidance through the Ph.D. program. I acknowledge him for providing funds for my Ph.D. studies through the Robert H. Quenon Endowed Fund. I am grateful to my Ph.D. committee members for their valuable contributions that improved the work. I am thankful to Tina, Judy, and Steve for their support. I thank Jade Sinnott, my Graduate Advisor, for her assistance. I am grateful to the mine that provided the data for this research.

I am also indebted to my parents, Clement and Beatrice Kansake for their prayers, investments, and support throughout my life. I acknowledge my siblings and friends for encouraging me through difficult times. Special thanks to my loving wife, Charlotte, and kids, Anewe and Wepeere, for their patience, emotional support, and encouragement.

I am thankful to my research group members, Danish Ali and Kramer Hall for their encouragement and knowledge sharing through the Ph.D. program. I thank Drs. Kaba, Tiile, Arthur, Wardeh, Gbadam, Mborah, Somua-Gyimah, and Waqas, for sharing their experiences with me. Thanks to Dr. Nyaaba for permitting me to use his tire model. My appreciation to Bharath and Atta for their assistance throughout the program. I thank the Ghanaian community in Rolla for the good times they shared with me. I also thank Drs. Awuah-Offei and Oboh-Ikuenobe and Mrs. Grace Frimpong for their valuable counsel during my time in Rolla. I owe special thanks to Drs. Raymond Suglo, Charles Abbey and Kenneth Bansah, who have played key roles for the successful completion of the Ph.D. program and our (my family and I) stay in Rolla.

TABLE OF CONTENTS

LIST OF ILLUSTRATIONS

LIST OF TABLES

NOMENCLATURE

Symbol	Description
P	Tire pressure (kPa)
t_w	Single tire load (metric tons)
Z_{CBR}	Haul road layer thickness based on single wheel loading (t_w)
Z_{CBR}	Haul road layer thickness based on equivalent single wheel loading ($1.2*t_w$)
Y	Tire lateral/side force (F_y), longitudinal force (F_x) or aligning moment (M_z)
D	Peak value/factor
B	Stiffness factor
C	Shape factor
E	Curvature factor
S_h	Horizontal shift
S_v	Vertical shift
X	Longitudinal or lateral, slip angle
σ'_{ij}	Effective principal and shear stresses
p'	Mean effective stress
q	Deviator stress
v	Specific volume
e	Void ratio
$f(\sigma, P_c)$	Yield function of the M-C, C-C and MCC models

M	Slope of the critical state line (CSL) in the p – q plane
p_c	Preconsolidation pressure
λ, κ	Drucker-Prager materials constants
J_2	Second invariant of the stress deviator tensor
I'_1	First invariant of the stress tensor
σ'_1, σ'_2, σ'_3	Effective major, intermediate and minor principal stresses, respectively
c	Material cohesion
φ	Internal friction angle
τ	Shear stress
m_i, k_i, c_i	Component mass, and spring stiffness and damping
$F_i(t)$	External force acting on truck
F_{ki}, F_{ci}	Spring and damping forces, respectively
q_i	Generalized coordinates
$\mathbf{r}$	Position vector
δW	Work done by the applied force
$\dot{q}_i$	Generalized velocities
$\ddot{q}$	Generalized accelerations
$Q_i(t)$	Generalized external force
L	Lagrangian ($L = T - V$)
$G(n)$	Power spectral density (PSD) for wavenumber n
$G(n_0)$	PSD for the reference wavenumber
$G_x(n_i)$	Cross power spectral density (Cross-PSD)

n	Road roughness frequency/wavenumber (cycles/m)
n_0	Reference wavenumber or roughness frequency
n_{min}, n_{max}	Lower and upper limit wavenumbers, respectively
Z_r, Z_l	Right and left parallel road profiles
N	Number of frequencies over the road length considered
Δn	Frequency increment [$\Delta n = (n_{max} - n_{min})/N$]
X	Length of road considered
φ_i, θ_i	Random phase angles of parallel road profiles
I_2	Moment of inertia of the truck chassis
[M], [C], [K]	Mass, damping and stiffness matrices, respectively
$\left\{\ddot{Z}(t)\right\}$	System acceleration vector
$\left\{\dot{Z}(t)\right\}$	System velocity vector
$\{Z(t)\}$	System displacement vector
$\{F(t)\}$	Vector of external forces
α_j, β_j	Rear outer, rear inner tires influence coefficients on road layer displacement
n_j, m_j	Rear outer and rear inner tires influence power on layer displacement
μ_{stat}, μ_{dyn}	Static and dynamic friction coefficients, respectively
$R_l(\delta)$, $R_r(\delta)$, $R(\delta)$	Left side, right side and the general autocorrelation functions
$R_{lr}(\delta)$, $R_{rl}(\delta)$, $R_x(\delta)$	Right-left, left-right and general cross-correlation functions

α, β	Newmark integration coefficients ($\alpha = 0.5$, $\beta = 0.25$)
Δt	Integration time step
X_i, X_j	Global x coordinate of the I and J markers, respectively
Y_i, Y_j,	Global y coordinate of the I and J markers, respectively
Z_i, Z_j	Global z coordinate of the I and J markers, respectively
δ, $\partial\delta/\partial t$	Spring deformation and deformation velocity, respectively
F_n, k_n	Tire normal force and normal stiffness, respectively
F_t, F_l	Tire lateral and longitudinal forces, respectively
M(q)	Generalized mass matrix (in MSC.ADAMS)
$Q(\dot{q},q,t)$	Generalized external force acting on the system at the generalized coordinate q
Φ_q	Displacement kinematic constraint of the system
β_i	Regression model coefficients
P	Truck payload (tons)
gs_l	Loaded truck speed (mph)
gs_e	Empty truck speed (mph)
sh	Truck service hours
ρ_o	Initial density of road materials
V_o, V	Initial and final volumes of road materials, respectively
σ_{xx}, σ_{yy} and σ_{zz}	Principal stresses
σ_{xy}, σ_{xz}, σ_{yz}	Shear stresses
ρ	Density of the road materials
b_x, b_y, b_z	Body accelerations in the x, y and z directions, respectively

$\ddot{x}$, $\ddot{y}$, $\ddot{z}$	Nodal accelerations in x, y and z directions, respectively
$\dot{e}$	The energy of the system
$\dot{\varepsilon}_{xx}$, $\dot{\varepsilon}_{yy}$, $\dot{\varepsilon}_{zz}$, $\dot{\varepsilon}_{xy}$, $\dot{\varepsilon}_{yz}$ and $\dot{\varepsilon}_{zx}$	Principal and shear strain rates
$\dot{x}_i^{n+1/2}$, $\dot{x}_i^{n-1/2}$	Mid-incremental nodal velocities
h	Characteristic dimension of an element
c_m	Local material sound speed in an element
g_i, τ_i	Prony series constants
Ci (i = 1, 2)	First and second WLF model constants
h_c	Coefficient of thermal convection
K	Loss modulus due to anharmonic loading
C_v	Specific heat capacity at constant volume
α	Shear coefficient
μ_i, α_i	Ogden strain energy potential constants
$\varepsilon_{elastic}$, $\varepsilon_{plastic}$, ε_{total}	Elastic, plastic and total nodal strains, respectively
S	Stress deviator
p	Equivalent pressure stress
q, **σ**	Mises stress and stress tensor, respectively
R_{mc}	Mohr-Coulomb deviatoric stress
Θ	Deviatoric polar angle
F_{dyn}^{max}, F_{dyn}^{ave}	Maximum and average dynamic tire force (N), respectively
t_w^{dyn}	Dynamic tire load (metric tonnes)
U_i	Haul road nodal translational displacement at the road edges
UR_i	Haul road nodal rotational displacement at the road edges

1. INTRODUCTION

This section covers the background of the problem, statement of the problem, and research scope and objectives. The section also contains the research methodology and limitations, expected scientific and industrial contributions and main research novelty.

1.1. PROBLEM BACKGROUND

Mining is a major economic activity in many countries across the globe. It contributes substantially to national income and employment. It also supplies raw materials such as metals for manufacturing, aggregates for construction and strategic minerals for security and other critical aspects of the global economy. The mining industry is also a major supplier of energy minerals, which are the backbone of national economies. Globally, coal contributed 38% of power generation (Figure 1.1). It is the largest contributor in the global power generation mix and this is projected to be sustained for a considerable time into the future, as exploration continues into new and alternative sources, such as renewable energy.

Mining remains vital to the US economy, with significant direct and indirect contributions. It supplies critical resources for national defense, and technological and infrastructural advancement. The US produces about 78 major commercial mineral commodities [1]. The US produced 253.2 metric tons of gold in 2018, making it the fourth largest producer of gold in the world [2]. It hosts 5.6% of global gold reserves [3]. The US ranked as the tenth largest producer of silver, producing 3.33% of global silver and hosting 4.5% of global silver reserves. It ranked as the fourth largest producer of copper (5.7% of

global copper production) and hosts 5.8% of global copper reserves. It is the leading producer of diatomite (29.3% of global diatomite production) [3]. The mining industry also produces a significant amount of aggregates to feed the ever-expanding construction/infrastructure industry.

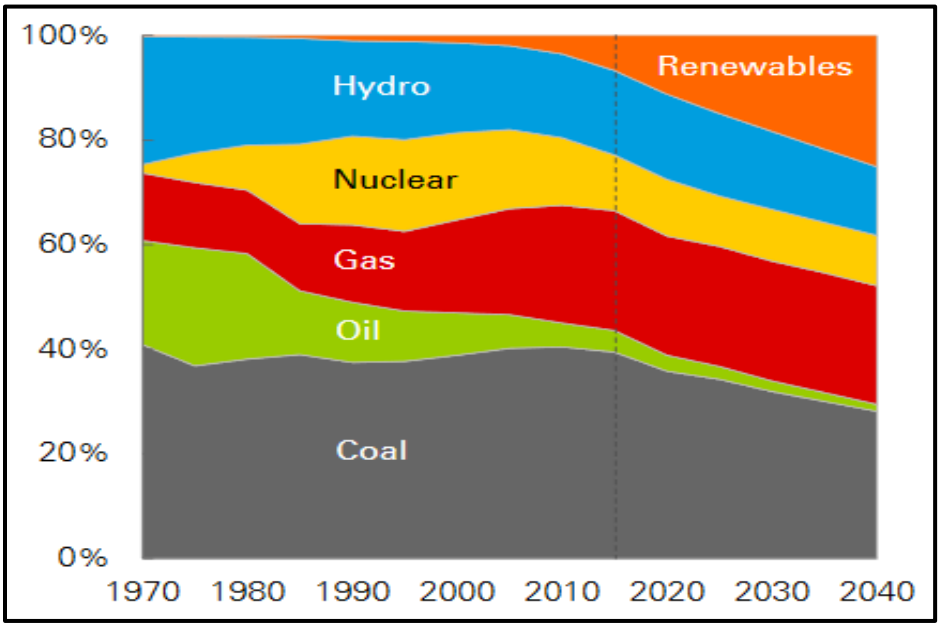

Figure 1.1 Global fuel shares in power generation for 2017 [4]

It is estimated that industries that consume processed minerals produced from mining contributed about 14.74% (US$2.78 trillion) of the gross domestic product (GDP) of the US [5]. In 2016, coal was the second largest source of electricity in the US, contributing 30.4% of electricity [6]. Uranium, another energy mineral produced by mining, contributed 20% of US electricity [1]. The US Armed Forces and other security agencies also rely on domestic minerals to produce sophisticated weapons and transport systems for national defense [7]. Thus, mining plays a critical role in the US economy.

Minerals are mined using both surface and underground mining methods, with surface mining being the dominant method. Over 65% of coal [1], 92% of metals and 96% of industrial minerals are mined using surface mining methods [8]. The shovel-truck haulage system remains the preferred choice for moving ore and waste in surface mining operations due to its efficiency, flexibility and high productivity [9]. Due to economies of scale [10], and to meet the ever-increasing production demands of industry, truck capacities have increased significantly over the years, with the concept that "bigger is better" [11]. High payload trucks offer better cost efficiency due to several direct and indirect cost savings such as savings in labor, equipment components, and consumables.

Due to their numerous advantages, ultra-large trucks ($\geq$ 220 tons capacity) are becoming dominant in the mining industry, with a current population exceeding 40% of dump trucks in the mining industry [12]. Recent truck models have payload capacities of 400 tons, with empty truck operating weights in excess of 300 tons. These capacities might increase further as truck automation reaches commercial production stages and gains global acceptance. Operating these ultra-large trucks in rugged mining environments results in significant haulage costs, reaching 45 to 50% of total mining costs [13], [14]. These ultra-large dump trucks, with high payloads, impose very high dynamic loads on haul roads during haulage, with the resultant effect of increased road-user costs. The large dynamic loads result from the road surface roughness/unevenness, which subjects the trucks to more severe vertical excitations. The impact of these dynamic forces is severe in soft rock formations such as oil sands, as roads deform easily and reduce truck efficiency.

The safety, productivity and life of these ultra-large trucks are reliant on well-designed, constructed and maintained haul roads [12]. The largest proportion (22.3%) of

surface mine equipment fatalities is truck-related [15]. Further analysis of surface mine haul truck fatalities by [16] showed that majority of truck-related accidents occur on haul roads. These accidents may result from poor haul road conditions, such as potholes, slippery road surface, and poor sight distances. Poor haul road conditions also reduce mine productivity due to decreased truck speed resulting in increased cycle times. They can interrupt mine production. Road conditions, such as surface ruts, can develop due to poor haul road structure.

Further, machine components, and tire wear and damage increase significantly due to poor haul road conditions. A major component of truck operating costs is tire repair/replacement. Truck tires are unable to meet their designed tire life due to rough operating conditions. Frequent tire replacement significantly increases operating costs. The truck frame, struts, and other components experience excessive stresses when the truck travels on rough roads. This can reduce truck component life and adversely affect truck availability, utilization, and productivity. Extreme truck body twisting also subjects the operator to extreme whole-body vibrations (WBV), which can be detrimental to operators' health if sustained over long periods.

Efficient haul road design, construction, and maintenance are precursors to efficient surface mining operations. This encompasses designing and building roads of sufficient structural integrity that can absorb the high dynamic loads from ultra-large trucks, to reduce maintenance costs. The benefits of well-built haul roads include safety, reduced operating costs, higher productivity due to shorter cycle times and effective utilization of road maintenance equipment [17]. Good haul roads also improve equipment and operator health due to reduced vibrations. Building good haul roads usually has a high initial cost, but the

long-term benefits of efficient haulage, minimal road maintenance, improved productivity, improved safety, operator and machine health, outweigh this cost [9]. It is estimated that the maintenance cost of poorly designed and constructed haul roads can be ten times the cost of well-constructed haul roads [14].

The structural design of mine haul roads has received little attention in the literature and in practice. Much attention has focused on the geometric and functional design of haul roads. Fundamental research is required to understand the behavior of haul roads under high impact loads to serve as a foundation for better haul road design for economic and safe haulage operations. Current design techniques (experience-based and California bearing ratio) are inappropriate for designing haul roads due to the extremely high tire loads generated by these trucks. This research is a pioneering effort toward providing an enhanced understanding of ultra-large truck-haul road interactions, and haul road response to dynamic loads generated by ultra-large trucks during haulage. It also provides understanding into the impact of truck dynamic forces on truck health. This study forms the basis for designing structurally competent haul roads capable of sustaining the high dynamic impact loads from ultra-large trucks. This will improve truck performance, safety, health, and efficiency, and reduce road maintenance costs.

1.2. STATEMENT OF THE PROBLEM

There is a continuously increasing demand for minerals, coal, and aggregates from the ever-increasing technological, energy and construction industries. This demand, coupled with the economies of scale, has resulted in the demand for high capacity mining trucks, which have high efficiency, flexibility, and productivity. These trucks, which are

now very popular in the mining industry, require competent haul roads for efficient uninterrupted haulage operations. The practice has been to increase the thickness of haul roads to accommodate the higher capacity haul trucks as seen in Figure 1.2. This strategy, however, is not always optimal, as the costs of building haul roads increase significantly.

Ultra-large truck operations in rugged mining environments is challenging and inherently hazardous. When trucks interact with haul roads during haulage operations, they experience vibrations due to the road surface roughness. The vibrations expose truck operators to health risks [18]–[21]. Smets et al. [22] measured exposure of dump truck operators to WBV levels during haulage and found that the recorded levels exceeded the safe limits recommended by ISO 2631-1. Kumar [23] made similar observations when he studied the exposure levels of truck operators to vibrations during haulage. Wolfgang and Burgess-Limerick [24] observed that well-maintained haul roads exposed operators to substantially lower vibrations.

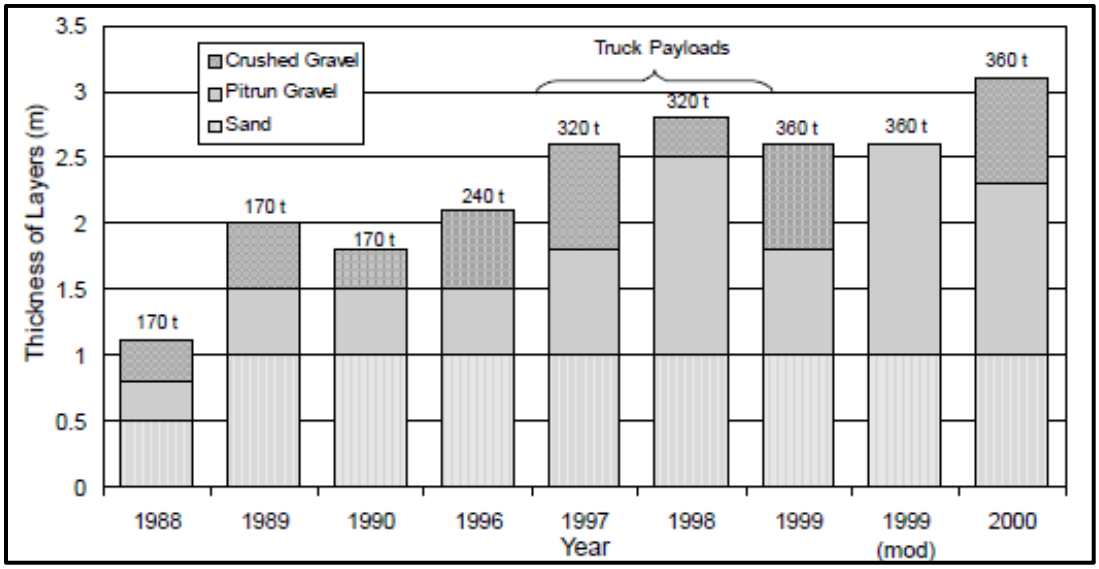

Figure 1.2 Road thickness with increasing truck capacity [25]

Experimental studies have found that vibration exposure limits exceeded acceptable safe limits by up to 600% when unloaded trucks traveled on haul roads. Vibration levels during traveling exceeded the vibrations during loading and dumping [26]. Various authors have corroborated these findings [27]–[29].

In addition, truck components experience extreme twisting forces due to road conditions and can cause equipment components (e.g. frame, tires, suspension, power train) damage, resulting in increased maintenance cost and reduced availability, utilization, and productivity. Tuck component life reduced significantly when used on rough roads at high speed [25]. Surface roughness is a significant parameter affecting truck component life during haulage. Unbalanced payloads also result in extreme loading of equipment components and can significantly shorten the life of affected components [30]. Particularly, truck tires damage quicker under extreme truck kinematics. Tire costs constitute a major component of truck haulage costs, with costs experiencing continuous escalation. Understanding the tire-terrain interaction is required for designing structurally competent haul roads to improve tire performance.

The current methods for haul road design include the California Bearing Ratio (CBR) and Experience Based methods. Thompson and Visser [31] developed an improved technique called the Limiting Vertical Strain (LVS) method, which is based on the elastic layer theorem. Data for these design techniques are usually gathered through the dynamic cone penetrometer (DCP) test [32]–[34], and multi-depth deflectometer (MDD) test [31], [35]. The CBR technique is based on penetration tests conducted on the road layer materials. Road layer thicknesses are then selected based on the CBR values (calculated from the tests) and maximum static tire loads. The maximum wheel loads limit this method:

it gives unreliable designs beyond truckloads of 4,400 kN [36]. The method also assumes static truckloads based on the gross static weight of the truck, which are generally less than the corresponding dynamic loads on typical haul roads. Hence, the CBR method is not reliable for the design of mine haul roads for ultra-large truck applications.

The LVS technique uses static loads to calculate the vertical strains experienced by each road layer. The design is then modified until the vertical strain in the layers is below a given threshold (1,500 to 2,000 microstrains). Layer thicknesses that result in this "safe vertical strain" are then used as the final design thickness and the road is built accordingly.

The CBR and LVS methods take the maximum tire load as a fraction of the gross machine weight (GMW), based on the weight distribution of the loaded truck. In real truck operations, however, trucks are subjected to vertical excitations due to the road surface roughness/unevenness, generating dynamic loads, which can be greater than the static loads. Thus, the CBR and LVS techniques may underestimate the maximum truckloads transmitted to the road. A design that captures the dynamic forces can improve haul road structural design significantly.

Current literature on truck-haul road dynamic modeling has been used for studying tire stress distributions [37], [38], establishing the impact of tire-road interaction on haulage costs [39] and establishing operator hazards during haulage. Li and Frimpong [38] studied road deformation, but only modeled the road as a two-layer system made of masses, springs, and dashpots. No literature exists on mine haul road response to dynamic impact loads from ultra-large mining trucks. Such knowledge is critical for designing haul roads for extended service life, while significantly improving mine productivity, safety, and road-user health. Truck component health studies are also scarce in the literature. Thus, this

research makes a significant contribution to the literature and has the potential to improve the efficiency of trucks in surface mine environments.

To design structurally competent haul roads, the impact loads imposed on the haul road by moving trucks need to be accurately modeled as input for road design. This would require incorporating haul road surface roughness into dump truck tire-haul road interaction models. Mathematical and virtual prototype modeling provides reliable solutions to these problems and will be explored in this study. The dynamic force models developed in this research study were validated using field data from a large-scale open-pit mine that uses ultra-large trucks. Results from the validated dynamic force models were used as input to a 3D finite element model in ABAQUS CAE for studying the impact of increasing dynamic forces on the road response. Field data obtained from a large-scale open-pit mine employing ultra-large trucks was also used to evaluate the effect payload imbalance on truck component health and durability. The data was also used to generate multiple linear regression models for predicting truck strut pressure during haulage.

1.3. OBJECTIVES AND SCOPE OF RESEARCH

The primary research objective is to provide understanding into ultra-large truck-haul road interactions and road response to truck dynamic loads for enhancing haul road structural integrity. The research also seeks to provide understanding into the impact of truck payload imbalance on the life and durability of truck components. The specific elements of this objective are to develop:

(i) Mathematical models that incorporate haul road surface roughness/unevenness in modeling ultra-large truck-haul road dynamic forces;

(ii) A virtual prototype model, based on rigid multi-body dynamics, for simulating truck dynamic forces during haulage;

(iii) Empirical models that incorporate truck dynamic forces in haul road structural design;

(iv) Multiple linear regression models for predicting truck strut pressure during haulage operations; and

(v) A 3D finite element model of truck tire-haul road interactions for understanding haul road dynamic response to ultra-large truck dynamic forces.

The research is limited to ultra-large truck-haul road interaction modeling to determine truck tire dynamic forces generated during haulage and road response under impact loads from ultra-large trucks. The research simulated road response under various truck payloads and haul road properties. Truck health was evaluated using the three parameters; rack, roll and pitch, proposed by Caterpillar Australia. The parameters were computed using real-time truck strut pressures obtained from an open-pit mine that uses ultra-large trucks.

The models developed in this research study are useful for the design of haul roads in surface mining operations. They may also find applications in civil construction operations employing ultra-large trucks. The underpinning theory, mathematical and virtual models may find wider applications in other off-road environments. The models were developed to predict dynamic impact forces from ultra-large trucks on the haul road and stress/strain propagation through the various layers of the haul road. Operating strategies have been proposed to reduce the road response (stresses, deformation, and strains) to minimal levels to adequately protect the subgrade. The virtual simulators provide

valuable information on road design and performance, which are useful to the mining industry especially, as truck capacities increase with automation.

1.4. ORIGINALITY OF Ph.D. RESEARCH

This research is a pioneering effort to provide understanding on ultra-large truck tire-haul road interaction and haul road response to dynamic loads from ultra-large haul trucks. The research provides new knowledge towards solutions of haul road structural performance problems, reducing structural failures and minimizing road maintenance. This research provides a novel and comprehensive method for estimating truck dynamic forces. A novel load propagation model was developed using Lagrange formulation, to capture the truck-haul road system dynamics during haulage. This model describes the mechanics of load transfer from the truck to the road. A virtual prototype of the truck-haul road system was built for simulating truck dynamic forces during haulage.

The research also used 3D explicit dynamic finite element modeling to provide knowledge on stress/strain propagation through a multi-layer haul road traversed by an ultra-large truck. Techniques were explored to reduce road stresses, deformation, and strains to levels that cannot damage the subgrade. This model is an improvement over previous models that either modeled the truckloads as static or the haul road as a two-layer pavement or used a 2D axisymmetric model for the haul road.

Truck health has not been comprehensively studied in the literature and not much field data is available to provide a realistic understanding of this important phenomenon. With significant field data based on real-time monitoring, this research provides useful information to mine operators for maximizing equipment life. It also provides data for the

validation of numerical and artificial intelligence models in this area. It provides Knowledge on the impact of road roughness and payload imbalance on truck health. The multiple linear regression models developed in this research study provide insight on factors the influence truck strut pressure and provide a tool for predicting the strut pressure. No such models exist in the literature.

1.5. RESEARCH METHODOLOGY

A critical literature review was undertaken to understand the existing body of knowledge and the frontiers of this research domain. Review of existing literature covered existing methods for haul road design, road surface roughness models, tire-terrain interaction and road response to truck loads. Numerical and experimental modeling techniques and solution algorithms available in the literature were also reviewed as a basis for this research.

Mathematical models of truck-haul road interactions were developed to fully describe the truck kinematics and dynamics during haulage. The truck-haul road dynamic model was built using the Lagrangian formulation, which is based on the energy method. The Newmark numerical integration scheme was used for solving the mathematical model in MSC.ADAMS software. A simplified solution of the mathematical model was also obtained using MATLAB/SIMULINK®. The simplified solution was obtained for a single truck tire rolling on a class D rough road. The complete mathematical model was built using a half truck model (one front and two rear tires), with 18 degrees of freedom. In the multi-body dynamic model, the truck-road system was modeled using the mass-spring-damper system from [38] and [40].

A 72-DOFs virtual prototype model was built in MSC.ADAMS, using the CAT 797F dump truck with six 59/80R63 tires. It was for experimenting the impact the truck over-loading on truck dynamic forces imposed on the haul road. The dynamic force models in MSC.ADAMS and SIMULINK were validated using field data obtained from a large open-pit mine, which deploys ultra-large trucks for moving ore and waste. The results from the MSC.ADAMS model were used to propose empirical relations that capture truck dynamic loads in haul road structural design.

Haul road response to truck loading is dependent on the road construction materials, layer thicknesses, degree of compaction, and moisture content. A 3D FEM in ABAQUS environment was used to simulate the effect of increasing truck payload and road layer elastic modulus on haul road response. The haul road was modeled using an elastoplastic Mohr-Coulomb model. The tire-road contact was modeled using the penalty method implemented in ABAQUS. The tire rubber materials were modeled using the third-order Ogden and Prony series models. The tire model was adopted from [37], who modeled the thermomechanical stress and fatigue life of an ultra-large truck tire.

Field data of truck strut pressure was used to formulate multiple linear regression (MLR) models in JMP that relate truck strut pressure to the truck payload, speed, and age (service hours). The MLR was based on least-squares fitting. The data was also used to evaluate the impact of payload imbalance on truck health using the application severity analysis (ASA) method described by [30].

1.6. SCIENTIFIC AND INDUSTRIAL CONTRIBUTIONS

This research advances knowledge and frontiers in haul road response to dynamic impact loads from ultra-large mining trucks. Its scientific contributions are the development of novel mathematical and virtual dynamic force models for the complex problem of ultra-large truck tire-haul road interactions towards improving haul road structural integrity. It also contributes to the body knowledge by proposing empirical relations for incorporating ultra-large truck dynamic forces in empirical haul road design. The real-time data-driven MLR models for predicting ultra-large truck dynamic strut pressure are a valuable scientific contribution towards achieving healthy truck operations. The 3D finite element model developed for simulating road response to ultra-large truck dynamic forces presents a significant advancement towards improved haul road design.

The results from this research study have valuable industry significance. They form a basis for designing structurally competent haul roads for improved haulage efficiency, improved operator safety and comfort and truck health. The MLR models for predicting truck strut pressures can be used for establishing optimal operating parameters such as truck safe speed and maximum payload for ensuring healthy truck operations.

1.7. STRUCTURE OF DISSERTATION

This dissertation is organized in seven sections. Section 1 presents the introduction to the research. It covers the research background, problem statement, research objectives and scope, research methodology and originality and research contributions. Section 2 focuses on critical review of the relevant literature. It comprises previous works on haul road structural design, road roughness modeling, vehicle-terrain interaction dynamics and

road response modeling. It also covers road material models and presents the PhD research rationale.

Section 3 contains the mathematical model that captures the mechanics of load transfer from the truck to haul road. It contains the detailed derivation of the dynamic force EOMs and road roughness model. Section 4 contains the numerical solution algorithm for the dynamic force model. The section also presents the mathematical model implementation in MATLAB/SIMULINK® and virtual prototype modeling procedure for the dynamic force model, as well as the verification and validation of the dynamic force model.

Section 5 presents the finite element modeling of the tire-road interaction, which is used to study road response to dynamic tire loading. Section 6 focuses on the analysis and discussions on the research results and Section 7 presents the conclusions, contributions of the research and recommendations for future work.

2. LITERATURE REVIEW

This section establishes the research frontier on haul roads through a critical review of previous research efforts aimed at improving road structural performance. It covers the haul road structure and structural design techniques, road roughness modeling and vehicle-road interaction dynamics, as well, as road response modeling. This section also covers the review of models for characterizing pavement materials. The section ends with a description of the research rationale and a summary of the literature to establish the frontier for the current work. Symbols and abbreviations used are defined in the nomenclature section of this dissertation.

2.1. OVERVIEW OF HAUL ROADS

Design of mine haul roads can be categorized into four distinct groups; (i) geometric, (ii) structural, (iii) functional and (iv) maintenance designs. Haul road design usually begins with geometric design and entails the design of the road layout and alignment [34]. It involves the design of road features, such as the width, curves, sight distances, stopping distances, superelevation, grades, berms, escape lanes, and road junctions. There are established guidelines for the geometric design of haul roads for safe and efficient haulage [25]. Structural design is concerned with the design of haul road layers to ensure that the road is of sufficient structural integrity to carry the loads imposed by the dump trucks. This design component focuses on the strength of the road. Key parameters of interest include road layer thicknesses, degree of compaction, bearing

capacity and modulus of elasticity of the road materials. Materials are selected, and layer thicknesses designed to provide strength over the planned life of the road.

The functional design of mine haul roads refers to the selection, application, and maintenance of the wearing surface materials. This is critical as the wearing surface interacts with the tires and controls haulage performance and tire life to a large degree. Poor functional design results in poor ride quality, excessive dust, slippery road surfaces, increased tire wear and damage, with resultant loss of productivity [34].

Design and execution of maintenance plans play a key role in road performance. Haul roads need to be maintained to provide a good platform for efficient haulage. Effective maintenance ensures optimal road performance, with reduced road-user costs. A good road design incorporates all the four major design components, resulting in efficient haulage systems, which translate into safe and highly productive operations.

2.2. HAUL ROAD STRUCTURE

Haul roads are designed and constructed to be able to carry the imposed dynamic loads from trucks for the intended road life without excessive maintenance [31]. These roads are usually multi-layered, with the number of layers varying based on site-specific needs. Generally, haul roads are composed of four major layers (Figure 2.1); wearing course/surface, base, subbase, and subgrade.

2.2.1. Wearing Surface. It is the topmost layer of the road that controls truck-road interaction. Kaufman and Ault [41] indicated that the rolling resistance and adhesion (in wet and dry conditions) are the key parameters to consider in choosing the wearing course.

Thompson and Visser [34] indicated that good wearing course materials should have low rolling resistance, high coefficient of adhesion and be economical/cheap.

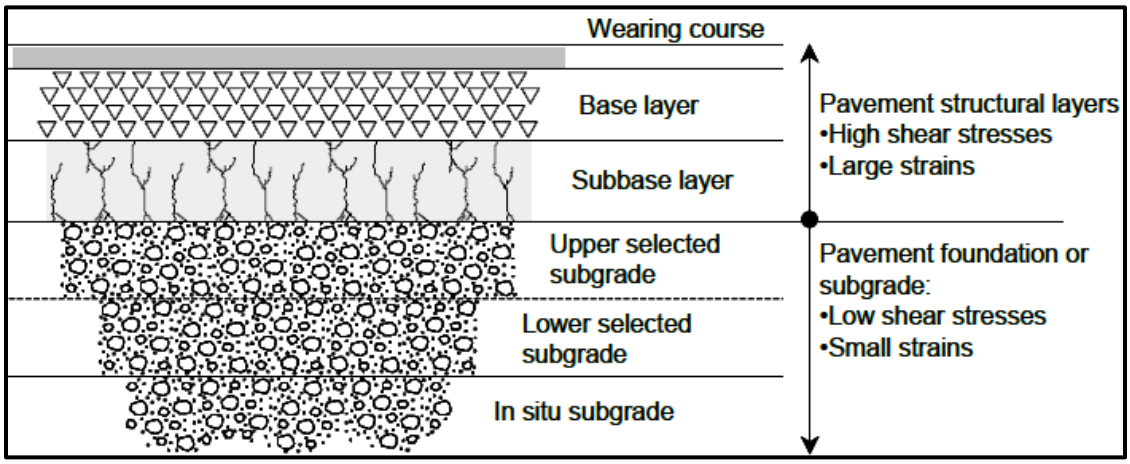

Figure 2.1 Haul road cross-section [42]

The wearing surface provides traction, transmits tire loads to the base thus, reducing stresses at the base, and seals the base against surface water infiltration [43]. It also controls ride quality. The wearing surface is usually constructed with fine gravel [25], crushed mine waste rock [44], asphaltic concrete or stabilized earth [41]. The grading of the material is carefully chosen to minimize dust generation and slippery conditions. It is cheaper when local material is suitable for use as the wearing course. However, if local material is unsuitable, using it for the wearing course material can result in poor road performance, with resultant increased haulage costs. Thus, the ideal wearing course material should [34]:

- be able to provide a safe and vehicle-friendly ride, with minimal maintenance;
- provide adequate trafficability in both dry and wet road conditions;
- allow drainage of the road without excessive erosion;

- resist abrasion action by truck tires;
- be free from excessive dust during dry conditions;
- be free from slipperiness when wet; and
- be cheap and easy to maintain.

Maximum particle size and CBR values of 40 mm and 80%, respectively, are recommended for the wearing course of haul roads [34]. In terms of the shrinkage product and grading coefficient, Figure 2.2 can be used to derive the recommended values.

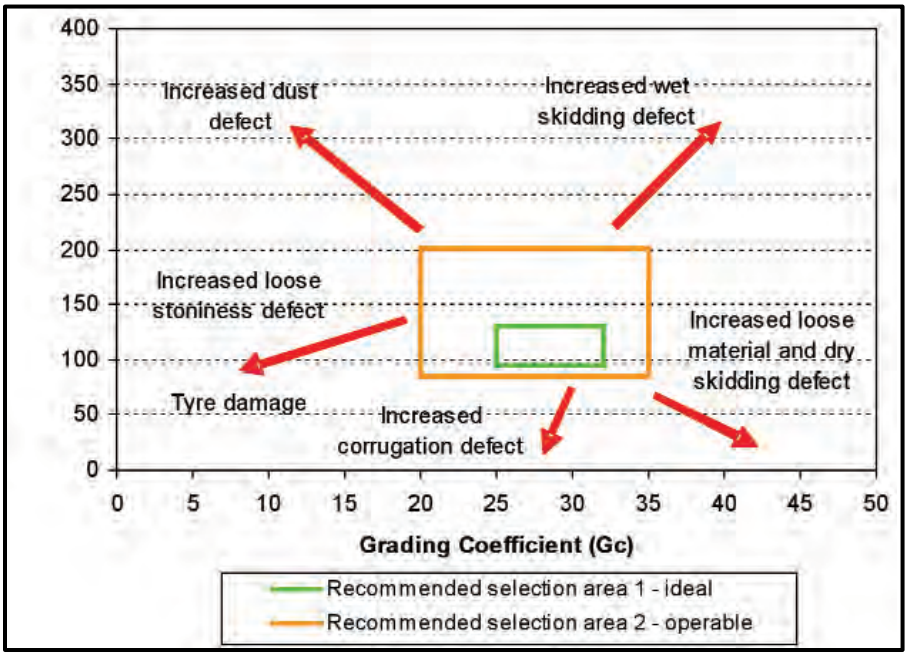

Figure 2.2 Mine haul road wearing course selection guidelines [45]

2.2.2. Base. This is the layer immediately below the wearing surface, and in the absence of a subbase, sits directly on the subgrade. According to [43], this layer consists of high stability and high-density material, with primary functions including effective distribution of truck tire loads, insulation of subgrade from frost and prevention of subgrade

degradation. It is the main source of road structural strength, and thus, usually selected using more stringent considerations for material strength, plasticity, and size distribution [25]. The base is constructed from locally available materials (pit run gravel), with stabilization if required to improve its strength. It is recommended that the maximum particle size the base layer materials be two-thirds of the layer thickness [25]. Thompson [12] recommended particle sizes in the range of 200 to 300 mm. The material for the base layer construction should not contain weathered rock, clay or soil. The amount of fines in the ideal base course should not exceed 20% [12]. Bigger boulders are also not suitable for building the base layer as these are difficult to compact and result in voids surrounded by fine soft/unconsolidated material. This can lead to the formation of potholes and other surface defects due to truck loads or seeping water.

2.2.3. Subbase. The subbase overlies the subgrade and underlies the base in a four-layer haul road. It performs similar functions to the base. It is used when the subgrade is weak. It is constructed of compacted granular materials, which are either cemented or untreated. It provides a working platform for equipment during construction operations. At the subbase, vehicular induced stresses are reduced to levels bearable by the subgrade. The thickness of the subbase is dependent on the strength of the subgrade; the stronger the subgrade, the thinner the subbase. For mines with very competent rocks, the haul road may be constructed without base and subbase.

2.2.4. Subgrade. The subgrade is the in-situ material that supports the total loads imposed on the road. It could also comprise previously placed landfill, mine spoil or other existing material underlying the road. Soft subgrade formations require thick and competent upper layers to be able to provide adequate support for truckloads, while

competent subgrades may not require upper layers. Weak subgrades may be improved by compaction or using geotextiles. Excessively weak subgrade formations may be removed and replaced with more competent material that will ensure extended road service life.

2.3. HAUL ROAD STRUCTURAL DESIGN METHODS

Generally, there are two types of pavements; rigid and flexible pavements. Rigid (concrete) pavements are not common in the mining industry. Haul roads are usually unpaved, and thus, can be considered as flexible. Adequate structural bearing capacity of haul roads is critical for sustainable uninterrupted material movement. Such design seeks to produce haul roads that can support the maximum dynamic loads imposed by ultra-large trucks over the life of the road. Though structural competence of haul roads is critical to mine productivity, it has not been widely researched and structural design of haul roads is typically based on experience.

The pioneering work by [41] discussed the structural design of haul roads and outlined best practices for their design and construction. Various methods exist for designing pavements. The ultimate objective is to design pavement thicknesses, based on the properties of the available construction material, which can sustain the imposed loads. Pavement structural design methods can be grouped into empirical, mechanistic and mechanistic-empirical methods (Figure 2.3).

2.3.1. Empirical Pavement Design. The empirical pavement design method has been used for pavements design since the development of the public roads soil classification system, which classifies the subgrade as uniform or non-uniform [46]. This did not require any strength tests. It went through a series of changes until the development

of the CBR method, which relates the pavement layer thicknesses to the CBR values of the layers. CBR is widely used in designing haul roads, though it was developed for applications in commercial roads.

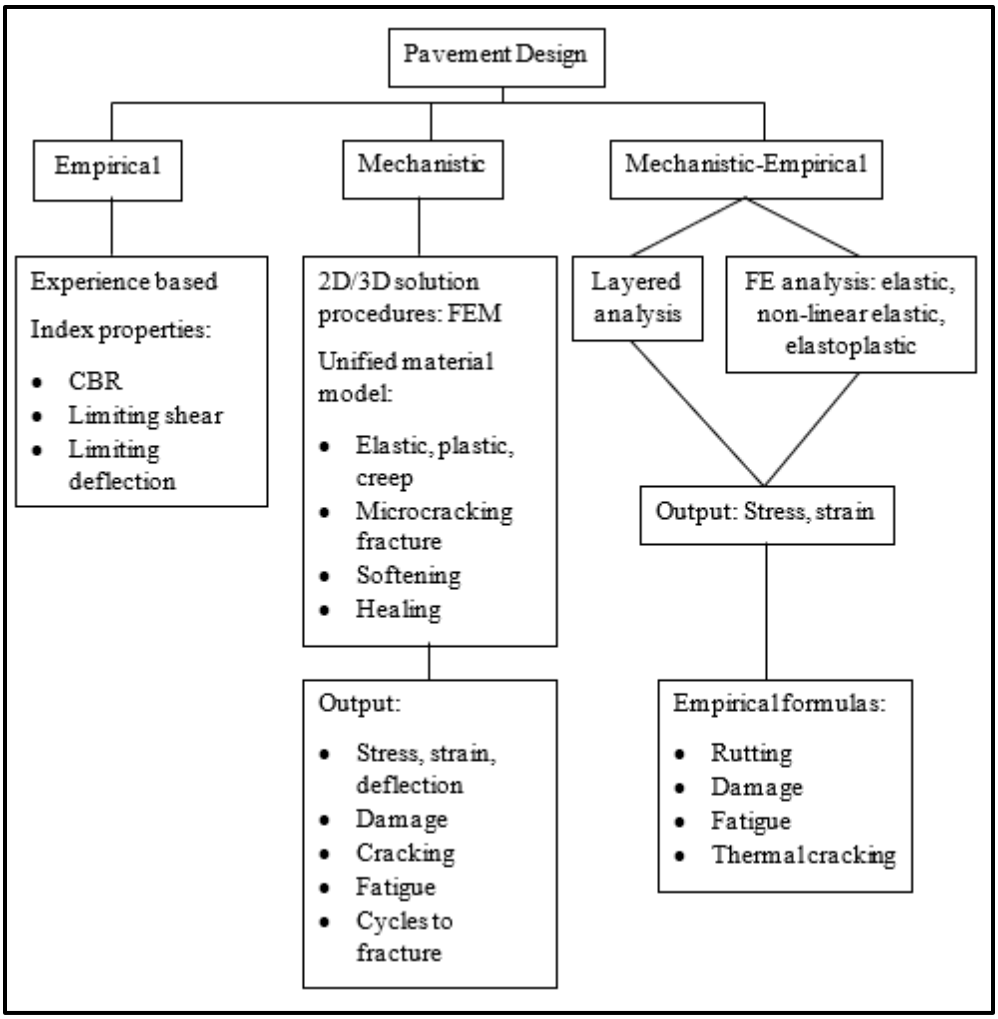

Figure 2.3 Pavement design and analysis methods [47]

CBR is the ratio of the bearing capacity of a given soil as a percentage of the bearing capacity of a standard-crushed rock [25]. The method uses empirically developed curves to generate the required road layer thickness based on the materials CBR and the maximum

wheel loads of the trucks. Equations 2.1 and 2.2 can also be used to determine the road layer thicknesses [48], [49]. The use of CBR curves (Figure 2.4) for haul road design was first proposed by [41].

$$Z_{CBR} = \frac{9.81t_w}{P}\left[0.104 + 0.331e^{(-0.0287t_w)}\right]\left[2 \times 10^{-5\left(\frac{CBR}{P}\right)}\right]\left[\left(\frac{CBR}{P}\right)^{-\left(0.415+P\times10^{-4}\right)}\right] \quad (2.1)$$

$$Z_{ESWL} = Z_{CBR} + \left[0.184 + \left(0.086CBR + \frac{17.76CBR}{t_w}\right)\right]^{-1} \quad (2.2)$$

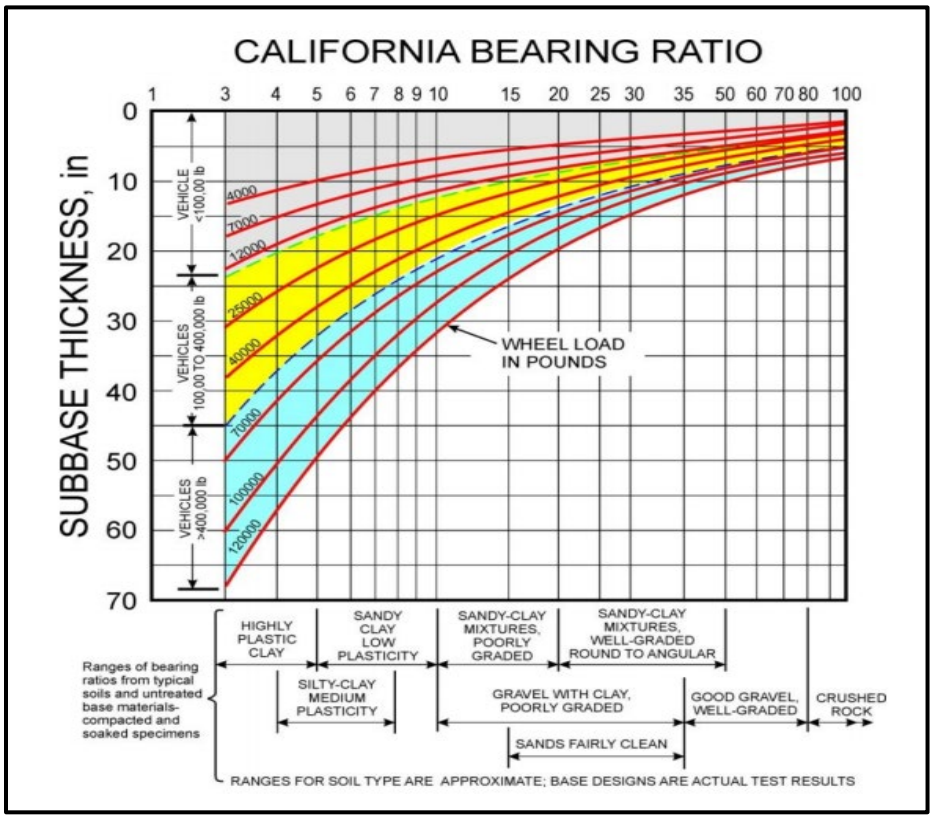

Figure 2.4 CBR cover curve [50]

Z_{CBR} is based on single wheel loading, while Z_{ESWL} is based on the equivalent single wheel loading, a concept that incorporates the effect of the interaction of the rear dual tires.

To use the chart in Figure 2.4, the maximum wheel/tire load is first computed using the gross machine weight (GMW) of the truck. This is generated based on the loaded weight distribution of the truck. The loaded weight distribution of most conventional rear dump ultra-large trucks is 67% of the load to the rear and 33% to the front. To capture the effects of the rear dual tires, the equivalent maximum wheel/tire load is computed by multiplying the maximum rear wheel load by 1.2. This factor accounts for the interaction of the rear dual tire assembly. The CBR method is simple to use and is well understood for road design. The required data is easy to obtain. However, it has several shortcomings including its assumption of constant elastic modulus for different pavement layer materials. It was also developed for paved roads and airfields, and thus, its use for haul road design is not entirely appropriate, as haul roads are unpaved and subject to loading from a different class of vehicles. The curves are also limited for use with ultra-large mine trucks. The CBR curve in Figure 2.4 is sufficient for wheel loads up to 120,000 lbs. Ultra-large trucks have wheel loads exceeding this limit. For example, the CAT 797F, which has a rated gross weight of 623.7 metric tons (1,375,000 lbs), has a maximum wheel load of 230,312.5 lbs and an equivalent maximum wheel load of 276,375 lb. These wheel loads far exceed the range of current CBR charts, and thus, the CBR method is unreliable for haul road design for operations employing ultra-large trucks. The method also assumes constant static wheel loads, which is unrealistic as dynamic loads generated during haulage are typically greater than the static loads.

2.3.2. Mechanistic and Mechanistic-Empirical Pavement Design (MEPD). The method is based on finite element modeling [47] and allows for the computation of road responses (stresses, deflections, and strains) based on selected road design parameters. The

method assumes the road to be a linear-elastic multi-layer system [31], [36]. It is based on the linear elastic layer theorem proposed by Burmister [51], [52]. The design is modified until the response indicators meet the design objectives. In mining applications, the limiting vertical strain (LVS) has been proposed as a reliable response parameter for designing haul roads. The recommended values of the LVS based on the road class are given in Table 2.1.

The responses generated from the mechanistic predictions are used as input into empirical relations to calculate pavement distresses such as rutting, damage, cracking under mechanical and thermal load, and cycles to failure [47]. Thus, the name mechanistic-empirical design approach. If the empirical relations are not used, it is referred to as the mechanistic method. The method presents several advantages compared to the CBR method. It is iterative and can be used satisfactorily without extensive test results. The method has not been widely used for the design and analysis of haul roads, partly due to its complexity. Its other disadvantage is the assumption of static tire loads. In addition, the analysis has been limited to 2D models.

Table 2.1 LVS values for haul road categories [34]

Haul road category	Description	Typical service life (years)	LVS (microstrains)
Category I	Permanent high-volume main haul roads (ex-pit) from ramps to ROM pad or waste dumps	10 – 20	<900
Category II	Semi-permanent high-volume ramp or in-pit haul roads	5 – 10	900 – 1500
Category III	Semi-permanent medium to low volume in-pit bench access or ex-pit waste roads	<5	1500 - 2000

2.4. ROAD SURFACE ROUGHNESS MODELING

Haul roads are usually unpaved and constructed from gravel or crushed mine waste rock. The construction and maintenance typically end with grading. These activities inherently leave haul road surfaces with roughness and undulations, which affect the dynamics of vehicles that interact with the roads. Even the best-constructed and maintained haul roads are not perfectly smooth. Road surface roughness and undulations subject trucks to vertical excitations, resulting in higher impact forces at the tire-road contact. Quinn and Wilson [53] used experimental studies to show that pavement unevenness has a significant impact on the magnitude of tire-pavement contact forces. The excitations also subject truck components and operators to more severe vibrations, which can exceed safe recommended levels. Thus, it is important to consider road surface roughness in vehicle dynamics studies to fully characterize the phenomenon, provide realistic solutions to the problem of road response to truck dynamic loads, operator health, and truck component durability.

Road surface roughness is usually measured using the international roughness index (IRI), which was developed and recommended by the World Bank [54]. The IRI measures the surface roughness using a test vehicle that traverses the test pavement at a constant speed. Sayers [55], [56] presented guidelines for conducting field measurements and calibration of the IRI.

In the mining industry, road surface roughness is measured using real-time truck strut pressure measurements. Strut pressures exceeding a given limit (500 psi) give an indication of rough road surfaces. Onboard systems monitored by the operators give a real-time indication of road surface conditions. When values exceed the given limit, truck operators communicate with motor grader operators to grade the affected road segment.

Roughness models based on power spectral density (PSD) also provide a reliable description of road surface profiles. These PSD models generate a random road profile, which is usually used to evaluate vehicle response, suspension system optimization and dynamic pavement loading. Dodds and Robson [57] presented mathematical models for describing road surface roughness. From experimental and analytical results, they stated that road surface undulations, in the absence of major irregularities like potholes, can be treated as homogenous and isotropic processes. Thus, they can be modeled using a stationary zero-mean random process [58]. Kamash and Robson [59], [60] confirmed this assumption and proposed a road classification system ranging from very good (motorways and principal roads) to very poor (unpaved or damaged roads), based on the PSD of the road surface. The paper indicated the need for more experiments to validate the proposed road classes.

Kondo [61] studied the relation between haul road surface roughness and damage of off-highway trucks. The study designed a road profiler for measuring off-highway road roughness using a laser beam and conducted a global survey on haul road surface conditions. The paper proposed a classification system, which was a modification of the ISO draft system (ISO/TC108), for classifying mine haul road roughness. A global survey of haul roads classified most haul roads as “B” (poor) and “C” (very poor), with a few being classified as “A” (very good or good) due to proper maintenance. Poorly constructed and maintained roads generally fell under classes “D” and “E”. Results showed that road roughness greatly affected truck durability and operator comfort. Truck damage increased over a hundredfold when the same truck moved from class “A” to class “D” roads. The paper did not assess the impact of road roughness on the road structural damage.

Sun [54] presented a simulation-based approach for modeling road surface IRI based on known PSD of the road. Using a quarter-vehicle model, the paper modeled the vehicle response to road surface-induced vertical excitations using numerical models. Regression models were built to relate road surface PSD roughness to the roughness wave numbers. The regression models were built for highways, which typically have smoother surfaces compared to haul roads. Sun and Kennedy [62] established an analytical quarter-vehicle model for studying the effects of pavement roughness, vehicle speed and vehicle parameters (e.g. mass, suspension, and tire properties) on dynamic loads imposed on roads. They found that the various vehicle parameters have varying effects on pavement loading. In addition, they stated that road roughness has a tremendous effect on pavement loading. Law and Zhu [63] made similar observations for multi-span bridges using numerical and experimental studies. The bridge was modeled as a multi-span continuous Bernoulli-Euler beam with a non-uniform cross-section.

Kim et al. [64] used 3D numerical models to study the impact of bridge roughness on bridge-vehicle interactions. They derived the EOMs for the vehicle-bridge system using Lagrange formulation and solved the equations using the Newmark-β numerical solution algorithm. Ding et al. [65] stated that a vehicle moving on a bridge impacts two distinct forces on the bridge: the deterministic moving dynamic force due to the vehicle's weight and the random interaction force due to the pavement roughness. They computed these two components of the vehicle-bridge interaction force using the Runge-Kutta method and found the total dynamic force as the sum of the two components. They also found that vehicle dynamic forces were highly reliant on the road surface roughness and significantly greater than the static force of the vehicle.

Yin et al. [66] modeled the response of a bridge to vehicular loading using a non-stationary random road surface model, based on the covariance equivalence technique. They used a two-axle vehicle with three different bridge models to study the behavior of the bridge under varying vehicular speed. It was observed that the amplitude of the vehicle wheel response increased as the vehicle speed increased. They stated that using stationary random models could underestimate or overestimate the vehicle dynamic response.

Oliva et al. [67], [68] studied the dynamics of a full vehicle moving on a concrete bridge using the finite element method. They considered the influence of parallel road profiles (Figure 2.5) on vehicle dynamics and found that the dynamics of one side of the vehicle affect the other side. The road profiles were prescribed as vertical displacement on each wheel of the vehicle. The papers also presented PSD based models for generating parallel road profiles for the left and right wheels based on ISO 8608 models. Oliva et al. [69] produced a software, PRP generator, whose bedrock is the ISO 8608 PSD road roughness model, for generating road profiles. This product simplified the generation of random road surfaces.

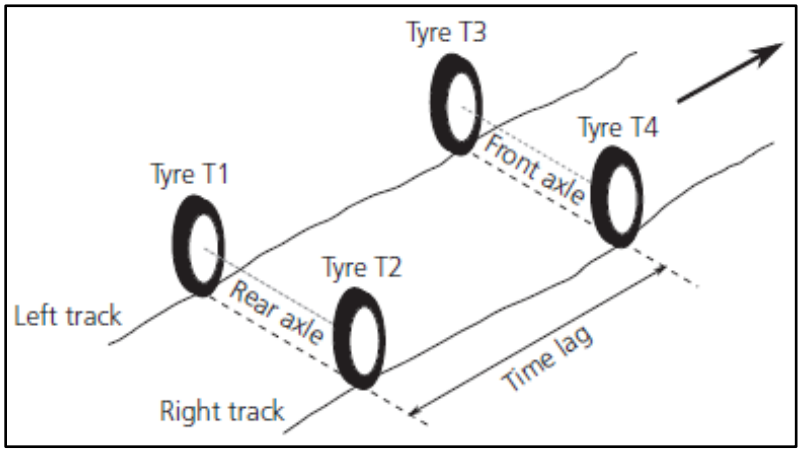

Figure 2.5 Parallel road profiles for full vehicle dynamics simulation [67]

Andren [58] provided a comprehensive survey of road roughness models. He stated that road surfaces should obey the stationary random process assumption in order to use PSD models to describe their surface roughness. A stationary random process is defined as a process/phenomenon whose statistical properties do not change over time or over the length of the road. The road profile must also be homogenous and isotropic. Gorges et al. [70] presented a three-part road classification model for describing road horizontal curviness, road slope/grade changes (hilliness of the road) and road surface roughness. They indicated that such models were necessary for defining vehicle design targets.

Very few studies have considered haul road surface roughness in modeling truck dynamics. Prem [71] showed that haul road unevenness is a major factor in determining the fatigue life of haul truck mainframes and other major components. The study obtained experimental road roughness data using a walking profiler and constructed a 3D rough road model in MSC.ADAMS, to study truck response to road roughness. The study found that truck tire dynamic loads can be 1.7 times the static loads during lane change, and 1.3 times the static load on straight route travel. The dynamic loads were projected to increase as the road roughness increased. It was stated that such higher dynamic loads can increase tire heat buildup and cause rapid tire damage.

Rahimdel et al. [28] studied the impact of haul road roughness on vibrations that reach the truck operators. He modeled the road roughness using the ISO 8608 road roughness model and conducted numerical experiments to study the vibrations reaching the operator at varying road surface roughness and truck speed. It was found that road roughness has a higher impact on operator exposure to vibrations than the truck speed.

Hugo [72] and Hugo et al. [73] used a quarter vehicle model to study haul truck response during haulage and formulated maintenance plans based on identified road defects. They modeled the truck as a 7 DOF system and conducted field measurements of truck dynamic response during haulage. The import of the work was to use measured truck dynamics to identify haul road defects and plan maintenance. The models gave a satisfactory correlation between vehicle dynamics and road defects. This then formed the basis for planning road maintenance schedules to improve road surface conditions.

Ngwangwa et al. [74]–[76] used artificial neural network (ANN) models to reconstruct road surface defects based on measured vehicle responses (vehicle vertical accelerations). The haul truck dynamics were excited by subjecting it to vertical motions using the ISO 8608 road roughness model for road classes ranging from A (very good) to H (terribly bad). The ANN models proved to work satisfactorily under varying truck payloads, road classes, and truck speeds. The study also showed that the ISO PSD road roughness model could be used in combination with the much popular international roughness index (IRI) to enhance the interpretation of road roughness data.

None of these works focused on haul road structural response to dynamic impact loads due to road roughness. The works generally focused on the truck components and the operator. Thus, there is the need to determine the impact of dynamic truck tire loads on haul road structural performance to aid the robust structural design of mine haul roads. None of the works gave a quantitative assessment of truck health based on the dynamic loads. Data-driven models do not exist for predicting strut pressure during haulage. This study modeled the response of haul roads to dynamic loads, the impact of haul road

roughness and imbalanced loading on truck health and the formulation of data-driven models for truck strut pressure prediction.

2.5. VEHICLE-ROAD INTERACTION DYNAMICS

Understanding truck-haul road interaction during haulage is necessary for the design of structurally sustainable haul roads. The interaction is important for accurate estimation of truck tire dynamic forces, which serve as the main input for road response computations. Vehicle-terrain interaction has been widely studied by several authors.

Yap [77] emphasized that tire-road interaction impacts truck operations cost and safety, as well as pavement life. Experimental studies were conducted to assess the influence of truck operational parameters (inflation pressure, tire load, wheel alignment, vehicle speed, and vehicle suspension) on tire-road contact pressures. The studies estimated the effect of tire load and inflation pressure on contact stresses. He stated that the tire load and velocity generate three-component forces; the vertical, lateral and longitudinal forces. The tire longitudinal and lateral forces are generated due to the bending of the tire under loads. He also asserted that the maximum tire contact pressures occur at the midpoint of the contact area as shown in Figure 2.6.

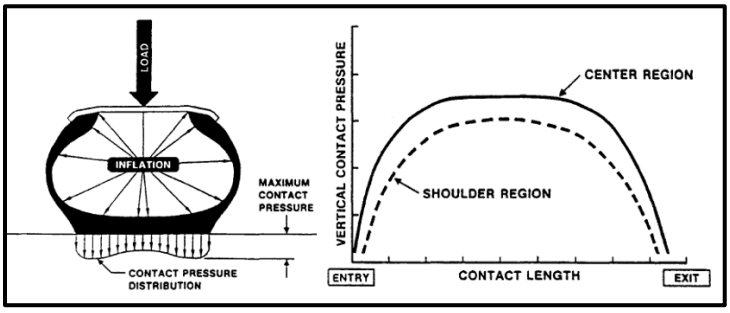

Figure 2.6 Contact pressure distribution [77]

Tire vertical stresses are mainly influenced by tire construction and design. The bias-ply tire generates lower contact pressures compared to the radial-ply tire. Higher inflation pressures resulted in higher contact pressures. Increasing truckloads also caused a corresponding increase in contact pressure.

Bakker et al. [78] formulated a model for predicting tire longitudinal and lateral forces and aligning moment using coefficients that describe the tire-road contact behavior in steady-state maneuvers. They used a sine function as shown in Equations 2.3 and 2.4, to model the three tire dynamic quantities for pure cornering, pure braking and combined cornering and braking maneuvers.

$$\mathrm{Y} = \mathrm{D}\sin(\arctan(\mathrm{B}\phi)) + S_v \tag{2.3}$$

$$\phi = (1 - \mathrm{E})(\mathrm{X} + S_h) + (E/B)\arctan(\mathrm{B}(\mathrm{X} + S_h)) \tag{2.4}$$

The peak factor, D, defines the peak lateral or longitudinal force or peak aligning moment. The product BCD defines the slip stiffness at zero slip. The factors of the model are determined by fitting experimental data to the model. This model is now referred to as the magic formula (MF). It is known to accurately predict tire dynamics and extrapolate well outside the known data domain.

Pacejka and Besselink [79] extended the work of Bakker et al. [78] to predict tire horizontal dynamics during transient maneuvers. The improved MF incorporated non-steady state vehicle travels and proposed a simple model for longitudinal and lateral transient responses restricted to relatively low time and path frequencies of road roughness. They also introduced the concept of pneumatic trail and residual aligning moments for

computing the tire aligning moment. The transient contact properties were modeled using the contact mass approach, which assumes a mass attached to the tire-ground contact. This mass can undergo translational deflections and hence is modeled as a mass-spring-damping system. Higuchi and Pacejka [80] provided a mathematical model for the transient force and moment characteristics of tires involving large slip and camber.

Ružinskas and Sivilevičius [81] applied the MF tire model for tire-ice interaction. They used the least-squares minimization technique to fit experimental data to the MF model and determined the model coefficients for icy roads. Another fitting technique used to determine MF coefficients is genetic algorithms [82], [83].

The MF tire model has many coefficients, which require experimental data for parameterization. Acquisition of the required data is very costly; thus, some attempts have been made to develop less expensive experimental methods for acquiring the required data. Smith and Blundell [84] presented a method for efficiently deriving the magic formula coefficients with fewer tests. The procedure, known as the GS2MF FreeRolling test, is a nine-stage test procedure leading to the generation of tire forces and moments under varying inflation pressures, and for small and large slip and camber angles.

Van Gennip and McPhee [85] also developed an alternative test method for generating tire dynamic forces and moments under steady-state and transient conditions. Unlike the conventional and GS2MF test procedures, which require dedicated tire test facilities, the authors presented an on-road test method called the Vehicle Measurement System (VMS). The procedure requires that three main sensors be attached to each vehicle tire. These sensors are the Wheel Force Sensor (WFS) for measuring the wheel dynamic forces and moments and Wheel Position Sensor (WPS) for measuring real-time 3D wheel

position. The last sensor is the Laser Ground Sensor/Laser Doppler Velocimeter (LGS/LDV) for measuring wheel longitudinal and lateral speed and vehicle height, which are used to determine the effective wheel radius.

Pacejka [86] and [87] presented several models for vehicle dynamics in the steady and non-steady state under pure cornering, braking, and combined maneuvers. The brush tire model was presented, in addition to the MF model. The model is premised on the assumption that the tire tread elements in contact with the road can deflect in a direction parallel to the road, like how the bristles of a brush deflect when it is rolled on a hard surface. This model can predict tire horizontal forces and moments in conditions of pure and combined slip. A major advantage of the brush model is that it requires fewer input parameters [88] and does not need curve fitting to determine model coefficients.

In addition to the MF tire model (empirical) and brush model (physics-based), analytical and finite element tire models exist for studying tire-terrain interactions. Li and Shindler [89], [90] and [91] modeled the tire as a 3D solid assembly consisting of the tread block, belt, and carcass layers, sidewall, beads, and rim. Nyaaba [37] used a similar, but much detailed approach, to model an ultra-large mining truck tire using hyperelastic (Ogden) and linear viscoelastic (Prony Series) rubber material models. These models are very comprehensive and represent the tire much better. However, they require strong computational facilities and long model run times, limiting their applicability. They also require experimental data for model calibration.

Analytical models are based on the works of [92], [93] and [94]. Tires are described as either rigid or deformable. Rigid tires maintain the same radius throughout their operation, while deformable tires have a continuously changing radius, which is typically

smaller than the unloaded radius. Tires that have very high inflation pressure are assumed to show no appreciable deformation during operation. Thus, they are assumed rigid. Those that show significant deformation during operation or when loaded are considered deformable. The terrain is also modeled as either soft/deformable or rigid. Rigid terrains do not allow tire penetration, while deformable terrains allow significant tire penetration.

Machine-terrain interaction has been studied in mining for several reasons including tire stress profiling, truck vibrations, and bench structural integrity modeling. Li and Frimpong [38] and [95] used flexible multi-body dynamics in MSC.ADAMS to study truck-road interaction dynamics, tire stress profiling, and road deformation. A two-layer oil sands road (surface and subgrade) was modeled as a series of soil units connected via spherical joints (Figure 2.7). The road surface was assumed perfectly flat and smooth. Soil elasticity was modeled using springs and dampers.

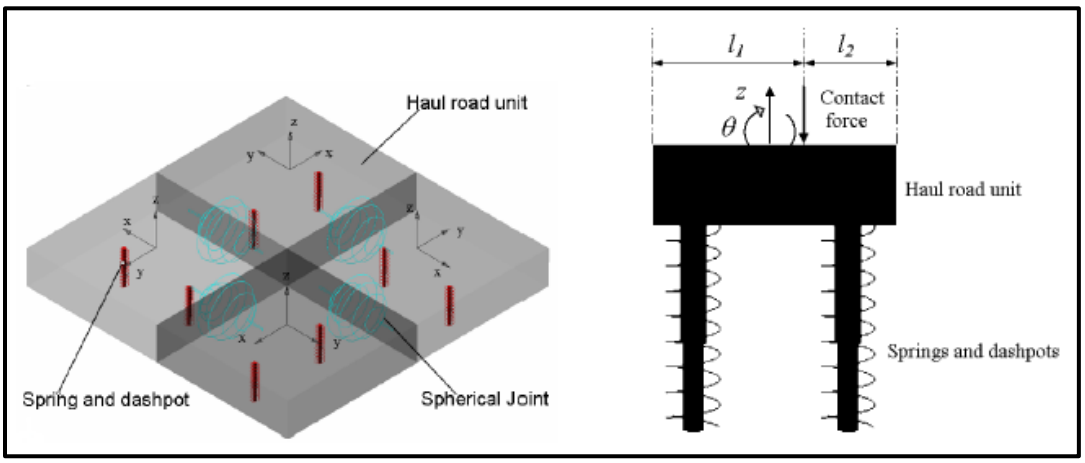

Figure 2.7 Mass-spring-damper haul road model [95]

Aouad and Frimpong [96], used a 3D rigid multi DOF virtual prototype model in MSC.ADAMS to study operator exposure to whole-body vibrations (WBV) during high

impact shovel loading operations (HISLO). MSC.ADAMS has also been used to study the kinematics [97], [98] and dynamics [99] of shovel crawler-oils sands terrain interactions. The oil sands were modeled as soil units connected by spherical joints.

Siegrist [100], and Siegrist and McAree [39] used the extended Kalman filter to study the dynamics of dump truck tire-haul road interaction. They developed a framework for the real-time estimation of tire-road contact forces. Virtual prototype modeling in MSC.ADAMS was used to estimate tire forces based on truck-road interaction dynamics for various maneuvers. Tire dynamic forces were generally greater than the static forces.

Lu et al. [101] used numerical and experimental studies based on multi-body dynamics, to study the stochastic dynamic tire forces under varying truckloads, speed, tire stiffness, and road roughness. MSC.ADAMS was used to develop a virtual prototype for conducting detailed experiments, saving cost, time and risk. Lagrangian mechanics was used to derive the EOMs, which were numerically solved by MSC.ADAMS. The results indicated that tire dynamic forces were less affected by vehicle speed, while the truckload had a significant influence on dynamic tire loading. Tire stiffness and road roughness had a great influence on tire dynamic load. Silva et al. [102] used MSC.ADAMS and MATLAB/SIMULINK co-simulation to model the tire dynamics for vehicle control purposes.

Other multi-body dynamic commercial packages like LMS-DADS and VEHDYN [103] have been successfully used to model vehicle-terrain interactions. Further information on vehicle-terrain models can be obtained from [104], which presented a comprehensive review of existing tire-terrain interaction models applied in different environments.

2.6. ROAD RESPONSE MODELING

Understanding the phenomenon of road response to vehicle induced stresses is necessary for designing roads of sufficient structural strength to sustain the increasing vehicle loads. This is particularly important in the mining industry, where truck capacities have increased significantly. A peculiar challenge is presented in the mining environment where ultra-large trucks must be operated on unpaved roads constructed with locally available materials for economic reasons. However, haul road structural response modeling has not been widely investigated in the existing body of knowledge.

Beskou and Theodorakopoulos [105] provided a comprehensive review of pavement analysis techniques. They stated that the pavement could be modeled as a plate, beam or top layer of a layered pavement system. Pavement foundations have been modeled as a system of elastic springs and dashpots, a homogeneous or layered half-space. Vehicle loads are modeled as concentrated or distributed static or dynamic loads on circular, rectangular or elliptical contact areas. The analysis techniques can generally be classified as analytical, numerical and hybrid analytical-numerical techniques. Numerical techniques employed include the FEM, discrete element method (DEM) and boundary element method (BEM). Kausel [106] added that discrete dynamic models could be used to model pavement structures and other continuum systems. Plane strain, axisymmetric and 3D modeling techniques have been employed to model pavements.

Burmister theory of stress distributions in layered pavement systems has been used as the basis for developing solutions to road response problems. Burmister [51] developed the general theory for stresses and displacements in a two-layered pavement system (Figure

2.8). The theory utilized Boussinesq equations for the derivation of the stress equations and provided a numerical evaluation of pavement displacements.

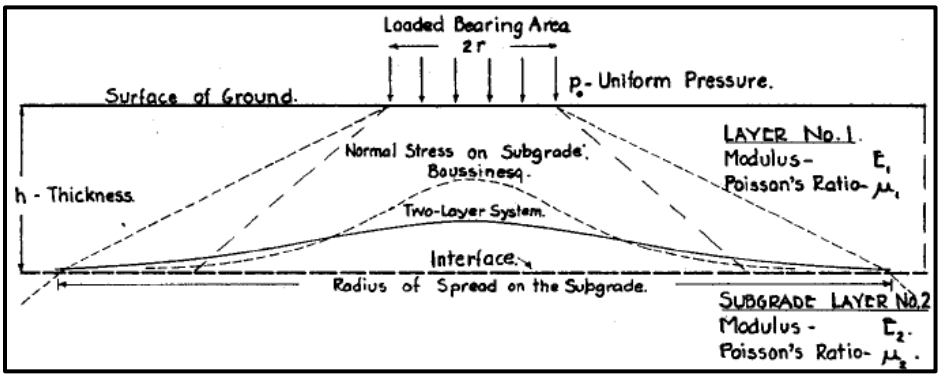

Figure 2.8 Burmister's two-layer pavement system [51]

Boussinesq equations assume that each pavement layer is homogeneous, isotropic and linear elastic, and thus, can be characterized by the elastic modulus and Poisson ratio. Burmister [51] advanced the stress and displacement theory for the case where there is frictionless contact between the two layers. Further advancement of the theories for three-layered pavements was presented by [52]. Bufler [107] provided solutions to the elasticity equations for stress and displacement in multi-layered pavements using the integral transforms and matrix analysis.

Due to the rise in computational power, robust and efficient computer programs have been developed for studying the road response to vehicular loading. Most of these programs are based on FEM and DEM. Al-Qadi et al. [108] developed a 3D FE model using implicit dynamic analysis in ABAQUS for studying the response of an asphalt road to dynamic vehicle loads. The hot-mix-asphalt (HMA) surface layer was modeled as a viscoelastic layer underlain by granular layers. The study found that longitudinal tensile

strains were the critical responses for thin asphalt pavements, whereas the vertical shear strains were most important in thick asphalt pavements.

Wang and Al-Qadi [109] extended the work of [108] to study the influence of tire-terrain contact pressure on HMA response to dynamic loads. They found that the 3D contact stresses induced higher shear strains and octahedral shear stresses near the pavement surface, while at greater depths, transverse tensile and compressive strains were higher. The importance of non-uniform tire-road contact stresses was highlighted, as the uniform contact stress assumption appeared to underestimate road response.

Green [110] studied the response of flexible asphalt pavements under dynamic vehicle loading using field experimentation and the FE method in ABAQUS. The work examined pavement response under varying vehicle speed and pavement temperatures. It was discovered that asphalt pavement response was heavily influenced by pavement temperature, with vehicle speed playing a less critical role.

Picoux et al. [111] develop a 2D multi-layered FEM to predict the dynamic response of flexible pavements to vehicle dynamic loads. The study showed that dynamic responses were significantly higher than the static road responses. It also stated that various materials constituting the different road layers obey different deformation laws. Their numerical model was solved using the central difference method (CDM). Experimental results were obtained from falling weight deflectometer (FWD) tests for model validation.

Kim et al. [112] made a comparative analysis of the FEM and MEPD technique proposed by the American Association of State Highway and Transportation Officials (AASHTO). They stated that the MEPD guide is limited for predicting the mechanical response of asphalt pavements to vehicle loading due to its use of simple elastic layered

theory and assumption of circular tire loading. Their FEM model, developed in ABAQUS, accounted for the viscoelastic behavior of the pavement material, which better characterized HMA pavements than the elastic layered theory.

Wu et al. [113] used FEM to simulate the structural performance of the stabilized base and subbase/subgrade materials under repeated vehicular loading. They proposed a permanent deformation elastoplastic material model for characterizing the base and subbase materials. A predictive transfer function was also developed for modeling permanent pavement deformation under vehicular loading. Results from the simulations showed that lime/fly ash treated soil could be a viable alternative to cement-treated soil for pavement base and subbase/subgrade construction. The sensitivity analysis of model geometry showed that an axisymmetric model was both computationally efficient and accurate for modeling pavement response.

Huang et al. [114] developed a nonlinear viscoelastic-viscoplastic constitutive model for modeling the response of HMA pavements to static vehicle loading. A 3D FEM model was developed for modeling the response of a three-layer road structure to varying vehicle loads under various temperatures. The simulations show that cracking in the asphalt layer was induced by tensile viscoplastic strain accumulations at the pavement surface. The study also found that, at high pavement temperatures (≥40 °C), tensile viscoplastic strains developed at the sides of the applied load due to asphalt mixture heave associated with permanent deformation.

Zheng et al. [115] used experimental and numerical methods to study the dynamic stresses and deformation of a four-layered pavement system subjected to vehicle dynamic forces. A physical four-layered road (wearing surface, base, subbase, and subgrade) was

subjected to tire loads that were assumed to act on a circular contact area. Transducers were installed in the various road layers to measure tire forces and road elastic and plastic deformation under tire loading. The transmission and reflection matrix (TRM) method was used to solve the dynamic response of the layered road structure. The experiments examined the influence of road layer elastic modulus and thickness on the road response. The study found that dynamic loading resulted in higher pavement stress and deformation compared to static loading. It also found that road layer response is sensitive to layer modulus and thickness. Thus, these parameters must be carefully selected in road design.

Cui et al. [116] used experimental studies based on the FWD tests to study traffic-induced settlement of road subgrade under dynamic vehicular loading. The FLAC 3D program, a numerical analysis software, which uses finite difference approximations, was used for simulating the road subgrade response to loading. The study found that the area between a set of vehicle dual tires experiences the largest stress. As the layer depth increased, stresses reduced significantly.

Tang et al. [117] used the shakedown concept to study the traffic-induced load influence depths on clayey subgrade materials. Three distinct depths of influence were identified, based on experimental tests; (1) The threshold depth (the maximum depth of influence), beyond which the dynamic effect of the traffic loads is considered negligible; (2) the plastic shakedown limit depth, within which the subsoil experiences noticeable and continuous deformation; (3) the critical failure depth, within which the soil would undergo failure due to excessive strain. These depths of influence were determined for different vehicle classes, ranging from a lightweight car to an over-loaded truck. Heavier vehicles had higher depths of influence, implying that the stresses induced by the heavier vehicles

traveled deeper into the pavement. Understanding the depth of influence served as a basis for determining strategies to improve the bearing capacity of roads.

Lu et al. [118] used analytical techniques to evaluate the response of highway embankment to dynamically imposed wheel loads. The vehicle was modeled as a multi DOF system, while the road was modeled as two elastic layers resting on a poroelastic soil medium (subgrade). The dynamic stiffness matrix method was used to solve the dynamic response of the layered road-ground structure interaction. The wheel–pavement contact dynamics were captured via a Hertzian contact spring between the wheel and the pavement. The spatial fast Fourier transform (FFT) algorithm was used for numerically solving the system of equations. The study found that pavement surface unevenness and rigidity significantly affect dynamic forces imposed on the road, which also affect road response.

Beskou et al. [119] used 3D time-domain FEM in ANSYS to study the dynamic response of a three-layered flexible pavement to vehicle loads. Linear elastic material models were used to model the pavement and supporting road layers. Eight-node 3D elements, with three translational DOF per node, were used for meshing the road model in ANSYS. Dynamic loading caused more pavement damage than static loading.

Liu et al. [120] used a semi-analytical finite element method (SAFEM) to study the response of asphalt pavements to heavy traffic loading. SAFEM is a 3D FE program that requires a 2D mesh with the third dimension incorporated via the Fourier series. The method improved the computational efficiency of the traditional FEM and had satisfactory accuracy. The program developed was verified using experimental results. The study indicated that asphalt pavement thickness and stiffness should be increased adequately to ensure satisfactory structural performance under heavy loads.

Chen and Zhou [121] studied the dynamic response of railway subgrade materials under double-line high-speed trains using 3D FEM implemented in ABAQUS. The subgrade layer was subdivided into three layers. Train speeds ranged from 250 to 360 km/hr. The rails were modeled using Euler-Bernoulli beam elements, while the slab, subgrade, foundation, and other layers were modeled using eight-node hexahedral solid elements. The Mohr-Coulomb model was used for the subgrade. They found that the maximum vertical subgrade displacement decreased with increasing train speed. In addition, maximum vertical stresses occurred right beneath the rails on the subgrade surface, with asymmetric stress distributions on the subgrade.

Ling et al. [122] conducted a dynamic stress analysis of homogeneous and inhomogeneous subgrade under single moving aircraft loads using SAFEM. Like the SAFEM proposed by [120], the method used Fourier transform to reduce the 3D FEM to a 2D problem. The study indicated that the dynamic stresses in the subgrade under single-wheel moving aircraft load are mainly vertical normal stresses and in-plane shear stresses.

Very few studies have been conducted to understand and quantify the impact of dynamic truckloads on haul roads. None of the studies has considered ultra-large trucks. Most studies have focused on operator exposure to truck induced vibrations and on understanding truck-haul dynamic force generation. Li and Frimpong [38] and [95] studied the impact of dynamic truck loading on haul road response for CAT 775E. They used flexible multi-body and soil dynamics formulations to virtually simulate dump truck tire-haul road interactions in MSC.ADAMS and MSC.NASTRAN. The studies examined truck tire dynamic forces, haul road deformation and tire stress distributions under varying truck loads and road material elasticity. It was found that road deformation increased non-

linearly with increasing truckload and decreased non-linearly with increasing road elasticity. The work considered the haul road as a two-layer pavement. The CAT 775E has low payload and is phasing out gradually in the mining industry. Ultra-large trucks impose high dynamic forces and require research efforts to quantify their impact on haul roads.

2.7. ROAD MATERIAL MODELS

When the tire interacts with the road, stresses are generated in the layers, as shown in Figure 2.9. Well-suited material models need to be defined for each road layer to model their response to vehicle induced stresses. Several models exist for characterizing pavement materials. These can generally be classified as elastic, plastic, elastoplastic, viscoelastic, viscoplastic, hypoelastic and their combinations. The choice of a model is influenced by the material response, computational resources, and input data availability.

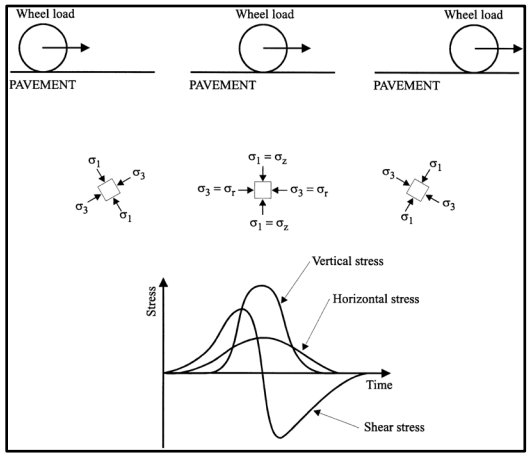

Figure 2.9 Stresses beneath a rolling wheel load [123]

Some of the available material models for granular geomaterials are the Mohr-Coulomb (M-C), Cam-Clay (C-C), and modified Cam-Clay (MCC), Matsuoka-Nakai,

Lade-Duncan, and Drucker-Prager models. These models have been implemented in various commercial numerical modeling packages like ABAQUS, ANSYS and FLAC.

2.7.1. Cam-Clay (C-C) and Modified Cam-Clay (MCC). The C-C and MCC models are critical state soil mechanics (CSSM) models for describing the behavior of soft soils/clays under stress conditions. They were formulated by [124], [125] and [126] to determine soil strength, dilatancy/compression and the critical state at which soil elements can experience unlimited distortion without any changes in stress or volume. The C-C/MCC models require three main input parameters, namely, the mean effective stress in Equation 2.5, deviatoric stress in Equation 2.6 and specific volume in Equation 2.7. Equations 2.5 and 2.6 can be found in [127], [128]. Effective stress, σ'_{ij}, is the difference between total stress and pore water pressure. The yield criteria for the Cam-Clay and modified Cam-Clay models are defined in Equations 2.8 and 2.9, respectively [129].

$$p' = \frac{1}{3}(\sigma'_{11} + \sigma'_{22} + \sigma'_{33}) \tag{2.5}$$

$$q = \frac{1}{\sqrt{2}}\sqrt{(\sigma'_{11} - \sigma'_{22})^2 + (\sigma'_{22} - \sigma'_{33})^2 + (\sigma'_{33} - \sigma'_{11})^2 + 6(\sigma'_{12} + \sigma'_{23} + \sigma'_{13})^2} \tag{2.6}$$

$$v = 1 + e \tag{2.7}$$

$$f(\sigma, p_c) = q + M p \ln\left(\frac{p}{p_c}\right) = 0 \tag{2.8}$$

$$f(\sigma, p_c) = \frac{q^2}{M^2} + p(p - p_c) = 0 \tag{2.9}$$

M is the slope of the critical state line (CSL) in the p – q plane (Figure 2.10) and p_c is the stress-like hardening variable, called pre-consolidation pressure.

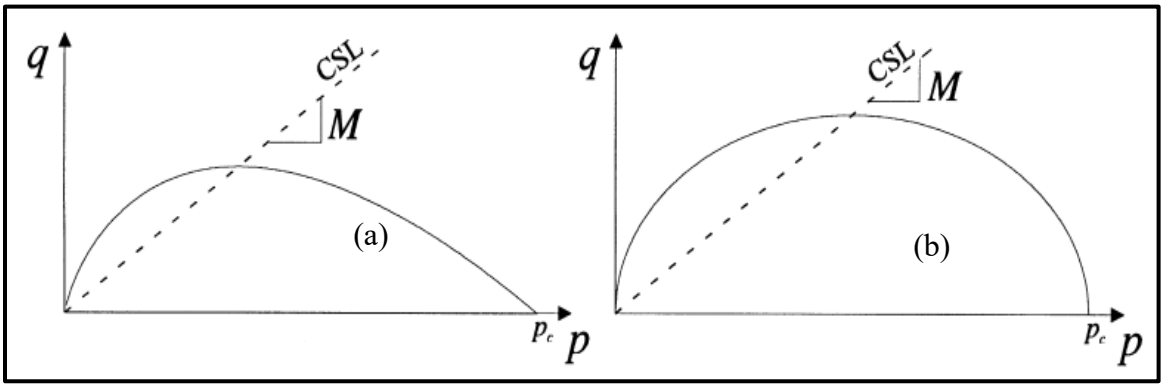

Figure 2.10 Yield curves for (a) C-C and (b) MCC in p – q plane [129]

The C-C and MCC models have been used to characterize granular pavement materials. White et al. [130] stated that clayey pavement layers can satisfactorily be modeled using the C-C model, which uses a strain rate decomposition. The layer deformation is composed of elastic and plastic deformation. The model, however, has parameters, which are complicated and require expensive laboratory tests. The model is also computationally expensive, limiting its use in commercial FE codes.

Takeuchi et al. [131] modeled the cyclic loading of tri-axial compression of a granular base course material using a revised MCC model. They indicated that the model could be used for compacted and normally consolidated clayey subgrade, granular base course, and open grade asphalt materials. The revised model incorporated rotational hardening in the MCC model. Chai and Miura [132] used the MCC model to model the response of soft subsoil under pavement layers subjected to traffic loads. Sukumaran et al. [133] used the C-C to model a clayey subgrade under an airfield pavement. Saad et al. [134], [135] used an elastoplastic strain hardening MCC model for clayey and silty subgrade materials.

The review shows that the C-C and MCC models are used for fine-grained materials and, on a few instances, for coarse granular materials and asphalt materials. Most of the works reviewed used the C-C and MCC models for subgrade materials. The major limitations to its applications are the expensive computational times and difficult-to-acquire model parameters.

2.7.2. Drucker-Prager Model. The Drucker-Prager model is a non-linear elastoplastic [130], [136], [137] and 3D pressure-dependent [138] model for estimating the stress distributions through granular geomaterials. It is a generalization of the Mohr-Coulomb failure law. At low stress levels, the materials show elastic behavior, until the yield stress is reached, beyond which the materials exhibit plastic deformation, as shown in Figure 2.11 [139]. Thus, the total strain is a sum of the elastic and plastic strains.

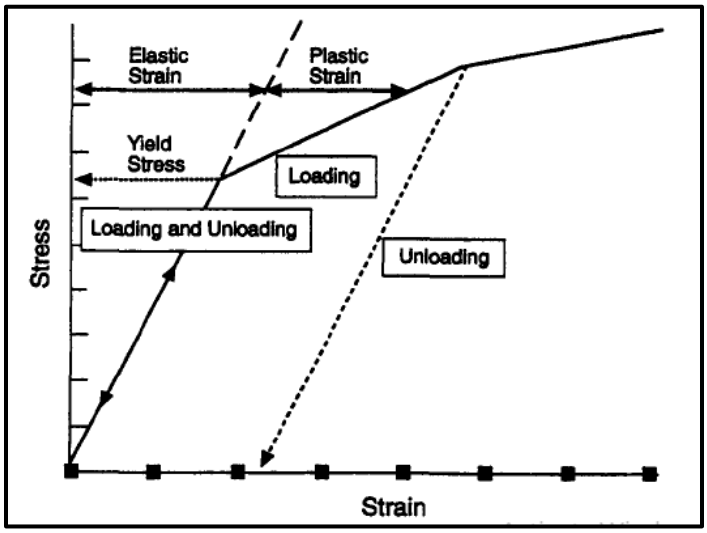

Figure 2.11 Drucker-Prager model for granular geomaterials [130]

According to [138], the Drucker-Prager failure criterion is generally defined using Equation 2.10. J_2 and I'_1 are given by Equations 2.11 and 2.12, respectively. The material

constants, λ, and κ, are functions of the material cohesion (c) and internal friction angle (φ), as given by Equations 2.13 and 2.14.

$$\sqrt{J_2} = \lambda I'_1 + \kappa \tag{2.10}$$

$$J_2 = \frac{1}{6}[(\sigma'_1 - \sigma'_2)^2 + (\sigma'_1 - \sigma'_3)^2 + (\sigma'_2 - \sigma'_3)^2] \tag{2.11}$$

$$I'_1 = \sigma'_1 + \sigma'_2 + \sigma'_3 \tag{2.12}$$

$$\lambda = \frac{2\sin\varphi}{\sqrt{3}(3-\sin\varphi)} \tag{2.13}$$

$$\kappa = \frac{6c\times\cos\varphi}{\sqrt{3}(3-\sin\varphi)} \tag{2.14}$$

The main strengths of the Drucker-Prager model lie in its simplicity, and its smooth and symmetric failure surface in the stress space [138]. These strengths make its implementation in numerical packages easy. However, it overestimates rock strength and produces unreliable results when used to model triaxial extension [138]. The Drucker-Prager model has been incorporated into commercial numerical codes such as ANSYS, ABAQUS, COMSOL, FLAC, and PFC, and utilized for modeling pavement response.

Seibi et al. [140] found, through experimental data fitting, that the Drucker-Prager model was best for characterizing asphalt concrete (AC) pavement materials subjected to vehicular loading. The model was implemented in ABAQUS for modeling AC pavement material response. Huang et al. [141], [142] and [143] applied an elastic-plastic Drucker-Prager criterion to model the granular base and subgrade layers of concrete pavement.

Park et al. [144] modified the conventional Drucker-Prager model to account for differences in tensile and compressive yield stresses in HMA pavements. The model

satisfactorily fitted experimental and numerical results. The model captured important properties of HMA such as its confinement dependency, dilation, friction, and cohesive and adhesive properties [114], [144]. Tashman et al. [145] formulated an anisotropic viscoplastic continuum damage model by modifying the original Drucker-Prager model to accommodate asphalt material anisotropy and microstructural damage. The revised model included a damage parameter to capture the nucleation of cracks and growth of air voids and cracks during asphalt layer deformation. Masad et al. [146] and [147] used an extended elastoplastic Drucker-Prager model to characterize the response of concrete slabs to explosive loads. The soil formation underlying the slabs was modeled using a modified Drucker-Prager/Cap model. The explosives were hung and blasted at varying heights above the concrete slab. They used the propagation of cracks in the concrete slabs to indicate the location and quantity of explosives used during terrorist attacks. Ivorra et al. [148] also modeled concrete behavior using the Drucker-Prager model.

Chazallon et al. [149] used the Drucker-Prager model to compute the permanent deformation of pavement materials under traffic loading based on the shakedown theory. Al-Khateeb et al. [150] used FEM to model pavement rutting under repeated static loads. The pavement materials were modeled using a linear elastoplastic Drucker-Prager model implemented in ABAQUS. A comparison of the model results using field results of the FWD tests showed that the Drucker-Prager model performed satisfactorily for granular pavement materials. Gu et al. [151] also satisfactorily applied a modified Drucker-Prager model to granular pavement materials. The review shows that the Drucker-Prager model is good for granular materials such as road wearing courses, base and subbase materials.

2.7.3. Mohr-Coulomb (M-C) Model. The Mohr-Coulomb (M-C) model is probably the most widely used material model for geomechanics applications. It has also found application in medicine, where it has been used to model bone fracture using FEM techniques [152], [153]. The model has also been modified and used to predict ductile fracture of metals [154]. It is an elastoplastic model and can be used to model materials undergoing strain softening/hardening.

The model consists of a set of linear equations in principal stress space describing the conditions for which an isotropic material will fail [155]. The M-C failure criterion is generally given by Equation 2.15, which relates the material strength to its inherent shear strength (cohesion) and internal friction angle [156], [155]. It assumes that the material yields when the shear stress, τ, on any point in the material reaches a threshold value, which depends linearly on the normal stress [157]. In terms of principal stresses, the M-C criterion is defined by Equation 2.16 [156]. The M-C model is diagrammatically represented in Figure 2.12. According to [157], the yield criterion (f) is defined by Equation 2.17.

$$\tau = c + \sigma \tan\varphi \tag{2.15}$$

$$\sigma_1 = \sigma_3 \, tan^2\left(45 + \frac{1}{2}\varphi\right) + 2c \, tan\left(45 + \frac{1}{2}\varphi\right) \tag{2.16}$$

$$f = \sigma_1 - \sigma_3 \left(\frac{1+sin\,\varphi}{1-sin\,\varphi}\right) + 2c \left(\sqrt{\frac{1+sin\,\varphi}{1-sin\,\varphi}}\right) \tag{2.17}$$

The M-C model has been incorporated into several numerical modeling software and used to model pavement materials by various researchers. Fahey and Carter [158] used the Mohr-Coulomb failure criterion, implemented in CAMFE commercial 1D FE code, to

model the unload-reload stress-strain behavior of sand. Though the 1D model is inadequate for modeling the problem, computational power at the time was limited. The model served as a basis for building advanced models as computational resources advanced over time.

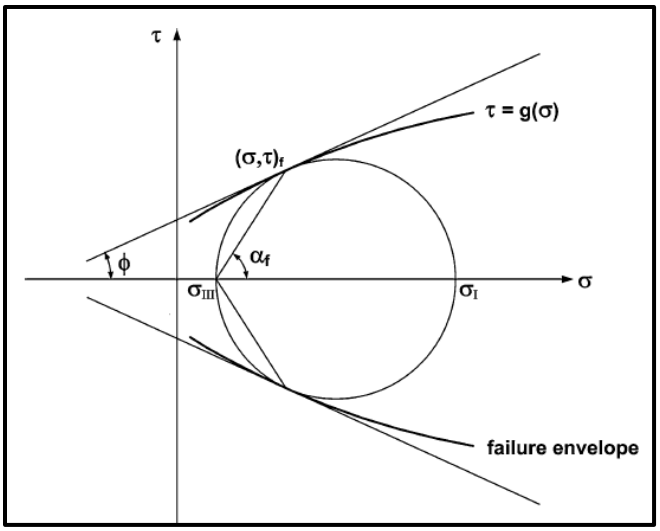

Figure 2.12 Mohr diagram and failure envelopes [155]

Sloan [159] modified the original M-C model using linear programming theories. The modified model was used for computing lower bound limit loads in the soil in plane strain conditions using FEM. The technique developed was recommended for producing stability charts for various soil mechanics applications. Collins et al. [160] used the M-C failure criterion to analyze the mechanical response of granular unbound pavement materials to repeated traffic loading. They modeled the pavement as a layered elastic-plastic system whose response was described using the shakedown concept. The shakedown concept assumes that when the pavement is subjected to repeated loading beyond its elastic limit, the buildup of residual stresses and changing material properties

can be such that the response is purely elastic [161]. No further permanent strains occur beyond this limit [160].

Ling and Liu [162] modeled the response of asphalt pavement with geogrid reinforcement to monotonic loading using an elastoplastic M-C criterion with associated and non-associated flow rules. The models were implemented in a commercial FE code called PLAXIS. Howard and Warren [163] also applied the M-C model for natural subgrade materials due to its relative simplicity. Gbadam and Frimpong [157] employed the FEM, in ABAQUS, to model oil sands bench structural integrity under power shovel crawler static loads. The oil sands were modeled using the Mohr-Coulomb model. The study provided understanding into crawler-oil sands interactions and oil sands response to heavy machinery loading. Some advantages of the M-C model are the simplicity of gathering its input data and its appropriateness for modeling the response of granular materials subjected to dynamic loading. Thus, an elastoplastic MC model in ABAQUS was used in this research for modeling the response of a four-layer haul road to ultra-large truck dynamic loads.

2.8. Ph.D. RESEARCH RATIONALE

Haul roads play a critical role in mine operations and directly impact mine safety, productivity, and profitability. They also influence truck components and operator health. When a truck interacts with the haul road, dynamic loads are imposed on the haul road by the truck tires, inducing stresses into the road structure. The dynamic loads are significantly influenced by road surface roughness and truck payload. Prem [71] used a rigid body virtual prototype to simulate the dynamics of a mine haul truck undergoing various

maneuvers. Results from the study showed that dynamic tire forces, due to road roughness could be 1.7 times the rated static tire load. These higher dynamic tire forces induce greater stresses on the road compared to the static loads and can cause accelerated road deterioration.

Li and Frimpong [38] studied the dynamic tire forces for a rigid body dump truck and modeled the deformation of the haul road due to the dynamic tire forces. Their study considered trucks with much lower payload ratings than current ultra-large mining trucks. They also assumed flat and perfectly smooth haul road surfaces. This is impractical in mining environments. Haul roads inherently have very rough surfaces since they are usually unpaved. The model also considered the haul road to be a two-layer road consisting of a surface resting on a subgrade. Mine haul roads typically have four layers. No study has modeled the effect of ultra-large truck dynamic loading on haul roads. Thus, advanced research initiatives are required to model ultra-large truck dynamic forces for rough roads and the response of the road to these dynamic forces. Research is also required to understand the impact of payload imbalance and truck operating parameters on truck health. This research is being advanced to provide knowledge in these directions towards improved haul road structural design and truck health. This research explored mathematical and virtual prototype modeling to achieve the research objectives. The mathematical and virtual prototype models are based on multi-body dynamics (MBD) and finite element modeling (FEM). Field data was also obtained for model validation and for gaining insights on the impact of road roughness and imbalanced payloads on truck health during haulage.

Road surface roughness is typically modeled using PSD models. The ISO 8608 road roughness model has been proven to adequately represent road surfaces of varying

roughness. This research applies the ISO 8608 PSD based road roughness model, implemented in PRP generator [69], to generate random road roughness for various road classes. The literature shows that most haul roads are of the Class D type due to their unpaved nature, and thus, this work focuses on class D roads.

Detailed mathematical modeling based on Lagrangian formulation was used to understand the mechanics of truck-haul load transfer during haulage. The mathematical model was formulated using an 18 DOF model consisting of a half truck model and four-layer haul road. The model incorporated road surface roughness using the ISO 8608 model. A reduced solution of the mathematical model was obtained for a single truck tire in MATLAB/SIMULINK®. The detailed solution, based on Newmark-β integration, was obtained using a 72-DOFs virtual prototype model in MSC.ADAMS. The virtual prototype model is based on rigid multi-body dynamics theory and consists of rigid bodies connected via joints and spring-damper elements [38], [71].

Advancement in computational resources has resulted in the use of efficient commercial FE software for modeling pavement structures under dynamic vehicle loads. Several authors have studied the response of flexible/asphalt [151], [164], [165] and rigid/concrete pavements to static and dynamic loads. The approaches have been applied to commercial roads and airfields. To date, no attempt has been made to model haul road response to ultra-large truck dynamic loads. This study is a pioneering effort to provide understanding of haul road stress-strain response under ultra-large truck dynamic loads.

A 3D explicit dynamics FEM approach was adopted in this research to model the response of haul road to dynamic truck loads. The dynamic tire forces generated from MSC.ADAMS were used as input to the FE models. Detailed experimentation was

conducted to establish the effect of the base, subbase and subgrade elastic modulus and truck payloads on the road response. FE modeling was conducted in ABAQUS, which has proven to be very robust and efficient for modeling pavements.

Road layer materials have been modeled as linear elastic, elastoplastic, plastic, viscoelastic and viscoplastic materials. Characterizing the materials with the appropriate model is very necessary to model its response. A guiding principle in choosing the appropriate model is the availability of input data and the easy incorporation of the model into available software. An elastoplastic Mohr-Coulomb model was implemented in ABAQUS to model the haul road layers.

2.9. SUMMARY

A detailed literature review has been undertaken to understand the existing body of knowledge and to lay a solid foundation for this research. The review points out important contributions and advancements of modeling techniques for vehicle-terrain interaction and pavement response modeling, which are the core of this research. It also identifies gaps for further work, some of which this research study addresses to advance the frontier. The review shows that ultra-large trucks are preferred due to their economies of scale, efficiency, and high productivity. These ultra-large trucks impose very high dynamic loads on the haul road during haulage. However, there has not been much research undertaken on haul road structural performance.

Haul road design has primarily been conducted using experience and empirical approaches [41]. Mechanistic approaches discussed in literature have generally applied 2D FE models, with static truck loading [25]. The only available 3D dynamic model [38] has

maximum truck wheel loads of 57 tons. The work also modeled the road as a two-layer road. Current ultra-large trucks (≥220 tons) present unique dynamic interactions with haul roads. In addition, conventional mine haul roads have four layers.

This research contributes to the existing body of knowledge by (i) formulating mathematical and virtual MBD models for computing truck tire dynamic forces imposed on the haul road during haulage, (ii) conducting truck health analysis using the ASA and formulating data-driven models for computing truck strut pressure during haulage, and (iii) modeling a four-layer haul road response to ultra-large truck dynamic forces using 3D FEM. These contributions advance knowledge towards improvement in ultra-large truck health and haul road structural design.

3. MECHANICS OF ULTRA-LARGE TRUCK-ROAD INTERACTION

The gross machine weight of a fully loaded truck is transferred unto the haul road when the loaded dump truck interacts with the road. The objective of haul road design is to reduce the truck induced stresses to near zero at the surface of the subgrade to ensure long-term stability. The CBR method has been used to achieve this objective. However, the method gives unreliable designs for mine environments since it was designed for light vehicle traffic on commercial roads. Ultra-large trucks have equivalent maximum tire loads up to 276,375 lbs, while the CBR curves are applicable for tire loads up to 120,000 lbs as shown in Figure 2.4. This section presents an 18-DOF mathematical model that captures the mechanics of load transfer from ultra-large truck body through the suspension systems and tires to haul roads. The mathematical model provides a tool for analytically examining truck-haul road dynamics, which formed the basis for the 72-DOF rigid MBD modeling and experimentation in MSC.ADAMS.

The model was built on the basis that the truck-haul road system is a multi-body system (MBS) consisting of rigid elements (masses) connected via springs and dampers, representing the suspension systems. The Lagrangian formulation, which relies on the energy method, was used to develop the governing EOMs for the system. The system was modeled using a half truck and four-layered haul road model, with 18 DOFs. The DOFs account for the vertical displacement of each system component of the truck and haul road during haulage. The DOFs are defined as:

- One (1) DOF representing the truck body vertical displacement;
- Two (2) DOFs for the chassis vertical and pitch motions;

- Three (3) DOFs representing the vertical displacement of the front and set of rear tires; and
- Twelve (12) DOFs representing the vertical displacement of the units of wearing surface, base, subbase and subgrade under the front, rear outer and rear inner tires.

The half truck consists of the truck body (with operator cabin), chassis, and three tires (one front and set of rear dual tires). The assumption behind the use of the half truck-road model is that the truck and road have longitudinal symmetry. Thus, the truck can be divided into two halves, left and right, along the x-axis, with each half experiencing similar kinematics and dynamics during haulage.

The truck was represented with six (6) DOFs consisting of the truck body (with payload and operator cabin) vertical motion, chassis vertical displacement and pitch motion, and displacement of front and set of rear dual tires. The truck considered in this research is CAT 797F conventional rear dump truck as shown in Figure 3.1.

Figure 3.1 CAT 797F conventional rear dump truck [166]

The haul road was modeled as a four-layer (wearing surface, base, subbase, and subgrade) structure having twelve (12) DOFs. The road was assumed to consist of distinct

units, with each unit modeled as a mass-spring-damper system [38], [40]. A unit each from each road layer is assumed to underlie each truck tire. Thus, twelve units (representing the 12 DOFs) are used to represent the road; four units under the front and eight under the set of rear tires. The final mathematical model is a system of eighteen coupled second-order differential equations.

The model initially assumed that there is no interaction between the two rear tires. This generated the solutions for the response of the system to exclusive loading from each tire. An interaction model was then developed that captures the combined effect of the dual rear tires. These equations completely capture the dynamics of the truck-haul road system during haulage. Solutions to these equations generate the truck dynamic forces that serve as input for the haul road response model.

3.1. LOAD TRANSFER MECHANICS OF THE TRUCK-HAUL ROAD SYSTEM

When a loaded truck travels on the haul road, the dynamic forces generated from the GMW are transferred to the road through a series of springs and dampers representing the truck suspension systems. The final transfer points are the tires, where the forces generated from the truck GMW are transferred to the haul road through the tire-road contact. These dynamic forces are dependent on the truck payload and haul road surface roughness/undulations. Figure 3.2 illustrates the load transfer mechanism from the truck to the haul road during haulage.

An accurate model of the forces imposed on the haul road by the trucks is an important step for the design of structurally competent haul roads. Since the imposed dynamic forces and road response are the focus of this study, the truck model was simplified by considering

the operator cabin assembly and truck bucket as one component. In this model, the vertical downward forces are considered positive. The longitudinal forward motion and lateral forces to the left are also considered positive.

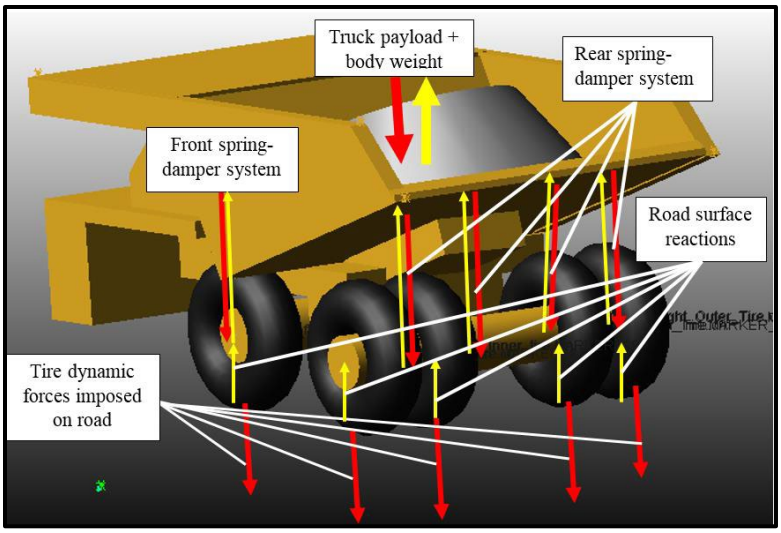

Figure 3.2 Load transfer from truck body to haul road

Figure 3.2 shows that the truckload gets distributed on each tire through the spring and damper system connecting the truck body to each tire. This load is ultimately transferred to the haul road via the truck tires. The suspension systems and road generate reactive forces that are assumed to act in the vertical direction only. The truck dynamic forces are a function of the vehicle component masses, payload, road surface roughness, suspension system properties, and tire stiffness and damping coefficients, the vehicle traveling speed and other operating variables. Truck dynamic forces include the force due to truck body and payload, spring reactions to the payload/machine forces and tire forces due to tire mass, stiffness and damping. The haul road, which is modeled as a mass-spring-damper system, also generates internal forces in response to the induced truckloads.

Figure 3.3 is a schematic of the truck-haul road system, showing the masses connected via spring-damper systems. In Figure 3.3, the suspension systems that connect the truck body to the chassis (represented by k_1 and c_1) are placed at a distance, a, from the center of gravity (CG) of the chassis. The one connecting the truck chassis to the front tires (k_{2f} and c_{2f}) is placed at a distance, e, from CG of the chassis.

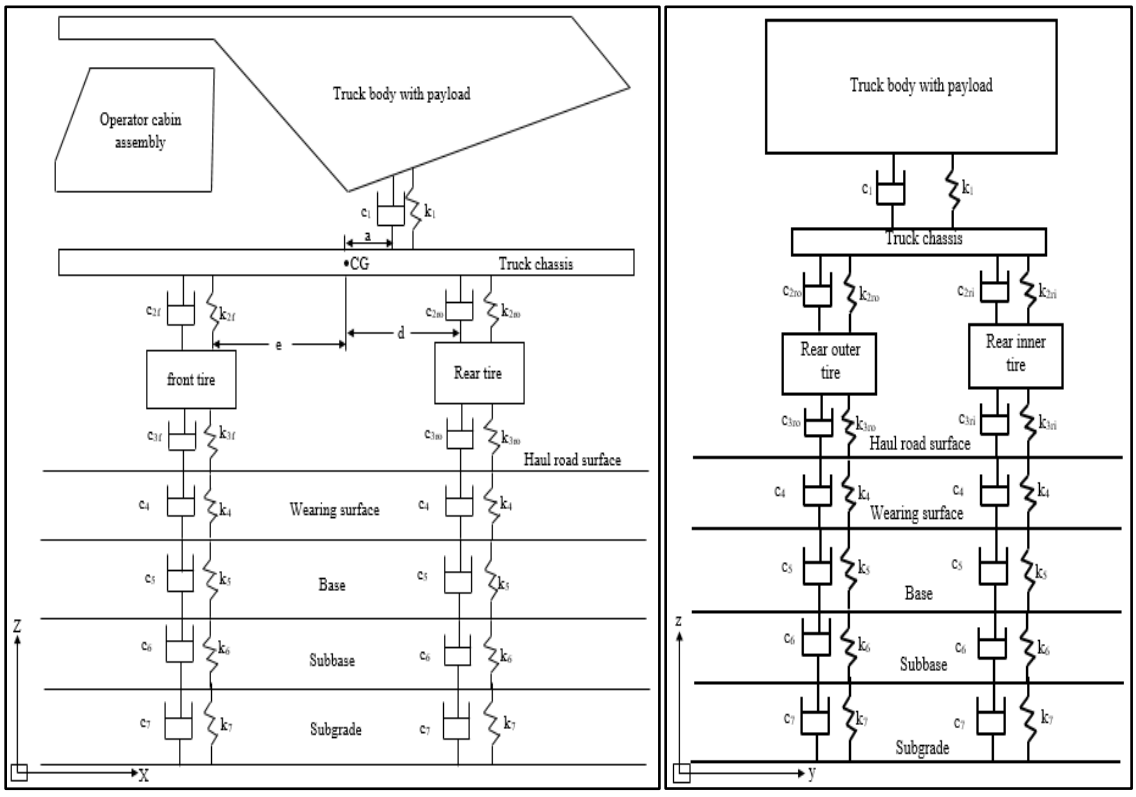

(a) (b)

Figure 3.3 Dump truck-haul road response to dynamic truck forces (a) side and (b) rear views

The suspension systems connecting the chassis to the rear outer (k_{2ro} and c_{2ro}) and rear inner (k_{2ri} and c_{2ri}) tires are at a distance, d, from CG of the chassis. The front tires are

represented by k_{3f} and c_{3f}, while the rear outer tires are represented by k_{3ro} and c_{3ro}, and the rear inner tires are represented by k_{3ri} and c_{3ri}.

Similarly, the wearing surface, base, subbase and subgrade units under the front tire are represented by k_{4f} and c_{4f}, k_{5f} and c_{5f}, k_{6f} and c_{6f}, and k_{7f} and c_{7f}, respectively. The road layer units under the rear outer tire are represented by k_{4ro} and c_{4ro}, k_{5ro} and c_{5ro}, k_{6ro} and c_{6ro}, and k_{7ro} and c_{7ro}, respectively, for the wearing surface, base, subbase, and subgrade. The road layer units under the rear inner tire are represented by k_{4ri} and c_{4ri}, k_{5ri} and c_{5ri}, k_{6ri} and c_{6ri}, and k_{7ri} and c_{7ri}, respectively, for the wearing surface, base, subbase, and subgrade. The k's and c's describe the spring stiffness and damping coefficients, respectively, of the various system spring-dampers. A free-body diagram (FBD) describing the load transfer from the truck external force, $F_1(t)$, to the road subgrade is given in Figure 3.4. Figure 3.4 also shows the vertical displacement, z_i, experienced by each component of the system in response to the external force.

The mass of the truck body, chassis, font tire, rear outer tire, and rear inner tire are given by m_1, m_2, m_{3f}, m_{3ro}, and m_{3ri}, respectively. The mass of the units of wearing surface, base, subbase, and subgrade under the truck tires are represented by m_4, m_5, m_6, and m_7, respectively. The external force, $F_1(t)$, imposed on the truck by the payload is transferred through the suspension systems connecting the truck body to the chassis. This generates the spring and damping forces, F_{k1} and F_{c1}, caused by the downward-upward displacement of the truck body by an amount, z_1. There is also pitching of the chassis with respect to the road surface at an angle θ.

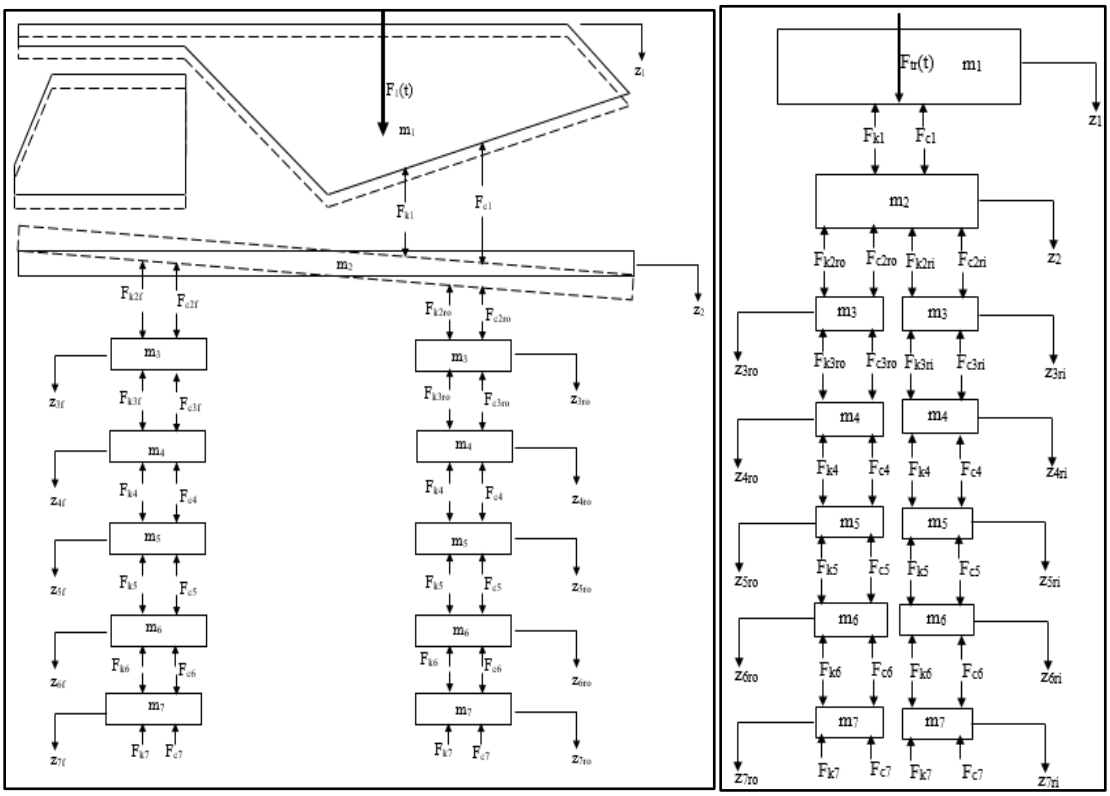

Figure 3.4 FBD of truck-haul road under dynamic forces in the (a) side and (b) rear views

The chassis then responds to this force by being displaced downward-upward by an amount, z_2. This generates the forces, F_{k2f} and F_{c2f}, at the front suspension system connecting the chassis to the front tire. The corresponding forces on the suspension systems connecting the chassis to the rear outer and rear inner tires are F_{k2ro} and F_{c2ro}, and F_{k2ri} and F_{c2ri}, respectively. Other components of the system are displaced in a similar manner, generating the corresponding inertia, spring and damping forces as shown in Figure 3.4. Finally, reactions forces, $F_{k7f,}$ F_{c7f}, F_{k7ro}, F_{c7ro}, $F_{k7ri,}$ and F_{c7ri}, are generated at the bottom of the subgrade, which is considered fixed with respect to the in-situ formation since it is assumed that deformation at the bottom of the subgrade is zero.

Some components of the excitations at the road surface are transmitted to the operator seat, subjecting the operator to WBV, which can be harmful to operators beyond safe limits defined by ISO 2631 [40]. The excitations can also subject the truck to high torsional stresses, which can reduce component durability. The component that is transmitted to the haul road subjects the road to stresses, which can cause structural defects such as ruts and potholes. The developed structural defects cause haulage inefficiencies, expose truck components and operators to higher vibrations and ultimately, reduce productivity and increase operating costs. Therefore, the road layers must be designed to reduce the stresses at the subgrade below its bearing capacity to ensure sustained road life, reduced road user cost and improved productivity and safety.

3.2. GENERALIZED LAGRANGIAN FORMULATION

The EOMs governing the behavior of the truck-haul road system were formulated using Lagrangian formulation, which is based on the energy method. The energy method, based on the principle of conservation of energy, assumes that the total mechanical energy in a system remains constant and it can only be transformed from one form to another. The Lagrangian method describes the mechanics of a particle or system of particles using the generalized coordinates and velocities. This method relies on the total energy of the system, composed of the kinetic and potential energies, to describe the system dynamics. The resulting equations are known as Lagrange equations or Euler-Lagrange EOMs. The equations in this section were derived from [40] and form the basis for formulating the EOMs in Sections 3.3 and 3.4.

Assume a system of N particles (N = 18 for the 18 DOFs), each of mass, m_i, and position vector, **r**, expressed as a function of generalized coordinates, q_i, as shown in Equation 3.1.

$$\mathbf{r} = \mathrm{f}(q_i, q_j, q_k, \mathrm{t}) \tag{3.1}$$

The force applied to each mass in the system can then be expressed as the gradient of the potential energy function, V(r, t), which depends on the position of each mass at a given time, as shown in Equation 3.2.

$$F = -\nabla V = -\frac{\partial V}{\partial q_i} \tag{3.2}$$

The position/motion of each mass, at any time, can be fully described by six independent DOFs consisting of three displacement (r_i) and three velocity (r'_i) DOFs. The velocity DOFs are a time derivatives of the displacement DOFs. Therefore, the motion of a system component, at any given time, can be represented by its position expressed as cartesian coordinates, x, y, and z, and velocities, v_x, v_y, and v_z, defined by Equation 3.3.

$$\begin{pmatrix} v_x \\ v_y \\ v_z \end{pmatrix} = \begin{pmatrix} \frac{\partial x}{\partial t} \\ \frac{\partial y}{\partial t} \\ \frac{\partial z}{\partial t} \end{pmatrix} \tag{3.3}$$

The work done by the applied force (due to the payload and truck weight) on an arbitrary particle with mass, m, having undergone a displacement, δr, can be defined as δW = F.δr, which can be written as Equation 3.4, according to Newton's second law of motion.

$$F.\delta r = m\ddot{r}\delta \mathrm{r} \tag{3.4}$$

Re-writing Equation 3.4 in terms of q_i and the corresponding $\dot{q}_i$, the left-hand side of Equation 3.4 transforms to Equation 3.5, while the right-hand side transforms into Equation 3.6.

$$F.\delta r = -\nabla V \sum_i \frac{\partial r}{\partial q_i}\delta \mathrm{q}_i = -\sum_{\mathrm{i,j}} \frac{\partial V}{\partial r_j}\frac{\partial r}{\partial q_i}\delta \mathrm{q}_i = -\sum_i \frac{\partial V}{\partial q_i}\delta \mathrm{q}_i \tag{3.5}$$

$$m\ddot{r}\delta \mathrm{r} = \sum_i \left[\frac{d}{\mathrm{dt}}\frac{\partial T}{\partial \dot{q}_i} - \frac{\partial T}{\partial q_i}\right]\delta \mathrm{q}_i \tag{3.6}$$

T and V can be found using Equations 3.7 and 3.8, respectively. The work done on a particle can then be computed using Equation 3.9.

$$T = \frac{1}{2}m\dot{r}^2 \tag{3.7}$$

$$V = \frac{1}{2}\mathrm{kr}^2 \tag{3.8}$$

$$\sum_i \left[\frac{d}{\mathrm{dt}}\frac{\partial T}{\partial \dot{q}_i} - \frac{\partial (T-V)}{\partial q_i}\right]\delta \mathrm{q}_i = 0 \tag{3.9}$$

Since the potential and kinetic energies of the particle cannot be zero during haulage, δq_i from Equation 3.9 should be equal to zero. Equation 3.7 shows that the kinetic energy, T, is only a function of generalized velocities. From Equation 3.8, the potential energy is dependent on the generalized coordinates. Since V is independent of the generalized velocities, its derivative with respect to the generalized velocities is zero, as shown in Equation 3.10.

$$\frac{d}{\mathrm{dt}}\frac{\partial V}{\partial \dot{q}_i} = 0 \tag{3.10}$$

Putting Equation 3.10 into 3.9 and defining the Lagrangian, L = T – V, yields the Lagrange equations for a system as presented in Equation 3.11.

$$\frac{\partial L}{\partial q_i} = \frac{d}{\mathrm{dt}}\frac{\partial L}{\partial \dot{q}_i} \tag{3.11}$$

Equation 3.11 is written for each generalized coordinate, q_i, representing each DOF. When the generalized coordinates, q_i, are the same as the cartesian coordinates, r_i, the Lagrange equations reduce to Newton's second law of motion. Equation 3.11 assumes that the system is conservative, that is, the work done by the force is independent of its path and equivalent to the difference between the final (kinetic) and initial (potential) energies of the system. Conservative systems do not dissipate energy and are completely reversible.

The assumption of a conservative system is not applicable to the truck-road interaction problem studied in this research. The truck has components such as the

suspension systems, which dissipate energy through the dampers when an external force is introduced or when the system is disturbed. This allows the system to come to rest from a disturbed state. The various road layers also have dissipation characteristics represented by the dampers. Thus, the truck-road interaction problem during haulage cannot be an ideal conservative system. Equation 3.11 is modified to appropriately capture the system dissipation characteristics by including a dissipation energy term (R) and the generalized external forces acting on the system, $Q_i(t)$. Equation 3.12 completely describes the behavior of the non-conservative truck-haul road system under external excitation.

$$\frac{d}{\mathrm{dt}}\left(\frac{\partial L}{\partial \dot{q}_i}\right) - \frac{\partial L}{\partial q_i} + \frac{\partial R}{\partial \dot{q}_i} = Q_i(t) \tag{3.12}$$

R is given by Equation 3.13. $Q_i(t)$ represents any form of external force on the truck-road system. In this research, the payload force is taken as the only external force acting on the truck.

$$\mathrm{R}=\frac{1}{2}c\dot{r}^2 \tag{3.13}$$

3.3. EOMs FOR THE TRUCK-HAUL ROAD SYSTEM

The EOMs for the eighteen (18) DOFs system were derived using the Lagrangian formulation in Equation 3.12. The equations presented in this section were novel developments, unless specified by the source. They were developed for the CAT 797F truck but are applicable to trucks with similar construction as the CAT 797F. Figure 3.5

gives a detailed FBD of the forces acting on the truck-haul road system. For the eighteen (18) DOFs system, 18 governing equations result for completely describing the dynamics of the truck-haul road system.

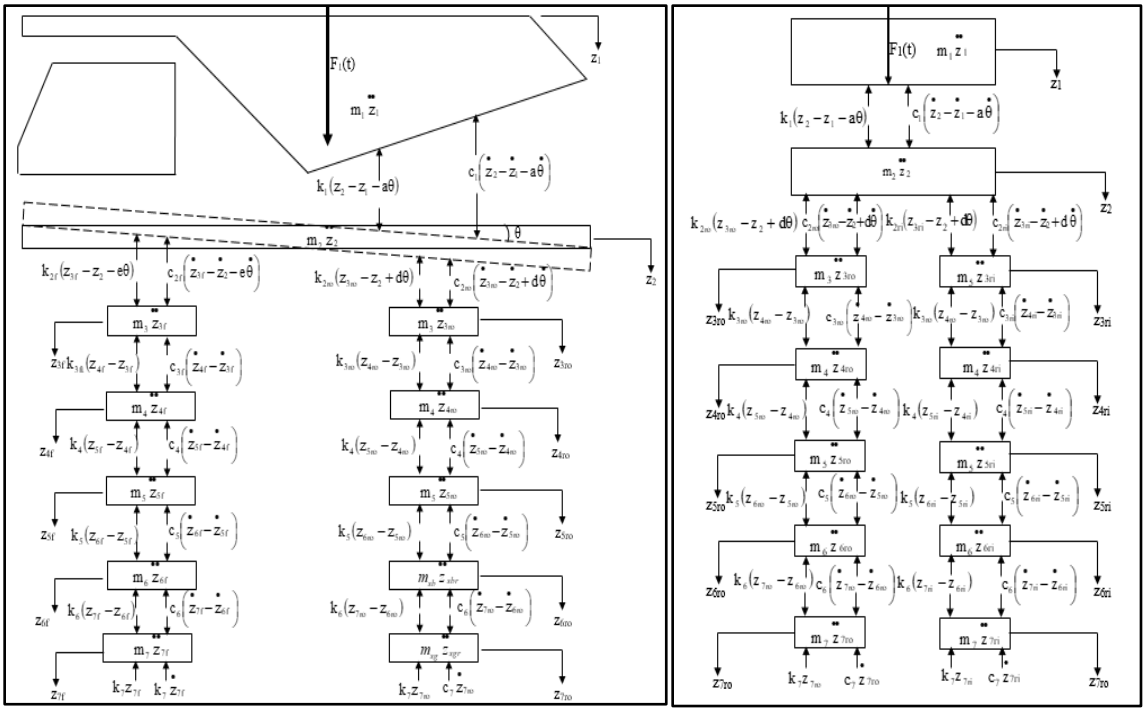

(a) (b)

Figure 3.5 FBD of forces acting on the truck-haul road system in (a) side and (b) rear views

The forces captured in this model include the external force due to the material/payload weight and the internal forces consisting of inertia, spring and damping forces. Using the Lagrangian formulation, the kinetic, potential and strain/dissipation energies of the system were first found as required by Equation 3.12. From Figure 3.5, the total kinetic (T), potential (V) and dissipation (R) energies of the truck-haul road system can be given by Equations 3.14, 3.15 and 3.16, respectively.

$$T = \frac{1}{2}m_1\dot{z}_1^2 + \frac{1}{2}m_2\dot{z}_2^2 + \frac{1}{2}I_2\dot{\theta}^2 + \frac{1}{2}m_3\left(\dot{z}_{3f}^2 + \dot{z}_{3ro}^2 + \dot{z}_{3ri}^2\right) + \frac{1}{2}m_4\left(\dot{z}_{4f}^2 + \dot{z}_{4ro}^2 + \dot{z}_{4ri}^2\right)$$
$$+ \frac{1}{2}m_5\left(\dot{z}_{5f}^2 + \dot{z}_{5ro}^2 + \dot{z}_{5ri}^2\right) + \frac{1}{2}m_6\left(\dot{z}_{6f}^2 + \dot{z}_{6ro}^2 + \dot{z}_{6ri}^2\right) + \frac{1}{2}m_7\left(\dot{z}_{7f}^2 + \dot{z}_{7ro}^2 + \dot{z}_{7ri}^2\right) \quad (3.14)$$

$$V=\frac{1}{2}k_1(z_2\text{-}z_1\text{-}a\theta)^2 + \frac{1}{2}k_{2f}(z_{3f}\text{-}z_2\text{-}e\theta)^2 + \frac{1}{2}k_{2ro}(z_{3ro}\text{-}z_2\text{+}d\theta)^2 + \frac{1}{2}k_{2ri}(z_{3ri}\text{-}z_2\text{+}d\theta)^2$$
$$+\frac{1}{2}k_4[(z_{5f}\text{-}z_{4f})^2 + (z_{5ro}\text{-}z_{4ro})^2 + (z_{5ri}\text{-}z_{4ri})^2] + \frac{1}{2}k_{3f}(z_{4f}\text{-}z_{3f})^2 + \frac{1}{2}k_{3ro}(z_{4ro}\text{-}z_{3ro})^2$$
$$+\frac{1}{2}k_{3ri}(z_{4ri}\text{-}z_{3ri})^2 + \frac{1}{2}k_5[(z_{6f}\text{-}z_{5f})^2 + (z_{6ro}\text{-}z_{5ro})^2 + (z_{6ri}\text{-}z_{5ri})^2] + \frac{1}{2}k_7(z_{7f}^2+z_{7ro}^2+z_{7ri}^2)$$
$$+\frac{1}{2}k_6[(z_{7f}\text{-}z_{6f})^2 + (z_{7ro}\text{-}z_{6ro})^2 + (z_{7ri}\text{-}z_{6ri})^2] \quad (3.15)$$

$$R=\frac{1}{2}c_1\left(\dot{z}_2 - \dot{z}_1\text{-}a\dot{\theta}\right)^2 + \frac{1}{2}c_{2ro}\left(\dot{z}_{3ro} - \dot{z}_2\text{+}d\dot{\theta}\right)^2 + \frac{1}{2}c_{2ri}\left(\dot{z}_{3ri} - \dot{z}_2\text{+}d\dot{\theta}\right)^2$$
$$+\frac{1}{2}c_{3f}\left(\dot{z}_{4f} - \dot{z}_{3f}\right)^2 + \frac{1}{2}c_{3ro}\left(\dot{z}_{4ro} - \dot{z}_{3ro}\right)^2 + \frac{1}{2}c_4\begin{bmatrix}\left(\dot{z}_{5f} - \dot{z}_{4f}\right)^2 \\ +\left(\dot{z}_{5ro} - \dot{z}_{4ro}\right)^2 + \left(\dot{z}_{5ri} - \dot{z}_{4ri}\right)^2\end{bmatrix}$$
$$+\frac{1}{2}c_{3ri}\left(\dot{z}_{4ri} - \dot{z}_{3ri}\right)^2 + \frac{1}{2}c_5\left[\left(\dot{z}_{6f} - \dot{z}_{5f}\right)^2 + \left(\dot{z}_{6ro} - \dot{z}_{5ro}\right)^2 + \left(\dot{z}_{6ri} - \dot{z}_{5ri}\right)^2\right]$$
$$+\frac{1}{2}c_{2f}\left(\dot{z}_{3f} - \dot{z}_2\text{-}e\dot{\theta}\right)^2 + \frac{1}{2}c_6\left[\left(\dot{z}_{7f} - \dot{z}_{6f}\right)^2 + \left(\dot{z}_{7ro} - \dot{z}_{6ro}\right)^2 + \left(\dot{z}_{7ri} - \dot{z}_{6ri}\right)^2\right]$$
$$+\frac{1}{2}c_7\left(\dot{z}_{7f}^2 + \dot{z}_{7ro}^2 + \dot{z}_{7ri}^2\right) \quad (3.16)$$

Rewriting Equation 3.12 for the truck-haul road system considered in this study results in Equation 3.17 [40]. The generalized force vector, $Q_i(t)$ is replaced by the vector of external forces acting on the truck-haul road system, $F_i(t)$. The only non-zero component of $F_i(t)$ is the gravitational force due to the payload, $F_1(t)$. Aerodynamic forces were neglected in this study. This assumption stems from the fact that the truck weight is very

high, and trucks usually travel at relatively lower speeds compared to commercial vehicles on highways. Thus, the air resistive forces have a negligible influence on the truck.

$$\frac{d}{\mathrm{dt}}\left(\frac{\partial T}{\partial \dot{q}_i}-\frac{\partial V}{\partial \dot{q}_i}\right)-\frac{\partial T}{\partial q_i}+\frac{\partial V}{\partial q_i}+\frac{\partial R}{\partial \dot{q}_i}=F_i(t) \tag{3.17}$$

Since the potential energy (V) is only a function of the generalized coordinates, and the kinetic energy is a function of the generalized velocity, the terms $\frac{\partial V}{\partial \dot{q}_i}$ and $\frac{\partial T}{\partial q_i}$ in Equation 3.17 will be equal to zero. Hence, the final Lagrange formulation for the truck-haul road system can be written as Equation 3.18 [40].

$$\frac{d}{\mathrm{dt}}\left(\frac{\partial T}{\partial \dot{q}_i}\right)+\frac{\partial V}{\partial q_i}+\frac{\partial R}{\partial \dot{q}_i}=F_i(t) \tag{3.18}$$

Applying Equation 3.18 to the truck body displacement variable (z_1) results in Equation 3.19. The same procedure was carried out for each DOF, resulting in 18 final Lagrange EOMs for the truck-haul road system.

$$\frac{d}{\mathrm{dt}}\left(\frac{\partial T}{\partial \dot{z}_1}\right)+\frac{\partial V}{\partial z_1}+\frac{\partial R}{\partial \dot{z}_1}=F_1(t) \tag{3.19}$$

Substituting Equations 3.14 to 3.16 into Equation 3.19 yields Equation 3.20 for the truck body (i.e. i = 1) and its suspension system. The same procedure was followed to

derive the EOM for each DOF, resulting in Equations 3.21 to 3.38. These equations are the governing EOMs for completely describing the truck-haul road system dynamics.

$$m_1\ddot{z}_1 + c_1\left(\dot{z}_1 - \dot{z}_2 + a\dot{\theta}\right) + k_1(z_1 - z_2 + a\theta) = F_1(t) \tag{3.20}$$

$F_1(t)$ is the truck external/payload force. For the chassis and its suspension systems, the EOM is given as Equation 3.21.

$$m_2\ddot{z}_2 + c_1\left(\dot{z}_2 - \dot{z}_1 - a\dot{\theta}\right) + c_{2f}\left(\dot{z}_2 - \dot{z}_{3f} + e\dot{\theta}\right) + c_{2ro}\left(\dot{z}_2 - \dot{z}_{3ro} - d\dot{\theta}\right) + c_{2ri}\left(\dot{z}_2 - \dot{z}_{3ri} - d\dot{\theta}\right)$$
$$+ k_1(z_2 - z_1 - a\theta) + k_{2f}(z_2 - z_{3f} + e\theta) + k_{2ro}(z_2 - z_{3ro} - d\theta) + k_{2ri}(z_2 - z_{3ri} - d\theta) = F_2(t) \tag{3.21}$$

$F_2(t)$ is the external force acting on the chassis. For the front tire, rear outer and rear inner tires, the EOMs are given by Equations 3.22, 3.23 and 3.24, respectively.

$$m_3\ddot{z}_{3f} + c_{2f}\left(\dot{z}_{3f} - \dot{z}_2 - e\dot{\theta}\right) + c_{3f}\left(\dot{z}_{3f} - \dot{z}_{4f}\right) + k_{2f}(z_{3f} - z_2 - e\theta) + k_{3f}(z_{3f} - z_{4f}) = F_{3f}(t) \tag{3.22}$$

$$m_3\ddot{z}_{3ro} + c_{2ro}\left(\dot{z}_{3ro} - \dot{z}_2 + d\dot{\theta}\right) + c_{3ro}\left(\dot{z}_{3ro} - \dot{z}_{4ro}\right) + k_{2ro}(z_{3ro} - z_2 + d\theta) + k_{3ro}(z_{3ro} - z_{4ro}) = F_{3ro}(t) \tag{3.23}$$

$$m_3\ddot{z}_{3ri} + c_{2ri}\left(\dot{z}_{3ri} - \dot{z}_2 + d\dot{\theta}\right) + c_{3ri}\left(\dot{z}_{3ri} - \dot{z}_{4ri}\right) + k_{2ri}(z_{3ri} - z_2 + d\theta) + k_{3ri}(z_{3ri} - z_{4ri}) = F_{3ri}(t) \tag{3.24}$$

The EOMs governing the response of the wearing surface to the front, rear outer and rear inner tires dynamic loading are given by Equations 3.25, 3.26 and 3.27, respectively.

$$m_4\ddot{z}_{4f}+c_{3f}(\dot{z}_{4f}-\dot{z}_{3f})+c_4(\dot{z}_{4f}-\dot{z}_{5f})+k_{3f}(z_{4f}-z_{3f})+k_4(z_{4f}-z_{5f})=F_{4f}(t) \quad (3.25)$$

$$m_4\ddot{z}_{4ro}+c_{3ro}(\dot{z}_{4ro}-\dot{z}_{3ro})+c_4(\dot{z}_{4ro}-\dot{z}_{5ro})+k_{3ro}(z_{4ro}-z_{3ro})+k_4(z_{4ro}-z_{5ro})=F_{4ro}(t) \quad (3.26)$$

$$m_4\ddot{z}_{4ri}+c_{3ri}(\dot{z}_{4ri}-\dot{z}_{3ri})+c_4(\dot{z}_{4ri}-\dot{z}_{5ri})+k_{3ri}(z_{4ri}-z_{3ri})+k_4(z_{4ri}-z_{5ri})=F_{4ri}(t) \quad (3.27)$$

Equations 3.28 to 3.30 govern the response of the base layer under the dynamic loading of the front, rear outer and rear inner tires, respectively.

$$m_5\ddot{z}_{5f}+c_4(\dot{z}_{5f}-\dot{z}_{4f})+c_5(\dot{z}_{5f}-\dot{z}_{6f})+k_4(z_{5f}-z_{4f})+k_5(z_{5f}-z_{6f})=F_{5f}(t) \quad (3.28)$$

$$m_5\ddot{z}_{5ro}+c_4(\dot{z}_{5ro}-\dot{z}_{4ro})+c_5(\dot{z}_{5ro}-\dot{z}_{6ro})+k_4(z_{5ro}-z_{4ro})+k_5(z_{5ro}-z_{6ro})=F_{5ro}(t) \quad (3.29)$$

$$m_5\ddot{z}_{5ri}+c_4(\dot{z}_{5ri}-\dot{z}_{4ri})+c_5(\dot{z}_{5ri}-\dot{z}_{6ri})+k_4(z_{5ri}-z_{4ri})+k_5(z_{5ri}-z_{6ri})=F_{5ri}(t) \quad (3.30)$$

Equations 3.31 to 3.33 are the EOMs for the response of the subbase layer units under the dynamic loading of the front, rear outer and rear inner tires, respectively.

$$m_6\ddot{z}_{6f}+c_5(\dot{z}_{6f}-\dot{z}_{5f})+c_6(\dot{z}_{6f}-\dot{z}_{7f})+k_5(z_{6f}-z_{5f})+k_6(z_{6f}-z_{7f})=F_{6f}(t) \quad (3.31)$$

$$m_6\ddot{z}_{6ro}+c_5(\dot{z}_{6ro}-\dot{z}_{5ro})+c_6(\dot{z}_{6ro}-\dot{z}_{7ro})+k_5(z_{6ro}-z_{5ro})+k_6(z_{6ro}-z_{7ro})=F_{6ro}(t) \quad (3.32)$$

$$m_6\ddot{z}_{6ri}+c_5(\dot{z}_{6ri}-\dot{z}_{5ri})+c_6(\dot{z}_{6ri}-\dot{z}_{7ri})+k_5(z_{6ri}-z_{5ri})+k_6(z_{6ri}-z_{7ri})=F_{6ri}(t) \quad (3.33)$$

The response of the subgrade layer units under the dynamic loading of the front, rear outer and rear inner tires can be described using Equations 3.34 to 3.36, respectively.

$$m_7\ddot{z}_{7f} + c_6\left(\dot{z}_{7f} - \dot{z}_{6f}\right) + c_7\dot{z}_{7f} + k_6(z_{7f} - z_{6f}) + k_7 z_{7f} = F_{7f}(t) \quad (3.34)$$

$$m_7\ddot{z}_{7ro} + c_6\left(\dot{z}_{7ro} - \dot{z}_{6ro}\right) + c_7\dot{z}_{7ro} + k_6(z_{7ro} - z_{6ro}) + k_7 z_{7ro} = F_{7ro}(t) \quad (3.35)$$

$$m_7\ddot{z}_{7ri} + c_6\left(\dot{z}_{7ri} - \dot{z}_{6ri}\right) + c_7\dot{z}_{7ri} + k_6(z_{7ri} - z_{6ri}) + k_7 z_{7ri} = F_{7ri}(t) \quad (3.36)$$

Finally, the EOM that captures the pitching of the chassis can be derived from Equation (3.37). The resulting EOM is given by Equation 3.38.

$$\frac{d}{dt}\left(\frac{\partial T}{\partial \dot{\theta}}\right) + \frac{\partial V}{\partial \theta} + \frac{\partial R}{\partial \dot{\theta}} = F_2(t) \quad (3.37)$$

$$\begin{aligned} &I_2\ddot{\theta} + c_1 a\left(\dot{z}_1 - \dot{z}_2 + a\dot{\theta}\right) + c_{2f} e\left(\dot{z}_2 - \dot{z}_{3f} + e\dot{\theta}\right) + c_{2ro} d\left(\dot{z}_{3ro} - \dot{z}_2 + d\dot{\theta}\right) \\ &+ c_{2ri} d\left(\dot{z}_{3ri} - \dot{z}_2 + d\dot{\theta}\right) + k_1 a(z_1 - z_2 + a\theta) + k_{2f} e(z_2 - z_{3f} + e\theta) \\ &+ k_{2ro} d(z_{3ro} - z_2 + d\theta) + k_{2ri} d(z_{3ri} - z_2 + d\theta) = F_2(t) \end{aligned} \quad (3.38)$$

Equations 3.20 to 3.38 can be written in a matrix form as given in Equation 3.39.

$$[M]\left\{\ddot{Z}(t)\right\} + [C]\left\{\dot{Z}(t)\right\} + [K]\{Z(t)\} = \{F(t)\} \quad (3.39)$$

$\left\{\ddot{Z}(t)\right\}$, $\left\{\dot{Z}(t)\right\}$, $\{Z(t)\}$ and {F(t)} are the 18×1 acceleration, velocity, displacement and external force vectors, respectively, as given in Equation 3.40. [C], [K] and [M] are the 18×18 mass, damping and stiffness matrices given by Equation 3.41, 3.42 and 3.43, respectively. The parameters in the stiffness and damping matrices are defined in Equation 3.44.

$$\{Z(t)\} = \begin{Bmatrix} z_1 \\ z_2 \\ z_{3\mathrm{f}} \\ z_{3\mathrm{ro}} \\ z_{3\mathrm{ri}} \\ z_{4\mathrm{f}} \\ z_{4\mathrm{ro}} \\ z_{4\mathrm{ri}} \\ z_{5\mathrm{f}} \\ z_{5\mathrm{ro}} \\ z_{5\mathrm{ri}} \\ z_{6\mathrm{f}} \\ z_{6\mathrm{ro}} \\ z_{6\mathrm{ri}} \\ z_{7\mathrm{f}} \\ z_{7\mathrm{ro}} \\ z_{7\mathrm{ri}} \\ \theta \end{Bmatrix}, \left\{\dot{Z}(t)\right\} = \begin{Bmatrix} \dot{z}_1 \\ \dot{z}_2 \\ \dot{z}_{3\mathrm{f}} \\ \dot{z}_{3\mathrm{ro}} \\ \dot{z}_{3\mathrm{ri}} \\ \dot{z}_{4\mathrm{f}} \\ \dot{z}_{4\mathrm{ro}} \\ \dot{z}_{4\mathrm{ri}} \\ \dot{z}_{5\mathrm{f}} \\ \dot{z}_{5\mathrm{ro}} \\ \dot{z}_{5\mathrm{ri}} \\ \dot{z}_{6\mathrm{f}} \\ \dot{z}_{6\mathrm{ro}} \\ \dot{z}_{6\mathrm{ri}} \\ \dot{z}_{7\mathrm{f}} \\ \dot{z}_{7\mathrm{ro}} \\ \dot{z}_{7\mathrm{ri}} \\ \dot{\theta} \end{Bmatrix}, \left\{\ddot{Z}(t)\right\} = \begin{Bmatrix} \ddot{z}_1 \\ \ddot{z}_2 \\ \ddot{z}_{3\mathrm{f}} \\ \ddot{z}_{3\mathrm{ro}} \\ \ddot{z}_{3\mathrm{ri}} \\ \ddot{z}_{4\mathrm{f}} \\ \ddot{z}_{4\mathrm{ro}} \\ \ddot{z}_{4\mathrm{ri}} \\ \ddot{z}_{5\mathrm{f}} \\ \ddot{z}_{5\mathrm{ro}} \\ \ddot{z}_{5\mathrm{ri}} \\ \ddot{z}_{6\mathrm{f}} \\ \ddot{z}_{6\mathrm{ro}} \\ \ddot{z}_{6\mathrm{ri}} \\ \ddot{z}_{7\mathrm{f}} \\ \ddot{z}_{7\mathrm{ro}} \\ \ddot{z}_{7\mathrm{ri}} \\ \ddot{\theta} \end{Bmatrix}, \{F(t)\} \begin{Bmatrix} F_1 \\ F_2 \\ F_{3\mathrm{f}} \\ F_{3\mathrm{ro}} \\ F_{3\mathrm{ri}} \\ F_{4\mathrm{f}} \\ F_{4\mathrm{ro}} \\ F_{4\mathrm{ri}} \\ F_{5\mathrm{f}} \\ F_{5\mathrm{ro}} \\ F_{5\mathrm{ri}} \\ F_{6\mathrm{f}} \\ F_{6\mathrm{ro}} \\ F_{6\mathrm{ri}} \\ F_{7\mathrm{f}} \\ F_{7\mathrm{ro}} \\ F_{7\mathrm{ri}} \\ F_2 \end{Bmatrix} \tag{3.40}$$

$$[M] = \begin{bmatrix} m_1 & 0 & 0 & 0 & 0 & 0 & 0 & 0 & 0 & 0 & 0 & 0 & 0 & 0 & 0 & 0 & 0 & 0 \\ 0 & m_2 & 0 & 0 & 0 & 0 & 0 & 0 & 0 & 0 & 0 & 0 & 0 & 0 & 0 & 0 & 0 & 0 \\ 0 & 0 & m_3 & 0 & 0 & 0 & 0 & 0 & 0 & 0 & 0 & 0 & 0 & 0 & 0 & 0 & 0 & 0 \\ 0 & 0 & 0 & m_3 & 0 & 0 & 0 & 0 & 0 & 0 & 0 & 0 & 0 & 0 & 0 & 0 & 0 & 0 \\ 0 & 0 & 0 & 0 & m_3 & 0 & 0 & 0 & 0 & 0 & 0 & 0 & 0 & 0 & 0 & 0 & 0 & 0 \\ 0 & 0 & 0 & 0 & 0 & m_4 & 0 & 0 & 0 & 0 & 0 & 0 & 0 & 0 & 0 & 0 & 0 & 0 \\ 0 & 0 & 0 & 0 & 0 & 0 & m_4 & 0 & 0 & 0 & 0 & 0 & 0 & 0 & 0 & 0 & 0 & 0 \\ 0 & 0 & 0 & 0 & 0 & 0 & 0 & m_4 & 0 & 0 & 0 & 0 & 0 & 0 & 0 & 0 & 0 & 0 \\ 0 & 0 & 0 & 0 & 0 & 0 & 0 & 0 & m_5 & 0 & 0 & 0 & 0 & 0 & 0 & 0 & 0 & 0 \\ 0 & 0 & 0 & 0 & 0 & 0 & 0 & 0 & 0 & m_5 & 0 & 0 & 0 & 0 & 0 & 0 & 0 & 0 \\ 0 & 0 & 0 & 0 & 0 & 0 & 0 & 0 & 0 & 0 & m_5 & 0 & 0 & 0 & 0 & 0 & 0 & 0 \\ 0 & 0 & 0 & 0 & 0 & 0 & 0 & 0 & 0 & 0 & 0 & m_6 & 0 & 0 & 0 & 0 & 0 & 0 \\ 0 & 0 & 0 & 0 & 0 & 0 & 0 & 0 & 0 & 0 & 0 & 0 & m_6 & 0 & 0 & 0 & 0 & 0 \\ 0 & 0 & 0 & 0 & 0 & 0 & 0 & 0 & 0 & 0 & 0 & 0 & 0 & m_6 & 0 & 0 & 0 & 0 \\ 0 & 0 & 0 & 0 & 0 & 0 & 0 & 0 & 0 & 0 & 0 & 0 & 0 & 0 & m_7 & 0 & 0 & 0 \\ 0 & 0 & 0 & 0 & 0 & 0 & 0 & 0 & 0 & 0 & 0 & 0 & 0 & 0 & 0 & m_7 & 0 & 0 \\ 0 & 0 & 0 & 0 & 0 & 0 & 0 & 0 & 0 & 0 & 0 & 0 & 0 & 0 & 0 & 0 & m_7 & 0 \\ 0 & 0 & 0 & 0 & 0 & 0 & 0 & 0 & 0 & 0 & 0 & 0 & 0 & 0 & 0 & 0 & 0 & I_2 \end{bmatrix} \tag{3.41}$$

$$[C] = \begin{bmatrix}
c_1 & -c_1 & 0 & 0 & 0 & 0 & 0 & 0 & 0 & 0 & 0 & 0 & 0 & 0 & 0 & 0 & 0 & \mathrm{ac}_1 \\
-c_1 & \mathrm{A}^* & -c_{2\mathrm{f}} & -c_{2\mathrm{ro}} & -c_{2\mathrm{ri}} & 0 & 0 & 0 & 0 & 0 & 0 & 0 & 0 & 0 & 0 & 0 & 0 & \mathrm{B}^* \\
0 & -c_{2\mathrm{f}} & c_{2\mathrm{f}} + c_{3\mathrm{f}} & 0 & 0 & -c_{3\mathrm{f}} & 0 & 0 & 0 & 0 & 0 & 0 & 0 & 0 & 0 & 0 & 0 & -\mathrm{ec}_{2\mathrm{f}} \\
0 & -c_{2\mathrm{ro}} & 0 & c_{2\mathrm{ro}} + c_{3\mathrm{ro}} & 0 & 0 & -c_{3\mathrm{ro}} & 0 & 0 & 0 & 0 & 0 & 0 & 0 & 0 & 0 & 0 & \mathrm{dc}_{2\mathrm{ro}} \\
0 & -c_{2\mathrm{ri}} & 0 & 0 & c_{2\mathrm{ri}} + c_{3\mathrm{ri}} & 0 & 0 & -c_{3\mathrm{ri}} & 0 & 0 & 0 & 0 & 0 & 0 & 0 & 0 & 0 & \mathrm{dc}_{2\mathrm{ri}} \\
0 & 0 & -c_{3\mathrm{f}} & 0 & 0 & c_{3\mathrm{f}} + c_4 & 0 & 0 & -c_4 & 0 & 0 & 0 & 0 & 0 & 0 & 0 & 0 & 0 \\
0 & 0 & 0 & -c_{3\mathrm{ro}} & 0 & 0 & c_{3\mathrm{ro}} + c_4 & 0 & 0 & -c_4 & 0 & 0 & 0 & 0 & 0 & 0 & 0 & 0 \\
0 & 0 & 0 & 0 & -c_{3\mathrm{ri}} & 0 & 0 & c_{3\mathrm{ri}} + c_4 & 0 & 0 & -c_4 & 0 & 0 & 0 & 0 & 0 & 0 & 0 \\
0 & 0 & 0 & 0 & 0 & -c_4 & 0 & 0 & c_4 + c_5 & 0 & 0 & -c_5 & 0 & 0 & 0 & 0 & 0 & 0 \\
0 & 0 & 0 & 0 & 0 & 0 & -c_4 & 0 & 0 & c_4 + c_5 & 0 & 0 & -c_5 & 0 & 0 & 0 & 0 & 0 \\
0 & 0 & 0 & 0 & 0 & 0 & 0 & -c_4 & 0 & 0 & c_4 + c_5 & 0 & 0 & -c_5 & 0 & 0 & 0 & 0 \\
0 & 0 & 0 & 0 & 0 & 0 & 0 & 0 & -c_5 & 0 & 0 & c_5 + c_6 & 0 & 0 & -c_6 & 0 & 0 & 0 \\
0 & 0 & 0 & 0 & 0 & 0 & 0 & 0 & 0 & -c_5 & 0 & 0 & c_5 + c_6 & 0 & 0 & -c_6 & 0 & 0 \\
0 & 0 & 0 & 0 & 0 & 0 & 0 & 0 & 0 & 0 & -c_5 & 0 & 0 & c_5 + c_6 & 0 & 0 & -c_6 & 0 \\
0 & 0 & 0 & 0 & 0 & 0 & 0 & 0 & 0 & 0 & 0 & -c_6 & 0 & 0 & c_6 + c_7 & 0 & 0 & 0 \\
0 & 0 & 0 & 0 & 0 & 0 & 0 & 0 & 0 & 0 & 0 & 0 & -c_6 & 0 & 0 & c_6 + c_7 & 0 & 0 \\
0 & 0 & 0 & 0 & 0 & 0 & 0 & 0 & 0 & 0 & 0 & 0 & 0 & -c_6 & 0 & 0 & c_6 + c_7 & 0 \\
\mathrm{ac}_1 & \mathrm{B}^* & -\mathrm{ec}_{2\mathrm{f}} & \mathrm{dc}_{2\mathrm{ro}} & \mathrm{dc}_{2\mathrm{ri}} & 0 & 0 & 0 & 0 & 0 & 0 & 0 & 0 & 0 & 0 & 0 & 0 & \mathrm{D}^*
\end{bmatrix} \tag{3.42}$$

$$[K] = \begin{bmatrix}
k_1 & -k_1 & 0 & 0 & 0 & 0 & 0 & 0 & 0 & 0 & 0 & 0 & 0 & 0 & 0 & 0 & 0 & \mathrm{ac}_1 \\
-k_1 & \mathrm{E}^* & -k_{2\mathrm{f}} & -k_{2\mathrm{ro}} & -k_{2\mathrm{ri}} & 0 & 0 & 0 & 0 & 0 & 0 & 0 & 0 & 0 & 0 & 0 & 0 & \mathrm{F}^* \\
0 & -k_{2\mathrm{f}} & k_{2\mathrm{f}} + k_{3\mathrm{f}} & 0 & 0 & -k_{3\mathrm{f}} & 0 & 0 & 0 & 0 & 0 & 0 & 0 & 0 & 0 & 0 & 0 & -\mathrm{ek}_{2\mathrm{f}} \\
0 & -k_{2\mathrm{ro}} & 0 & k_{2\mathrm{ro}} + k_{3\mathrm{ro}} & 0 & 0 & -k_{3\mathrm{ro}} & 0 & 0 & 0 & 0 & 0 & 0 & 0 & 0 & 0 & 0 & \mathrm{dk}_{2\mathrm{ro}} \\
0 & -k_{2\mathrm{ri}} & 0 & 0 & k_{2\mathrm{ri}} + k_{3\mathrm{ri}} & 0 & 0 & -k_{3\mathrm{ri}} & 0 & 0 & 0 & 0 & 0 & 0 & 0 & 0 & 0 & \mathrm{dk}_{2\mathrm{ri}} \\
0 & 0 & -k_{3\mathrm{f}} & 0 & 0 & k_{3\mathrm{f}} + k_4 & 0 & 0 & -k_4 & 0 & 0 & 0 & 0 & 0 & 0 & 0 & 0 & 0 \\
0 & 0 & 0 & -k_{3\mathrm{ro}} & 0 & 0 & k_{3\mathrm{ro}} + k_4 & 0 & 0 & -k_4 & 0 & 0 & 0 & 0 & 0 & 0 & 0 & 0 \\
0 & 0 & 0 & 0 & -k_{3\mathrm{ri}} & 0 & 0 & k_{3\mathrm{ri}} + k_4 & 0 & 0 & -k_4 & 0 & 0 & 0 & 0 & 0 & 0 & 0 \\
0 & 0 & 0 & 0 & 0 & -k_4 & 0 & 0 & k_4 + k_5 & 0 & 0 & -k_5 & 0 & 0 & 0 & 0 & 0 & 0 \\
0 & 0 & 0 & 0 & 0 & 0 & -k_4 & 0 & 0 & k_4 + k_5 & 0 & 0 & -k_5 & 0 & 0 & 0 & 0 & 0 \\
0 & 0 & 0 & 0 & 0 & 0 & 0 & -k_4 & 0 & 0 & k_4 + k_5 & 0 & 0 & -k_5 & 0 & 0 & 0 & 0 \\
0 & 0 & 0 & 0 & 0 & 0 & 0 & 0 & -k_5 & 0 & 0 & k_5 + k_6 & 0 & 0 & -k_6 & 0 & 0 & 0 \\
0 & 0 & 0 & 0 & 0 & 0 & 0 & 0 & 0 & -k_5 & 0 & 0 & k_5 + k_6 & 0 & 0 & -k_6 & 0 & 0 \\
0 & 0 & 0 & 0 & 0 & 0 & 0 & 0 & 0 & 0 & -k_5 & 0 & 0 & k_5 + k_6 & 0 & 0 & -k_6 & 0 \\
0 & 0 & 0 & 0 & 0 & 0 & 0 & 0 & 0 & 0 & 0 & -k_6 & 0 & 0 & k_6 + k_7 & 0 & 0 & 0 \\
0 & 0 & 0 & 0 & 0 & 0 & 0 & 0 & 0 & 0 & 0 & 0 & -k_6 & 0 & 0 & k_6 + k_7 & 0 & 0 \\
0 & 0 & 0 & 0 & 0 & 0 & 0 & 0 & 0 & 0 & 0 & 0 & 0 & -k_6 & 0 & 0 & k_6 + k_7 & 0 \\
\mathrm{ak}_1 & \mathrm{B}^* & -\mathrm{ek}_{2\mathrm{f}} & \mathrm{dk}_{2\mathrm{ro}} & \mathrm{dk}_{2\mathrm{ri}} & 0 & 0 & 0 & 0 & 0 & 0 & 0 & 0 & 0 & 0 & 0 & 0 & \mathrm{G}^*
\end{bmatrix} \tag{3.43}$$

$$\begin{cases} A^* = c_1 + c_{2f} + c_{2ro} + c_{2ri} \\ B^* = -ac_1 + ec_{2f} - dc_{2ro} - dc_{2ri} \\ D^* = a^2 c_1 + e^2 c_{2f} + d^2 c_{2ro} + d^2 c_{2ri} \\ E^* = k_1 + k_{2f} + k_{2ro} + k_{2ri} \\ F^* = -ak_1 + ek_{2f} - dk_{2ro} - dk_{2ri} \\ G^* = a^2 k_1 + e^2 k_{2f} + d^2 k_{2ro} + d^2 k_{2ri} \end{cases} \tag{3.44}$$

For the truck-haul road problem, the only external force acting on the system is the force due to truck payload force/weight. The external force vector for the system is thus given by Equation 3.45.

$$\begin{Bmatrix} F_1(t) \\ F_2(t) \\ F_{3f}(t) \\ F_{3ro}(t) \\ F_{3ri}(t) \\ F_{4f}(t) \\ F_{4ro}(t) \\ F_{4ri}(t) \\ F_{5f}(t) \\ F_{5ro}(t) \\ F_{5ri}(t) \\ F_{6f}(t) \\ F_{6ro}(t) \\ F_{6ri}(t) \\ F_{7f}(t) \\ F_{7ro}(t) \\ F_{7ri}(t) \\ F_2(t) \end{Bmatrix} = \begin{Bmatrix} F_1(t) \\ 0 \\ 0 \\ 0 \\ 0 \\ 0 \\ 0 \\ 0 \\ 0 \\ 0 \\ 0 \\ 0 \\ 0 \\ 0 \\ 0 \\ 0 \\ 0 \end{Bmatrix} \tag{3.45}$$

3.4. DUAL TIRE ASSEMBLY INTERACTION

The rear dual tire assembly has a higher effect on the haul road due to the interaction of the tire loads (Figure 3.6). Current design techniques capture this interaction by

multiplying a factor of 1.2 with the maximum single tire load to generate the effective maximum tire loading. This is then used as input to design the road layer thicknesses. In this section, novel equations were proposed to model the rear dual tire interactions.

In this work, the contribution of the rear outer and rear inner tires to the road layer response is given by coefficients α and β, respectively. The combined layer response, in terms of vertical displacement, is then given by Equation 3.46.

$$z_{\text{jr}} = \alpha_j \left(z_{\text{jro}}\right)^{q_j} + \beta_j \left(z_{\text{jri}}\right)^{r_j} \tag{3.46}$$

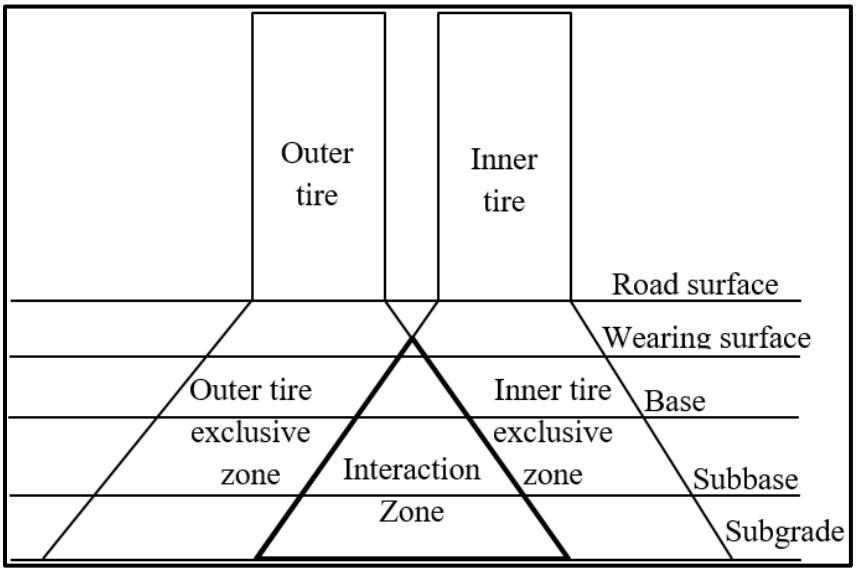

Figure 3.6 Dual tire assembly interaction effect

z_{jr} is the road layer displacement due to the interaction of rear dual tire loads on the layer; z_{jro} is the displacement of the road layer caused by the outer rear tire, and z_{jri} is the displacement of the road layer caused by the rear inner tire. The value of j denotes the road layer (4 = wearing surface, 5 = base, 6 = subbase and 7 = subgrade). The values of q_j and

r_j depend on the interaction relationship between the two tires. For a perfectly linear contribution of each tire, $q_j = r_j = 1$. For non-linear interaction, $q_j \neq 1$ and $r_j \neq 1$. This is expressed as Equation 3.47. The values of α_j and β_j range from 0 to 1, with the constraint given by Equation 3.48. In the outer tire exclusive zone, $\alpha = 1$ and $\beta = 0$. Conversely, in the inner tire exclusive zone, $\beta = 1$ and $\alpha = 0$.

$$\begin{cases} q_j = r_j = 1 & \forall \text{ interaction is linear} \\ q_j \neq r_j \neq 1 & \forall \text{ interaction is non-linear} \end{cases} \tag{3.47}$$

$$1 \leq \alpha_j + \beta_j \leq \gamma_j \tag{3.48}$$

γ_j is the maximum combined effect of the two rear tires on the j^{th} road layer displacement. Equation 3.47 can be expanded for each of the layers as given by Equations 3.49 to 3.52 for the wearing surface, base, subbase, and subgrade, respectively.

$$z_{4r} = \alpha_4 (z_{4ro})^{q_4} + \beta_4 (z_{4ri})^{r_4} \tag{3.49}$$

$$z_{5r} = \alpha_5 (z_{5ro})^{q_5} + \beta_5 (z_{5ri})^{r_5} \tag{3.50}$$

$$z_{6r} = \alpha_6 (z_{6ro})^{q_6} + \beta_6 (z_{6ri})^{r_6} \tag{3.51}$$

$$z_{7r} = \alpha_7 (z_{7ro})^{q_7} + \beta_7 (z_{7ri})^{r_7} \tag{3.52}$$

Equations 3.49 to 3.52 are used to model the road layer response due to the interaction of the set of rear dual tires. Using the combined effects, the governing equations for the truck-haul road dynamics were reformulated to capture the interaction of the dual tires. The equations that describe the dynamics of the truck body, chassis, front tire and

road layers under the front tire remain unchanged since these are not affected by the interaction. Equations for the two rear tires and the layers under the two tires are modified to capture the interaction. Equations 3.53 and 3.54 describe the dynamics of the rear outer and rear inner tires for the combined effects.

$$m_3\ddot{z}_{3ro} + c_{2ro}\left(\dot{z}_{3ro} - \dot{z}_2 + d\dot{\theta}\right) + c_{3ro}\left(\dot{z}_{3ro} - \dot{z}_{4r}\right) + k_{2ro}(z_{3ro} - z_2 + \mathrm{d}\theta)$$
$$+k_{3ro}(z_{3ro} - z_{4r}) = F_{3ro}(t) \tag{3.53}$$

$$m_3\ddot{z}_{3ri} + c_{2ri}\left(\dot{z}_{3ri} - \dot{z}_2 + d\dot{\theta}\right) + c_{3ri}\left(\dot{z}_{3ri} - \dot{z}_{4r}\right) + k_{2ri}(z_{3ri} - z_2 + \mathrm{d}\theta)$$
$$+k_{3ri}(z_{3ri} - z_{4r}) = F_{3ri}(t) \tag{3.54}$$

The response of the wearing surface, base, subbase and subgrade layers to the combined effect of the rear tires are captured by Equations 3.55 to 3.58, respectively.

$$m_4\ddot{z}_{4r} + c_{3ro}\left(\dot{z}_{4r} - \dot{z}_{3ro}\right) + c_{3ri}\left(\dot{z}_{4r} - \dot{z}_{3ri}\right) + c_4\left(\dot{z}_{4r} - \dot{z}_{5r}\right) + k_{3ro}(z_{4r} - z_{3ro})$$
$$+k_{3ri}(z_{4r} - z_{3ri}) + k_4(z_{4r} - z_{5r}) = F_{4r}(t) \tag{3.55}$$

$$m_5\ddot{z}_{5r} + c_4\left(\dot{z}_{5r} - \dot{z}_{4r}\right) + c_5\left(\dot{z}_{5r} - \dot{z}_{6r}\right) + k_4(z_{5r} - z_{4r}) + k_5(z_{5r} - z_{6r}) = F_{5r}(t) \tag{3.56}$$

$$m_6\ddot{z}_{6r} + c_5\left(\dot{z}_{6r} - \dot{z}_{5r}\right) + c_6\left(\dot{z}_{6r} - \dot{z}_{7r}\right) + k_5(z_{6r} - z_{5r}) + k_6(z_{6r} - z_{7r}) = F_{6r}(t) \tag{3.57}$$

$$m_7\ddot{z}_{7r} + c_6\left(\dot{z}_{7r} - \dot{z}_{6r}\right) + c_7\dot{z}_{7r} + k_6(z_{7r} - z_{6r}) + k_7z7\mathrm{r} = F_{7r}(t) \tag{3.58}$$

Combining these equations with other unchanged equations, the expanded matrix form can be written as given in Equation 3.39. The displacement, velocity, acceleration and external force vectors are given by Equation 3.59. The mass, damping and stiffness

matrices are given by Equations 3.60 to 3.62, respectively. The parameters in the stiffness and damping matrices are defined in Equation 3.63.

$$\{\ddot{z}(t)\} = \begin{Bmatrix} \ddot{z}_1 \\ \ddot{z}_2 \\ \ddot{z}_{3f} \\ \ddot{z}_{3ro} \\ \ddot{z}_{3ri} \\ \ddot{z}_{4f} \\ \ddot{z}_{4r} \\ \ddot{z}_{5f} \\ \ddot{z}_{5r} \\ \ddot{z}_{6f} \\ \ddot{z}_{6r} \\ \ddot{z}_{7f} \\ \ddot{z}_{7r} \\ \ddot{\theta} \end{Bmatrix}, \{\dot{z}(t)\} = \begin{Bmatrix} \dot{z}_1 \\ \dot{z}_2 \\ \dot{z}_{3f} \\ \dot{z}_{3ro} \\ \dot{z}_{3ri} \\ \dot{z}_{4f} \\ \dot{z}_{4r} \\ \dot{z}_{5f} \\ \dot{z}_{5r} \\ \dot{z}_{6f} \\ \dot{z}_{6r} \\ \dot{z}_{7f} \\ \dot{z}_{7r} \\ \dot{\theta} \end{Bmatrix}, \{Z(t)\} = \begin{Bmatrix} z_1 \\ z_2 \\ z_{3f} \\ z_{3ro} \\ z_{3ri} \\ z_{4f} \\ z_{4r} \\ z_{5f} \\ z_{5r} \\ z_{6f} \\ z_{6r} \\ z_{7f} \\ z_{7r} \\ \theta \end{Bmatrix}, \{F(t)\} \begin{Bmatrix} F_1 \\ F_2 \\ F_{3f} \\ F_{3ro} \\ F_{3ri} \\ F_{4f} \\ F_{4r} \\ F_{5f} \\ F_{5r} \\ F_{6f} \\ F_{6r} \\ F_{7f} \\ F_{7r} \\ F_2 \end{Bmatrix} \tag{3.59}$$

$$[M] = \begin{bmatrix} m_1 & 0 & 0 & 0 & 0 & 0 & 0 & 0 & 0 & 0 & 0 & 0 & 0 & 0 \\ 0 & m_2 & 0 & 0 & 0 & 0 & 0 & 0 & 0 & 0 & 0 & 0 & 0 & 0 \\ 0 & 0 & m_3 & 0 & 0 & 0 & 0 & 0 & 0 & 0 & 0 & 0 & 0 & 0 \\ 0 & 0 & 0 & m_3 & 0 & 0 & 0 & 0 & 0 & 0 & 0 & 0 & 0 & 0 \\ 0 & 0 & 0 & 0 & m_3 & 0 & 0 & 0 & 0 & 0 & 0 & 0 & 0 & 0 \\ 0 & 0 & 0 & 0 & 0 & m_4 & 0 & 0 & 0 & 0 & 0 & 0 & 0 & 0 \\ 0 & 0 & 0 & 0 & 0 & 0 & m_4 & 0 & 0 & 0 & 0 & 0 & 0 & 0 \\ 0 & 0 & 0 & 0 & 0 & 0 & 0 & m_5 & 0 & 0 & 0 & 0 & 0 & 0 \\ 0 & 0 & 0 & 0 & 0 & 0 & 0 & 0 & m_5 & 0 & 0 & 0 & 0 & 0 \\ 0 & 0 & 0 & 0 & 0 & 0 & 0 & 0 & 0 & m_6 & 0 & 0 & 0 & 0 \\ 0 & 0 & 0 & 0 & 0 & 0 & 0 & 0 & 0 & 0 & m_6 & 0 & 0 & 0 \\ 0 & 0 & 0 & 0 & 0 & 0 & 0 & 0 & 0 & 0 & 0 & m_7 & 0 & 0 \\ 0 & 0 & 0 & 0 & 0 & 0 & 0 & 0 & 0 & 0 & 0 & 0 & m_7 & 0 \\ 0 & 0 & 0 & 0 & 0 & 0 & 0 & 0 & 0 & 0 & 0 & 0 & 0 & I_2 \end{bmatrix} \tag{3.60}$$

$$[C] = \begin{bmatrix} c_1 & -c_1 & 0 & 0 & 0 & 0 & 0 & 0 & 0 & 0 & 0 & 0 & 0 & \mathrm{ac}_1 \\ -c_1 & \mathrm{H}^* & -c_{2\mathrm{f}} & -c_{2\mathrm{ro}} & -c_{2\mathrm{ri}} & 0 & 0 & 0 & 0 & 0 & 0 & 0 & 0 & \mathrm{I}^* \\ 0 & -c_{2\mathrm{f}} & c_{2\mathrm{f}} + c_{3\mathrm{f}} & 0 & 0 & -c_{3\mathrm{f}} & 0 & 0 & 0 & 0 & 0 & 0 & 0 & -\mathrm{ec}_{2\mathrm{f}} \\ 0 & -c_{2\mathrm{ro}} & 0 & c_{2\mathrm{ro}} + c_{3\mathrm{ro}} & 0 & -c_{3\mathrm{ro}} & 0 & 0 & 0 & 0 & 0 & 0 & 0 & \mathrm{dc}_{2\mathrm{ro}} \\ 0 & -c_{2\mathrm{ri}} & 0 & 0 & c_{2\mathrm{ri}} + c_{3\mathrm{ri}} & 0 & -c_{3\mathrm{ri}} & 0 & 0 & 0 & 0 & 0 & 0 & \mathrm{dc}_{2\mathrm{ri}} \\ 0 & 0 & -c_{3\mathrm{f}} & 0 & 0 & c_{3\mathrm{f}} + c_4 & 0 & -c_4 & 0 & 0 & 0 & 0 & 0 & 0 \\ 0 & 0 & 0 & -c_{3\mathrm{ro}} & -c_{3\mathrm{ri}} & 0 & \mathrm{J}^* & 0 & -c_4 & 0 & 0 & 0 & 0 & 0 \\ 0 & 0 & 0 & 0 & 0 & -c_4 & 0 & c_4 + c_5 & 0 & -c_5 & 0 & 0 & 0 & 0 \\ 0 & 0 & 0 & 0 & 0 & 0 & -c_4 & 0 & c_4 + c_5 & 0 & -c_5 & 0 & 0 & 0 \\ 0 & 0 & 0 & 0 & 0 & 0 & 0 & -c_5 & 0 & c_5 + c_6 & 0 & -c_6 & 0 & 0 \\ 0 & 0 & 0 & 0 & 0 & 0 & 0 & 0 & -c_5 & 0 & c_5 + c_6 & 0 & -c_6 & 0 \\ 0 & 0 & 0 & 0 & 0 & 0 & 0 & 0 & 0 & -c_6 & 0 & c_6 + c_7 & 0 & 0 \\ 0 & 0 & 0 & 0 & 0 & 0 & 0 & 0 & 0 & 0 & -c_6 & 0 & c_6 + c_7 & 0 \\ \mathrm{ac}_1 & \mathrm{K}^* & -\mathrm{ec}_{2\mathrm{f}} & \mathrm{dc}_{2\mathrm{ro}} & \mathrm{dc}_{2\mathrm{ri}} & 0 & 0 & 0 & 0 & 0 & 0 & 0 & 0 & \mathrm{L}^* \end{bmatrix} \tag{3.61}$$

$$[K] = \begin{bmatrix} k_1 & -k_1 & 0 & 0 & 0 & 0 & 0 & 0 & 0 & 0 & 0 & 0 & 0 & \mathrm{ak}_1 \\ -k_1 & \mathrm{M}^* & -k_{2\mathrm{f}} & -k_{2\mathrm{ro}} & -k_{2\mathrm{ri}} & 0 & 0 & 0 & 0 & 0 & 0 & 0 & 0 & \mathrm{N}^* \\ 0 & -k_{2\mathrm{f}} & k_{2\mathrm{f}} + k_{3\mathrm{f}} & 0 & 0 & -k_{3\mathrm{f}} & 0 & 0 & 0 & 0 & 0 & 0 & 0 & -\mathrm{ek}_{2\mathrm{f}} \\ 0 & -k_{2\mathrm{ro}} & 0 & k_{2\mathrm{ro}} + k_{3\mathrm{ro}} & 0 & -k_{3\mathrm{ro}} & 0 & 0 & 0 & 0 & 0 & 0 & 0 & \mathrm{dk}_{2\mathrm{ro}} \\ 0 & -k_{2\mathrm{ri}} & 0 & 0 & k_{2\mathrm{ri}} + k_{3\mathrm{ri}} & 0 & -k_{3\mathrm{ri}} & 0 & 0 & 0 & 0 & 0 & 0 & \mathrm{dk}_{2\mathrm{ri}} \\ 0 & 0 & -k_{3\mathrm{f}} & 0 & 0 & k_{3\mathrm{f}} + k_4 & 0 & -k_4 & 0 & 0 & 0 & 0 & 0 & 0 \\ 0 & 0 & 0 & -k_{3\mathrm{ro}} & -k_{3\mathrm{ri}} & 0 & \mathrm{P}^* & 0 & -k_4 & 0 & 0 & 0 & 0 & 0 \\ 0 & 0 & 0 & 0 & 0 & -k_4 & 0 & k_4 + k_5 & 0 & -k_5 & 0 & 0 & 0 & 0 \\ 0 & 0 & 0 & 0 & 0 & 0 & -k_4 & 0 & k_4 + k_5 & 0 & -k_5 & 0 & 0 & 0 \\ 0 & 0 & 0 & 0 & 0 & 0 & 0 & -k_5 & 0 & k_5 + k_6 & 0 & -k_6 & 0 & 0 \\ 0 & 0 & 0 & 0 & 0 & 0 & 0 & 0 & -k_5 & 0 & k_5 + k_6 & 0 & -k_6 & 0 \\ 0 & 0 & 0 & 0 & 0 & 0 & 0 & 0 & 0 & -k_6 & 0 & k_6 + k_7 & 0 & 0 \\ 0 & 0 & 0 & 0 & 0 & 0 & 0 & 0 & 0 & 0 & -k_6 & 0 & k_6 + k_7 & 0 \\ \mathrm{ak}_1 & \mathrm{Q}^* & -\mathrm{ek}_{2\mathrm{f}} & \mathrm{dk}_{2\mathrm{ro}} & \mathrm{dk}_{2\mathrm{ri}} & 0 & 0 & 0 & 0 & 0 & 0 & 0 & 0 & \mathrm{R}^* \end{bmatrix} \tag{3.62}$$

$$\begin{cases} H^* = c_1 + c_{2f} + c_{2ro} + c_{2ri} \\ I^* = -ac_1 + ec_{2f} - dc_{2ro} - dc_{2ri} \\ J^* = c_{3ro} + c_{3ri} + c_4 \\ K^* = -ac_1 + ec_{2f} - dc_{2ro} - dc_{2ri} \\ L^* = a^2 c_1 + e^2 c_{2f} + d^2 c_{2ro} + d^2 c_{2ri} \\ M^* = k_1 + k_{2f} + k_{2ro} + k_{2ri} \\ N^* = -ak_1 + ek_{2f} - dk_{2ro} - dk_{2ri} \\ P^* = k_{3ro} + k_{3ri} + k_4 \\ Q^* = -ak_1 + ek_{2f} - dk_{2ro} - dk_{2ri} \\ R^* = a^2 k_1 + e^2 k_{2f} + d^2 k_{2ro} + d^2 k_{2ri} \end{cases} \quad (3.63)$$

3.5. TIRE NORMAL/VERTICAL FORCE MODEL

The dynamic vertical forces imposed by each of the six tires on the surface of the haul road can be estimated using the Lagrange EOMs. As stated, a half truck model, with one front and two rear tires, suffices for the mathematical model. The external force, $F_1(t)$ is primarily imposed by the truck payload. The truck then imposes impact loads on the road at the tire-road contact. The tire vertical forces largely depend on the roughness and surface undulations of the haul road and truck payload. Thus, to adequately model the dynamic forces, the model must incorporate road surface roughness.

3.5.1. Road Roughness Model. Since a half truck model is used for generating the EOMs, it is assumed that the front tire travels on the same road profile as the rear outer tire, while the rear inner tire travels on a different profile. This requires the generation of two separate road profiles, which serve as input for the truck tire dynamic forces. The ISO 8608 road roughness models presented by [67], [68] and [69] were used for generating the parallel road profiles. The road roughness equations were obtained from [63]-[65]. This model is a displacement power spectral density (PSD) based model that generates random

road profiles based on the road class. Equation 3.64 is used for computing the road PSD. The road profile is then generated as a sum of a series of harmonics, as given by Equation 3.65 [67].

$$G(n) = G(n_o)\left(\frac{n}{n_o}\right)^{-2} \tag{3.64}$$

$$Z_l = \sum_1^N \sqrt{2\mathrm{G}(n_i)\Delta n}\cos(2\pi n_i X + \varphi_i) \tag{3.65}$$

G(n) is a function of the road class; n has values of 0.01 cycles/m to 10 cycles/m. Values of $G(n_o)$ are defined by ISO 8608 for roads of varying roughness and n_o is 0.1 cycle/m. φ_i is uniformly distributed from 0 to 2π. Representing road surfaces as the sum of a series of harmonics captures the random elevation changes of the road surface, which translates into the vehicle vertical excitations during vehicle travel. The frequency increment, Δn, is defined by Equation 3.66. n_{min} (capturing road profile changes) and n_{max} (capturing tire filtering effect) filter out road undulations, which will not significantly affect tire dynamics. ISO 8608 suggests n_{min} value of 0.01 cycles/m (i.e. 1 cycle of undulations per 100 m of road length), and n_{max} of 10 cycles/m [69].

$$\Delta \mathrm{n} = \frac{n_{\max} - n_{\min}}{N} \tag{3.66}$$

Equation 3.65 generates one profile. According to [67], the two parallel road surface profiles exhibit similar statistical properties independent of direction or position, if the assumptions of homogeneity and isotropy hold. Thus, the left and right parallel profiles

have a similar autocorrelation function given by Equation 3.67 and cross-correlation functions given by Equation 3.68.

$$R_l(\delta) = R_r(\delta) = R(\delta) \tag{3.67}$$

$$R_{lr}(\delta) = R_{rl}(\delta) = R_x(\delta) \tag{3.68}$$

The cross-correlation, $R_x(\delta)$, and autocorrelation, $R(\delta)$, functions are defined by Equations 3.69 and 3.70, respectively.

$$R_x(\delta) = R\left(\sqrt{\delta^2 + (2b)^2}\right) \tag{3.69}$$

$$R(\delta) = \int_0^\infty G(n)\cos(2\pi\delta n)dn \tag{3.70}$$

Putting Equation 3.64 into 3.70 yields Equation 3.71, which is the equation for the parallel road cross-correlation function.

$$R_x(\delta) = \frac{2G(n_0)}{n_0^{-2}}\left(n_a^{-1}\frac{sin\left[2\pi n_a\sqrt{\delta^2+(2b)^2}\right]}{\left[2\pi n_a\sqrt{\delta^2+(2b)^2}\right]} + \int_{n_a}^\infty n^{-2}\,cos\left[2\pi n\sqrt{\delta^2+(2b)^2}\right]dn\right) \tag{3.71}$$

An analytical algorithm for solving Equation 3.71 using the sine integrals can be found in [67] and [69]. Since the autocorrelation and cross-correlation functions of the two profiles are equal, their corresponding direct and cross-spectral densities are also equal i.e. $G_l(n) = G_r(n) = G(n)$ and $G_{lr}(n) = G_{rl}(n) = G_x(n)$. A coherency function, which relates the left and right profiles, can then be derived as given in Equation 3.72. With the cross-PSD,

G_x, for the given width between tires/profiles, the other profile is computed by adding to the first profile in Equation 3.65 to another sum of a series of harmonics, as done for the first profile. A new set of random phase angles is used, and the difference between the direct PSD and the cross PSD [G(n) - G_x(n)] is used instead of G(n). This results in Equation 3.73 for computing the right road profile.

$$g(n) = \frac{|G_x(n)|}{G(n)} \tag{3.72}$$

$$Z_r = \sum_1^N \sqrt{2\mathrm{G}(n_i)\Delta n}\cos(2\pi n_i X + \varphi_i) + \sum_1^N \sqrt{2[G(n_i)\text{-}\mathrm{G}_x(n_i)]\Delta n}\cos(2\pi n_i X + \theta_i) \tag{3.73}$$

Equations 3.65 and 3.73 are used for modeling the longitudinal road surface roughness, which will be imposed as vertical motions on the truck tires, generating the tire dynamic impact forces.

3.5.2. Truck Tire Dynamic Vertical Forces. The accurate estimation of the dynamic forces imposed on the haul road is a critical precursor to the robust structural design of haul roads. It is widely known in the literature that the impact loads imposed on the road by moving vehicles comprise of the static and dynamic (Figure 3.7) components [87]. The static force is due to the weight of the truck and its payload. The dynamic component is controlled by the road surface irregularities, vehicle component characteristics (springs and dampers) and vehicle speed. This section presents detailed novel mathematical formulations for modeling the impact (static and dynamic) loads imposed on haul road surfaces by moving trucks.

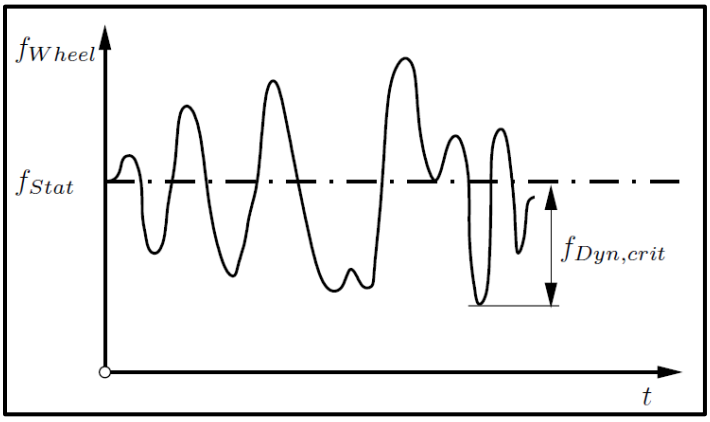

Figure 3.7 Static and dynamic wheel loads [87]

The static load is computed based on the truckload distribution between the front and rear tires. The weight distribution for a CAT 797F is 33% for the front and 67% for the rear tires. Thus, the total vertical static load imposed by the truck through the front and rear tires can be computed using Equations 3.74 and 3.75, respectively.

$$F_s(\text{front}) = \left[\frac{0.33*GMW}{2}\right] * g \tag{3.74}$$

$$F_s(\text{rear}) = \left[\frac{0.67*\text{GMW}}{4}\right] * g \tag{3.75}$$

The dynamic tire force is generated from solutions to the dynamic model presented in Equation 3.39. From the solutions to the dynamic model, the dynamic vertical tire forces for the front, rear outer and rear inner tires can be given by Equations 3.76, 3.77 and 3.78, respectively. These comprise the sum of the inertial, spring and damping forces for the various suspension systems connecting truck components and the tires. It was also assumed

that the rated weight distribution (33%:67% for front: rear) of the truck holds for the dynamic forces.

$$F_d(\text{front}) = \frac{0.33\left(m_1\ddot{z}_1 + F_{\text{k1}} + F_{\text{c1}} + m_2\ddot{z}_2\right)}{2} + F_{\text{k2f}} + F_{\text{c2f}} + m_{\text{ft}}\ddot{z}_{3\text{f}} + F_{\text{k3f}} + F_{\text{c3f}}$$

$$+k_{3\text{f}}Z_l + c_{3_f}\dot{Z}_l \tag{3.76}$$

$$F_d(\text{rear outer}) = \frac{0.67\left(m_1\ddot{z}_1 + F_{\text{k1}} + F_{\text{c1}} + m_2\ddot{z}_2\right)}{4} + F_{\text{k2ro}} + F_{\text{c2ro}} + m_{\text{ro}}\ddot{z}_{3\text{ro}}$$

$$+F_{\text{k3ro}} + F_{\text{c3ro}} + k_{3\text{ro}}Z_l + c_{3\text{ro}}\dot{Z}_l \tag{3.77}$$

$$F_d(\text{rear inner}) = \frac{0.67\left(m_1\ddot{z}_1 + F_{\text{k1}} + F_{\text{c1}} + m_2\ddot{z}_2\right)}{4} + F_{\text{k2ri}} + F_{\text{c2ri}} + m_{\text{ri}}\ddot{z}_{3\text{ri}} + F_{\text{k3ri}}$$

$$+F_{\text{c3ri}} + k_{3\text{ri}}Z_r + c_{3\text{ri}}\dot{Z}_r \tag{3.78}$$

The last two terms of Equations 3.76 to 3.78 capture the dynamic forces due to road surface roughness, Z_l and Z_r. The total vertical/impact forces imposed by the tires are then given by the sum of static and dynamic forces as given by Equation 3.79.

$$F_z = F_s + F_d \tag{3.79}$$

A parameter called the dynamic force coefficient (DFC) can be then be computed as the ratio of the total vertical/impact force to the static vertical force (Equation 3.80).

$$\text{DFC} = \frac{F_z}{F_s} = \frac{F_s + F_d}{F_s} \tag{3.80}$$

DFC normalizes the dynamic force using the static force. These values were used in ABAQUS for capturing the truck dynamic force in the road response model.

3.6. SUMMARY

The mathematical model that captures the dynamics of ultra-large mining truck-haul road interactions was developed in this section. The model captures the physics of load transfer from the payload to the road. It also captures the interaction effects of the rear dual tires. The EOMs have been derived for an 18 DOF ultra-large mining truck-haul road system using the Lagrangian formulation. The impact of road surface roughness has been incorporated into the model. The solutions to the EOMs yield the system component displacement, velocity, and acceleration, which are used for generating the tire vertical forces. A simplified solution of this model was implemented in MATLAB/SIMULINK® using a single tire. A numerical solution was implemented in MSC.ADAMS for generating truck tire dynamic forces, which were used as input for the road response model in ABAQUS. The numerical solution in MSC.ADAMS was for a full truck.

4. NUMERICAL SOLUTIONS AND VIRTUAL PROTOTYPE MODELING

This section presents the numerical solution procedures used in MSC.ADAMS for solving the truck-haul road interaction dynamic model presented in Section 3. It also presents the methodology used in building, verifying and validating the 3D dynamic virtual simulation model of the truck-haul road system in MSC.ADAMS. This model is used for conducting experiments to understand the tire-road interaction dynamics when the truck moves on the haul road. The simplified MATLAB/SIMULINK® solution of the mathematical model is also presented in this section.

4.1. NUMERICAL SOLUTION ALGORITHM

Several numerical solution algorithms exist for solving the EOMs for machine-formation dynamics problems. Some of these techniques are the central difference, linear acceleration, Duhamel's step integral, Z-transform, Newton-Raphson iteration algorithm, Newmark-β integration scheme, Runge-Kutta methods and Euler's methods [54], [167]–[170]. These are generally classified as implicit and explicit integration schemes. Explicit schemes are typically used for fast transient analyses, such as crash and impact studies. Explicit analysis techniques exhibit conditional stability and require very small-time steps. Implicit methods are unconditionally stable and are effective for structural analysis problems [171]. Implicit techniques include the Hilber-Hughes-Taylor (HHT), Newmark-β and Wilson-θ methods.

The Newmark integration scheme is commonly used in structural dynamics problems and was employed in this study due to its unconditional stability and accuracy.

The robust Newmark scheme implemented in MSC.ADAMS was used for solving the dynamic truck-road interaction model developed in Section 3. The numerical solution algorithm presented was taken from [54].

Let the displacement of a system component at time t be Z(t) and the displacement at a time (t+Δt) be Z(t+Δt), where Δt is the time step. The Taylor series expansion for the system component displacement and its time derivatives results in Equations 4.1 and 4.2.

$$\{Z(t+\Delta t)\} = \{Z(t)\} + \left\{\dot{Z}(t)\right\}\Delta t + \frac{1}{2}\left\{\ddot{Z}(t)\right\}(\Delta t)^2 + \frac{1}{6}\left\{\dddot{Z}(t)\right\}(\Delta t)^3 + \ldots \quad (4.1)$$

$$\left\{\dot{Z}(t+\Delta t)\right\} = \left\{\dot{Z}(t)\right\} + \left\{\ddot{Z}(t)\right\}\Delta t + \frac{1}{2}\left\{\dddot{Z}(t)\right\}(\Delta t)^2 + \ldots \quad (4.2)$$

Assuming linear acceleration between the time interval t and (t+Δt), Equation 4.3 can be obtained, which is used for deriving the Newmark equations.

$$\left\{\dddot{Z}(t)\right\} = \frac{1}{\Delta t}\left[\left\{\ddot{Z}(t+\Delta t)\right\} - \left\{\ddot{Z}(t)\right\}\right] \quad (4.3)$$

Putting Equation 4.3 into 4.1 and 4.2, Equations 4.4 and 4.5 are obtained for computing the system component displacement and velocity, respectively.

$$\{Z(t+\Delta t)\} = \{Z(t)\} + \left\{\dot{Z}(t)\right\}\Delta t + \left[\frac{1}{3}\left\{\ddot{Z}(t)\right\} + \frac{1}{6}\left\{\ddot{Z}(t+\Delta t)\right\}\right](\Delta t)^2 \quad (4.4)$$

$$\left\{\dot{Z}(t+\Delta t)\right\} = \left\{\dot{Z}(t)\right\} + \frac{1}{2}\Delta t\left[\left\{\ddot{Z}(t)\right\} + \left\{\ddot{Z}(t+\Delta t)\right\}\right] \quad (4.5)$$

The Newmark method introduces numerical coefficients, β, and α, to Equations 4.4 and 4.5, respectively, which control the solution stability and accuracy. This yields Equations 4.6 and 4.7 for the displacement and velocity of each system component.

$$\{Z(t+\Delta t)\} = \{Z(t)\} + \left\{\dot{Z}(t)\right\}\Delta t + \left[\left(\frac{1}{2}-\beta\right)\left\{\ddot{Z}(t)\right\} + \beta\left\{\ddot{Z}(t+\Delta t)\right\}\right](\Delta t)^2 \quad (4.6)$$

$$\left\{\dot{Z}(t+\Delta t)\right\} = \left\{\dot{Z}(t)\right\} + \left[(1-\alpha)\left\{\ddot{Z}(t)\right\} + \alpha\left\{\ddot{Z}(t+\Delta t)\right\}\right]\Delta t \quad (4.7)$$

If α = ½ and β = 1/6, Equations 4.8 and 4.9 result for computing the acceleration and velocity of the system components.

$$\left\{\ddot{Z}(t+\Delta t)\right\} = a_0\{Z(t+\Delta t)\} - a_0\{Z(t)\} - a_2\left\{\dot{Z}(t)\right\} - a_3\left\{\ddot{Z}(t)\right\} \quad (4.8)$$

$$\left\{\dot{Z}(t+\Delta t)\right\} = a_1\{Z(t+\Delta t)\} - a_1\{Z(t)\} - a_4\left\{\dot{Z}(t)\right\} - a_5\left\{\ddot{Z}(t)\right\} \quad (4.9)$$

The coefficients, a_0 to a_5, in Equations 4.8 and 4.9 are dependent on the numerical coefficients, α and β, and time step, Δt, of the analysis. They are defined by Equation 4.10.

$$a_0 = \frac{1}{\beta(\Delta t)^2},\ a_1 = \frac{\alpha}{\beta(\Delta t)},\ a_2 = \frac{1}{\beta(\Delta t)},\ a_3 = \frac{1}{2\beta} - 1,\ a_4 = \frac{\alpha}{\beta} - 1,\ a_5 = \frac{\Delta t}{2}\left(\frac{\alpha}{\beta} - 1\right) \quad (4.10)$$

Gavin [167] and [54] noted that the Newmark algorithm is unconditionally stable (i.e. stability does not depend on the size of the time step, Δt) and accurate if β = 0.25 and α = 0.5. These values were adopted in this work to ensure the numerical accuracy and

stability of the solution. Putting Equations 4.8 and 4.9 into Equation 3.39, Equation 4.11 can be derived as a solution to Equation 3.39. $\bar{K}$ is related to the stiffness, mass and damping matrices of the system as defined by Equation 4.12. $\bar{F}$is related to the force vector, and the mass and damping matrices as given by Equation 4.13.

$$\bar{K}\{Z(t+\Delta t)\} = \left\{\bar{F}(t+\Delta t)\right\} \tag{4.11}$$

$$\bar{K} = K + a_0 M + a_1 C \tag{4.12}$$

$$\left\{\bar{F}(t+\Delta t)\right\} = \{F(t+\Delta t)\} + M\left[a_0\{Z(t)\} + a_2\left\{\dot{Z}(t)\right\} + a_3\left\{\ddot{Z}(t)\right\}\right]$$

$$+C\left[a_1\{Z(t)\} + a_4\left\{\dot{Z}(t)\right\} + a_5\left\{\ddot{Z}(t)\right\}\right] \tag{4.13}$$

Solutions to Equation 4.11 yield the component displacements at time t+Δt in response to an external force, F(t+Δt). This can then be used to compute the velocity and acceleration of the components using Equations 4.7 or 4.9 and 4.8, respectively. These outputs are then used to compute the dynamic forces based on Equations 3.76 to 3.79.

4.2. ROAD ROUGHNESS MODELING

To incorporate road roughness into the dynamic force model developed in this study, the ISO 8608 roughness model, as presented in Section 3.5.1, was used to generate parallel random rough profiles for the left and right sides of the truck. PRP generator, a MATLAB program developed by [69] based on ISO 8608 model, was used for generating the road profiles. Input data for the models are presented in Tables 4.1 and 4.2. The input

data includes the road class, the reference PSD, road length and distance between profiles (center-to-center distance between tires).

Table 4.1 ISO 8608 road roughness classification [172]

Road class	Degree of roughness $G(n_o)$ (10^{-6} m^3/cycle) for n_o = 0.1 cycle/m		
	Lower limit	Geometric mean	Upper limit
A (Very good)	-	16	32
B (good)	32	64	128
C (Average)	128	256	512
D (Poor)	512	1,024	2,048
E (Very poor)	2,048	4,096	8,192

Table 4.2 Road roughness model input data

Parameter	Value
Road length, m	100
Distance between profiles, m	6.233
Number of sampling frequencies	10,000
Sampling distance, m	0.01

The generated road profiles are shown in Figures 4.1 to 4.5 for road classes A to E, respectively. Road classes A to C have relatively smooth surfaces. Surface undulations for road class A ranged from -4 mm to 10 mm as shown in Figure 4.1. The Class B road had surface undulations ranging from -20 mm to 20 mm (Figure 4.2), while the class C road had roughness within -40 mm and 20 mm (Figure 4.3). It is impractical to achieve such level of road surface smoothness in mining environments because mine haul roads are typically unpaved, and the surface course is mostly angular crushed rocks/aggregates. Classes A to C roads are mostly asphalt or concrete roads without surface defects. Thus,

classes A to C roads will not be used for further modeling of the truck dynamic forces since they are unachievable in mining environments.

As stated in Section 2.4, most mine roads are classified as class D roads based on a global survey of mine haul roads by [61]. The random profile generated for class D roads (Figure 4.4) shows roughness values within ±100 mm. Well-constructed and maintained haul roads are within this category. Class E roads (Figure 4.5) are rougher and will subject trucks and operators to extreme vibrations, reducing truck component life and endangering operator health. Thus, these are not common and only represent poor roads. With the assumption that most haul roads are well maintained, the class D road profile was used in MATLAB/SIMULINK® to model the truck tire dynamic forces caused by the vertical excitation of the tires due to rough road surfaces.

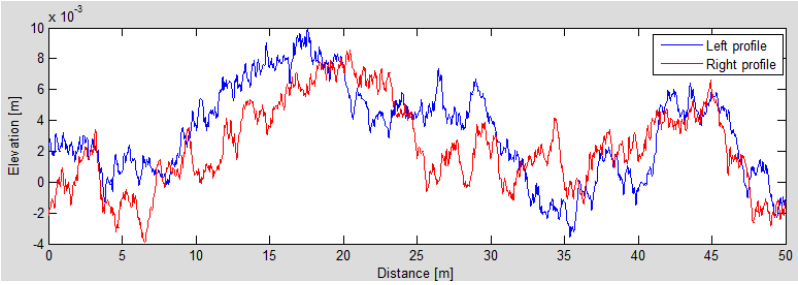

Figure 4.1 Generated road profiles for Class A roads

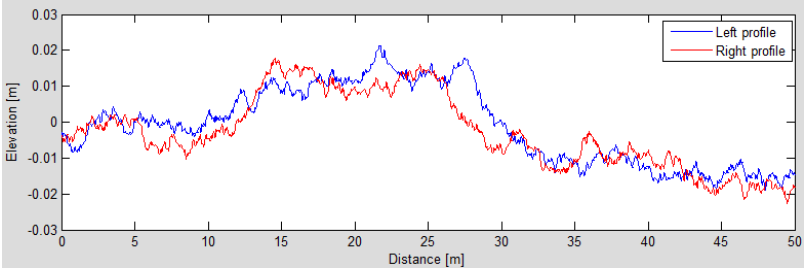

Figure 4.2 Generated road profiles for Class B roads

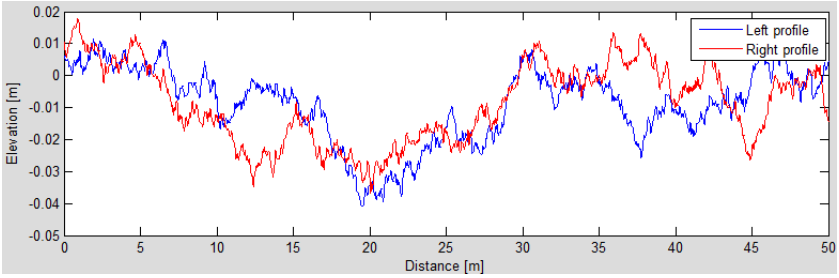

Figure 4.3 Generated road profiles for Class C roads

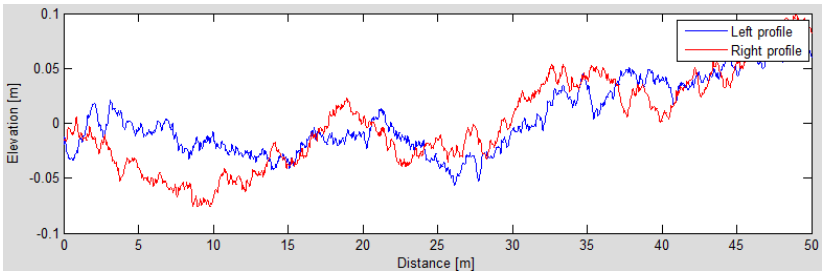

Figure 4.4 Generated road profiles for Class D roads

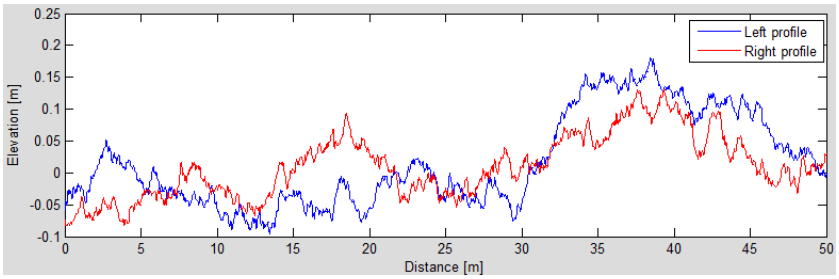

Figure 4.5 Generated road profiles for Class E roads

4.3. DYNAMIC FORCE MODEL IMPLEMENTATION IN MATLAB/SIMULINK

A simplified form of the mathematical model presented in Section 3 was solved in MATLAB/SIMULINK® to gain understanding of the impact of haul road roughness on truck impact forces imposed on the haul road. The simplified model used only one tire, the tire with the maximum load based on the weight distribution of the truck. It also

considered only class D roads since these are common in mining environments. The profile shown in Figure 4.4 was imposed as vertical displacement on the rear tire of a CAT 797F, generating the vertical excitations that contribute to the dynamic force. Tire travel speed was assumed constant throughout the time of the simulation. From the rimpull-gradeability curve of CAT 797F, a fully loaded truck on a flat road (zero grade resistance) with a 3% rolling resistance as commonly assumed in the mining industry, yields a maximum recommended speed of 57 km/hr (35.4 mph). This speed was used as the truck speed in the SIMULINK model.

The SIMULINK block diagram for obtaining the solutions is presented in Figure 4.6. The model in block (a) of Figure 4.6 uses the road profile (Figure 4.4) and truck speed to generate the truck vertical displacement induced by the road roughness during haulage.

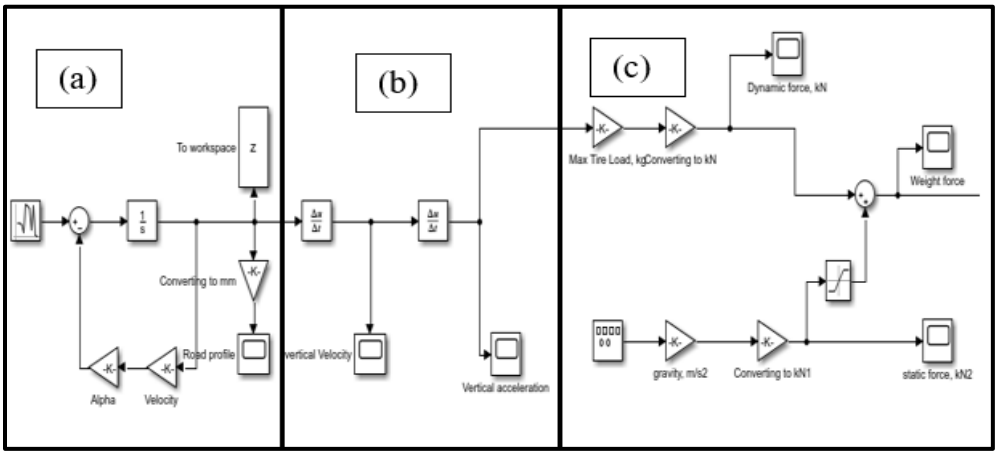

Figure 4.6 MATLAB/SIMULINK® model for computing tire dynamic forces

The displacement was then differentiated with respect to time to obtain the vertical velocity of the tire, which was also differentiated to obtain the tire vertical accelerations, as seen in block (b) of the SIMULINK model. In block (c), the dynamic force caused by

the vertical excitation is found by taking the product of the vertical accelerations and maximum tire load. The static force is computed as the maximum tire load multiplied by the acceleration due to gravity (9.81 m/s^2). The sum of the dynamic and static force then generates the total tire force imposed on the road surface, as expressed by Equation 3.79. This model ignored the truck suspension systems and tire stiffness and damping. The truck input parameters for the SIMULINK model are given in Table 4.3.

Table 4.3 Truck and tire input data [173]

Parameter	Value	Unit
Gross machine weight	623,690	kg
Weight distribution	33%: 67% (front: rear)	
Tire model	59/80R63	
Maximum tire load	104,468	kg
Tire unloaded diameter	4.025	m
Tire width	1.47	m
Maximum loaded speed	57	km/h

The mathematical model was verified by comparing its results with the results of the dynamic force virtual model developed in MSC.ADAMS. This verification ensured that the mathematical formulations accurately represent the truck tire-haul road system. It was validated using the field data obtained from a large-scale open-pit mine. The results of the verification and validation are presented in Section 4.8.

4.4. VIRTUAL MODELING IN MSC.ADAMS

Virtual prototype modeling in MSC.ADAMS was employed to model the dynamic truck-haul road interaction forces. A full truck-haul road model was created and solved in

MSC.ADAMS for modeling the truck dynamic forces generated during haulage. MSC.ADAMS was chosen for the detailed simulation due to the following:

i. The mathematical model was developed to aid understanding of the mechanics of load transfer of the truck-haul road system. Analytical solutions to the complete mathematical model are complex and time-consuming. Thus, the simplified solution cannot fully characterize the full truck-haul road problem.

ii. The virtual modeling capabilities and robust solver of MSC.ADAMS provide reliable tools for efficient simulation of the 3D full truck dynamics during haulage.

iii. The solution algorithm in MSC.ADAMS is time efficient since they are based on rigid MBD. The run times of the models are very short.

The model is a 72-DOFs rigid MBD model based on the Lagrange formulation and Newmark integration algorithm presented in Section 4.1. In the MSC.ADAMS environment, the x-axis is in the longitudinal direction (i.e. the direction of truck travel), the z-axis is in the lateral direction and the y-axis is in the vertical direction. Correspondingly, F_x, F_z, and F_y represent the longitudinal, lateral and vertical forces. In this research, F_y is of interest since the vertical impact forces are the dominant forces imposed on the haul roads.

The procedure employed in MSC.ADAMS for modeling the truck-haul road interaction problem can be summarized as shown in Figure 4.7. The process starts with the construction of the model geometry utilizing the CAD capabilities of MSC.ADAMS. The geometry of the truck was built by connecting rigid bodies using joints and spring-damper elements. The rigid bodies represent the various truck components. Each component has inertial properties automatically generated by MSC.ADAMS based on its geometry. The

components were also assigned user-defined mass properties, using data in the original equipment manufacturer (OEM) manuals.

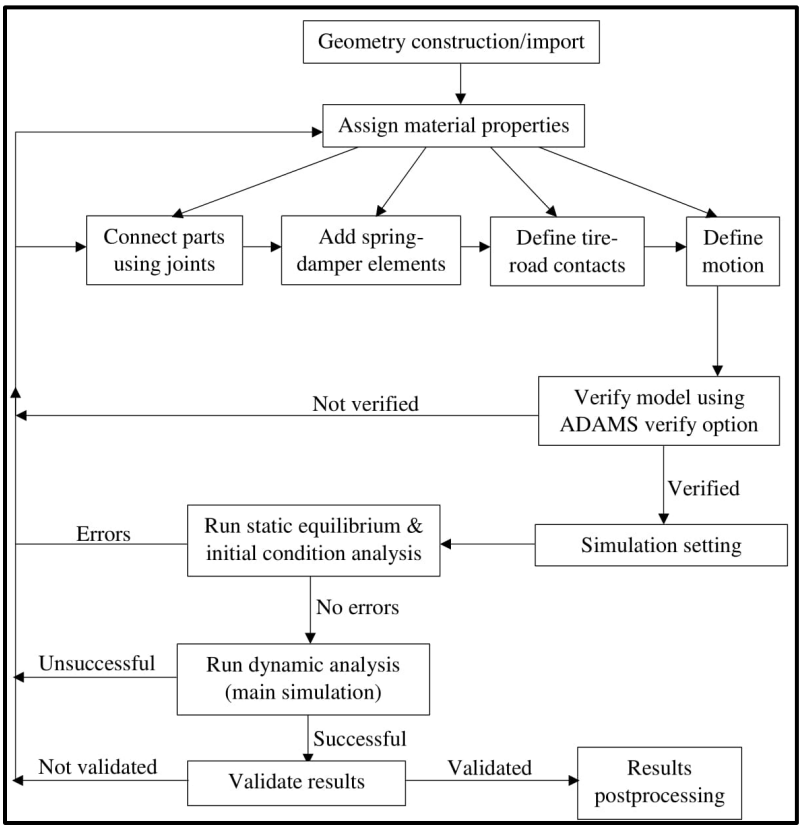

Figure 4.7 Flowchart for truck-road dynamic analysis in MSC.ADAMS

In MSC.ADAMS, each component adds 6 DOFs to the model. These include translation and rotations in the x, y and z directions. The constraints introduced into the model remove DOFs from the model, resulting in a constrained model with fewer DOFs than the unconstrained model.

The truck model (Figure 4.8) constructed in MSC.ADAMS consists of the body, the chassis, two axles, and six tires. For simplification purposes, the truck body was combined with the bucket, operators' cabin and other minor attachments to the truck body

into a single unit, referred to as the truck body. The bucket was constructed with several plates rigidly connected to each other. The cabin was modeled as a box sitting on the front assembly, which is also an assembly of several rigid boxes.

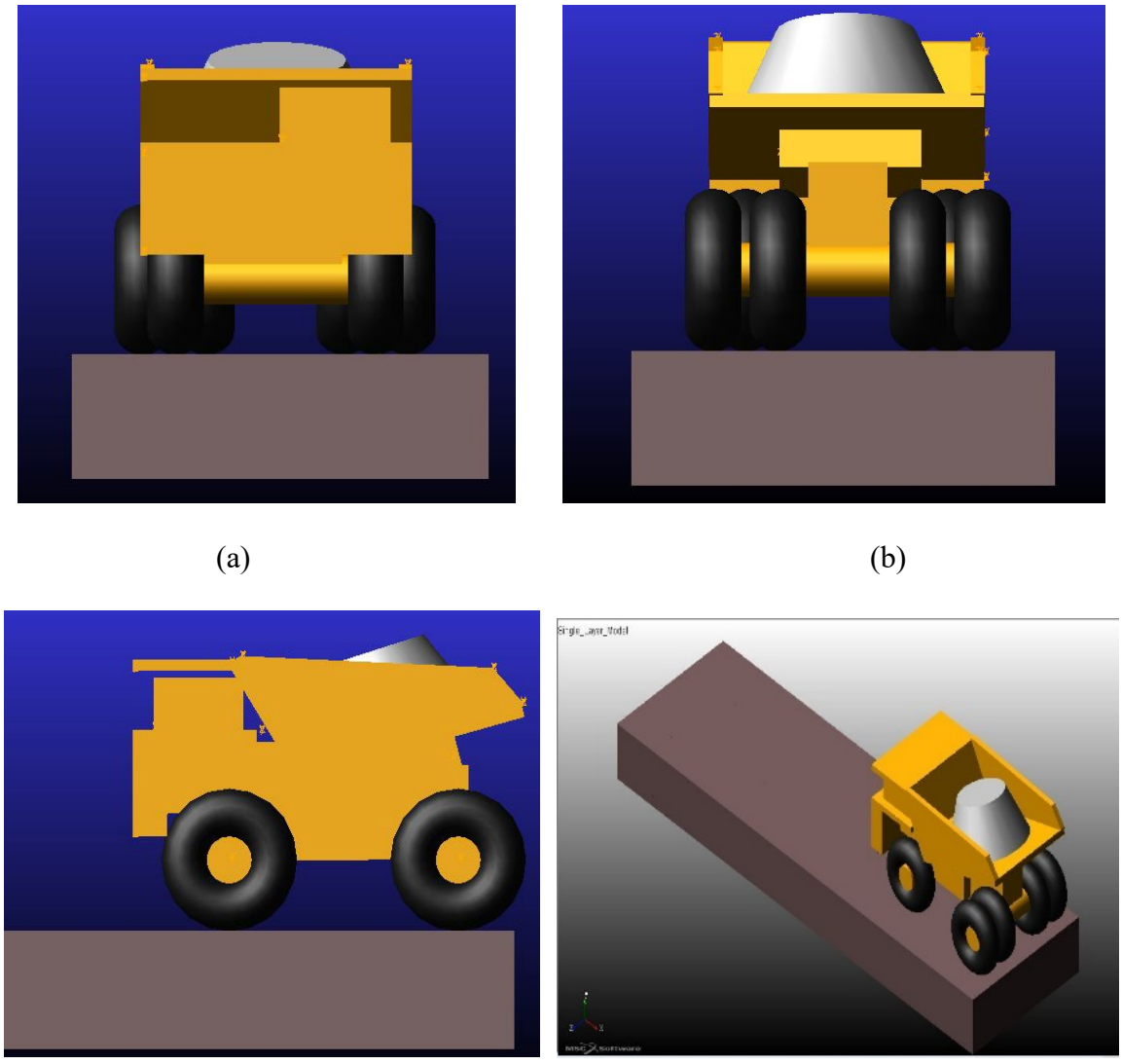

(a) (b)

(c) (d)

Figure 4.8 Truck-haul road model in (a) front (b) rear (c) side and (d) isometric views

The chassis was modeled as an assembly of rigid boxes, while the front and rear axles were modeled as rigid cylinders. The tires were modeled with torus elements [38] to represent the 59/80R63 tires used by CAT 797F. The truck model had 10 components; the truck body, chassis, two axles, and six tires. Thus, the unconstrained truck model had 60 DOFs, six each contributed by each component.

The truck payload was modeled as a frustum rigidly fixed to the bucket. This adds 6 DOFs to the model. The road was modeled as an assembly of boxes, representing the soil units making up the upper road layer. This introduces six more degrees of freedom to the model. Thus, the complete truck-haul road model is a 72-DOFs system consisting of rigid body elements.

4.5. MODEL DIMENSIONS AND INPUT DATA

The truck considered in this research is a CAT 797F conventional rear dump truck (Figure 4.9). The geometry was created in MSC.ADAMS to mimic the actual truck as closely as possible, while avoiding details that do not impact the model output. The model geometry was constructed using the dimensions shown in Table 4.4. The road geometry was built using units of blocks of dimension 5m × 5m × 5m. The road had a length of 50 m, a width of 15 m and a thickness of 5 m.

To ensure that the model represents the truck being studied, the sum of the component masses must be equal to the empty weight of the physical truck. Component masses were sourced from the equipment manual as presented in Table 4.5. The haul road properties considered are the material density, elastic modulus, and Poisson ratio, as given in Table 4.5.

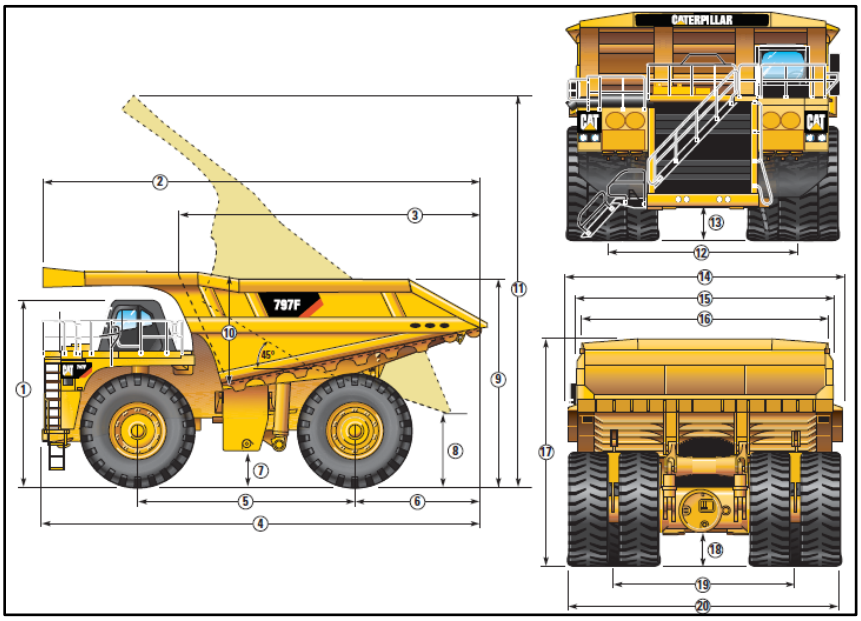

Figure 4.9 Dimensions of CAT 797F conventional rear dump truck [166]

Table 4.4 CAT 797F detailed truck dimensions [166]

Part No.	Part Name	Dimension (mm)
1	Height to Top of ROPS – Empty	6,526
2	Overall Body Length	14,802
3	Inside Body Length	9,976
4	Overall Length	15,080
5	Wheelbase	7,195
6	Rear Axle to Tail	3,944
7	Loaded Ground Clearance	786
8	Dump Clearance	2017
9	Loading Height – Empty	6,998
10	Inside Body Depth – Maximum	3,363
11	Overall Height – Body Raised	15,701
12	Centerline Front Tire Width	6,534
13	Engine Guard Clearance – Loaded	1,025
14	Outside Body Width	9,755
15	Overall Canopy Width	9,116
16	Inside Body Width	8,513
17	Front Canopy Height – Empty	7,709
18	Rear Axle Clearance – Loaded	947
19	Centerline Rear Dual Tire Width	6,233
20	Overall Tire Width	9,529

Table 4.5 Model input parameters [38], [166], [173]

Parameter	Value
Truck rated payload, kg	363,000
Truck body weight, kg	34,000
Chassis weight, kg	194,690
Axle (front & rear) weight, kg	4,000
Tire weight, kg	4,000
Tire unloaded diameter, m	4.028
Truck GMW, kg	623,690
Road density, kg/m^3	1,600
Road Young's modulus, MPa	140
Road Poisson ratio	0.3

4.6. MODEL CONSTRAINTS AND CONTACT MODELING

After constructing the model geometry, constraints were assigned to ensure that the truck-road system behaves like the real system. The truck components were connected via joints and spring-damper elements. The joints were chosen to mimic the real truck component connections and allow the necessary motions that significantly impact the truck dynamic forces. They were also chosen to ensure the appropriate relative motion between the connecting bodies. These joints introduced constraints into the model, reducing the DOFs of the unconstrained model.

A fixed joint was used to connect the payload to the truck bucket. The fixed joint ensures that there is no relative motion between the payload and the bucket. Thus, the payload was assumed to be stationary in the bucket during truck motion. The fixed joint removed 6 DOFs from the model; three translational and three rotational DOFs as given by Equation 4.14 and Equation 4.15, respectively [174]. In Equations 4.14 and 4.15, X_i and X_j represent the global x coordinate of the i^{th} (on the action body) and j^{th} markers (on the

reaction body), respectively. Y_i, Y_j, Z_i, and Z_j have similar definitions in the Y and Z axes, respectively.

$$X_i - X_j = 0;\ Y_i - Y_j = 0;\ Z_i - Z_j = 0 \tag{4.14}$$

$$X_i * X_j = 0;\ Y_i * Y_j = 0;\ Z_i * Z_j = 0 \tag{4.15}$$

The truck bucket was connected to the chassis via a translational joint, which allows vertical translational motion between the two bodies. A spring-damper element was also used to connect the bucket to the chassis, representing the suspension system (stiffness and damping) that connects the bucket to the chassis in the truck. The translational joint removed 5 DOFs; two translational (longitudinal and lateral) and all three rotational degrees of freedom, from the model. Therefore, only the vertical translational DOF remained between the bucket and chassis. The spring-damper element allows the vertical bouncing movement between the bucket and chassis, generating spring-damper forces, which contribute to the overall truck dynamics.

A translational joint each connected the front and rear axles to the chassis. This removes 10 DOFs; four translational and six rotational DOFs. These joints allow translational movement between the chassis and axles in the vertical direction. Also, four spring-damper elements connected the truck body to the rear axle and two spring-damper elements connected the front axle to the truck body. These elements capture the spring stiffness and damping properties of the suspension systems connecting the truck body to the axles. As the truck moves, forces are generated from these elements, contributing to the overall truck dynamics.

The tires were joined to the axles via six revolute joints, one joint for each tire. These joints allow rotational movement between the tires and the axles in the longitudinal direction, causing the spinning of the tires. The six revolute joints remove thirty DOFs (each removes two rotational and three translational DOFs) from the model. Two translational motions were applied to the front tires. These two motions remove 2 DOFs from the model and serve to drive the truck during the simulation. The two motions, together with the revolute joints, ensure the translational and spinning motion of the tires during the simulation as occurs when the truck is moving.

The tires were each represented by spring-damper elements that represent their stiffness and damping properties. The spring deformation (δ) and deformation velocity ($\partial\delta/\partial t$) contribute to the tire normal forces, as given by Equation 4.16 [38]. k_n and η are the normal tire stiffness and damping, respectively.

$$F_n = k_n - \eta \frac{\partial \delta}{\partial t} \tag{4.16}$$

The road was connected to the ground via a fixed joint to restrict road movement. This removed all the 6 DOFs that the road contributes to the model. To capture road stiffness and damping properties, the road units were represented with springs and dampers. Solid-to-solid contacts, with Coulomb friction, were defined between the truck tires and the road surface. This is where the tire contact forces are generated during simulation. MSC.ADAMS assumes that the contact behaves like a spring-damper, with specified stiffness and damping properties. The impact force function was used for the computation of the contact forces. Static (μ_{stat}) and dynamic (μ_{dyn}) friction coefficients were

specified at the contacts for computing the tire lateral and longitudinal forces using Equations 4.17 and 4.18, respectively [38]. μ_{stat} is used for computing the lateral and longitudinal forces just before the truck begins to move. Once the truck starts to move, μ_{dyn} is used for the computation of the lateral and longitudinal forces. μ_{stat} is typically greater than μ_{dyn}. F_n is the tire vertical dynamic force.

$$F_t = \mu_{stat/dyn} F_n \left(1 - e^{-kt|\alpha|}\right) \operatorname{sgn}(\alpha) \tag{4.17}$$

$$F_l = \left(\mu_{stat/dyn} - \gamma\right) F_n \tag{4.18}$$

The constraints introduced into the model can be summarized as follows:

- No motion between payload and truck bucket;
- Vertical translational motion between the truck body/bucket and chassis;
- Vertical translational motion between the chassis and axles;
- Rotational motion about the lateral axis between the axles and the tires;
- Longitudinal motion of the tires on the road; and
- No motion between the road and the ground.

The forces introduced in the model can be summarized as follows:

- Inertial forces due to each component mass and acceleration ($F_{inertial} = m\ddot{z}$);
- The spring forces due to the stiffness of the connecting springs and component displacements ($F_{spring}=kz$);
- The damping forces due to the damping effects of the suspension systems and the component velocities ($F_{damping}=c\dot{z}$);

- Reaction forces generated at all joints;
- Tire-road contact forces due to contact friction, tire penetration, contact stiffness and damping, and tire deflection.

The constrained virtual model is a 13-DOFs model for conducting a dynamic simulation of ultra-large dump truck-haul road interactions. Figure 4.10 shows the model force elements (spring-damper and contacts), while Figure 4.11 shows the constraints (joints and motions) applied to the virtual model. Table 4.6 summarizes the model construction and DOFs. Table 4.7 contains the stiffness and damping coefficients for the various spring-damper systems used in the model.

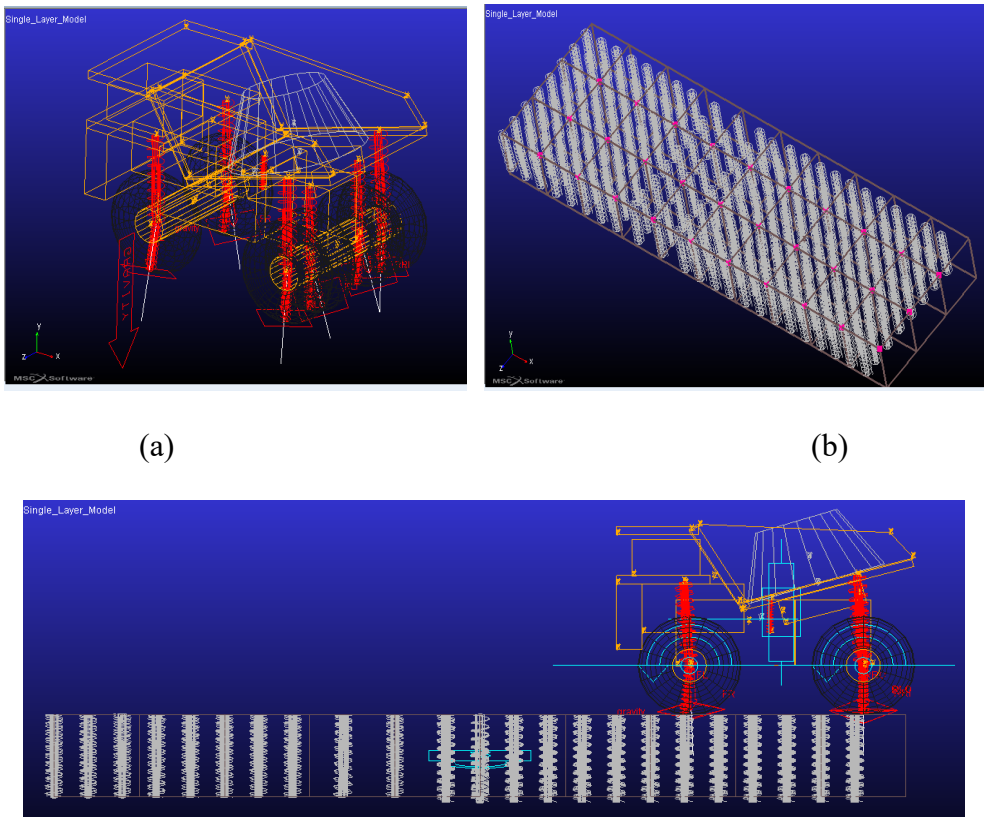

(a) (b)

(c)

Figure 4.10 Spring-damper elements and contacts for truck-haul road system

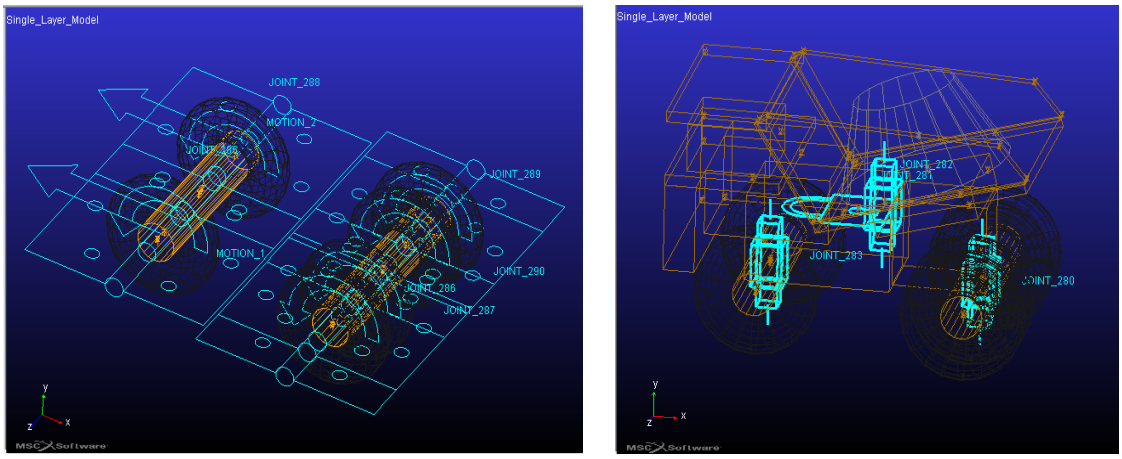

(a) (b)

Figure 4.11 Joint elements (a) axle-tire revolute joints (b) truck body-chassis-axles joints

Table 4.6 Summary of model constraints and DOFs

Parameter	Value
Bodies	12
Unconstrained model DOFs	(12*6) = 72
Revolute joints	6
Fixed joints	2
Translational joints	3
Translational motions	2
DOFs removed by revolute joints	(6*5) = 30
DOFs removed by fixed joints	(2*6) = 12
DOFs removed by translational joints	(3*5) = 15
DOFs removed by translational motions	(2*1) = 2
Constrained model DOFs	13

Table 4.7 Truck-road model stiffness and damping coefficients [37], [38], [40], [99]

Component	Stiffness coefficient (N/m)	Damping coefficient (Ns/m)
Bucket-chassis suspension	1.927×10^{7}	1.569×10^{6}
Front suspension	1.327×10^{7}	1.224×10^{6}
Rear suspension	1.927×10^{7}	1.569×10^{6}
Tires (front and rear)	3.786×10^{6}	470
Haul road (oil sands)	2×10^{7}	1.2×10^{5}
Contact	1×10^{8}	1×10^{4}

4.7. SOLUTION IMPLEMENTATION IN ADAMS/Solver

After the model geometry was built and appropriate constraints and forces assigned to it, ADAMS/Solver, the solution engine of MSC.ADAMS was used for running the dynamic analysis of the truck-road interaction problem. ADAMS/Solver is integrated into MSC.ADAMS/view. During the simulations, ADAMS/Solver sets the initial conditions (ICs) for each object in the model. The ICs for the truck-road system include zero translational and rotational displacements, velocities and accelerations for all model components at the beginning (t = 0).

After the ICs are defined, ADAMS/Solver compiles the EOMs of the system based on the component masses, stiffness and damping properties, and the contact properties. The EOMs also consider the system constraints introduced by the joints and motions imposed on the system. ADAMS/Solver formulates the EOMs based on Newtonian mechanics. The EOMs define how the system components move relative to each other based on the system constraints and forces. Three formulations are available in ADAMS/Solver for formulating the differential-algebraic equations (DAEs). These are the Index 3 (I3), Stabilized Index 2 (SI2) and Stabilized Index 1 (SI1) methods [175]. The I3 (index 3) formulation, which is the only one supported for the Newmark scheme, was used for formulating the EOMs in this work. This method is given in Equation 4.19, which is the Lagrange multiplier form of the constrained EOMs [176].

$$M(q)\ddot{q}+\Phi_q^T(q)\lambda=Q(\dot{q},q,t) \tag{4.19}$$

M(q) is the generalized mass matrix and Q($\dot{q}$,q, t) is the generalized external force acting on the system at the generalized coordinate, q. Φ_q is the displacement kinematic constraint of the system, which can be defined using Equation 4.20. Equation 4.20 ensures that the system components do not experience any displacement during the simulation. Thus, the components do not detach from each other and obey the restrictions imposed by the joints. The velocity and acceleration constraints of the system are given by Equations 4.21 and 4.22, which ensure zero velocity and acceleration of the system components during the simulation. These equations and details of the I3 formulation can be found in [176].

$$\Phi(q,t) = [\Phi_1(q,t)...\Phi_m(q,t)]^T=0 \tag{4.20}$$

$$\Phi q(q,t)\dot{q}+\Phi t(q,t)=0 \tag{4.21}$$

$$\Phi_q(q,t)\ddot{q} + (\Phi_q(q,t)\dot{q})_q\dot{q}+2\Phi_{qt}(q,t)\dot{q}+\Phi_{tt}(q,t)=0 \tag{4.22}$$

The total number of system constraints is given by m. λ is the Lagrange multiplier. Equations 4.19 to 4.22 describe the I3 formulation used by ADAMS/Solver to formulate the DAEs of the truck-haul road system. This method is fast and ensures that the solution satisfies all the constraints of the model [174].

Once the EOMs have been formulated, accuracy limits are set, and the solver is chosen for solving the EOMs. ADAMS/Solver has two main groups of dynamic solvers [174]; stiff solution methods that use implicit backward difference formulations and non-stiff solution methods employing explicit solution schemes. Stiff integrators include the gear (GSTIFF), modified gear (WSTIFF), constant backward difference formulations

(BDF) and the Runge-Kutta fourth-fifth (RKF45) algorithms. Only one non-stiff integrator is available, the Adams-Bashforth-Adams-Moulton (ABAM) integrator. More efficient implicit stiff integrators have been introduced into ADAMS/Solver [174]. These are the HHT (Hilber-Hughes-Taylor) and Newmark integrators.

The implicit Newmark integration scheme presented in Section 4.1 was used in ADAMS/Solver, which uses the C++ language, to solve the dynamic model. The dynamic simulation involves solutions to differential-algebraic equations (DAEs) governing the system. The accuracy and stability of the Newmark algorithm are controlled by two main parameters, β, and α. When $\beta = 0.25$ and $\alpha = 0.5$, the solution is unconditionally stable. The Newmark solver also has the advantage of being stable even at very small-time steps and reducing the number of evaluations of the Jacobian/partial differential matrix. The Jacobian matrix is evaluated using the modified Newton-Raphson approach.

After the simulation was run, ADAMS/Postprocessor was used for generating the results plots and animations. Kinematic system responses such as component displacements, velocities, and accelerations were obtained with respect to time. The spring-damper forces, joint reactive forces, and contact forces were also generated on the ADAMS/Postprocessor platform. The key output of interest in this study is the tire-road contact force. These forces were exported in .csv format for further analysis in MS Excel.

4.8. MODEL VERIFICATION AND VALIDATION

Verification was done to detect and correct all errors in the model to ensure that it behaves like a real truck-road system in mining environments. Validation involved

checking the model dynamic forces against data obtained from a large-scale open-pit mine to ensure that the model accurately predicts the truck dynamic forces imposed on the road.

4.8.1. Model Verification. A three-step verification process was employed to check that there were no errors in the model that will affect the accuracy of the output. First, the verification tool in MSC.ADAMS was used to verify the model. This tool computes the DOFs of the system using the Gruebler equation. The Gruebler equation computes the DOFs of the model as the sum of DOFs of the unconstrained model minus DOFs removed by model constraints. The ADAMS verification tool also identifies redundant constraints in the model and makes suggestions to handle/remove them. Redundant constraints are system constraints that remove identical DOFs from the model or constrain two parts in the same way, causing over-constraining of the model [174]. A model that has redundant constraints does not yield unique solutions as the automatic ADAMS/Solver removal of redundant constraint equations is arbitrary. Hence, different constraints might be removed from the model during different runs, generating different solutions for a model that has the same input data. The verification of the final truck-road model yielded Figure 4.12, which confirms the personal checks presented in Table 4.6.

A static equilibrium analysis was conducted next as a second stage verification procedure. During the static equilibrium analysis, Adams/Solver iteratively repositions all parts in the model to balance all the forces in the model. The modified Newton-Raphson iteration technique is used in ADAMS/Solver for conducting the static equilibrium simulation. This procedure showed that all forces were well balanced, and components were well connected to each other without any misalignments.

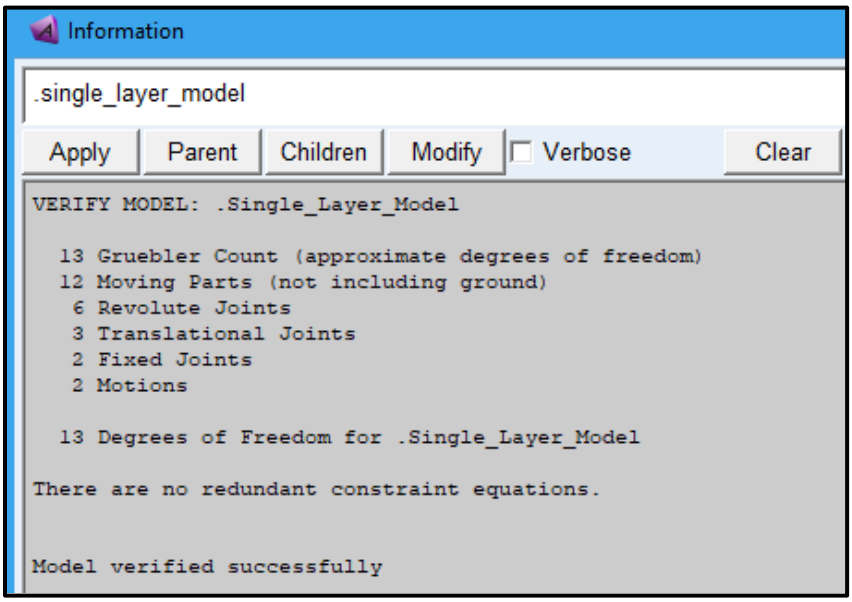

Figure 4.12 Model verification information window

The final verification stage involved viewing animations during the simulation process to help identify unusual and inaccurate system behavior that does not represent the real truck-road system behavior during haulage. Some unrealistic model behaviors that could render the model invalid are the truck losing contact with the road (flying) or not moving in the right direction. Other possible errors in system behavior include the road units or truck components getting detached, truck sinking into the road or tires not rolling as truck moves. These errors result from assigning inappropriate constraints to the model. Result plots were also studied during the simulation process to help identify unrealistic and inaccurate result patterns. This process also proved that the model behaved exactly like a real truck-road system. This three-stage verification was deemed enough to ensure that the model was producing the desired output and representative of the real truck-road system.

4.8.2. Model Validation. The MSC.ADAMS model was validated using data from a hard rock large-scale open-pit mine employing ultra-large trucks for moving ore and

waste. This section details the field data collection procedures and presents the validation of the dynamic force model.

4.8.2.1. Field measurement of truck dynamic forces. To validate the dynamic forces generated from the MSC.ADAMS model, field data were obtained from a large-scale open-pit mine employing ultra-large conventional rear dump trucks. The truck models used at the mine are CAT 793B, CAT 793C, and CAT 793D. These trucks have a rated payload capacity of 218 metric tons (240 US tons) and a gross machine weight of 384 metric tons (423 US tons). However, the mine has set a truck target payload of 240 metric tons (265 US tons). The mine employs a fleet of 140 trucks for ore and waste haulage.

4.8.2.2. Data. The data obtained for this research is real-time truck strut pressure data obtained through the Vital Information Management System (VIMS) of Caterpillar Inc. The trucks were equipped with sensors that measure a wide range of parameters during operation. These parameters include payload, speed, 3D location, strut pressures, tire temperature, and pressures and cycle time (loading, empty travel, loaded travel, dumping, waiting, queuing, etc.). Many other important parameters are measured for tracking truck performance and health. The data was recorded at 30 ft intervals along the haul road. The strut pressures for the truck during traveling (loaded) are typically used as an indication of road quality and indicate how much loads are imposed on the road as the truck travels. A strut pressure ≥500 psi (3,447.38 kPa) indicates a bad/rough road surface, while a strut pressure of ≤80 psi (551.58 kPa) indicates a good/smooth road profile. Thus, the strut pressures were used in this study for deriving the dynamic loads imposed on the road as the truck travels. Four strut pressures were measured and recorded during truck operation; the left front (LF), left rear (LR), right front (RF) and right rear (RR) strut pressures.

Data were obtained for 15 trucks; 5 each of CAT 793Bs, 793Cs, and 793Ds. The data was obtained for a duration of 31 days covering the entire month of July 2019. The data consists of the payload status (loaded/empty), actual payload, transmission gear, truck speed, truck service hours (indicating its operational age) and the four strut pressures (LF, LR, RF, and RR). There was no rain during the entire duration of data collection. Thus, road surfaces were very dry and tire penetration was insignificant.

4.8.2.3. Data collection. During truck operations, the data is recorded in real-time using sensors mounted on various components of the trucks. The data is transmitted through a wireless network to the dispatch control room. The dispatch control room uses the data to monitor real-time equipment performance and health, road conditions, and operator activity. The data is then transmitted to a company-wide web-based data system called Haul Truck Analytics (HTA). HTA operates on SAP Business Objects (BO), a software that uses a Web Intelligence (WEBI) interface and runs on SQL codes. The data can be queried in WEBI to generate reports of interest to the analyst and downloaded in .csv file format for further processing. A sample query used to obtain the data from WEBI for this study is shown in Figure 4.13.

The data was queried using the site code (indicating which site the data is from since the company has many mine sites), local date, equipment ID, service hours, payload status, ground speed, transmission gear, payload, and the four strut pressures. An example of daily strut pressure data from a CAT 793D truck is shown in Figure 4.14. Data from one CAT 793D was used for validating the MSC.ADAMS dynamic force and mathematical models. Data from two trucks each of CAT 793B, CAT 793C and CAT 793D was used for examining the impact of rough roads and imbalanced truckloads on the truck health.

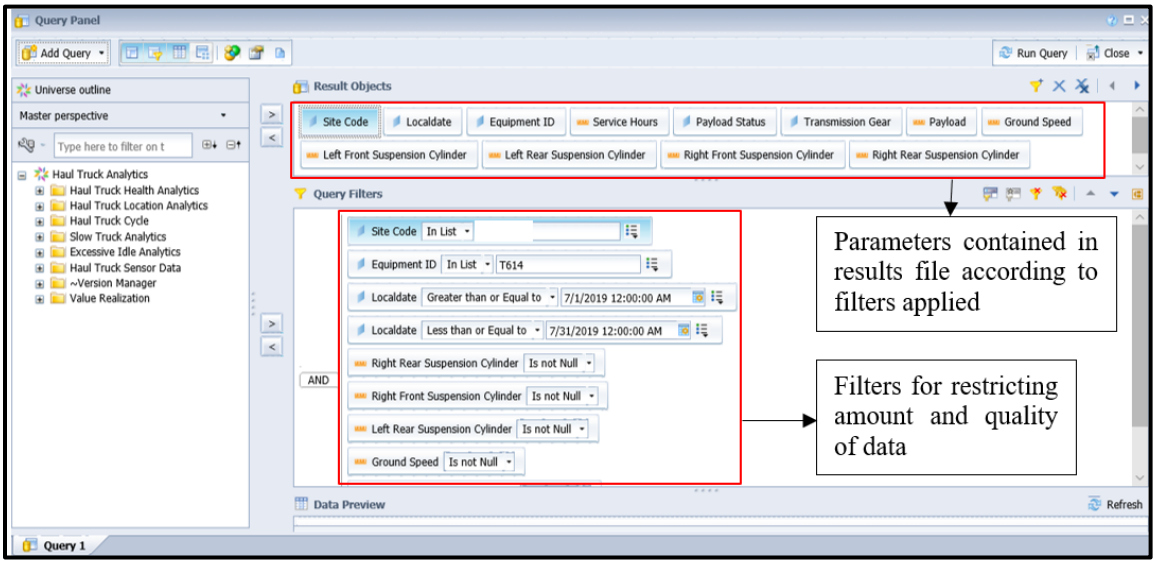

Figure 4.13 Sample data query in WEBI to obtain truck strut pressure data

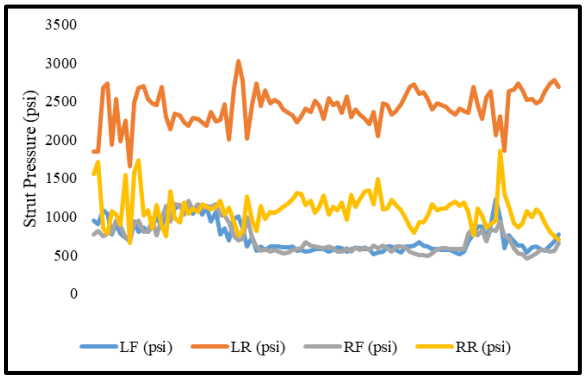

Figure 4.14 Sample strut pressure profile for a loaded CAT 793D traveling on a haul road

4.8.2.4. Deriving dynamic forces from strut pressure. The truck dynamic forces were derived from the dynamic strut pressures using Equation 4.23, which relates the dynamic force to the strut pressure and strut effective bearing area. The bearing areas of the front and rear struts were obtained from [30] as 0.126 m^2 and 0.114 m^2, respectively. It was assumed that the strut forces are the same as the tire forces imposed on the road, upon which assumption they are used as an indication of road quality. The dynamic forces

generated from Equation 4.23 were converted to the dynamic force coefficients (DFC) using Equation 4.24. DFC is a normalization of the forces to allow for the field data to be used for validating the MSC.ADAMS and mathematical models, whose forces were also converted to DFC. This normalization is also necessary since the model is for CAT 797F, which has a higher GMW compared to CAT 793. The assumption here is that a CAT 797F truck will behave in a similar manner as CAT 793s and hence, their normalized forces should be similar. The maximum static load for CAT 797F is 1,024.83 kN, while that for the CAT 793 truck is 667.8 kN, based on their weight distribution. Only the measured dynamic forces at the sixth truck gear, when the truck was running at maximum speed (33.64 mph or 54.14 km/hr), were used in the model validation. This was necessary since the speed of the truck for the MSC.ADAMS and mathematical models were taken as the maximum allowable speed of the truck.

$$Dynamic\ Force = \frac{Dynamic\ Strut\ Pressure\ (N/m^2)}{Effective\ Bearing\ Area\ of\ Struts\ (m^2)} \tag{4.23}$$

$$DFC = \frac{Dynamic\ Force}{Maximum\ Static\ Tire\ Load} \tag{4.24}$$

4.8.2.5. Model validation. Figure 4.15 shows the average DFC of all tire forces generated from the MSC.ADAMS model and the field results for an unloaded truck during haulage. It is seen that there is a satisfactory agreement between the model and field data. The average prediction error of the model when predicting the forces for an empty traveling truck was 8%. The minor differences in model and field data are probably caused by the uncertainty of model input data such as spring stiffnesses and damping coefficients. This

data was derived from other equipment since they could not be determined nor sourced from the literature for the CAT 797F truck. Other causes include extremely high values in the field data, which are likely caused by the occurrence of road surface defects such as potholes or rock pieces. Such high values are observed from 1.5 s to 1.7 s. The model did not include road surface defects since the ISO 8608 model cannot model road surface defects. However, an 8% error is acceptable for this work. Therefore, the model predicts empty truck forces satisfactorily.

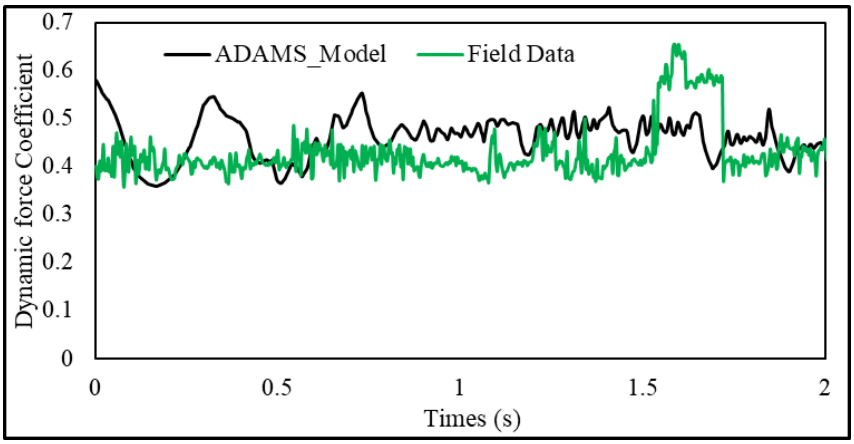

Figure 4.15 Validation of empty truck model using average tire forces

Figure 4.16 shows the dynamic forces generated from the MSC.ADAMS and mathematical model against the field data for a loaded truck. These results also show very good agreement. The mathematical model had an average prediction error of -19%, while the MSC.ADAMS model had an average error of -16%. It is also observed that the oscillations in the forces for the field data are like the oscillations in the mathematical model. The MSC.ADAMS model shows less pronounced force oscillations. The key reason for this trend is the inclusion of road roughness in the mathematical model, while

the MSC.ADAMS model assumed a smooth road surface. The field data implicitly captured the road roughness due to the rough nature of the haul roads. This explains the closer similarity of the field data with the mathematical model compared to the MSC.ADAMS model.

The validation results show that MSC.ADAMS and mathematical models perform satisfactorily and can be used for understanding truck tire dynamics during haulage. The validated model can be confidently used for examining the impact of truck over-loading and under-loading on the tire force and road response. It was used for simulating payload changes, which results served as input to the dynamic road response model in ABAQUS.

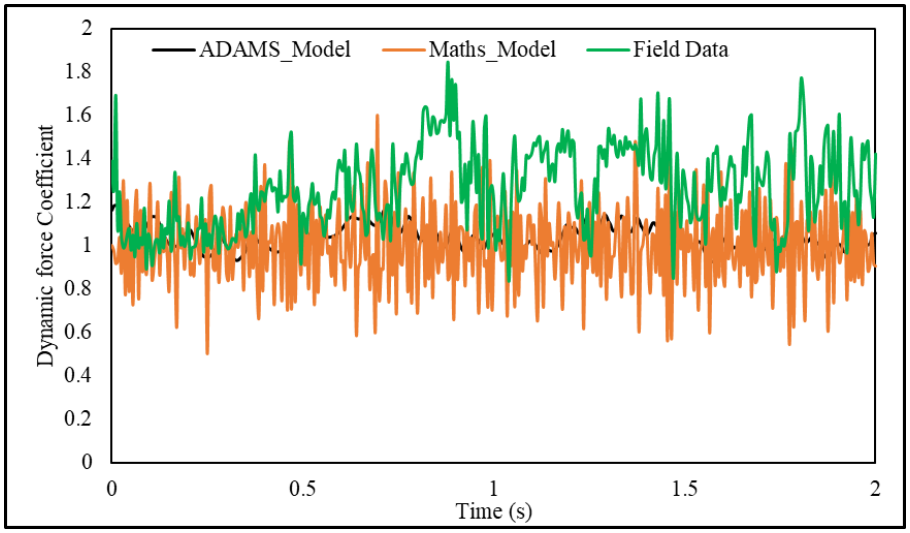

Figure 4.16 Validation of loaded truck model (at rated payload) using average tire forces

4.9. DYNAMIC MODEL EXPERIMENTAL DESIGN

Various factors affect the dynamic truck tire forces during truck operations. These include road and vehicle factors. The literature review established that the most important road factor that affects tire dynamics is the road surface roughness/unevenness. The most

important vehicle factor is vehicle weight/truck payload. Rough road surfaces subject vehicles to higher vertical oscillations, increasing the dynamic loading of the pavement. Vehicles with higher gross weights subject the road to higher loading.

During truck operations, the truck can either under-load (below the rated payload) or over-load (above the rated capacity). Experiments were conducted to study the effect of truckload variations on pavement loading. The mathematical and virtual dynamic force models were used for these experiments. The truck rated payload was varied within ±20% for MSC.ADAMS model and ±10% for the mathematical model, at intervals of 5%. An experiment was also conducted to evaluate the impact of an unloaded truck interacting with the road during hauling operations. Thus, a one-factor (payload) full factorial design was used in examining truck payload effects on pavement loading. A total of ten experiments were conducted in MSC.ADAMS environment, while 5 experiments were conducted using the SIMULINK model. Table 4.8 presents the payloads used for experimentation.

Table 4.8 Experimental design for dynamic model experimentation in MSC.ADAMS

MSC.ADAMS Experiment No	1	2	3	4	5	6	7	8	9	10
Maths model Experiment No.				1	2	3	4	5		
Payload (%)	0	80	85	90	95	100	105	110	115	120
Payload (metric tons)	0	290	309	327	345	363	381	399	417	436

4.10. LIMITATIONS OF THE DYNAMIC VIRTUAL MODEL

The tires have been assumed to have a torus shape. The treads and other tire components were assumed to be of no major significance and were not included in the

model. The most important tire parameters, which have been captured, are the tire dimensions (diameter and width), weight, stiffness, and damping. The complete tire, with treads, was, however, used in the ABAQUS model.

The model input data was sourced from the literature. Where data was not available in the literature, software default values were modified until results were intuitively representative of a CAT 797F truck. Due to propriety reasons, data on dump truck suspension stiffnesses and damping coefficients are not available from equipment manufacturers or in published literature. It is expensive to determine these parameters experimentally since there are no resources readily available for conducting such experiments. The values in literature have generally been approximated using data from other heavy machinery and agricultural equipment [40]. Tire stiffness data were obtained from [37], who determined tire stiffness and damping coefficients from static truck loading experiments. Data on haul road stiffness and damping were sourced from [95]. This data could vary from the actual data associated with ultra-large trucks and haul roads. For this work, however, they were deemed to be acceptable.

Based on knowledge of the static tire forces of the CAT 797F, the results generated from the models are intuitively accurate as the dynamic forces oscillate about the static force, similar to the representation in Figure 3.7. Also, the model has satisfactory agreements with field data, as shown in Figures 4.15 and 4.16. This demonstrates the accuracy of the model and shows that the model can reliably be used to study the truck-road dynamic force phenomenon.

4.11. TRUCK HEALTH ANALYSIS

The truck dynamics generated during haulage affect the truck, the road, and the operator. Caterpillar developed a concept called the Application Severity Analysis (ASA) for examining the health risks of trucks and for early detection of truck health issues such as frame cracking [30]. The ASA utilizes three parameters; rack, pitch, and roll (bias) to monitor truck health risks. These parameters are computed using the measured truck strut pressure. According to [177], values of these parameters beyond ±8,500 kPa (1,233 psi) put a CAT 793 at health risks such as premature cracking of the truck frame, axle, and other components. Rack, roll, and pitch were computed for 15 trucks consisting of five each of CAT 793B, CAT 793C, and CAT 793D. The computations were made for loaded and empty trucks traveling on the haul roads. Results from three trucks were used in this study to highlight the importance of payload balance in reducing truck health risks.

4.11.1. Rack. The rack is the diagonal twisting/torsional forces acting on the truck frame, which eventually transfer to other truck components such as the tires and axles. According to Mills (2002), the stresses and strains experienced by the truck structure are highly dependent on the rack. It is the main cause of dump truck frame cracking and can adversely affect truck frame life. The rack experienced by the truck frame was computed using Equation 4.25 [30] utilizing strut pressure data obtained from the mine. The rack experienced by the truck is illustrated in Figure 4.17.

$$\text{Rack} = (\text{LF} + \text{RR}) - (\text{RF} + \text{LR}) \tag{4.25}$$

A high positive rack is an indication of the over-loading of the left front or right rear tire or both. A high negative rack is an indication of the over-loading of the right front or left rear tire or both.

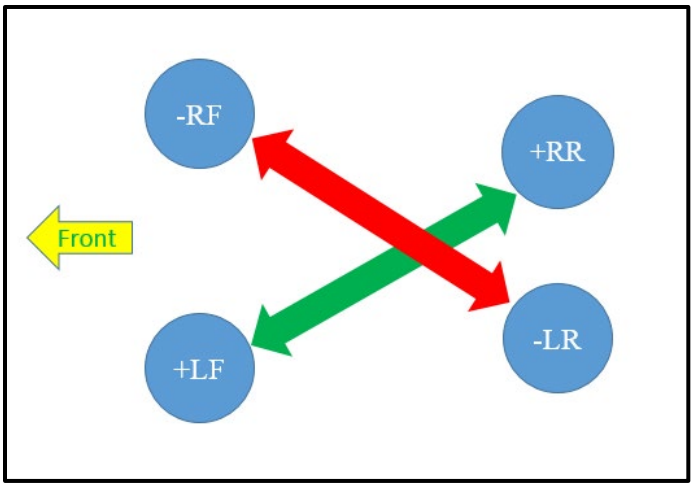

Figure 4.17 Truck suspension configuration for rack calculation [30]

4.11.2. Pitch. Pitch is the longitudinal stress on the truck body caused by an imbalanced load to the front or rear. It is computed using Equation 4.26 [30] and illustrated in Figure 4.18. When the load distribution of 33% front axle and 67% rear axle is not achieved, the pitch values are excessive.

$$\text{Pitch} = (\text{LF} + \text{RF}) - (\text{LR} + \text{RR}) \tag{4.26}$$

Figure 4.19 demonstrates the truck loading scenario that can result in excessive pitch. This can cause hastened damage to the tires, rims, bearings, steering components, suspension cylinders and other truck components. A high positive pitch is an indication of a truck that is over-loaded to the front, while a high negative pitch indicates over-loading

to the rear. Front over-loading occurs more often as the canopy of the truck is commonly loaded with material to get extra payload.

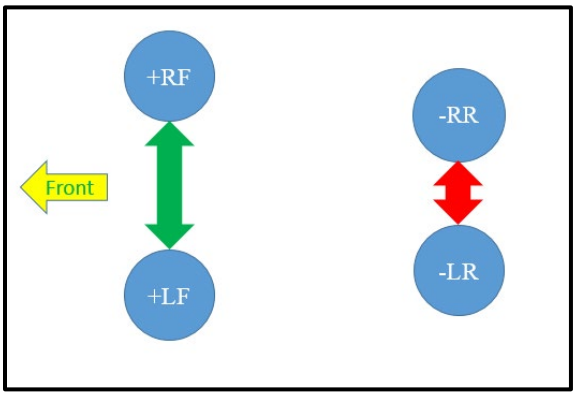

Figure 4.18 Truck suspensions configuration for pitch calculation [30]

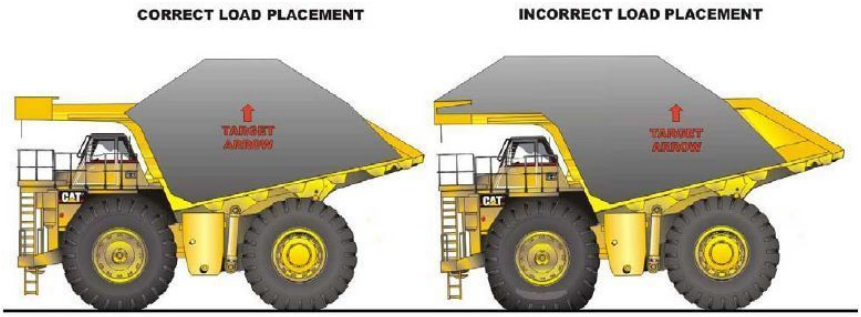

(a)

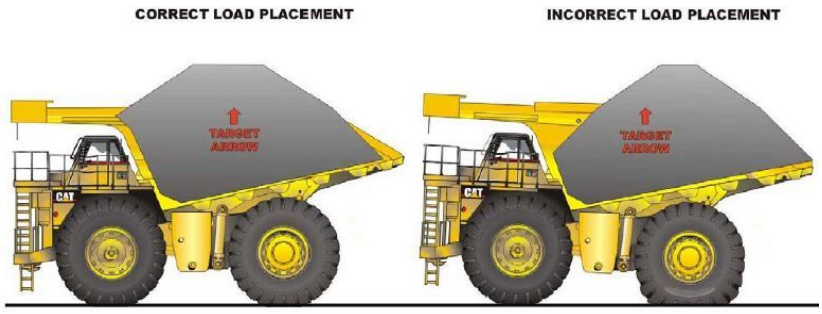

(b)

Figure 4.19 Dump truck (a) front and (b) rear over-loading [178]

4.11.3. Roll. Roll is the lateral stresses acting on the truck body caused by imbalanced loading to the right or left of the truck. A high positive roll means that the truck is over-loaded on the left side (left rear and left front tires) or negotiating a curve to the right. A high negative roll shows the truck is over-loaded on the right side (Figure 4.20) or negotiating a curve to the left. High roll events reduce the life of the final drives and wheel bearings and increase the probability of strut gas charge loss. The roll was computed using Equation 4.27 [30]. Figure 4.21 is an illustration of truck roll/bias.

$$\text{Roll} = (\text{LF} + \text{LR}) - (\text{RF} + \text{RR}) \tag{4.27}$$

Figure 4.20 Left and right truck over-loading [178], [30]

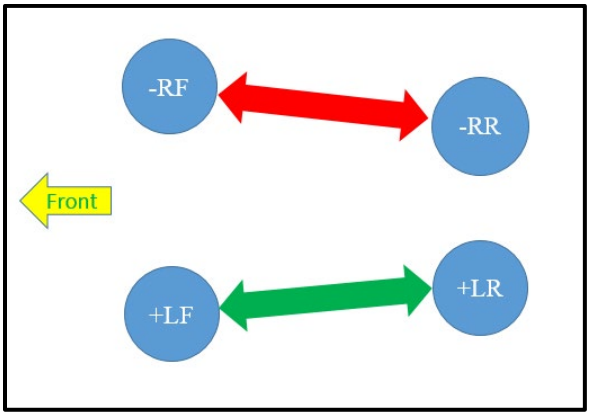

Figure 4.21 Truck suspensions configuration for roll calculation [30]

Figure 4.22 shows a sample of the measured strut pressures for a loaded truck that were used for computing the rack, roll and pitch of the trucks. This figure shows imbalanced truck loading, with loads biased to the rear right tire. This leads to excessive positive rack values and excessive negative roll and pitch values, which exceed the recommended thresholds, as shown in Figure 4.23. Figure 4.24 shows the measured strut pressures for an empty truck showing fairly uniform strut pressures. The corresponding rack, roll, and pitch experienced by the truck are within the safe limits (Figure 4.25).

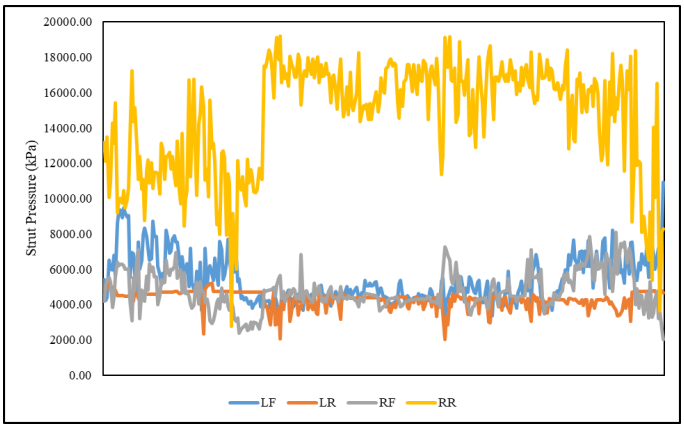

Figure 4.22 Loaded truck dynamic strut pressures

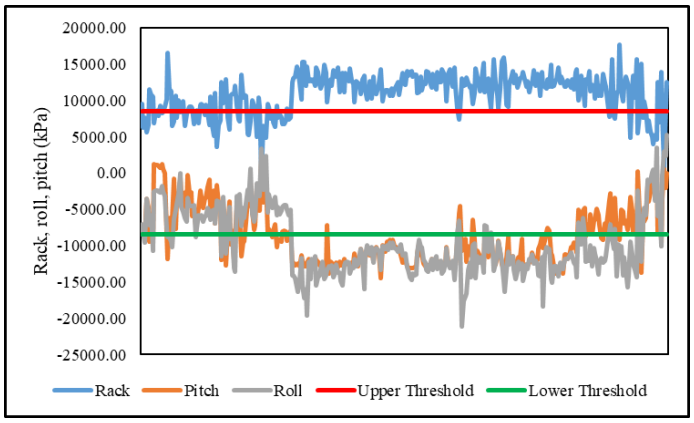

Figure 4.23 Loaded truck rack, roll, and pitch

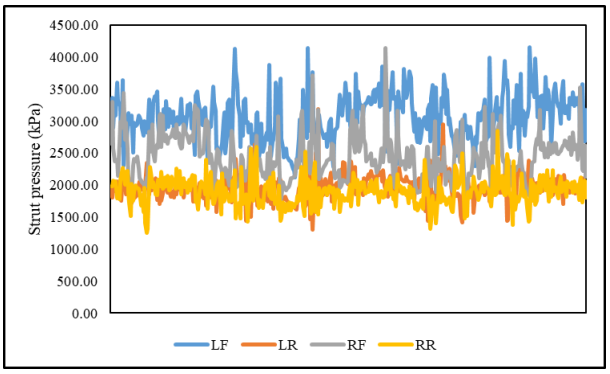

Figure 4.24 Empty truck dynamic strut pressure

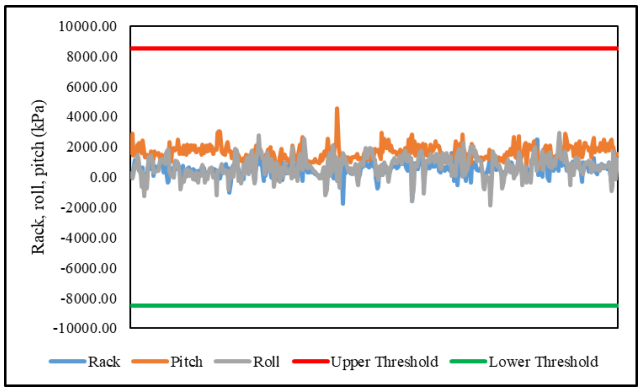

Figure 4.25 Empty truck rack, roll, and pitch

4.11.4. Multiple Linear Regression (MLR). Multiple linear regression (MLR) was conducted in JMP, a statistical analysis software. The MLR was conducted separately for loaded and empty trucks traveling on the haul road. The regression models relate truck service hours (operational age), payload and ground speed to the strut pressure. The modeling was conducted to formulate statistical models for predicting strut pressures, which can be used to identify optimal truck operating parameters, such as target payload and speed, to ensure healthy truck operations. Such optimal parameters will ensure the longevity of truck components and prevent premature component damage. For the loaded

trucks, Equation 4.28 is the general form of the MLR model used, while Equation 4.29 was used for the empty trucks. The major difference is that payload was factored into the loaded truck models as an input variable, while it was not included for the empty trucks.

$$sp_l = \beta_1 P + \beta_2 gs_l + \beta_3 sh + \beta_4 P * gs_l + \beta_5 gs_l * sh + \beta_6 P * sh + \beta_7 P * gs_l * sh + \alpha_l \quad (4.28)$$

$$sp_e = \beta_1 gs_e + \beta_2 sh + \beta_3 sh * gs_e + \alpha_e \quad (4.29)$$

β_i represents the contribution of each input variable to the strut pressure and α is the model intercept. P is the truck payload (US tons), gs is the truck ground speed (mph), sh is the truck service hours (hrs), and sp is the strut pressure (kPa). The subscripts e and l stand for empty and loaded trucks, respectively. Least-squares fitting (LSF) techniques were used to derive optimal values of the β_i that result in the least model errors and improved model performance.

The models incorporate the exclusive effect of each input variable, and the two-way and three-way interactions among the variables. A confidence interval of 95% was used for generating the models. Thus, variables that had a p-value > 0.05 were considered to have insignificant effects on the output. Such variables were excluded from the resulting regression models. The performance of the statistical models was evaluated using the root mean square error (RMSE), mean percentage error (MPE) and R^2.

4.12. SUMMARY

A 3D rigid multi-body truck-haul road model has been created in MSC.ADAMS for studying ultra-large truck-haul road contact dynamics. The model geometry was built

by connecting various rigid bodies to mimic the CAT 797F ultra-large truck. The various model components were assigned properties including masses, densities and elastic properties. The unconstrained model had 72 DOFs. Constraints were applied to the model via joints and motions, reducing the model to 13 DOFs. Forces were applied to the model via spring-damper elements. The spring-damper elements connect various components of the truck, representing the truck suspension systems. The tire and haul road stiffness and damping properties were modeled via spring-damper elements. Solid-to-solid contacts, with Coulomb friction, were defined at the tire-road contact. Contact forces were modeled using the impact force model. The dynamic analysis was conducted using the Newmark integration scheme implemented in ADAMS/Solver. The Newmark integration scheme was used due to its unconditional stability and computational efficiency.

The section also presented a solution to the mathematical model incorporating road roughness. The model was implemented in MATLAB/SIMULINK to compute truck tire forces. The models have been verified and validated and were used for experimentations. The truck health analysis conducted using the ASA proposed by Caterpillar has been described, as well as, MLR modeling for formulating empirical models for truck dynamic strut pressure estimation. The results of truck dynamic forces, truck health and MLR are based on the methods presented this section.

5. HAUL ROAD RESPONSE MODELING

This section discusses the governing equations and numerical solution procedures for conducting the finite element modeling (FEM) of haul road response to ultra-large truck dynamic loading. The FEM was conducted in ABAQUS CAE 2018 to compute the road response (stress, strain, and deformation) under ultra-large truck tire dynamic loading. This section details the FEM modeling procedure, including geometry modeling, meshing, boundary conditions, loading, and contact modeling. The verification and validation of the model are also discussed in this section. This section also discusses the experimental design for studying road performance under varying truck loading and road properties.

5.1. KEY MODELING ASSUMPTIONS

Several assumptions have been made to simplify the problem while including only the necessary details that affect the model behavior and output. The following assumptions were made in building the model:

- The road is a 3D four-layer pavement, consisting of the wearing surface, base, subbase, and subgrade. This represents a conventional mine haul road cross-section. The road geometry was first constructed as a single part and then partitioned, using cell partitioning, to create the various road layers, which were assigned different properties.
- Each layer was assumed to have homogenous and isotropic properties, such as elastic modulus, density, Poisson ratio, cohesion, and internal friction angle.

- It is computationally expensive to run a full truck-haul road model in ABAQUS with the available computer resources. Therefore, a single truck tire was used to represent the truckload. This simplification does not alter the accuracy of the model since the truck forces were computed using a full truck model in MSC.ADAMS. The average of the dynamic forces generated by all the tires in the MSC.ADAMS model was applied to the FEM tire in the road response model.
- The road is perfectly horizontal (zero grade) and straight (no curves) because horizontal roads present the maximum tire loading scenario.
- To reduce computational time, the tire was made rigid. This is necessary due to the excessive computational time of the model and the limited computer resources. Tires that have high inflation pressure can be assumed to be rigid (Kansake and Frimpong, 2018) since they do not deflect excessively.

FEM is a reliable tool for conducting a detailed stress-strain analysis of structures under dynamic loading conditions. Two groups of analysis are typically used for conducting dynamic FE analysis; the implicit and explicit dynamic analyses. The implicit analysis is preferred for long-duration events and linear systems. Explicit dynamic analysis yields more accurate results when the system contains non-linearities (material and/or geometric) and contacts. It is also recommended for fast duration events like impact analysis. In this research, explicit dynamic modeling was considered more appropriate due to the following system features:

- The tire loads imposed on the haul road are dynamic impact loads, and the loading happens within very short time intervals, especially at top truck speeds;
- The road exhibits non-linear response under dynamic loading; and

- The tire-road contacts are generally non-linear due to non-linearities in tire geometry and the tire-road response.

5.2. GOVERNING EQUATIONS

The governing equations of explicit dynamic analysis express the principles of conservation of mass, momentum, and energy in Lagrangian coordinates. The governing equations were obtained from [179]. Equation 5.1 expresses the principle of conservation of mass. For the Lagrangian formulation, the mesh moves and distorts with the material it models. This ensures that the masses of the undeformed and deformed models are equal. Thus, mass is conserved throughout the analysis.

$$\frac{\rho_0 V_0}{V} = \frac{m}{V} \tag{5.1}$$

As the structure is loaded, the density changes, with a corresponding change in volume. For example, when the tire load is applied on the road, the road undergoes strain hardening (density increases) due to road settlement/compression. The corresponding volume decrease ensures that the mass ($m = \rho_0 V_0 = \rho V$) remains the same.

The principle of conservation of momentum is expressed in Equations 5.2, 5.3 and 5.4. These equations relate the spatial acceleration in x, y and z directions to the stress tensor, σ_{ij}, which consists of three principal stresses (σ_{xx}, σ_{yy} and σ_{zz}) and three shear stresses ($\sigma_{xy} = \sigma_{yx}$, $\sigma_{xz} = \sigma_{zx}$ and $\sigma_{yz} = \sigma_{zy}$). Equation 5.5 defines the conservation of energy of the system. Equations 5.1 to 5.5, together with the materials models, initial conditions and boundary conditions, constitute the mathematical basis for the FE analysis. ABAQUS

solves these equations at each nodal point in the model using the central difference explicit numerical integration algorithm to compute the road stresses, strains, and deformation. Thus, the solution is a function of the element type, mesh size, the material model chosen for the road layers and constraints (boundary and initial conditions).

$$\rho\ddot{x} = b_x + \frac{\partial\sigma_{xx}}{\partial x} + \frac{\partial\sigma_{xy}}{\partial y} + \frac{\partial\sigma_{xz}}{\partial z} \tag{5.2}$$

$$\rho\ddot{y} = b_y + \frac{\partial\sigma_{yx}}{\partial x} + \frac{\partial\sigma_{yy}}{\partial y} + \frac{\partial\sigma_{yz}}{\partial z} \tag{5.3}$$

$$\rho\ddot{z} = b_z + \frac{\partial\sigma_{zx}}{\partial x} + \frac{\partial\sigma_{zy}}{\partial y} + \frac{\partial\sigma_{zz}}{\partial z} \tag{5.4}$$

$$\dot{e} = \frac{1}{\rho}\left(\sigma_{xx}\dot{\varepsilon}_{xx} + \sigma_{yy}\dot{\varepsilon}_{yy} + \sigma_{zz}\dot{\varepsilon}_{zz} + 2\sigma_{xy}\dot{\varepsilon}_{xy} + 2\sigma_{yz}\dot{\varepsilon}_{yz} + 2\sigma_{zx}\dot{\varepsilon}_{zx}\right) \tag{5.5}$$

5.3. CENTRAL DIFFERENCE METHOD

The governing equations presented in Section 5.2 are solved explicitly using the central difference method, as implemented in ABAQUS/Explicit. The equations presented in this section were sourced from [180]. When the truck tires impose the dynamic loads on the road, the finite element nodes are disturbed, causing the motion of the nodes. This motion produces element deformation. The deformation results in material strains, which are used with the constitutive laws and material models to compute the material stresses. These stresses are used to compute the nodal forces. The nodal accelerations, $\ddot{x}_i$, are then computed from the nodal forces, F_i, using Equation 5.6. The nodal accelerations are integrated explicitly to generate the nodal velocities using Equation 5.7 [179].

The size of the time step used in the explicit dynamic analysis is dependent on the size of the smallest element in the model. It is also controlled by the sonic velocity through

the element used for the analysis. To ensure stability and accuracy of the explicit dynamic analysis, the time step must obey Equation 5.8, which is derived from the Courant-Friedrichs-Lewy (CFL) principle.

$$\ddot{x}_i = \frac{F_i}{m} + b_i \tag{5.6}$$

$$\dot{x}_i^{n+1/2} = \dot{x}_i^{n-1/2} + \left(\frac{\Delta t^{(n+1)} + \Delta t^{(n)}}{2}\right)\ddot{x}^{(n)} \tag{5.7}$$

$$\Delta t \leq f * min\left[\frac{h}{C_m}\right] \tag{5.8}$$

Finally, the nodal displacement is obtained from the nodal velocity through an explicit integration step given by Equation 5.9.

$$x_i^{n+1} = x_i^n + \dot{x}_i^{n+1/2}\Delta t^{n+1/2} \tag{5.9}$$

This procedure was used for solving the road response under truck dynamic loads. It is implemented in ABAQUS CAE as ABAQUS/Explicit. The simulations were run on a high-performance computer (HPC) that has two cores, 72 processors and a RAM of 512 GB. Each model was run on 6 to 10 processors to increase the computation speed.

5.4. TIRE MODEL

Ultra-large truckloads are impacted on the road via large pneumatic tires, with high tire inflation pressure. Thus, an appropriate tire model is required to conduct the road response modeling. The tire model and data used in this work were adopted from [37], who

presented a comprehensive thermo-mechanical model of an ultra-large mining truck tire. Rubber is the dominant material in truck tires. Therefore, the tire exhibits hyperelastic (large recoverable strains) behavior under the loading/unloading cycle. The carcass provides the tire with the required strength to bear the excessive truck loads.

5.4.1. Tire Material Model. Tire exhibits hyperelastic behaviour under the loading/unloading cycle. There are many models available for describing the hyperelastic response of tires. These models include the Neo-Hookean, Mooney-Rivlin, Yeoh, polynomial and Ogden models. They are based on the strain energy density function of rubber. The Ogden model was used in this work to model tire rubber hyperelasticity. The mathematical formulations of the Ogden model has been presented by [181] and [182].

Data from simple tension (ST), planar tension (PT), equibiaxial tension (ET) and volumetric tension (VT) tests are required to determine the material constants. However, VT tests are not required for incompressible materials. Thus, data from ST, PT and ET tests were sufficient for deriving the material constants in this work since rubber is incompressible. Nyaaba [37] and [183] determined the Ogden material constants for an ultra-large mining tire from ST, PT and ET tests data as presented in Table 5.1. The ET and PT test data was derived from the ST test data by assuming isotropic linear elasticity. This allowed a complete hyperelastic characterization of the truck tire rubber materials.

The tire rubber also exhibits viscoelasticity. Viscoelastic materials exhibit both elastic and viscous responses to applied loads. A parallel rheological framework (PRF) model, the Prony series model, was used in ABAQUS to characterize tire rubber viscoelasticity.

Table 5.1 Third-order Ogden model parameters for ultra-large truck tire [37]

Tire Region	Test Temperature (ºC)	Model Parameters					
		μ_1	α_1	μ_2	α_2	μ_3	α_3
Apex	23	2.00E-03	-7.761	2.00E-02	12.448	2.277	-0.202
	35	1.27E-03	-6.209	1.60E-02	9.959	1.821	-0.161
	55	9.52E-04	-4.660	1.20E-02	7.469	1.366	0.121
Casing	23	1.15E+00	0.039	5.00E-03	11.249	0.007	-4.734
	35	9.18E-01	0.031	4.00E-03	8.999	0.006	-3.792
	55	6.88E-01	0.023	3.00E-03	6.750	0.004	-2.275
Inner Liner	23	2.83E-04	-7.966	1.50E-02	9.837	0.424	-0.352
	35	2.26E-04	-6.373	1.20E-02	7.869	0.340	-0.282
	55	1.69E-04	-4.779	9.00E-03	5.902	0.255	-0.211
Sidewall	23	2.66E-04	-7.362	4.00E-03	11.364	1.031	-0.099
	35	2.13E-04	-5.890	3.50E-03	9.092	0.825	-0.079
	55	1.59E-04	-4.417	2.60E-03	6.819	0.618	-0.059
Tread	23	1.50E-03	-5.332	1.20E-02	8.920	1.229	-0.107
	35	1.20E-03	-4.266	1.00E-02	7.136	0.984	-0.086
	55	8.81E-04	-3.199	7.00E-03	4.281	0.738	-0.064

The parameters of a time-domain Prony series (Table 5.2) were derived from experimental stress relaxation data and used for characterizing the tire viscoelastic behavior in ABAQUS. General tire properties used in the model are given in Table 5.3. These parameters were used for fully characterizing the tire material response under ultra-large truckloads.

Table 5.2 Tire components linear viscoelastic material properties [37]

Components	Prony Series Constants				WLF Constants	
	g_1	g_2	τ_1	τ_2	C_1 (deg. Celsius)	C_2 (deg. Celsius)
Apex	0.09	0.13	2.33	101.67	15	150
Casing	0.092	0.104	7.089	253.51		
Inner liner	0.12	0.129	8.62	235.55		
Sidewall	0.105	0.125	8.037	289.93		
Tread	0.057	0.067	8.007	322.93		

Table 5.3 Rubber thermomechanical material properties [37]

Density (tonne/mm^3)	Young's modulus (MPa)	α	h_c (mW/mm^{2k})	K (mW/mmK)	C_v (mJ/tonneK)
1.19E-09	100	6.70E-06	0.05882	0.153	1.88E+09

5.4.2. Tire Geometry. The model geometry was built from measurements taken from an out-of-service 56/80R63 tire. The tire has a diameter of 4,025 mm and a width of 1,500 mm. The thicknesses of the various tire components such as inner liner, belt layers, and tread, were obtained from circumferentially cut out sections of the out-of-service tire. These measurements were then used to build a 2D axisymmetric model of the tire in ABAQUS CAE, which provides CAD features.

The bead bundle and rim were modeled as rigid elements due to their relatively higher stiffness compared to other tire components. They were joined to the axle via a reference node (RP), which defined the midpoint of the tire. The steel cords and belt components were modeled using the 'wire' feature in ABAQUS. Other components of the tire were modeled using features provided by ABAQUS to represent the physical tire as closely as possible. The symmetric model generation (SMG), revolve, and symmetric results transfer (SRT) features in ABAQUS were used to revolve the axisymmetric model into a sector model, which was revolved into the full 3D model shown in Figure 5.1. The tire model was made rigid in this work, using the rigid constraint in ABAQUS to reduce computational time.

Figure 5.1 3D full tire geometry [37]

5.5. HAUL ROAD MODEL

This section gives a description of the haul road geometry and material modeling approaches used in this work and presents the key haul road model input data.

5.5.1. Material Model. The most commonly used material models for granular materials are the C-C/MCC, Drucker-Prager and M-C models. In this work, an isotropic linear elastoplastic Mohr-Coulomb model, with isotropic strain hardening, as implemented in ABAQUS 2018, was used for characterizing the road layers (wearing surface, base, subbase, and subgrade). Based on the literature in Section 2.7.3, the M-C model best characterizes granular pavement materials under dynamic loads. The material model equations presented in this section were obtained from [180].

The strain experienced by a structure under loading can be decomposed into elastic and plastic strains. Thus, the total nodal strain (ε_{total}) is a sum of elastic ($\varepsilon_{elastic}$) and plastic

($\varepsilon_{plastic}$) strains, as expressed in Equation 5.10. The plastic strains are mainly due to the particle rearrangement within the road layers. Plastic strains also result when the induced stresses exceed the strength of the material.

$$\varepsilon_{total} = \varepsilon_{elastic} + \varepsilon_{plastic} \tag{5.10}$$

According to the Mohr-Coulomb criterion, yielding occurs when the sum of the shear stress and mean applied pressure is equal to the internal strength or cohesion of the material. The criterion assumes that failure is controlled by the maximum shear stress, which is dependent on the normal stresses, as expressed in Equation 5.11, using the geomechanics convention (compression is negative). σ_m is defined using Equation 5.12. Equation 5.12 assumes that failure is independent of the intermediate principal stress.

$$\tau = c - \sigma_m tan\varphi \tag{5.11}$$

$$\sigma_m = \frac{\sigma_1 + \sigma_3}{2} \tag{5.12}$$

The Mohr-Coulomb model presented in Equation 5.11 is rewritten in terms of the equivalent pressure stress (Equation 5.13), Mises equivalent stress (Equation 5.14) and third stress invariant (Equation 5.15). **S** is the stress deviator as defined by Equation 5.16.

$$p = -\frac{1}{3} trace(\boldsymbol{\sigma}) \tag{5.13}$$

$$q = \sqrt{\frac{3}{2}(\boldsymbol{S}:\boldsymbol{S})} \tag{5.14}$$

$$r = \left(\frac{9}{2}\boldsymbol{S}.\boldsymbol{S}:\boldsymbol{S}\right)^{\frac{1}{3}} \tag{5.15}$$

$$\boldsymbol{S} = \boldsymbol{\sigma} + \boldsymbol{pI} \tag{5.16}$$

The yield surface of the Mohr-Coulomb model is then defined using Equation 5.17. R_{mc} in Equation 5.17 can be obtained using Equation 5.18. Θ is the deviatoric polar angle related to the third stress invariant and Mises stress by Equation 5.19.

$$F = R_{mc}q - ptan\varphi - c = 0 \tag{5.17}$$

$$R_{mc} = \frac{1}{\sqrt{3}cos\varphi} sin\left(\Theta + \frac{\pi}{3}\right) + \frac{1}{3} cos\left(\Theta + \frac{\pi}{3}\right) tan\varphi \tag{5.18}$$

$$cos(3\Theta) = \left(\frac{r}{q}\right)^3 \tag{5.19}$$

Each layer was assigned properties such as the elastic/Young's modulus, Poisson ratio, density, cohesion, internal friction angle, dilation angle and absolute plastic strain at the start of loading. The absolute plastic strain at the start of loading is zero since the road is unloaded at the beginning (before the tire starts rolling). The model input data are given in Tables 5.4 and 5.5.

Table 5.4 Young's modulus and Poisson ratios of haul road layers [42], [184]

Haul road layer	Young's modulus (MPa)	Poisson ratio
Wearing surface	150	0.3
Base	250	0.3
Subbase	150	0.3
Subgrade	41	0.3

Table 5.5 Other haul road input data [25], [185]

Layer	Density (kg/m^3)	Cohesion (kPa)	Internal friction angle (degrees)	Dilation angle (degrees)
Wearing coarse	1,800	47	52	26
Base	2,000	40	48	24
Subbase	2,200	40	43	21.5
Subgrade	2,500	23	35	17.5

5.5.2. Haul Road Geometry. The dimensions of the various road layers were chosen to closely represent a typical haul for ultra-large truck applications. The road geometry was built using the CAD capabilities of ABAQUS CAE. A single unit was constructed, whose thickness was equal to the overall thickness of the road. The road had a thickness of 7 m, a width of 15 m and a length of 100 m. The various layers were then created from the single unit using three-point cell partitioning. The road dimensions are shown in Table 5.6. The subgrade was assigned a significantly larger thickness to represent its infinite depth. The 3D tire-haul road model is shown in Figure 5.2.

Table 5.6 Haul road layer dimensions

Layer	Length (m)	Width (m)	Thickness (m)
Subgrade	100	15	3.5
Subbase	100	15	1.5
Base	100	15	1.5
Wearing Surface	100	15	0.5

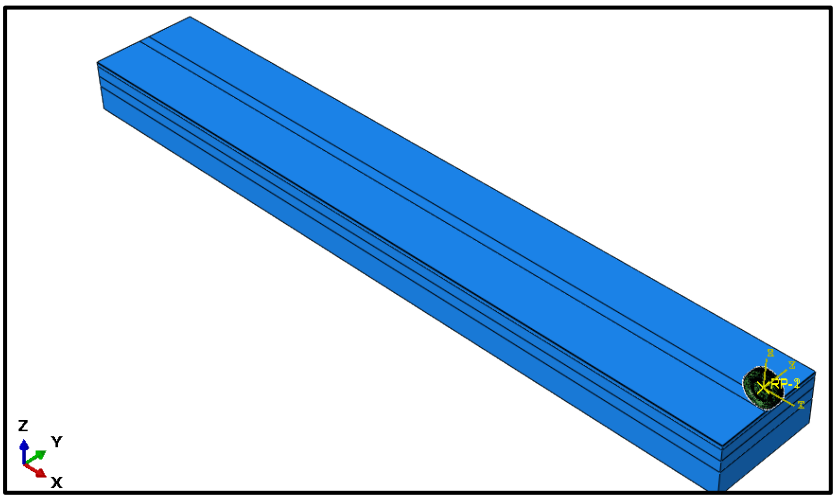

Figure 5.2 The 3D tire-haul road model

5.6. TIRE LOADING AND BOUNDARY CONDITIONS

The truckloads are delivered to the road through the tires. A reference point (RP) was created at the midpoint of the tire, where the dynamic force and velocity (translational and angular) were applied, as shown in Figure 5.3. The dynamic forces the MSC.ADAMS model were used as the applied loads in ABAQUS.

To apply the loads to the tire, a constant load equivalent to the maximum static tire force of CAT 797F was applied at the reference point. To make the load dynamic, the 'amplitude' was defined in ABAQUS/Explicit using the DFC values computed using Equation 3.81. Therefore, the dynamic forces applied to the tire are the product of the 'amplitude' and the static force. The static force was computed using Equation 5.20. The rated GMW of CAT 797F is 623,690 kg and g is the acceleration due to gravity (9.81 m/s^2). Thus, the maximum static tire force computed from Equation 5.20 was 1,024.83 kN.

$$Maximum\ static\ tire\ force = max\left[\left(\frac{0.33\times GMW\times g}{2}\right), \left(\frac{0.67\times GMW\times g}{4}\right)\right] \quad (5.20)$$

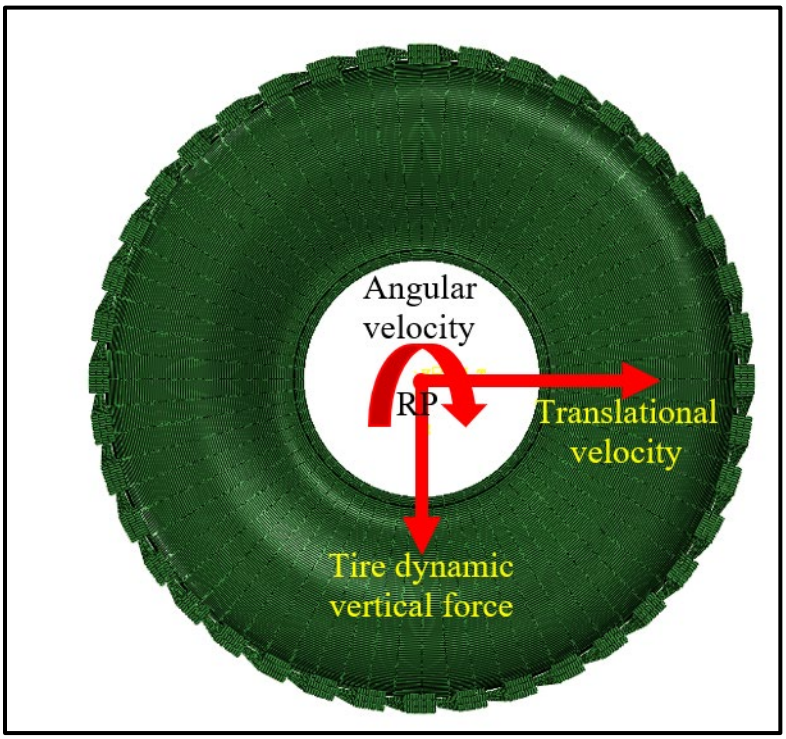

Figure 5.3 Tire loading and applied velocities

Angular and translational velocity BCs were also applied to the tire at RP to cause tire rotational and translational motions. A translational velocity of 15.6464 m/s (35 mph) and rotational velocity of 6.9 rads/s were applied to the tire. This is equal to the speed used in the MSC.ADAMS dynamic force model, which corresponds to the maximum speed of CAT 797F with a 3% effective resistance at rated GMW. The initial angular and translational velocities were taken as zero, corresponding to a stationary truck.

A pressure BC was also applied to the inner of the tire as shown in Figure 5.4. This represents the inflation pressure of the tire. Constant tire pressure of 820 kPa [37] was applied to the tire. Pneumatic tires with high inflation pressures show little tire deflection and can be assumed to be rigid. This assumption was used in this research to reduce the computational time of the model since tire response was not the focus of this study

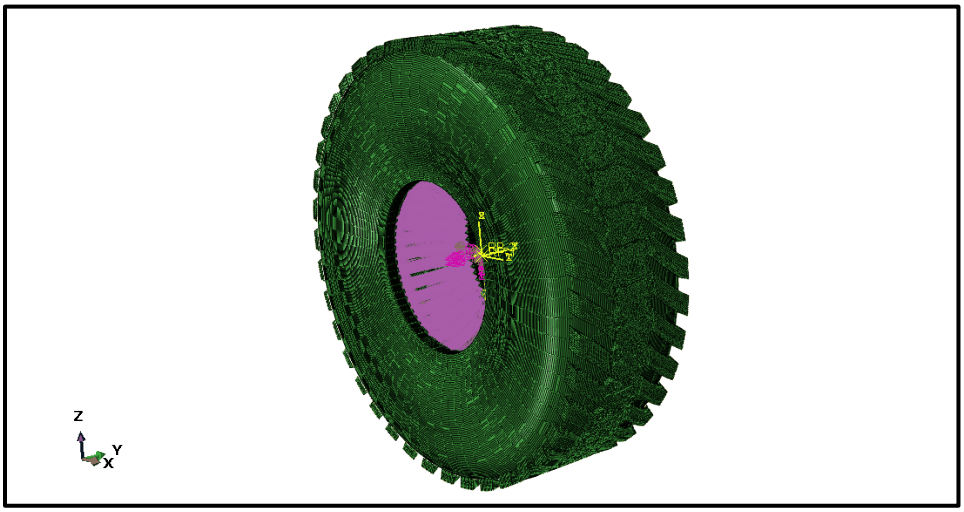

Figure 5.4 Applied tire inflation pressure

5.7. HAUL ROAD BOUNDARY CONDITIONS

Haul roads are typically very wide. The minimum width of a straight road travel segment that is sufficient to accommodate two-way traffic for CAT 797F is 34 m. Since this model does not simulate a full truck scenario, it was assumed that the road will not deform at the sides since the sides are far from the tire travel path [186]. Also, the road sides are supported by the natural ground/formation, which can be described as fixed supports. Thus, all the sides of the road were assigned fixed/encastre boundary conditions. Hence, the translational and rotational displacements at the road sides were taken as zero (i.e. $U_1 = U_2 = U_3 = 0$; $UR_1 = UR_2 = UR_3 = 0$). The road surface was allowed as a free boundary [186] that can deform in any direction. The lower boundary of the subgrade was assigned a fixed/encastre boundary condition. The subgrade typically has infinite depth. At such depth, the road responses are negligible, and it is justifiable to assume a fixed boundary. The haul road BCs are shown in Figure 5.5.

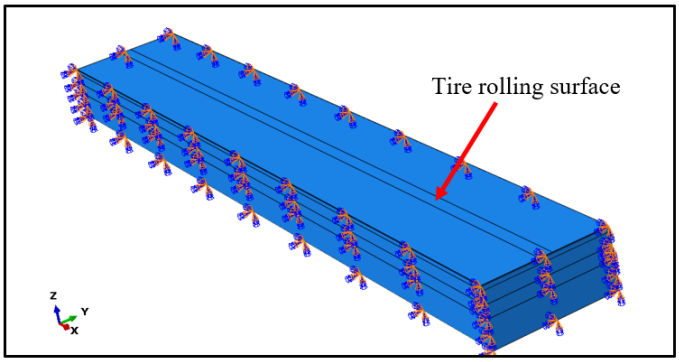

Figure 5.5 Haul road showing fixed boundary conditions at sides and bottom

5.8. TIRE-ROAD CONTACT MODELING

To model the tire-road interaction, an appropriate contact model is required, which defines the transfer of forces from the tire to the road causing the road response. Two contact methods are generally used; the penalty and Lagrange multiplier methods. The penalty contact method was used in this work to model the tire-road contact. The penalty method was chosen due to its time efficiency. It provides faster solutions since it does not add DOFs to the model like the Lagrange multiplier method [180]. This method requires the definition of a tire-road contact friction algorithm. This work used the tangential Coulomb friction model in ABAQUS for modeling the tire-road contact. A friction coefficient of 0.3 [25] was specified for the tire-haul road contact. A rolling surface was created on the haul road surface as seen in Figure 5.5. The contact defined was between the rolling surface defined on the road and the tire rolling surface.

5.9. MESHING AND MESH SENSITIVITY ANALYSIS

The 3D tire model shown in Figure 5.4 was meshed with 8-node 3D linear brick reduced integration (C3D8R) elements, and 4-node 3D quadrilateral surface (SFM3D4R)

elements with reduced integration [37]. The road layers were meshed with C3D8R elements as shown in Figure 5.6. The same mesh type and size were used for all the road layers since the response in all layers was important. Thus, all layers required a high-quality mesh to ensure accurate results.

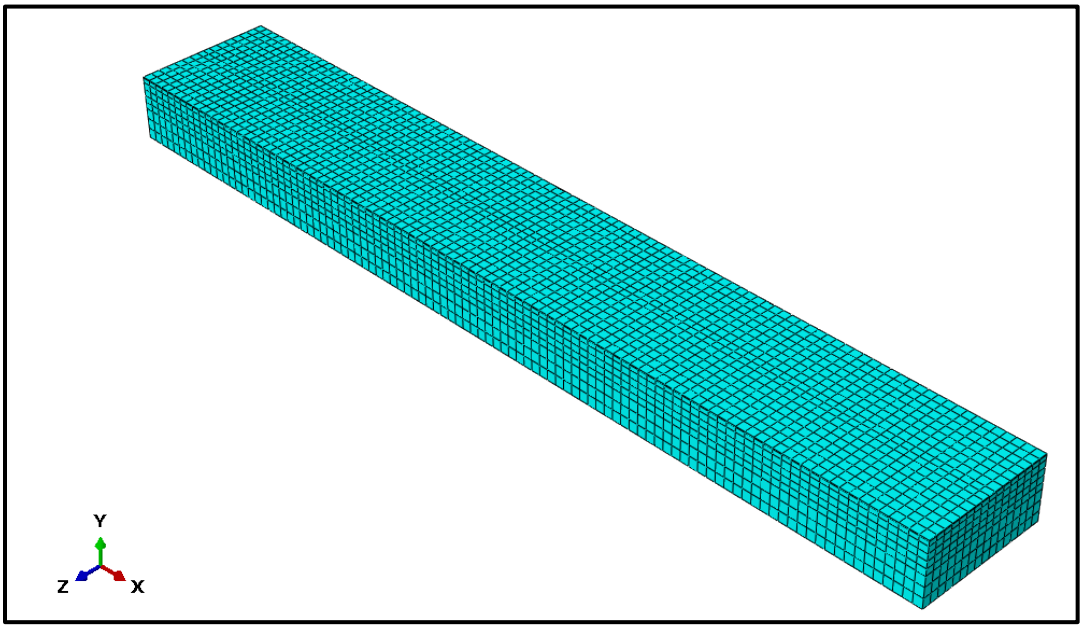

Figure 5.6 Meshed haul road model

The accuracy of the model is dependent on the quality of the mesh, which is determined by the mesh size/density. A very coarse mesh typically gives unreliable results, while a very fine mesh produces reliable results but increases the computational time. The tire mesh sensitivity analysis was conducted by [37] and resulted in an optimal mesh size of 15 mm. The final tire mesh had 1,247,083 nodes and 1,051,007 elements.

Mesh sensitivity for the road was conducted by varying the mesh size from 600 mm to 250 mm. Table 5.7 gives a summary of the haul road mesh sensitivity. The mesh

sensitivity simulations were run on the HPC with 10 processors for each model run. A mesh size of 300 mm was chosen for the road model based on the results from Table 5.7 and Figure 5.7. Mesh sizes <250 mm caused model convergence problems due to the limitations of the Academic version of ABAQUS CAE 2018. It is seen from Figure 5.7 that the maximum von Mises stress did not change significantly for the mesh finer than 300 mm (434,200 nodes). Thus, a mesh size of 300 mm gives an optimal compromise between results accuracy and computational time.

Table 5.7 Mesh sensitivity analysis

Mesh size (mm)	Number of elements	Number of nodes	Total duration (hrs)
250	696,000	733,830	111.62
300	407,592	434,200	105.59
500	93,000	102,912	90.29
600	58,450	65,520	77.27

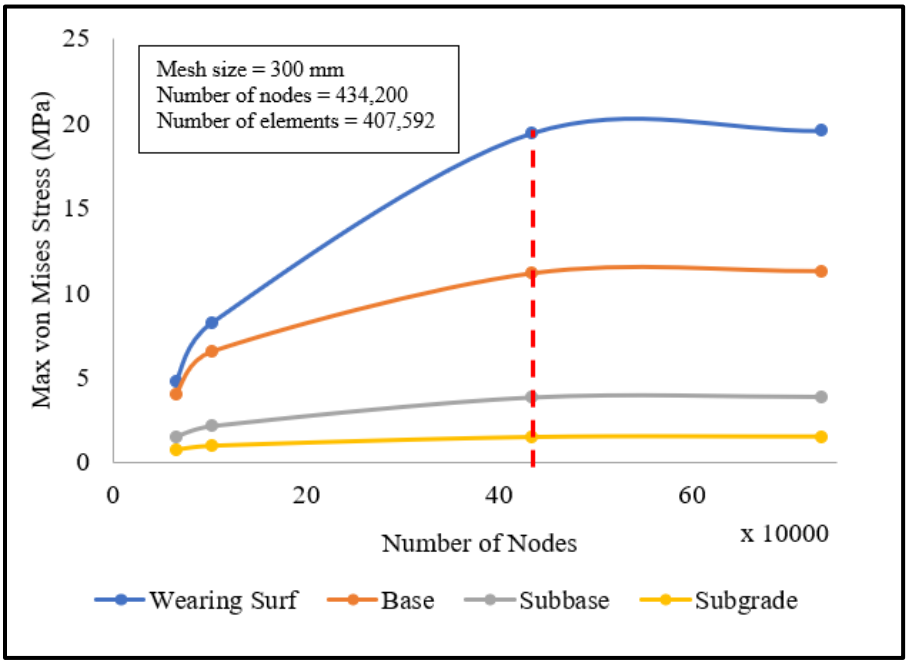

Figure 5.7 Maximum von Mises stresses from mesh sensitivity study of the haul road

5.10. MODEL VERIFICATION AND VALIDATION

A three-stage procedure was adopted to verify the tire-road FE model. After the model was created, the data check function in ABAQUS CAE was used to check the data to identify errors in the data that could affect the output of the model. It also checks the mesh quality to identify elements in the mesh that can cause convergence issues during simulation. This procedure showed an error-free dataset and mesh.

After ensuring an error-free input data, the model was run, and animations were viewed to ensure that the model behaved like a real tire-road system and according to the boundary and initial conditions specified for the model. The animations showed the tire rolling on the road, similar to a truck running on a haul road. This ensured the representative behavior of the model to the real-world system it represents.

The final stage involved reviewing the model results to ensure that they obeyed the input data and the boundary conditions. For example, fixed boundary conditions were specified on all sides of the road and at the bottom of the road. Thus, it was expected that the road deformation and strains at the sides and bottom would be zero. As shown in Figure 5.8, the strains at the road bottom (subgrade bottom) and sides were zero, as defined by the haul road boundary conditions. Also, the responses (e.g. von Mises stresses) decreased vertically (Figure 5.9), laterally and longitudinally (Figure 5.10) away from the tire-road contact area like shown in Figure 2.6. This further showed that the model behaved as expected since the highest stresses occur at the contact tire-road contact area. The road layers dissipate stresses, strains, and deformation away from the contact area. This three-stage procedure was used to verify the model and ensure it behaved like the real truck-road system and obeyed all specified boundary conditions/constraints.

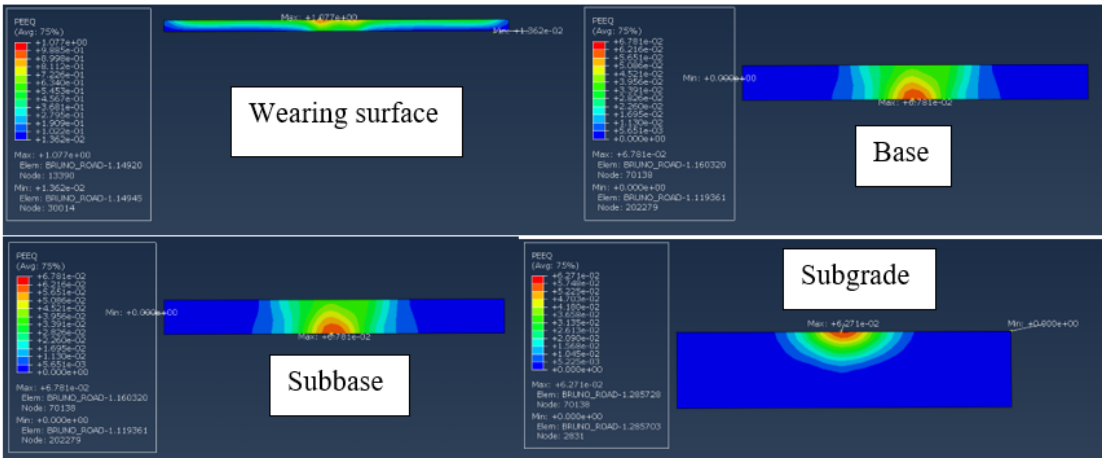

Figure 5.8 Haul road layer permanent strains showing agreement with BCs

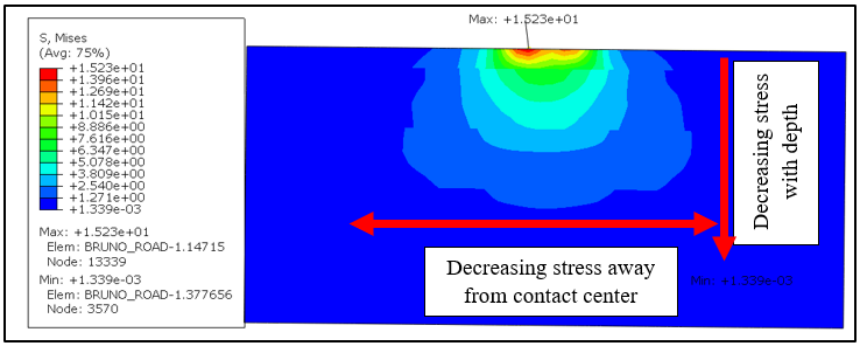

Figure 5.9 von Mises stress distribution through haul road vertical profile

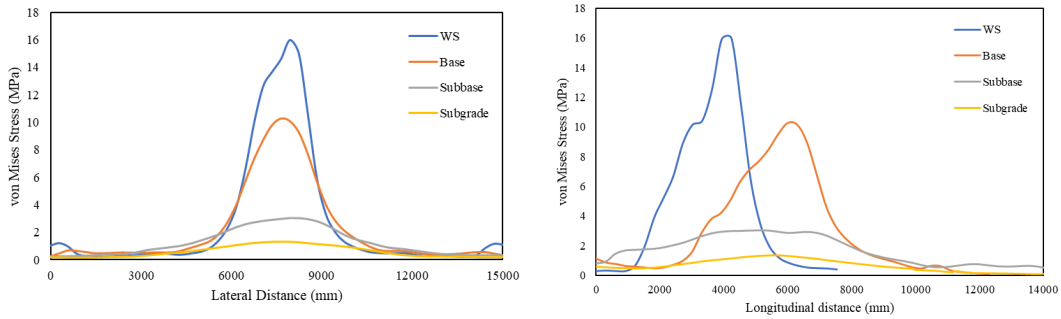

(a) (b)

Figure 5.10 von Mises stress distribution through haul road (a) lateral and (b) longitudinal profile

The model was validated using data from [25]. They modeled the strain distributions in a four-layer haul road subjected to a constant applied stress of 1 MPa on a circular contact area using a 2D axisymmetric FE model. Several experiments were conducted by varying road layer properties. The model used for validating this work had a wearing surface, base, subbase and subgrade elastic modulus of 150 MPa, 350 MPa, 500 MPa, and 50 MPa, respectively. The road wearing surface, base, and subbase had thicknesses of 0.6 m, 1.2 m, and 1.8 m, respectively.

The model from [25] had a maximum wearing surface, base, subbase and subgrade strains of 2,000 microstrains, 2,000 microstrains, 1,200 microstrains, and 200 microstrains, respectively. The 3D model developed in this study predicted maximum strains of 2,716 microstrains, 958.7 microstrains, 268.6 micro strains, and 76.33 microstrains for the wearing surface, base, subbase, and subgrade, respectively. The model in this research imposes dynamic loads on the haul road, while [25] applied a constant stress to a circular area. Since the dynamic forces are greater, the maximum strain predicted by this model exceeded that of [25] by 35.8%. Other reasons accounting for this error include the differences in road layer thicknesses, subgrade elastic modulus and model construction (2D vs 3D). In spite of these differences, the models had a similar trend of decreasing strains with depth and laterally away from the contact area. Thus, the model developed in this research is reliable for understanding road response to ultra-large truck dynamic forces. It is used for extensive experimentation of the layer elastic modulus and payload variations.

5.11. EXPERIMENTAL DESIGN AND EXPERIMENTATION

Several factors affect the response of the haul road to truck impact loads during haulage. Key among these factors are the truck dynamic impact loads and the strength of the haul road (elastic modulus). The variables used for experimentation in this study are the Young's modulus of the subgrade, base, and subbase and the truck payload. The truck payloads were varied to experiment the effect of truck under-loading and over-loading on the haul road structural response. The road base and subbase strengths were varied to simulate weak and competent layer response to truck loads. The subgrade strength modulus was varied to study the road response of competent and weak formations. These experiments studied varying realistic mining scenarios that pose different challenges for designing haul roads. This gave a complete understanding of road design challenges, upon which suggestions were made for improving haul road design.

5.11.1. Layer Strength Experimentation. The elastic modulus of the subgrade was varied from low (representing weak formations) to high (representing competent formations). Very competent formations, with high elastic modulus (>600 MPa), such as granite, usually have stable mine roads, and do not pose road structural integrity problems. Thus, these were not considered in the experimentation. Weak formations in this study refer to formations such as clayey, silty and sandy formations with modulus values from 10 to 200 MPa [187]. Competent or strong formations refer to formations with elastic modulus values >200 MPa but ≤600 MPa. Table 5.8 shows the elastic modulus values used for analyzing the impact of subgrade strength on the road response. Nine experiments, six for weak formations and 3 for competent formations, were conducted to study the response of the road at varying subgrade strength. These experiments were deemed sufficient to

understand the impact of the subgrade modulus on the road structural integrity. The experiments were run at rated truck payload and keeping other model inputs in Tables 5.4 and 5.5 constant.

Table 5.8 Road layer strength experimental values

Subgrade Exp. No.	Subgrade Modulus (MPa)	Subbase Exp. No.	Subbase Modulus (MPa)	Base Exp. No.	Base Modulus (MPa)
1	30	1	100	1	50
2	50	2	200	2	100
3	70	3	250	3	150
4	90	4	300	4	350
5	100	5	350	5	400
6	200	6	400	6	450
7	400	7	500	7	500
8	500				
9	600				

The subbase and base are the strength providing layers of the haul road. Thus, to evaluate the impact of road-building materials on the road response, the elastic modulus of the subbase and base have been varied to evaluate their impact on road structural integrity. Base and subbase elastic modulus values recommended by Tannant and Regensburg (2001) were used as a guide in choosing the experimental values. Table 5.8 presents the elastic modulus values considered in these experimental runs. The base subgrade modulus, as well as other parameters in Tables 5.4 and 5.5, remained constant in these experiments.

The experimental design given in Table 5.8 was sufficient to provide understanding on the effect of the layer elastic modulus on haul road structural integrity. The design also adequately represents various mine formations that pose haul road structural performance

challenges for ultra-large truck operations. It also adequately captures the various types of materials used for mine haul road construction for ultra-large applications.

5.11.2. Payload Experimentation. The truck dynamic forces generated using the MSC.ADAMS model were used for this set of experiments. Ten (10) experiments were conducted using varying payloads from 80% to 120%, at 5% increments according to the 10/10/20 policy adopted by Caterpillar for payload management as shown in Figure 5.11 [178]. The policy recommends that no more than 10% of truckloads should be greater than 110% of the rated truck payload and the payload should never exceed 120% of the rated payload [188]. The payloads considered in these experiments capture instances of truck under-loading and over-loading, as these phenomena occur frequently in the mining industry and need to be considered in haul road structural design.

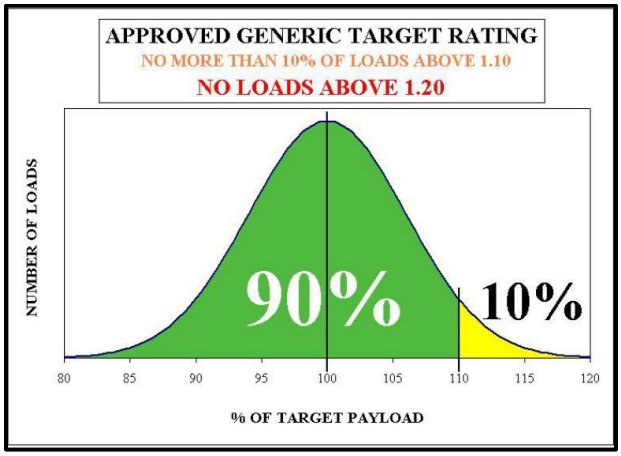

Figure 5.11 Caterpillar's 10/10/20 policy [178]

The experiments conducted in this study provide new information on the impact of operational and road parameters on the road response. They serve as a basis for formulating strategies to improve haul road structural design and performance. The results also provide

knowledge that will help in road construction material selection and managing truck payloads to achieve maximum road performance and minimal road damage/maintenance.

5.12. LIMITATIONS OF THE MODEL

The haul road input data presented in Tables 5.4 and 5.5 were obtained from the literature, as there were no resources for laboratory testing to obtain this data. Obtaining the properties of mine haul road materials from laboratory or field tests can improve the performance of the model. The data for validation of the model was obtained from previously developed 2D road response models that only considered static truck loading. Thus, the differences were wide as the scenarios differed significantly. Using results from field tests of haul road response under dynamic loads for validation of the model would significantly improve the model accuracy. However, based on intuition and the model verification and validation presented in Section 5.10, the model has acceptable accuracy and can be used for further experimentation.

5.13. SUMMARY

The FE model of tire-haul road interaction for studying road response has been developed, verified and validated in this section. The section also presented the modeling procedure, including the material models, solution procedures and mesh sensitivity. The experimental design and experimentation of the various road response parameters have been outlined in this section. It sets the basis for generating results that provide knowledge for extending road life and reducing premature road failures.

6. RESULTS AND DISCUSSIONS

This section presents the results of the experiments conducted to achieve the objectives of the research study. The section presents the results of experiments conducted to understand the impact of varying payloads on truck dynamic forces. These experiments were conducted using the mathematical model in MATLAB/SIMULINK® and the virtual rigid MBD model in MSC.ADAMS. The section also discusses the results of the ASA for understanding truck health. This was accomplished using the rack, roll and pitch stresses on the truck, computed using truck strut pressures measured real-time during truck operations. Multiple linear regression (MLR) was also conducted to relate truck payload, speed and service hours to the truck strut pressures. Finally, the section discusses the results of the FE modelling of road response to ultra-large truck dynamic loads.

6.1. DYNAMIC FORCE MODEL RESULTS

The mathematical model for understanding ultra-large dynamic forces was developed using Lagrangian mechanics as presented in Section 3. A reduced solution of the model was obtained using MATLAB/SIMULINK® as outlined in Section 4.3. Solutions to the mathematical model generate tire vertical displacement, velocity, and acceleration induced by the road surface roughness. Only Class D roads, under which typical mine haul roads are classified, were considered in this work. The tire vertical displacement induced by a class D haul road is shown in Figure 6.1.

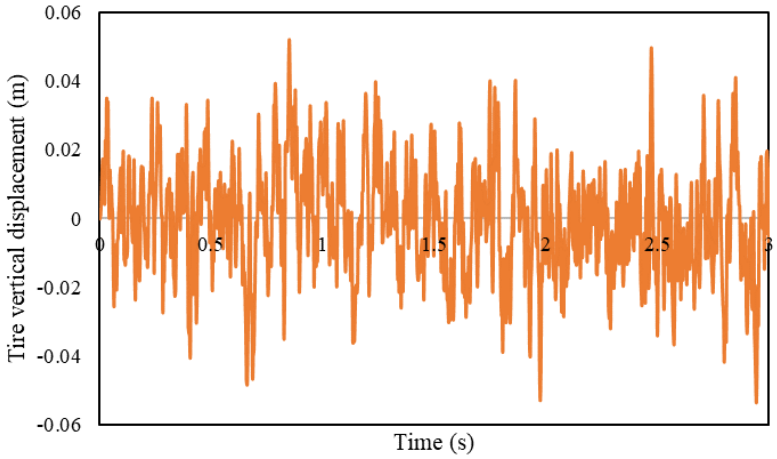

Figure 6.1 Truck tire vertical displacement induced by road surface roughness

In Figure 6.1, zero displacements indicate that the tire is moving on flat terrain and experiencing no vertical displacement. A positive displacement indicates the tire moving over random elevation rises on the road surface, while a negative displacement indicates the tire running over depressions on the road surface. The road surface roughness modeled in this work does not include road defects such as potholes. It only captures random roughness due to construction and/or maintenance imperfections, which inherently leaves rough road surfaces.

Figure 6.1 shows that the tire experiences vertical displacements ranging from -53.3 mm to 52 mm. These vertical excitations generate tire velocity and acceleration, which induce dynamic forces on the road. On higher (positive) road profiles, the tire vertical velocity (Figure 6.2) is reduced (similar to ascending a positive gradient), causing tire vertical deceleration (Figure 6.3). This phenomenon leads to reduced tire impact forces due to negative dynamic forces (Figure 6.4). As the tire runs over the depressions, the tire vertical velocity is increased, resulting in increased tire vertical acceleration. This increases

the tire impact forces imposed on the road surface due to increasing dynamic forces, as shown in Figure 6.4. Figure 6.3 does not include acceleration due to gravity.

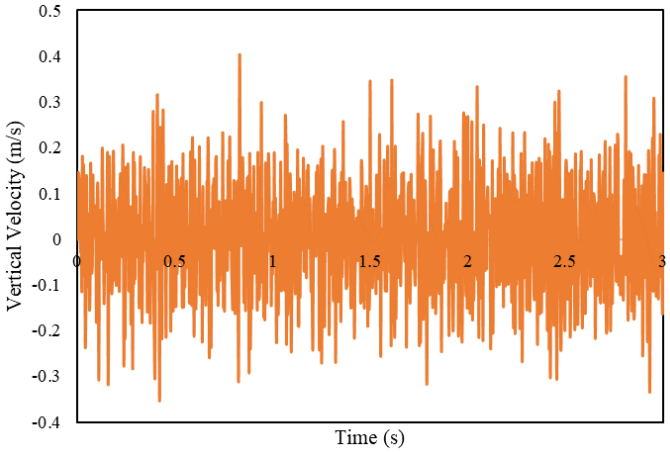

Figure 6.2 Tire vertical velocity due to road surface roughness

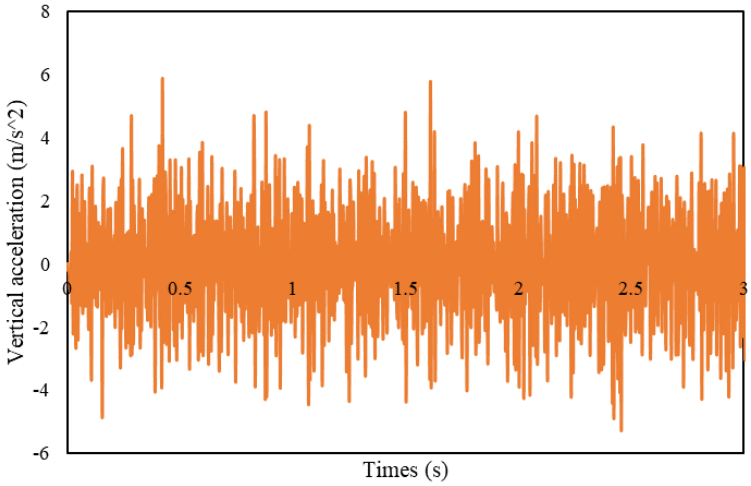

Figure 6.3 Tire vertical acceleration due to road surface roughness

Tire vertical velocity and acceleration range between ±0.4 m/s (Figure 6.2) and ±6 m/s^2 (Figure 6.3), respectively. This results in tire impact (weight forces) forces up to

1,638.7 kN at the rated payload (363 tonnes), though the rated maximum tire static force is 1,024.83 kN, as shown in Figure 6.5. It can be seen from Figure 6.5 that the dynamic component of the tire forces reaches a maximum of 613.8 kN. This results in the total impact forces exceeding the static force by 60%.

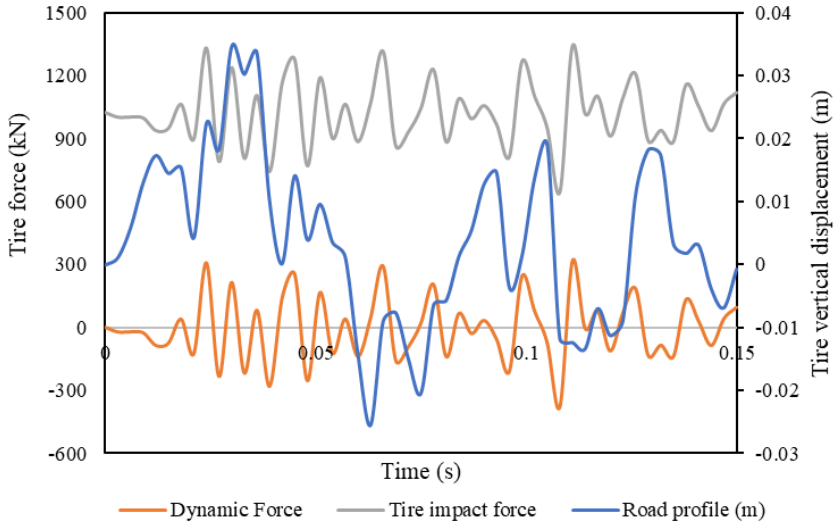

Figure 6.4 Tire dynamic and total impact forces vs tire displacement

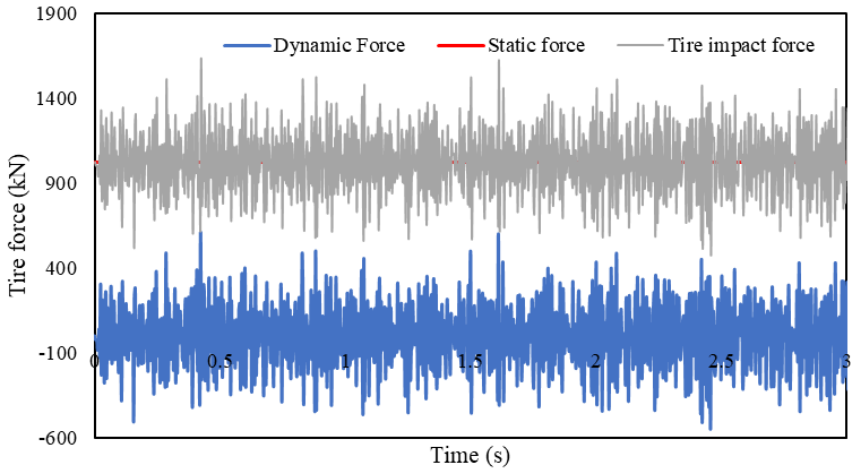

Figure 6.5 Tire dynamic and total impact forces

The results indicate that dynamic tire impact forces imposed on the haul road are 1.6 times the static tire loads. The higher dynamic forces were caused by road roughness since that is the only source of external excitation used in the model. This shows that road surface roughness has a significant effect on the impact forces imposed on the haul road. Such effects cannot be ignored when designing haul roads. This further highlights the shortcoming of current design techniques like CBR and mechanistic approaches, which assume static tire forces. This may lead to structurally weak roads, which cannot withstand the impact loads for the intended life of the road.

To evaluate the effect of truck payload on tire dynamic impact forces, the payloads were varied within ±10% (at 5% step increase) of the rated truck payload. This is to simulate instances of truck under-loading and over-loading typical of dump truck haulage. Figure 6.6 shows the results of the tire impact forces as the payload increased from 90% to 110% of rated payload. As the payload increased, tire impact forces increased linearly (Figure 6.7). This will subject haul roads to higher forces, which can hasten road deterioration, especially in weak formations like oil sands.

Over the range of payloads considered, the maximum impact forces increased by 22% from 1,474.8 kN at 90% payload (10% under-loading) to over 1,800 kN at 10% tire over-loading. The dynamic force coefficient (normalized impact force) increased from 1.44 at 90% payload to 1.76 at 110% payload, as shown in Figure 6.7 and 6.8. This increase in vertical impact loads can be detrimental to the road, vehicle components and operators. Incorporating these variations in haul road structural design is important for designing structurally sustainable haul roads. These results are of practical importance to the mining

industry for ensuring haul road longevity, truck component durability, and operator comfort/health. They are important in deciding truck payload policies.

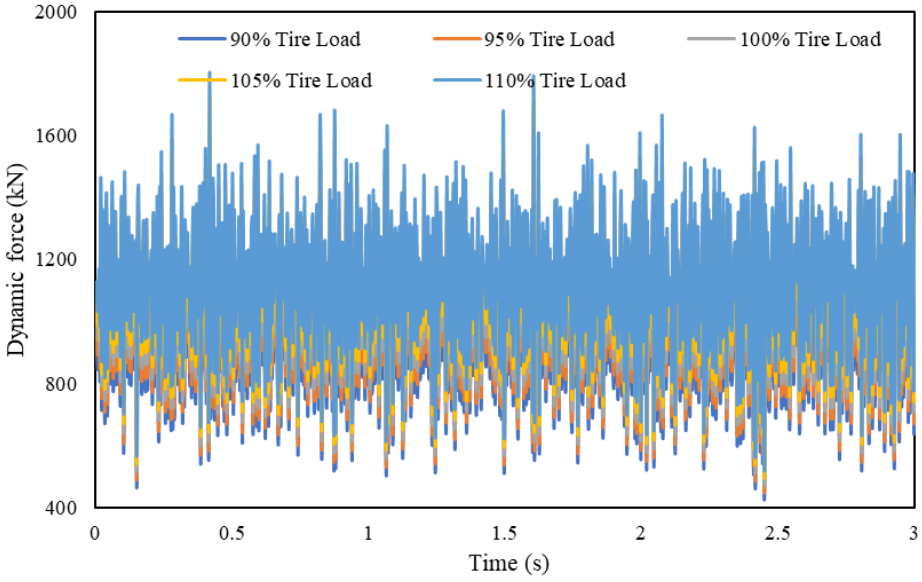

Figure 6.6 Truck tire impact forces at increasing payloads

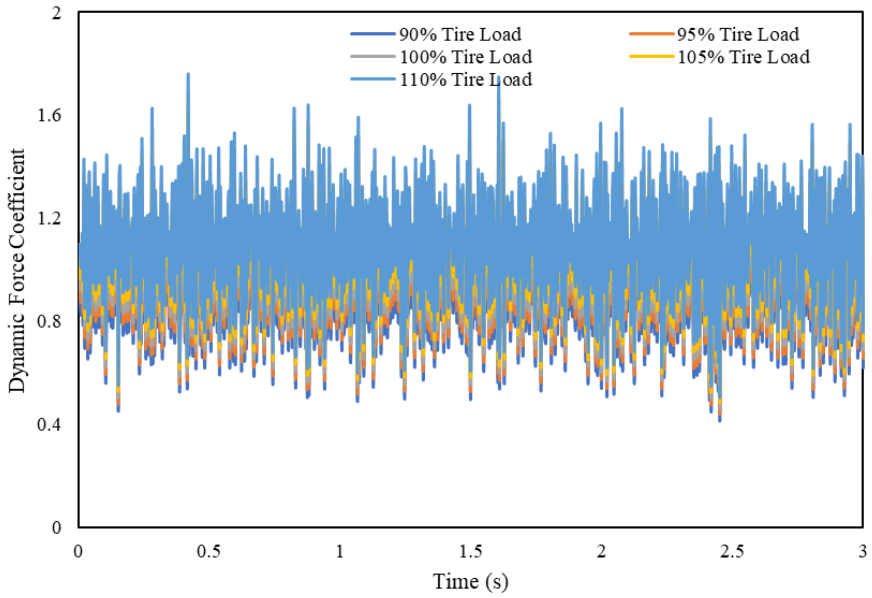

Figure 6.7 Dynamic force coefficient at increasing payloads

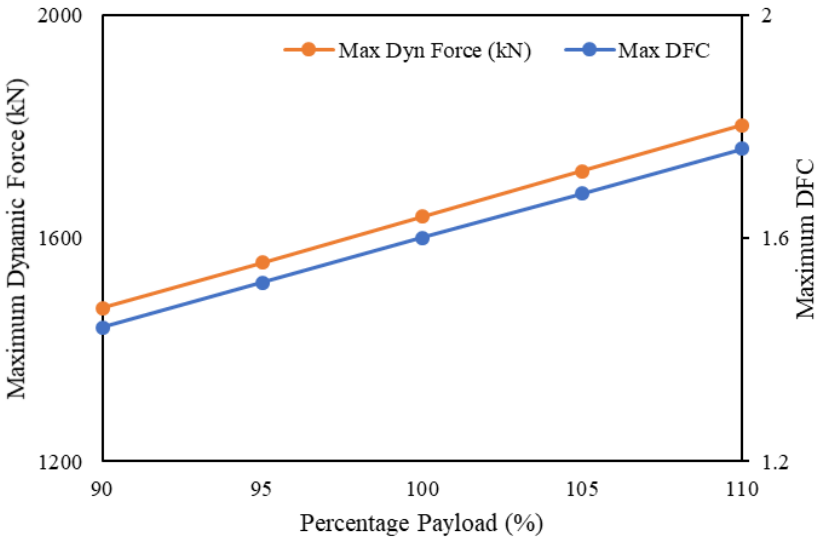

Figure 6.8 Summary of dynamic impact forces and DFC

6.2. DYNAMIC VIRTUAL MODEL RESULT

This section presents and discusses the results of the 3D full truck-haul road rigid MBD model built and solved in MSC.ADAMS for detailed computation of truck dynamic forces generated during haulage. The results focus on tire kinematics (vertical velocity and acceleration) and dynamics (tire vertical impact forces).

6.2.1. Tire Vertical Velocity and Acceleration. Before the truck began to move, the power delivered to the wheels to overcome the high inertial forces due to the high truck gross weight caused a sudden vertical oscillation of the truck suspension systems. This caused the tires to experience maximum vertical velocity and acceleration as shown in Figures 6.9 and 6.10, respectively. The maximum vertical velocity and acceleration were -1.64 m/s (occurred at 0.12 s) and 14.28 m/s^2 (occurred at 0.186 s), respectively. When the inertia was overcome and the truck began to move, the tire vertical responses decreased until steady behavior was achieved after 0.7 s. This behavior of the truck could be observed

from the animations generated during the dynamic simulation and is observed during the operation of ultra-large trucks in mining environments. After this time, the tire vertical velocity remained almost zero since the truck oscillated less. Just before the truck stopped, the vertical velocity and acceleration were approximately zero. For example, the rear right outer (RRO) tire had a vertical velocity of 0.0026 m/s and a vertical acceleration of -0.46 m/s^2 just before the truck stopped. All the truck tires had similar behavior in terms of vertical velocity and acceleration.

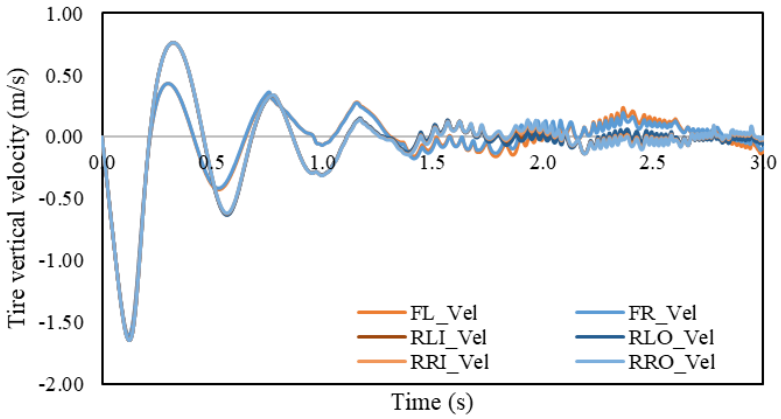

Figure 6.9 Tire vertical velocity at rated payload (363 metric tonnes)

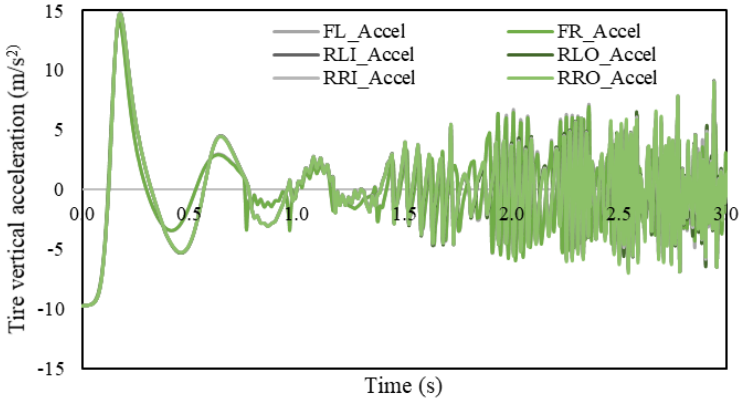

Figure 6.10 Tire vertical acceleration at rated payload

6.2.2. Tire Dynamic Forces. The vertical velocity and acceleration of the truck tires discussed in Section 6.2.1 resulted in dynamic forces, which significantly exceeded the static force of the truck. Since the vertical dynamic forces are the dominant forces imposed on the road by the truck tires, they were the focus of this study and the analysis is based on the vertical forces. In addition, the rear tires transmitted higher dynamic forces unto the road than the front tires. This is primarily caused by the loaded weight distributions of the truck [102], which apportions a greater payload to the rear than the front by design. The analysis was, therefore, focused on the rear tire dynamic forces as shown in Figure 6.11, which shows the dynamic vertical tire forces at rated payload (363 tonnes).

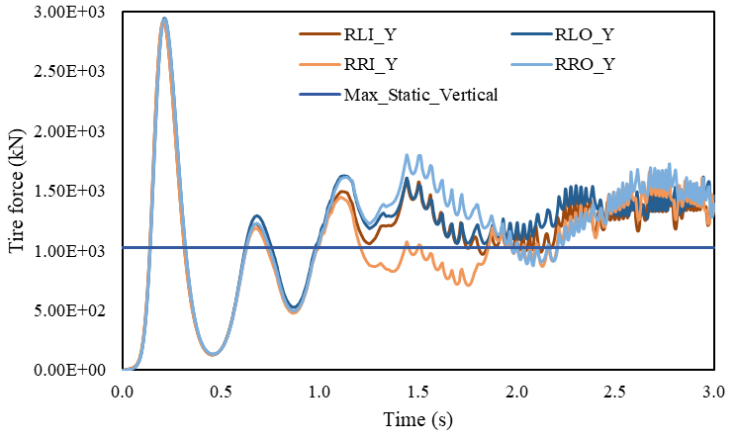

Figure 6.11 Dynamic vertical tire forces at the rated payload

Due to the high tire vertical velocity and acceleration generated at the start of truck motion, as described in Section 6.2.1, dynamic normal forces generated at the start of the truck motion were very high, reaching 2,930 kN (2.86 times the maximum static tire force at rated payload), as shown in Figure 6.11. The maximum static tire force of CAT 797F is 1,024.83 kN.

Since this force is generated at the start of motion, it is more critical at truck dumping and loading points and junctions along the haul road, as these are the points where the truck frequently stops and starts to move. This force probably partly accounts for the early development of depressions/ruts beneath the tires at truck dumping and loading points, and at junctions on the haul road. This occurrence is also common in parking lots used by commercial vehicles and truck parking grounds. In weak formations employing ultra-large trucks, these results can be used for designing truck parking pads and road junctions/intersections to minimize rampant rutting.

The dynamic forces reduced gradually until steady-state conditions were reached at about 0.7 s. The maximum dynamic vertical contact force after this time was 1,790 kN (1.75 times the maximum static force at rated payload). These results conform to previous simulation studies by [71] for CAT 797F and the mathematical model results presented in Section 6.1. Prem [71] found that dynamic forces induced by lane change maneuvers were 60% to 70% higher than the static forces (1.6 to 1.7 times the static force). These dynamic forces are generated due to the vibrations propagating through the suspension systems during haulage. Thus, steady-state dynamic normal forces should form the basis for haul road design to ensure the structural integrity of the road, especially in weak formations. Designing roads with static tire forces could lead to poor designs, with resultant rampant road damages requiring expensive maintenance. Poor designs can also adversely affect truck productivity and impact operators and truck health.

6.2.3. Impact of Payload Variations on Tire Kinematics and Dynamics. Figures 6.12 and 6.13 show the impact of varying payload on the tire vertical velocity and acceleration, respectively. The vertical velocities and accelerations did not change

significantly with an increased payload. The vertical velocity and acceleration only increased marginally as the payload increased. For all payloads, the vertical velocities and accelerations were maximum just before the truck began to move. Once the truck started moving (after 0.7 seconds), the vertical velocity and acceleration of the tires reduced until a steady state. After steady-state, they remained approximately constant and the velocity was nearly zero.

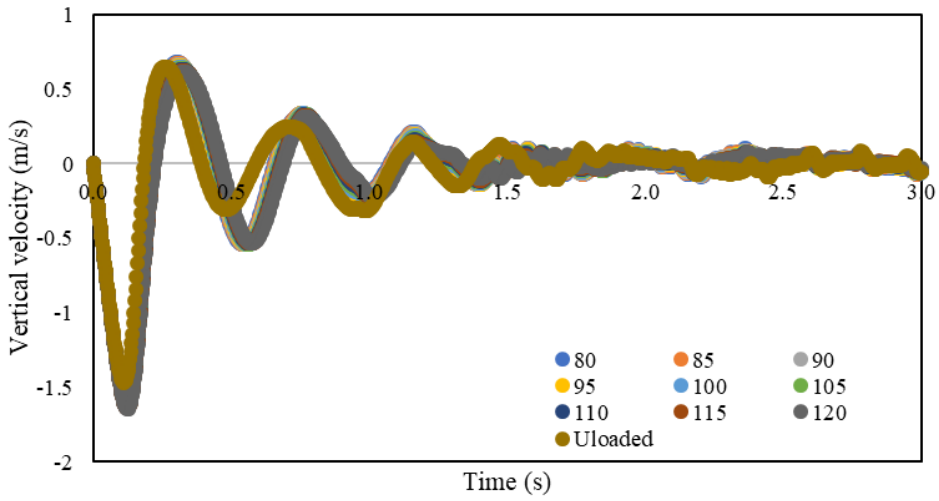

Figure 6.12 Tire vertical velocity at varying payloads

Unlike truck velocities and accelerations, the tire vertical/normal forces (Figure 6.14) increased significantly with increasing truck payload. The maximum and average dynamic vertical forces for the unloaded truck were 1,300 kN and 473.85 kN, respectively. At rated payload, the maximum and average dynamic forces were 2,850.43 kN and 1,059.75 kN, respectively (Figure 6.14). The normal forces increased from an average of 942.88 kN at 80% payload to 1,176.75 kN at 120% payload.

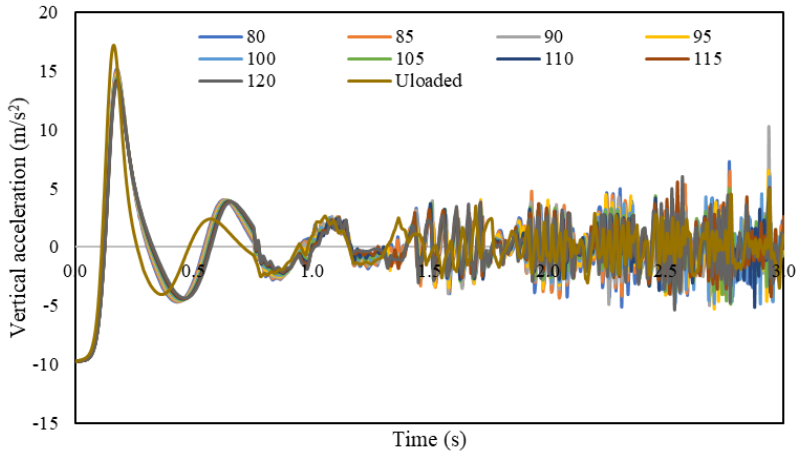

Figure 6.13 Tire vertical acceleration at varying payloads

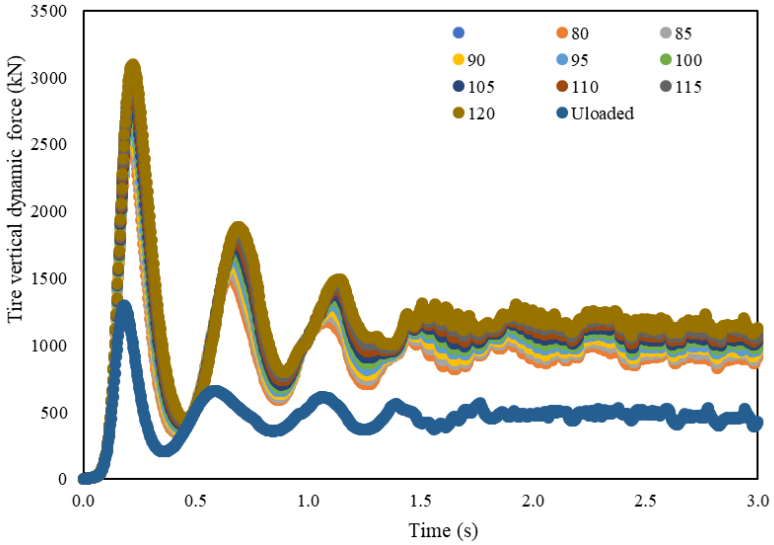

Figure 6.14 Truck dynamic vertical tire forces at varying payloads

The maximum dynamic forces generated right before the truck started moving ranged from 2,589.81 kN to 3,096.24 kN as payload increased from 80% to 120% of rated payload. This analysis further highlights and confirms the importance of incorporating truck over-loading into haul road structural designs. It is common for mining companies to

over-load trucks to increase production. However, it has been shown using truck onboard sensor data that as the truckload increases above the truck rated capacity, there is a noticeable decrease or leveling of the truck productivity [189]. This is typically caused by the increase in truck loading time and decrease in truck speed resulting in longer travel times. Thus, truck over-loading subjects the haul roads to higher dynamic impact loads, with insignificant or no increase in truck productivity. Prem [71] also showed that a 20% over-loading resulted in a 70% reduction in tire life. The reduction in tire life was attributed to increased tire flexing and heat build-up, caused by higher dynamic forces. Therefore, the virtual model results indicate that over-loading trucks can have long term disadvantages such as increased road deterioration, reduced or unchanged truck productivity, increased truck component damage and reduced tire life.

Figure 6.15 shows the DFC resulting from the payload variations, while Figure 6.16 is a summary of the average and maximum DFC at varying payloads. Like the truck dynamic forces, the DFC increased significantly with increasing payloads. The maximum DFC increased from 2.53 at 80% payload to 3.02 at 120% payload.

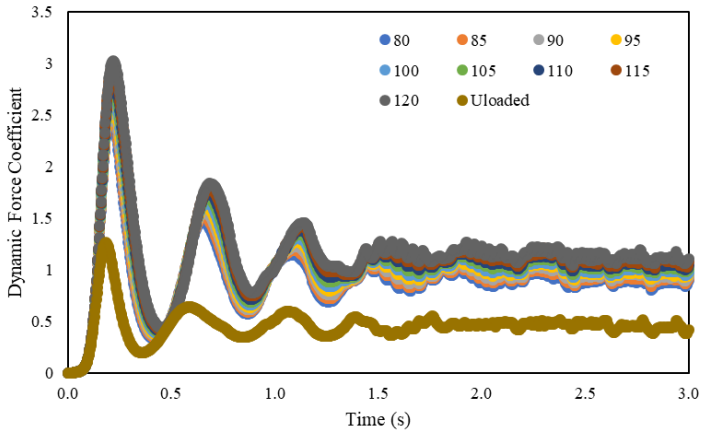

Figure 6.15 DFC for varying truck payloads

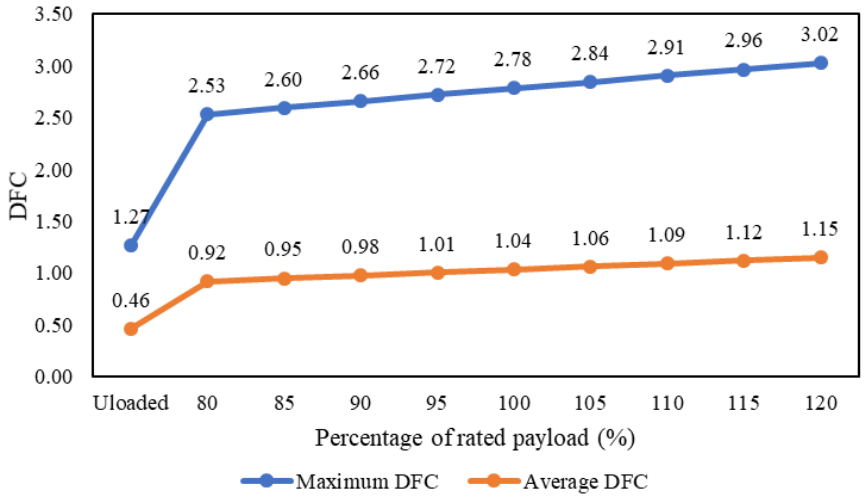

Figure 6.16 Maximum and average tire forces at the varying payloads

Even for an empty truck, the maximum DFC was 1.27, showing a higher dynamic force than the maximum rated static tire force. The average DFC increased from 0.92 at 80% payload to 1.15 (15% more than static force) at 120% payload. This highlights the importance of designing haul roads, especially in weak formations, using the dynamic forces as inputs rather than the static forces.

The maximum and average DFC showed a linear increase from 0 to 120% payload. This linear increment was expected because the payload, which was increased linearly in this work, primarily controls the tire normal/vertical forces. Average DFC increased by 25% as payload increased from 80% to 120% of the rated payload. The maximum DFC increased by 19.37% over the same range. Given the rising cost of ultra-large truck tires and continuous lag in their supply [189], these results are critical for improving tire life and reducing maintenance costs. The results also provide vital information for optimizing mining operations by designing roads of sufficient structural integrity to bear these high dynamic forces.

6.2.4. Incorporating Dynamic Forces in Haul Road Design. The results presented in Section 6.2.3 can be used with current empirical design relations for improving haul road structural design. Equations 6.1 and 6.2 can be derived from the results presented in Section 6.2.3 for estimating truck tire maximum and average dynamic forces at the rated payload. For varying payload, Equations 6.3 and 6.4 can be used for estimating the truck tire dynamic forces.

$$F_{dyn}^{max} = 2.86 * F_s \quad (6.1)$$

$$F_{dyn}^{ave} = 1.75 * F_s \quad (6.2)$$

$$F_{dyn}^{max} = 2.86 * \left(\frac{100 \pm P}{100}\right) * F_s \quad (6.3)$$

$$F_{dyn}^{ave} = 1.75 * \left(\frac{100 \pm P}{100}\right) * F_s \quad (6.4)$$

$$t_w^{dyn} = \frac{F_{dyn}}{1000 * g} \quad (6.5)$$

The values of P range from -20% (80% payload) to 20% (120% payload). Since the dynamic forces increased linearly with increasing payloads, the models can be used outside these payload ranges. Equations 6.3 and 6.4 are general forms of Equations 6.1 and 6.2, respectively, that allow for experimenting with different payloads. For example, if a mine anticipates 10% truck over-loading, Equations 6.3 and 6.4 can respectively be used for estimating the maximum and average truck dynamic tire forces imposed on the road. In this scenario, the maximum dynamic force becomes $2.86*1.1*F_s$ and the average dynamic force becomes $1.75*1.1*F_s$. A pessimistic haul road design (for weak formations) or a design for parking pads and junctions will use Equation 6.3, while an optimistic haul road

design (for competent formations) can use Equation 6.4. At rated payload (P = 0), Equations 6.3 and 6.4 are the same as Equations 6.1 and 6.2, respectively. The dynamic forces from Equations 6.1 to 6.4 can then be used to estimate the dynamic tire loads in metric tonnes using Equation 6.5. The tire load computed from Equation 6.5 can then be used as input to Equations 2.1 and 2.2 (CBR equations) for designing road layer thicknesses. Haul road layer thicknesses determined using this procedure incorporate dynamic loads and can withstand ultra-large truck dynamic loads generated during haulage. Equations 6.1 to 6.5 are simple and can be used by mining companies to capture dynamic effects into haul road designs. However, the equations require further experimental validation.

6.3. IMPACT OF TRUCK DYNAMICS ON TRUCK HEALTH

The truck dynamics generated during haulage operations subject the truck components to torsional stresses that can affect the health of the truck. This can adversely influence truck availability, utilization, and productivity. It can also significantly reduce the life of the components, resulting in increased maintenance expenditures. In this section, field data (strut pressure) recorded during the operation of ultra-large trucks (CAT 793 B, C, and D) was used to compute the torsional stresses acting on the truck during haulage. The results were compared with threshold values (±8,500 kPa), beyond which the truck components experience extreme twisting and can damage rapidly. The torsional stresses used in this analysis are the rack, pitch, and roll, as discussed in Section 4.11. The analysis was made using trucks traveling in loaded and unloaded conditions in the 6^{th} gear. This was used because the trucks run at maximum speed in the 6^{th} gear. At the maximum speed,

the torsional stresses are expected to be maximum, and thus, this gives the worst-case scenario. This section also uses MLR, based on least-squares fitting (LSF), to formulate models for predicting truck strut pressures.

6.3.1. Balanced Truck Payloads. The measured strut pressures for a loaded and an empty CAT 793B are shown in Figure 6.17. As expected, the loaded strut pressures are significantly higher than the empty strut pressures due to the payload. The maximum strut pressure for the loaded truck was 24,010.38 kPa, while the maximum strut pressure of the empty truck was 5,687.54 kPa. Thus, the loaded maximum strut pressure was 4.22 times the maximum empty strut pressure. The average loaded and empty strut pressures are 7,947.23 kPa and 2,595.12 kPa, respectively. Thus, the average loaded strut pressure is 3.06 times the average empty strut pressure.

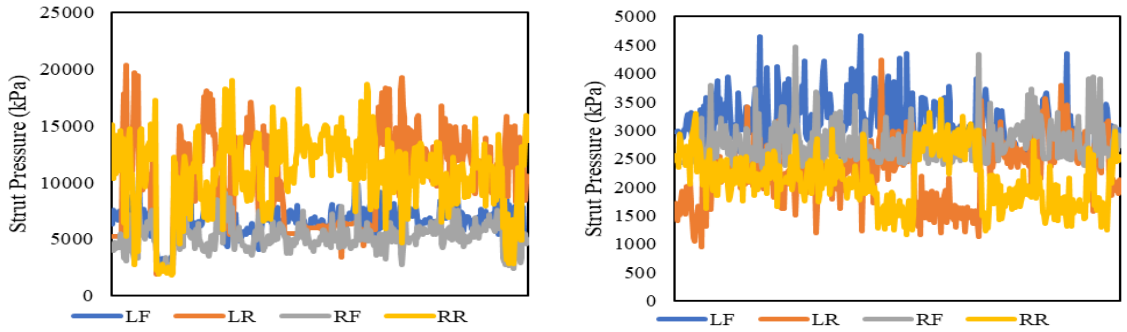

(a) (b)

Figure 6.17 Measured strut pressures for sample CAT 793B (a) loaded (b) empty

It is also observed from Figure 6.17 that the rear struts (LR and RR) experience higher dynamic strut pressure in the loaded truck. This is likely caused by the weight distribution of the truck that apportions higher weight to the rear than the front tires. Figure

6.17 shows that the truck payload was fairly balanced as the rear struts have fairly similar strut pressure profiles in the loaded condition. The front struts also have a fairly similar strut pressure profile in the loaded condition.

The strut pressures shown in Figure 6.17 result in the rack, pitch and roll stresses shown in Figure 6.18. Figure 6.18 shows that the roll stresses of the loaded truck occasionally exceed the threshold of 8,500 kPa but are mostly within the threshold. The loaded rack exceeds the threshold for a higher percentage of the time, while the pitch values were all within the threshold. The rack, pitch, and roll for the empty truck were all below the threshold. In fact, the empty rack, roll, and pitch stresses approached zero, which represents the ideal case that ensures very healthy truck operations.

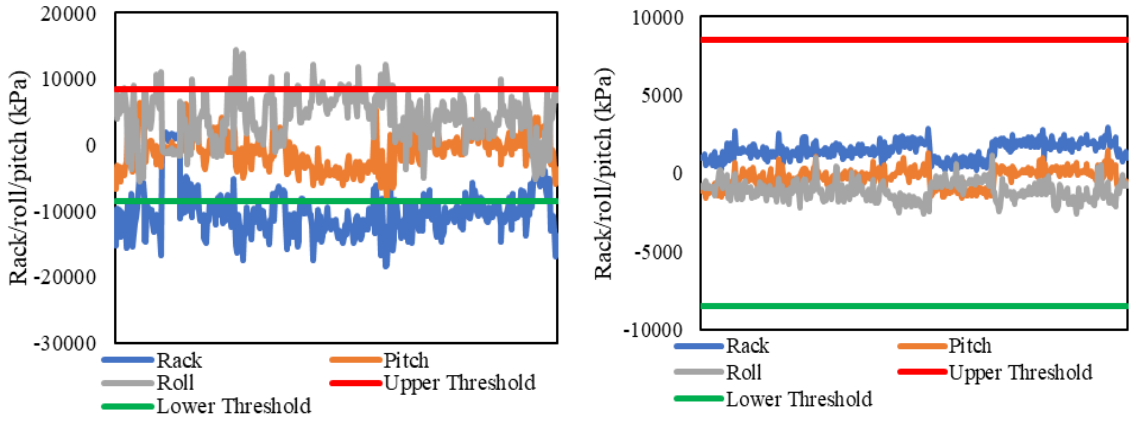

(a) (b)

Figure 6.18 Rack, pitch and roll for a sample CAT 793B (a) loaded truck (b) empty truck

The maximum loaded rack, roll, and pitch were -24,652.0 kPa, 19,956.94 kPa, and -11,248.02 kPa, respectively, representing 2.9, 2.35 and 1.3 times the threshold values. The average rack, roll, and pitch were 9,740.35 kPa, 3,741.56 and -740.64 kPa, respectively.

Excessive rack subjects the truck body/frame to premature cracking, while excessive roll reduces the life of the final drives and wheel bearings and causes premature loss of strut gas. Excessive pitch reduces the life of the tires, rims, wheel bearings and suspensions [30]. The relatively balanced truck loading observed in Figure 6.17 results in roll and pitch stresses which were mostly within the recommended threshold. The rack, however, mostly exceeded the threshold.

The balanced loading reduced the risks of premature damage to the final drives and wheel bearings. It also reduced the risks of strut gas loss due to the low roll stresses. The low pitch stresses also present advantages of improved durability of the tires, rims, wheel bearings and suspension systems. However, probably due to the rough road surfaces, there are risks of frame cracking due to the high rack stresses experienced by the truck.

6.3.2. Unbalanced Truck Payloads. Figure 6.19 shows the measured strut pressure for a CAT 793C. Like the CAT 793B, loaded strut pressures are significantly higher than the empty strut pressures. The maximum loaded and empty strut pressures were 21,037.78 kPa and 10,327.06 kPa. Thus, the maximum loaded strut pressure is 2.04 times the maximum empty strut pressure.

Unbalanced truck loading can be observed from the loaded strut pressure profile shown in Figure 6.19(a). The rear right (RR) strut pressure is significantly higher than the rear left (LR) strut pressure. The LR strut pressure is lower than the front strut pressures due to the biased placement of the payload on the RR of the truck. Under balanced loading, the RR and LR pressures should follow a similar profile as indicated in Figure 6.18. The unbalanced loading results in excessive rack, roll and pitch events, which significantly exceed the threshold values as shown in Figure 6.20(a).

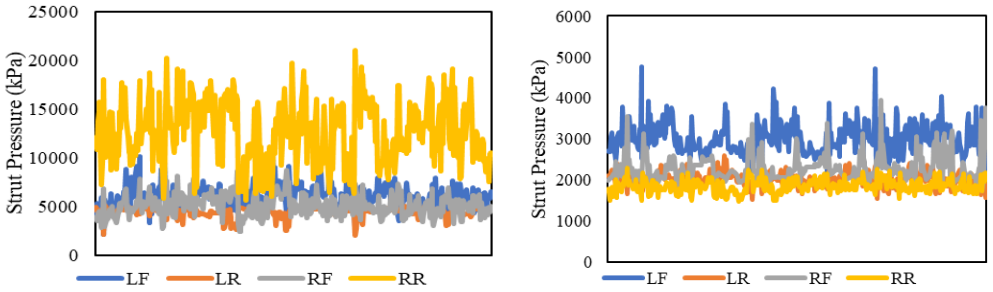

(a) (b)

Figure 6.19 Measured strut pressures for sample CAT 793C (a) loaded (b) empty

The maximum rack, roll, and pitch for the loaded truck were 16,043.12 kPa, -23,708.63 kPa and -14,092.91 kPa, respectively. The maximum rack, roll, and pitch are 1.89, 2.79 and 1.66 times the threshold value for the loaded truck. These excessive and rampantly occurring high torsional stresses subject the truck components to hastened deterioration. This can increase truck health issues as discussed in Section 6.3.1, including tire damage, frame and axle cracking and premature loss of strut gas. This results in increased equipment breakdowns, reduced availability and productivity of the equipment, with resultant increased maintenance costs.

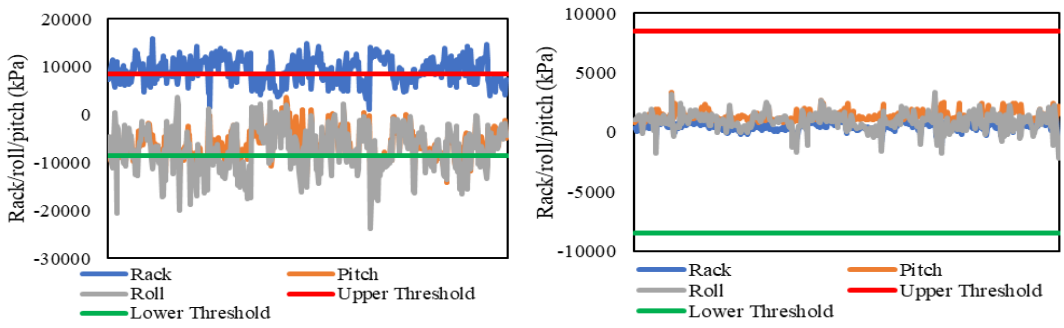

(a) (b)

Figure 6.20 Rack, pitch and roll for a sample CAT 793C (a) loaded truck (b) empty truck

The balanced truck had less frequent exceedance of the recommended rack, roll and pitch. Thus, the truck is exposed to less health risks in balanced loading than unbalanced loading. The empty truck shows very minimal rack, roll, and pitch, indicating healthy truck operations in empty conditions.

Contrary to the excessive payload imbalance observed in Figure 6.20(a), Figure 6.21(a) shows a moderately imbalanced truckload, where the rear left (LR) strut pressure was slightly above the rear right (RR) strut pressure. This results in minimal exceedance of the threshold pitch and roll. Figures 6.20(b) and 6.21(b) both follow a similar profile as 6.19(b). They show that the front strut pressures are higher than the rear strut pressures for an empty truck. Similar reasons as discussed in the immediately preceding section also account for this trend. Empty truck rack, roll, and pitch (Figure 6.22) were lower than the threshold and ensure safe and healthy truck components when the truck is traveling empty.

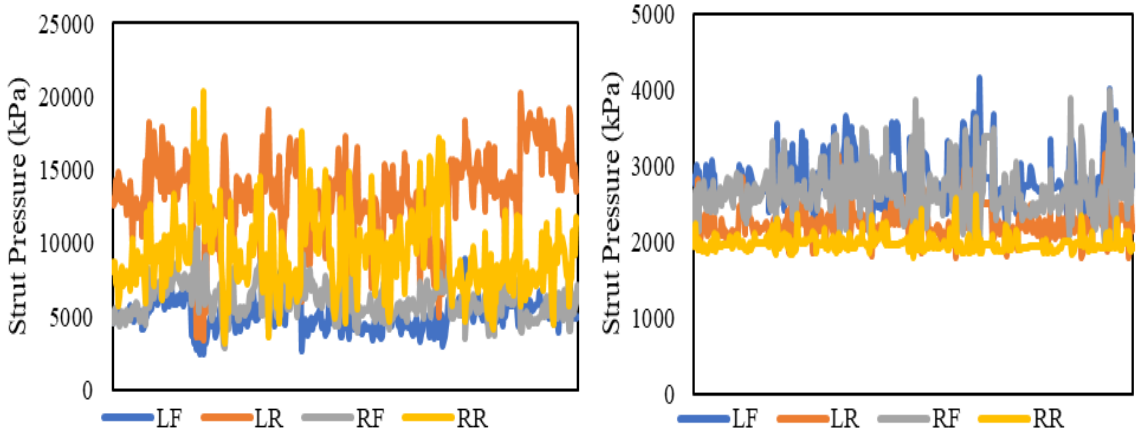

(a) (b)

Figure 6.21 Measured strut pressures for sample CAT 793D (a) loaded (b) empty

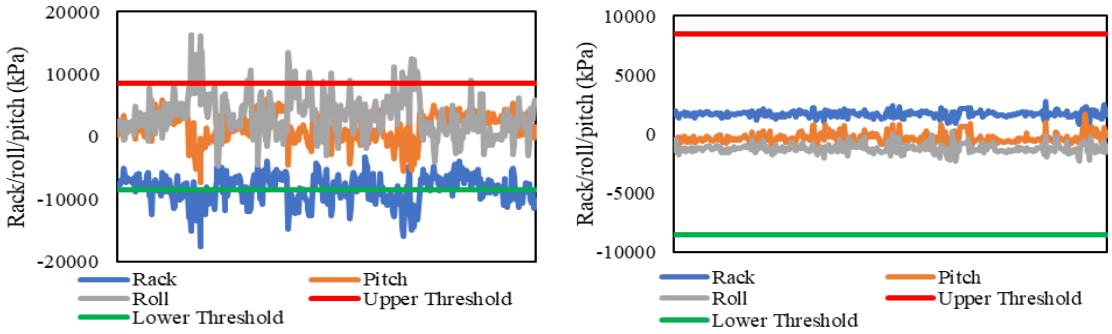

(a) (b)

Figure 6.22 Rack, pitch and roll for a sample CAT 793C (a) loaded truck (b) empty truck

6.3.3. MLR Modeling of Truck Strut Pressure. Table 6.1 gives a summary of the data used for the MLR modeling in JMP. A large amount of data was used for formulating the models to ensure that the models are representative of the phenomena. Equations 6.6 to 6.11 were formulated for predicting the truck strut pressure during ultra-large truck haulage operations in a large-scale open-pit mine. Equation 6.6 and 6.7 are the models for the CAT 793B truck in loaded and empty conditions, respectively. Equations 6.8 and 6.9 are for the CAT 793C in loaded and empty conditions, respectively, while the models for CAT 793 D in loaded and empty conditions are presented in Equations 6.10 and 6.11, respectively.

Table 6.1 Summary of data for MLR modeling

Truck class	Payload Status	Number of data points used	Mean sp (kPa)
CAT 793B	Loaded	13,154	8,066.8
	Empty	29,876	2,435.7
CAT 793C	Loaded	224,905	7,891.4
	Empty	136,908	2,373.9
CAT 793D	Loaded	321,531	7,827.1
	Empty	222,939	2,350.5

$$sp_l(CAT\ 793B) = 9474.49\ - 0.02 * sh + 12.87 * p + (sh - 169021.78) * [(p\ - 252.89)\ * -0.000014] - 51.04 * gs + (sh - 169021.78) * [(gs\ -\ 27.13) * -0.0025] + (p - 252.89)\ *\ [(gs - 27.13) * 0.53] + (sh\ -\ 169021.78) * [(p - 252.89) * \{(gs - 27.13)\ *\ -0.000022\}] \quad (6.6)$$

$$sp_e(CAT\ 793B) = 2774.08 - 0.0029 * sh + 5.42 *\ gs + (sh - 168668.73) * [(gs -\ \ 28.72) * 0.000012] \quad (6.7)$$

$$sp_l(CAT\ 793C) = 1948.41 + 0.15 * sh + 19.43 * p + (sh - 4050.3) * [(p\ - 257.26) *\ \ -0.016] + 35.42 * gs + (sh\ -\ 4050.3) * [(gs\ -\ 10.16) * 0.014] + (p - 257.26) * [(gs - 10.16) * 0.11] + (sh - 4050.3) * [(p - 257.26) * \{(gs - 10.16) * 0.00076\}] \quad (6.8)$$

$$sp_e(CAT\ 793C) = 2358.06 - 0.0025 * sh + 1.45 * gs + (sh - 4065.83) * [(gs - 19.9) *\ 0.0015] \quad (6.9)$$

$$sp_l(CAT\ 793D) = 11964.03 - 0.10 * sh + 17.08 * p + (sh - 88916.01) * [(p\ - 259.86) * 0.0076] + 35.54 * gs + (sh - 88916.01) * [(gs - 9.19) * -0.003] + (p - 259.86) * [(gs - 9.19) * 0.18] + (sh - 88916.01) * [(p - 259.86) * \{(gs - 9.19 * 0.00077\}] \quad (6.10)$$

$$sp_e(CAT\ 793D) = 5157.85 + -0.032 * sh + 5 * gs + (sh - 88895.83) * [(gs - 15.96) *\ \ -0.0084] \quad (6.11)$$

The model performance was evaluated using the R^2, root mean square error (RMSE) and mean percentage error (MPE). The significance of the models was evaluated using the model p-values. Since the confidence interval used for the modeling was 95%, models and variables with p-values <0.05 were considered significant. Table 6.2 summarizes the model performance results. Detailed model performance results are presented in Appendix A.

It can be observed from Table 6.2 that all the MLR models had p-values <0.001, indicating that they adequately model the represented phenomena. The models also had relatively high R^2 values for the loaded trucks than for the empty trucks. R^2 for the loaded CAT 793B, CAT 793C and CAT 793D were 19.1%, 45.7% and 44.5%, respectively. The R^2 for the empty CAT 793B, CAT 793C and CAT 793D were 2.5%, 0.8% and 3.6%, respectively. Figures 6.23 and 6.24 corroborate these trends. It can be observed from Figure 6.23 that there is a strong relationship between the predicted and actual strut pressures for the loaded trucks (CAT 793C used as an example). Thus, the loaded truck models explain the phenomena they represent much better than the empty truck models. Loaded strut pressures are more critical to truck health compared to empty strut pressures. Thus, the models are important for predicting truck health risks.

Figure 6.24 shows a weak relationship between the predicted and actual strut pressures for the empty trucks (CAT 793D used as an example). Thus, the models for the loaded trucks are more reliable than the models for empty trucks. The MPE of the loaded trucks ranges from 7% to 19%, while the MPE for the empty trucks ranges from 8% to 10%. Thus, the models for loaded and empty trucks can be relied upon for the prediction of strut pressures during haulage.

Table 6.2 MLR model performance summary

Truck class	Payload Status	R^2 (%)	RMSE (kPa)	MPE (%)	p-value
CAT 793B	Loaded (Eqn. 6.6)	19.1	1,517.0	19	<0.001
	Empty (Eqn. 6.7)	2.5	202.4	8	<0.001
CAT 793C	Loaded (Eqn. 6.8)	45.7	566.7	7	<0.001
	Empty (Eqn. 6.9)	0.8	168.5	7	<0.001
CAT 793D	Loaded (Eqn. 6.10)	44.5	557.6	7	<0.001
	Empty (Eqn. 6.11)	3.6	245.5	10	<0.001

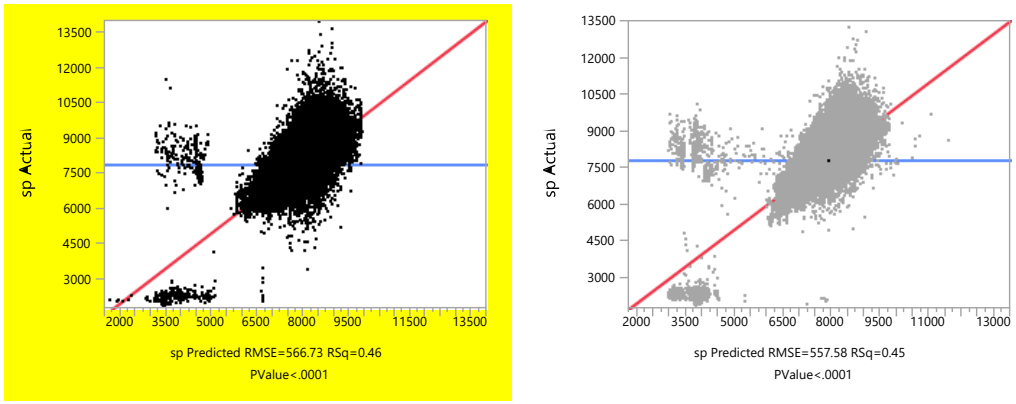

(a) (b)

Figure 6.23 Actual vs predicted strut pressure for loaded CAT (a) 793C and (b) 793D

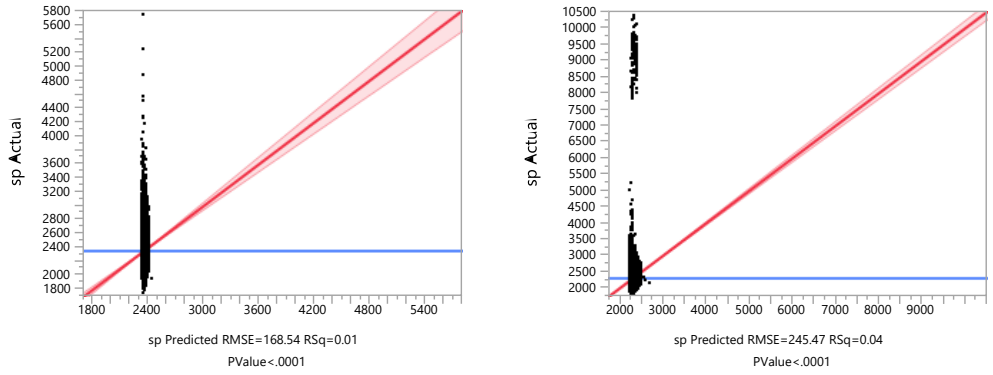

(a) (b)

Figure 6.24 Actual vs predicted strut pressure for empty CAT (a) 793C and (b) 793D

It should be noted that a low R^2 is not indicative of a weak model performance. It indicates that there may be other parameters that affect the model output that are not captured in the models. Including parameters such as the truck suspension stiffness and damping, and road roughness can significantly improve the model performance and result in a higher R^2. The models presented are only for trucks traveling on the 6^{th} gear and on flat road segments, representing trucks at maximum speed. Thus, the models cannot be extrapolated for lower gears or trucks running at curves or on road grades.

Figures 6.25 and 6.26 show the residual plots for CAT 793D in loaded and empty conditions, respectively. Figure 6.25 shows an even distribution of prediction residuals/errors for the loaded truck, while Figure 6.26 shows an uneven distribution of the residuals for an empty CAT 793D. The even distribution of residuals indicates strong model performance as the average error is approximately zero (blue line in Figure 6.25). The uneven distribution of residuals indicates weak model performance, with an average error greater than zero (blue line in Figure 6.26). This reinforces the assertion that the MLR models for the loaded trucks perform better than those for the empty trucks.

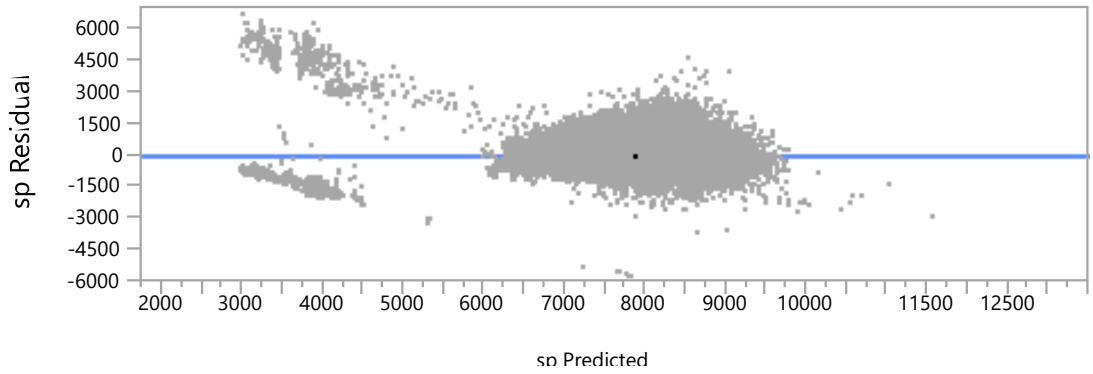

Figure 6.25 Distribution of residuals for a loaded CAT 793D

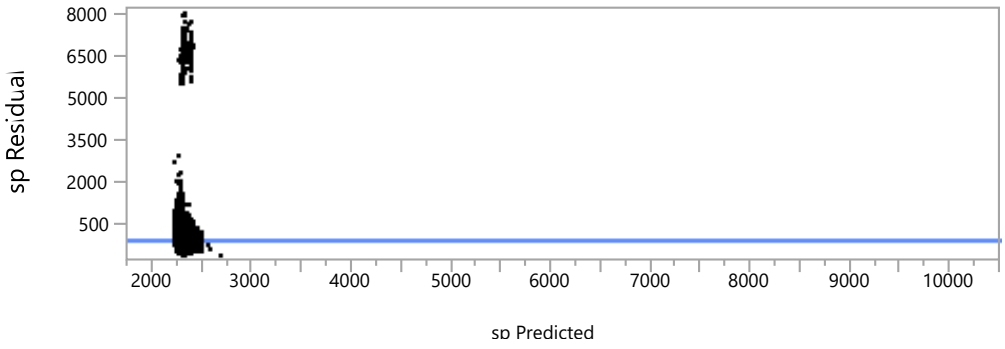

Figure 6.26 Distribution of residuals for an empty CAT 793D

Table 6.3 gives a summary of the interaction significance test results. Detailed parameter significance test results for CAT 793B in loaded and empty conditions are given in Tables 6.4 and 6.5, respectively. The detailed results are presented in Appendix A. Table 6.3 shows that all the parameters had an exclusive significance on the output. That is, the payload (P), service hours (sh) and ground speed (gs) significantly impact the truck strut pressures in loaded conditions. For empty trucks, gs and sh had a significant impact on the strut pressures. It was observed that the two-way interaction of payload (P) and service hours (sh) had an insignificant impact on the strut pressure for CAT 793B.

Table 6.3 Parameter significance test results

Truck class	Payload Status	Significant Variables (p-value < 0.05)	Significant interactions (p-value < 0.05)
CAT 793B	Loaded (Eqn. 6.6)	sh, P, gs	sh*gs, P*gs, sh*P*gs
	Empty (Eqn. 6.7)	sh, gs	No interaction
CAT 793C	Loaded (Eqn. 6.8)	sh, P, gs	sh*P, sh*gs, P*gs, sh*P*gs
	Empty (Eqn. 6.9)	sh, gs	sh*gs
CAT 793D	Loaded (Eqn. 6.10)	sh, P, gs	sh*P, sh*gs, P*gs, sh*P*gs
	Empty (Eqn. 6.11)	sh, gs	sh*gs

Table 6.4 Loaded CAT 793B MLR model parameter test

Term	Estimate	Std Error	Wald Chi-square	Prob > Chi-square	Lower 95%	Upper 95%
Intercept	9474.49	283.44	1117.33	<.0001*	8918.95	10030.03
sh	-0.02	0.0015	173.82	<.0001*	-0.023	-0.017
p	12.87441	0.28	2071.64	<.0001*	12.32	13.43
(sh-169022)*(p-252.89)	-1.4e-5	2.46e-5	0.32	0.5700	-6.23e-5	3.43e-5
gs	-51.04	4.31	140.26	<.0001*	-59.49	-42.59
(sh-169022)*(gs-27.13)	-0.0025	0.00049	26.06	<.0001*	-0.0034	-0.0015
(p-252.89)*(gs-27.13)	0.53	0.08	44.82	<.0001*	0.38	0.69
(sh-169022)*(p-252.89)*(gs-27.13)	-2.16e-5	7.02e-6	9.48	0.0021*	-3.54e-5	-7.85e-6

The sh and gs interaction for the loaded CAT 793B was also insignificant. Thus, any terms in the loaded CAT 793B model having the interaction of P and sh were excluded from the model. This reduces Equation 6.6 to Equation 6.12 for predicting the strut pressure of the loaded CAT 793B. The interaction of sh and gs was removed from the models for the empty CAT 793B. Therefore, Equation 6.7 reduced to Equation 6.13 for the empty CAT 793B. All other interactions were significant as seen in Table 6.3. Equations 6.8, 6.9, 6.10 and 6.11 are the final proposed strut pressure models for a loaded CAT 793C, empty CAT 793C, loaded CAT 793D and empty CAT 793D, respectively.

$$sp_l(CAT\ 793B) = 9474.49\ - 0.02 * sh + 12.87 * p - 51.04 * gs + (sh - 169021.78) *\ [(gs\ -\ 27.13) * -0.0025] + (p - 252.89)\ *\ [(gs - 27.13) * 0.53] + (sh\ -\ 169021.78) * [(p - 252.89) * \{(gs - 27.13)\ *\ -0.000022\}] \quad (6.12)$$

$$sp_e(CAT\ 793B) = 2774.08 - 0.0029 * sh + 5.42 *\ gs \quad (6.13)$$

Table 6.5 Empty CAT 793B MLR model parameter test

Term	Estimate	Std Error	Wald Chi-square	Prob > Chi-square	Lower 95%	Upper 95%
Intercept	2774.08	23.4	14056.71	<.0001*	2728.23	2819.94
sh	-0.0029	1.3e-4	531.66	<.0001*	-0.0032	-0.0027
gs	5.42	0.34	247.75	<.0001*	4.75	6.10
(sh-168669)*(gs-28.72)	1.23e-5	3.76e-5	0.11	0.7436	-6.14e-5	8.6e-5

6.4. ROAD RESPONSE TO DYNAMIC LOADING

The dynamic forces generated by the MSC.ADAMS model were used as input to a 3D truck tire-haul road FEM to study the stress, strain and deformation of the road in response to the truck dynamic loads. The results of the road response to the truck dynamic loads under varying payloads and road layer elastic modulus are presented in this section.

6.4.1. Impact of Layer Elastic Modulus. The layer elastic modulus plays an important role in improving the structural strength of the pavement. Experiments were conducted by varying the base, subbase and subgrade elastic modulus to establish how they affect road response to the tire induced stresses.

6.4.1.1. Base. Figure 6.27 shows the von Mises stress distributions through the four-layer haul road for the seven experiments conducted by varying base layer elastic modulus from 50 MPa to 500 MPa, covering weak and competent base materials. The maximum von Mises stresses ranged from 14.60 MPa to 18.21 MPa over the range of base modulus tested in the experiments (Figure 6.27). Increasing the base modulus from 50 MPa to 100 MPa, for example, increased the maximum von Mises stress by 63.36% and the major principal stress by 51.87%.

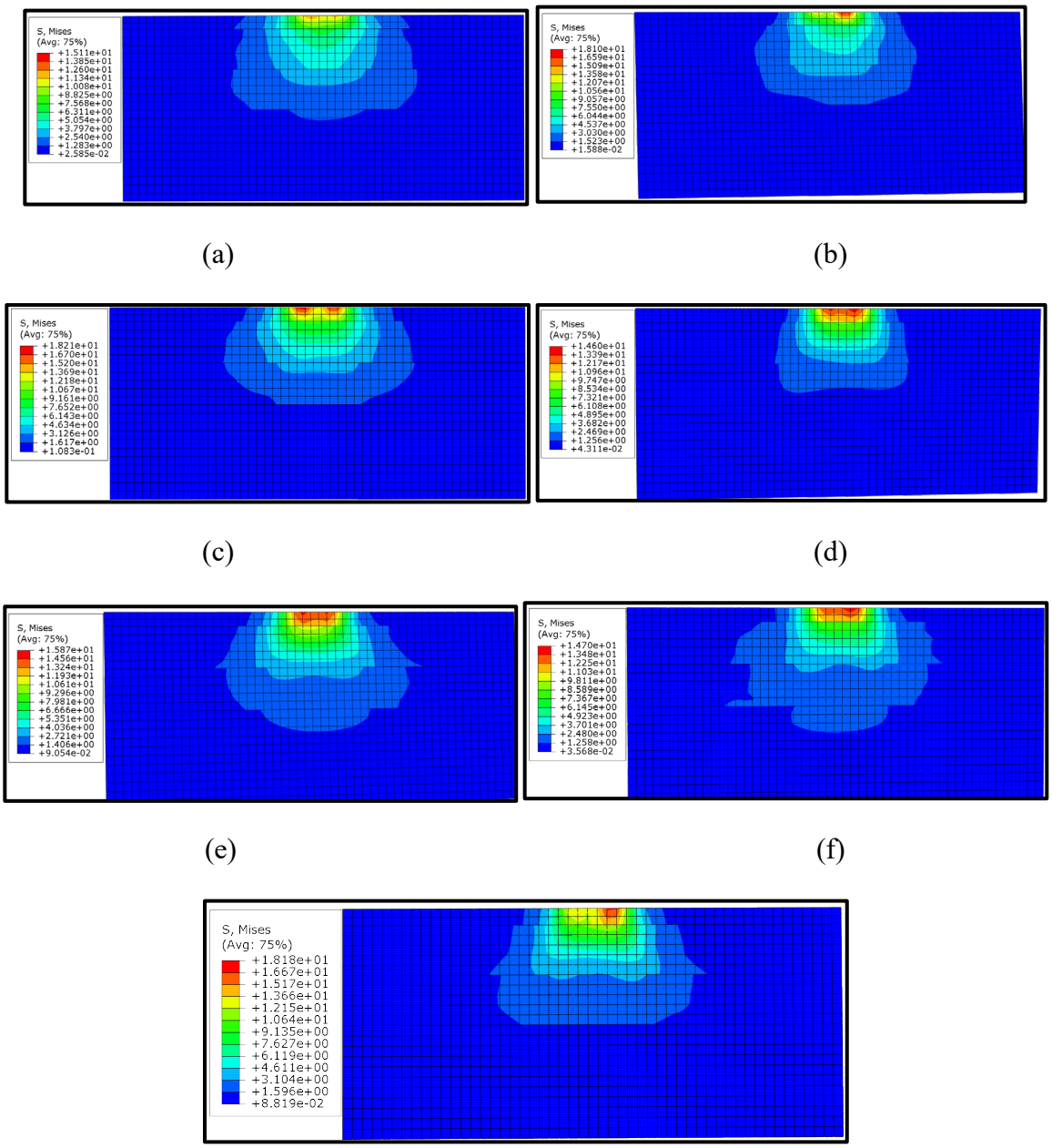

Figure 6.27 von Mises stress distributions (in MPa) through haul road for base modulus of (a) 50 MPa, (b) 100 MPa, (c) 150 MPa, (d) 350 MPa, (e) 400 MPa, (f) 450 MPa, and (g) 500 MPa

The maximum stresses occurred on the wearing surface at the tire-road contact area. They decreased laterally and longitudinally away from the contact area (Figure 6.28), and

vertically downwards (Figure 6.29). Figure 6.29 shows a decrease in layer stresses from the wearing surface to the subgrade. This is expected since the overlying layers dissipate the induced stresses to protect the underlying layers. The decrease is due to the stress spreading over a larger area down the road vertical profile as shown in Figure 6.28.

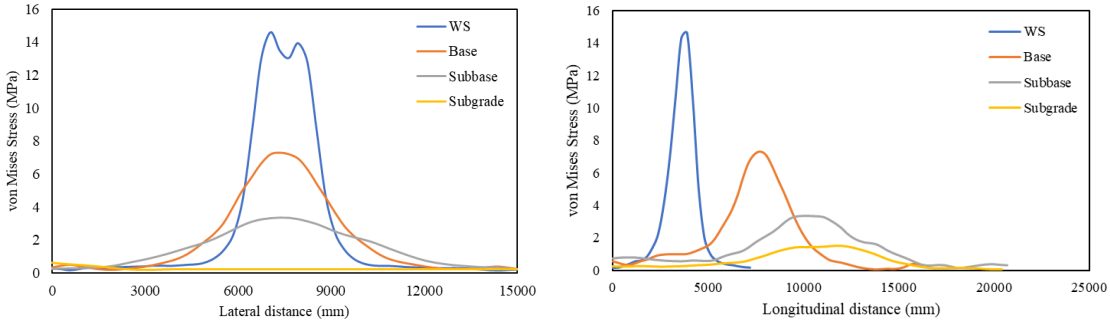

(a) (b)

Figure 6.28 Haul road surface (a) lateral, and (b) longitudinal stress distributions at 50 MPa base modulus

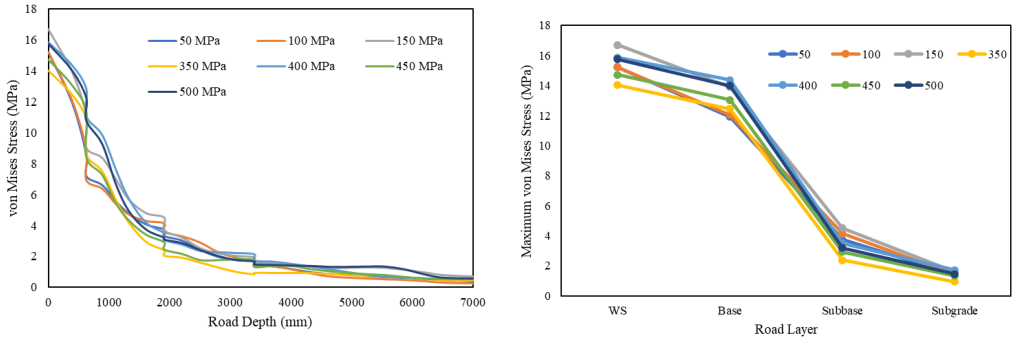

(a) (b)

Figure 6.29 Haul road (a) detailed von Mises and (b) maximum von Mises stresses at varying base modulus

As the base elastic modulus increased from 50 MPa to 500 MPa, the von Mises stress dissipation by the base increased from 54% to 64%. The 50 MPa base reduced the

maximum stresses from 7.315 MPa to 3.38 MPa, while the 500 MPa base reduced the stresses from 11.7 MPa to 4.204 MPa, as shown in Figure 6.29(b). Therefore, a stronger base layer offers better stress dissipation properties, which is desirable for adequate protection of the subbase and subgrade layers to enhance haul road structural performance.

The resulting deformation experienced by each layer of the road decreased with increasing base elastic modulus (Figure 6.30). For the weak base layers (50 – 150 MPa base modulus), the road experienced an increase in vertical deformation from the top to bottom of the wearing surface as shown in Figure 6.30(a). The deformation then decreased from the base to the road bottom. For the competent base (350 – 500 MPa), the maximum vertical deformation occurred at the top of the wearing surface and then decreased with depth to the road bottom. The maximum deformation experienced by the road ranged from 258.26 mm at 100 MPa base modulus to 61.67 mm at 450 MPa base modulus. The maximum deformation occurred at a road depth of 251.81 mm (towards the bottom of the wearing surface) for the roads with a weak base. The roads with competent base layers experienced relatively lower maximum deformation, which occurred at the top of the wearing surface as illustrated in Figure 6.30(a). This implies that a stronger base supports the wearing surface from excessive deformation. This minimizes the development of road surface defects and ultimately improves truck performance through increased truck speed, reduced fuel consumption and improved truck health. It also improves operator comfort since road surfaces remain relatively smooth for longer periods compared to when weak materials are used for building the base layer.

In addition, the stronger base protects the underlying layers (subbase and subgrade) better as seen in Figure 6.30(a). Towards the bottom of the base (road depth of ~2,000

mm), the weak base layers experienced deformations >60 mm and allowed deformations >45 mm at a road depth of 3,000 mm (within the subbase). The strong base layers experienced a maximum deformation of 24.6 mm (59% less than the deformation experienced the weak base layers) towards the bottom of the base (road depth of 2,000 mm). The competent base layers allowed a maximum deformation of 26.7 mm (40.7% less than the case with the weak base layers) at a road depth of 3,000 mm. At road depths >3,000 mm (subbase and subgrade), the roads with weak base layers still experienced higher deformation (up to 39.38 mm) compared to the roads with strong base layers, which experienced a maximum deformation of 15.94 mm (59.5% less than for the weak base).

The resulting strains in the road were higher for roads with weak base layers compared to roads with competent base layers, as shown in Figure 6.30(b). The maximum equivalent plastic strains, which occurred on the road surface for all cases tested, ranged from 0.8367 at 100 MPa to 0.2982 at 350 MPa. The strains decreased significantly to a maximum of 0.1211 at the bottom of the subbase (depth of ~4,000 mm). Beyond this depth, the weak base layers still resulted in higher strains (~0.1329) in the subgrade compared to the competent base layers (~0.0838). This implies that a strong base layer provides adequate protection to the underlying layers, reducing the road deformation and strains at the subbase and subgrade. This ensures the long-term performance of the road since damage to the underlying layers poses critical challenges for haulage operations. Excessive subbase and subgrade deformation are expensive to repair as it usually requires removal of the top layers. It can result in abandonment of the existing haul road if the repair works are prohibitively expensive and time consuming. This can interrupt haulage operations for a long time, resulting in high production losses and increased operating costs.

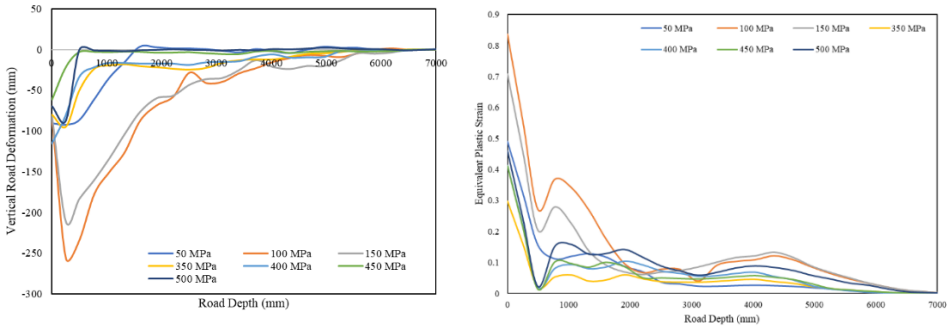

(a) (b)

Figure 6.30 Haul road (a) vertical deformation and (b) equivalent plastic strain at varying base modulus

6.4.1.2. Subbase. Figure 6.31 shows the stress distributions through the road for the seven experiments conducted by varying the subbase modulus from 100 MPa to 500 MPa. The maximum stress increased by 75%, from 15.19 MPa to 26.59 MPa, over the range of subbase modulus values tested, as shown in Figure 6.31.

The maximum stresses occurred at the tire-road contact area and decreased vertically (Figure 6.32), longitudinally and laterally (Figure 6.33) away from the contact area. The stress reduction is due to the load spreading property of the load layers (Figure 6.33). The maximum stresses on the road surface were higher when a competent subbase layer was used compared to a competent base layer. Thus, the subbase does not provide sufficient support to the wearing surface as does the base. This confirms the findings by [25] that it is preferable to place competent layers towards the road surface. Therefore, a competent subbase, with a weak base, results in early development of road surface defects.

As the subbase modulus increased from 100 MPa to 500 MPa, the von Mises stress dissipation from the subbase to subgrade increased from 58% to 67% [derived from Figure 6.32(b)], while the maximum principal stress dissipation increased from 47% to 74%. The

100 MPa subbase layer reduced the maximum von Mises stress from 2.983 MPa to 1.251 MPa, while the 500 MPa subbase layer reduced the maximum von Mises stress from 5.363 MPa to 1.792 MPa. Therefore, a competent subbase layer has higher stress dissipation capabilities, and better protects the subgrade from stresses.

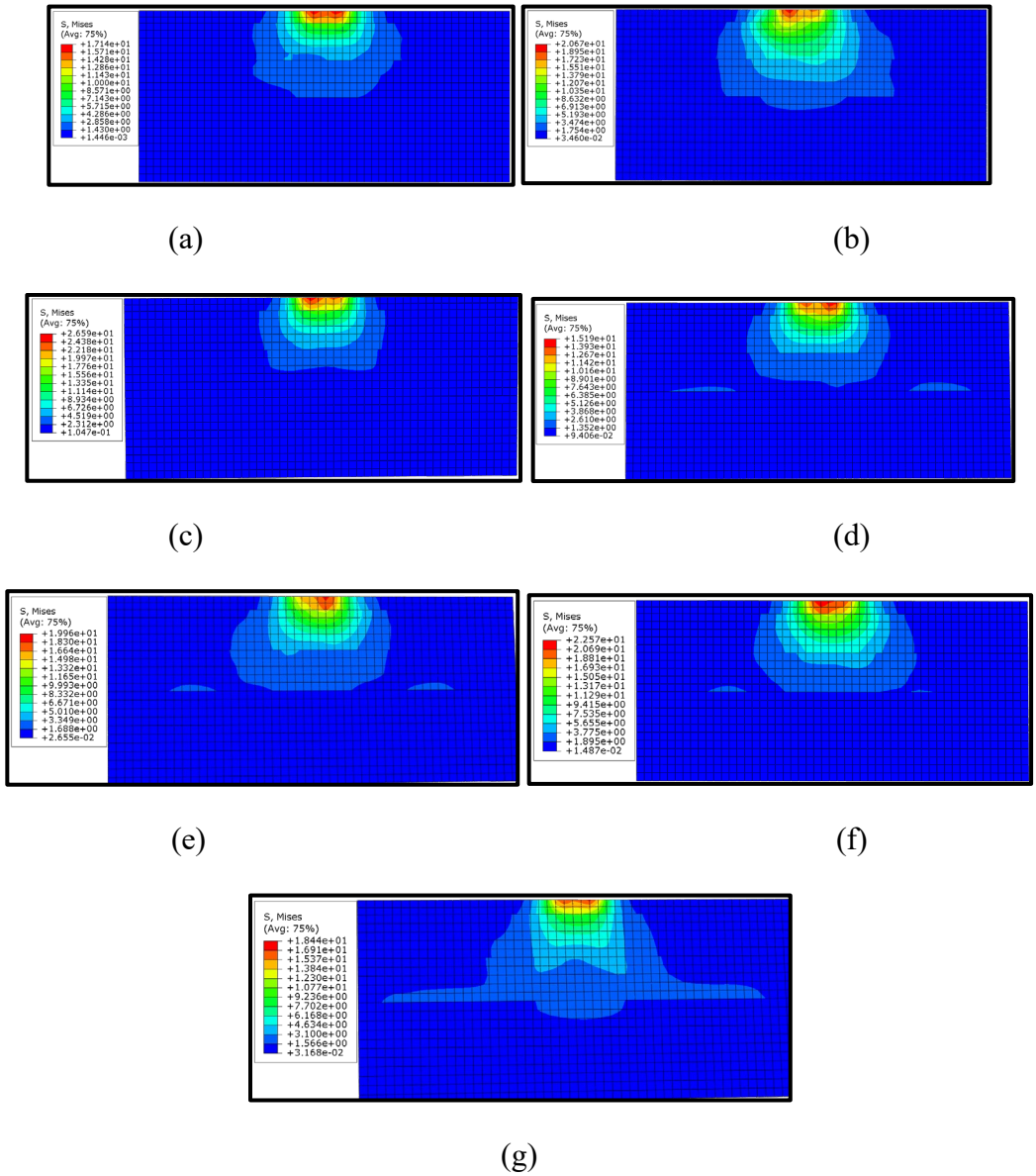

Figure 6.31 Mises stress distributions (in MPa) through haul road for subbase modulus of (a) 100 MPa, (b) 200 MPa, (c) 250 MPa, (d) 300 MPa, (e) 350 MPa, (f) 400 MPa, and (g) 500 MPa

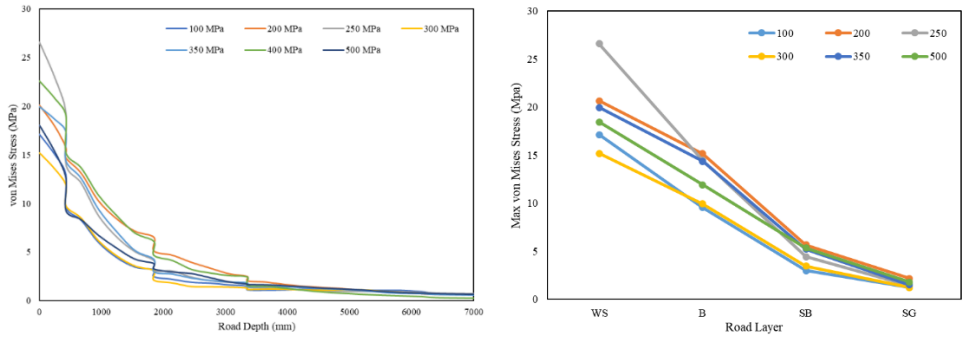

(a) (b)

Figure 6.32 Haul road (a) von Mises and (b) major principal stress at varying subbase modulus

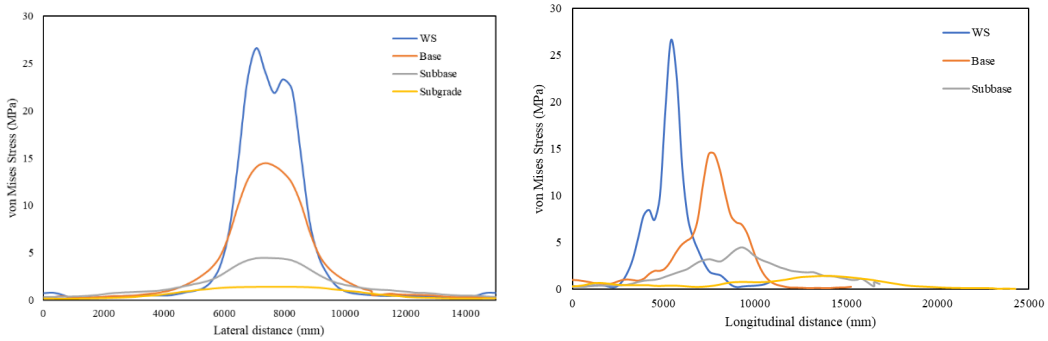

(a) (b)

Figure 6.33 Haul road surface (a) lateral, and (b) longitudinal stress distributions at 250 MPa subbase modulus

The maximum deformation, experienced at the road wearing surface, decreased with increasing subbase modulus, as shown in Figure 6.34(a). The maximum deformation at the surface of the road ranged from 159.563 mm at 100 MPa to 84.375 mm at 500 MPa. It decreased sharply to a maximum of 57.44 mm at a road depth of ~2,000 mm (bottom of base). From the subbase to the subgrade, the road deformation decreased further from a maximum of 46.3125 mm to 32.9373 mm at the top of the subgrade. The magnitude of the decrease from the subbase to subgrade was dependent on the subbase modulus. Layers with

higher subbase modulus reduced the road deformation more than layers with low elastic modulus. At the bottom of the subgrade, the road deformation was zero as imposed by the boundary conditions.

The maximum equivalent plastic strain ranged from 0.5512 to 0.1877 over the range of subbase modulus tested, as shown in Figure 6.34(b). At the bottom of the base (2,000 mm road depth), the maximum strain was 0.1573 and occurred at 100 MPa subbase modulus, while the minimum strain was 0.026, which occurred at 500 MPa subbase modulus. From the top of the subbase (depth of 2,000 mm) to the top of the subgrade (3,500 mm), the strains remained fairly constant. A significant reduction in the strain was observed from a road depth of ~4,300 mm to the bottom of the subgrade (7,000 mm), where the strains reduced from 0.1113 at 100 MPa and 0.0205 at 400 MPa to a maximum of 0.0035 at the road bottom.

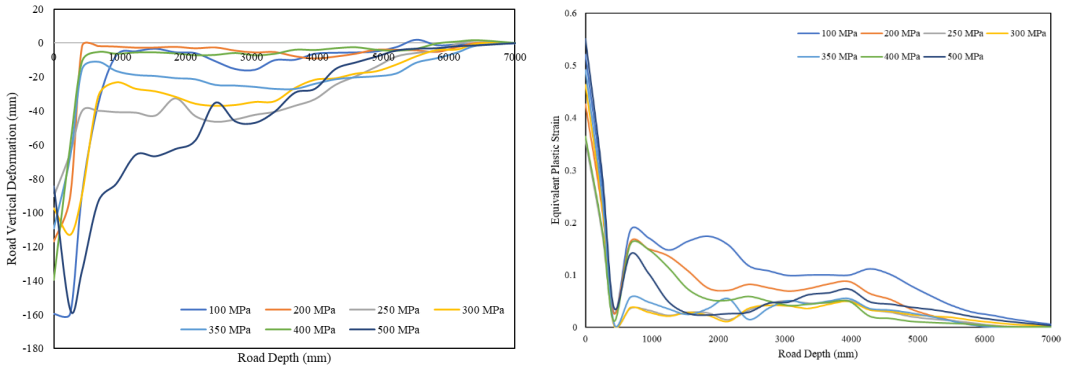

(a) (b)

Figure 6.34 Haul road (a) vertical deformation and (b) equivalent plastic strain at varying subbase modulus

The base and subbase modulus experiments revealed that much of the road structural strength is provided by the base. The wearing surface also plays an important

structural function as it reduced stresses, strains and deformation significantly as shown in the results in Figure 6.27 to 6.33. This had been observed by [25], who recommended that the wearing surface layer should be the most competent layer of the road if practically possible. Using very hard materials on the road surface can cause premature tire failures.

Though the subbase plays a structural role, the road response is less sensitive to the subbase strength compared to the base strength. However, this does not imply that weak subbase layers can be used, as Figures 6.33 and 6.34 have demonstrated that a weak subbase does not provide adequate protection for the subgrade. As a general rule of thumb, therefore, the base should be the most competent layer, followed by the subbase as the base supports the wearing surface and protects the subbase and subgrade against excessive deformation and strains. It is also impacted by higher stresses due to its closeness to the surface, and thus, should have sufficient strength to reduce these stresses significantly to minimize damage to the subbase and subgrade.

6.4.1.3. Subgrade. The subgrade is the ultimate supporting layer for the haul road. The ultimate goal of haul road design is to reduce the impact of the truck tire loads on the subgrade. The experiments discussed in this section evaluated the impact of the subgrade strength on the road integrity. The experiments were carried out to quantify how a haul road would perform under weak (modulus of 30 – 200 MPa) and strong (400 – 600 MPa modulus) subgrades. Figure 6.35 shows the haul road stress distributions at varying subgrade modulus. The maximum von Mises stress ranged from 14.41 MPa for a subgrade modulus of 50 MPa to 38.15 MPa for a subgrade modulus of 200 MPa. At the surface of the subgrade, the maximum von Mises stresses ranged from 5.52 MPa at 200 MPa subgrade modulus to 1.67 MPa at 600 MPa subgrade modulus, as shown in Figure 6.36.

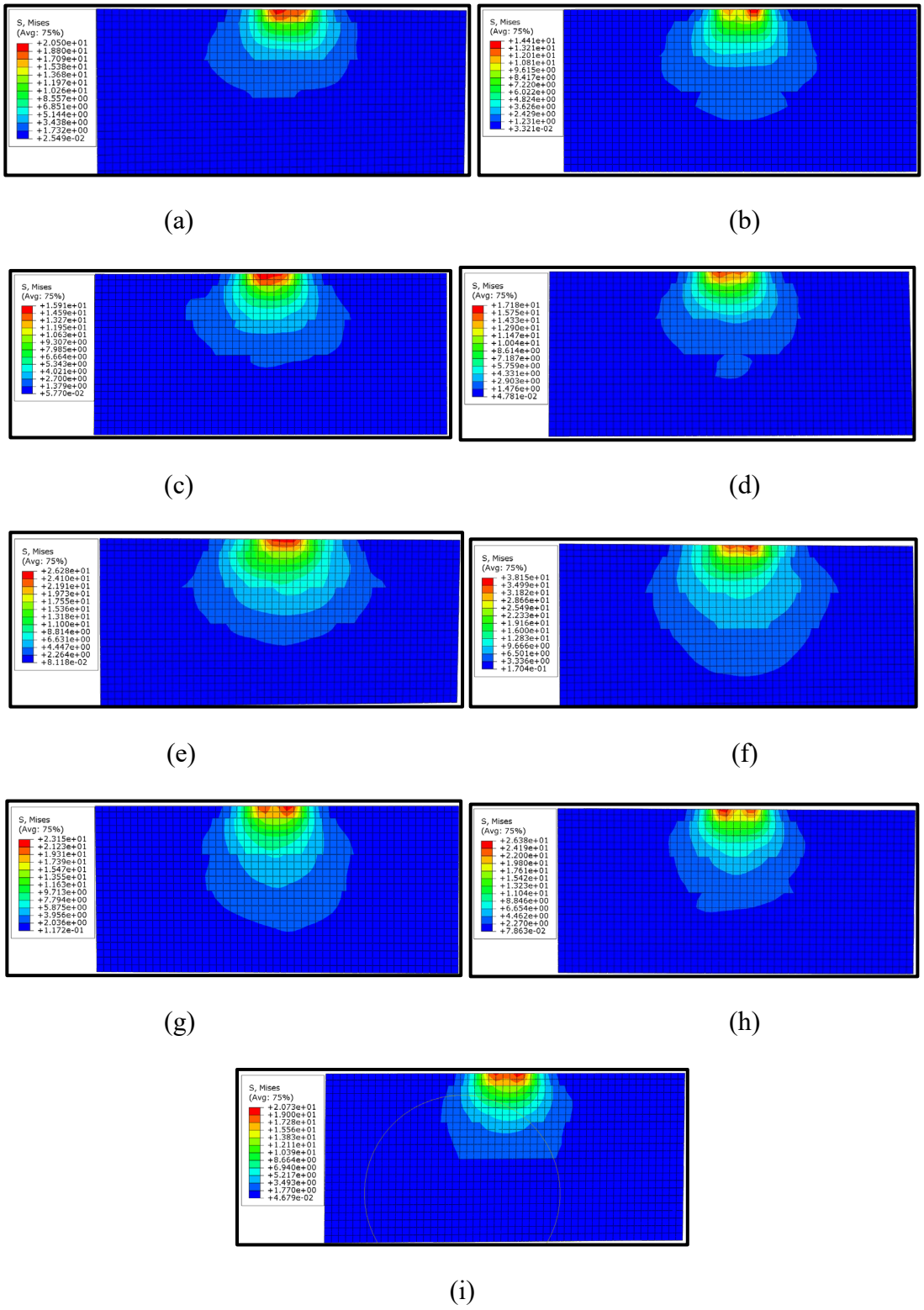

Figure 6.35 Mises stress distributions (in MPa) through haul road for subgrade modulus of (a) 30 MPa, (b) 50 MPa, (c) 70 MPa, (d) 90 MPa, (e) 100 MPa, (f) 200 MPa, (g) 400 MPa, (h) 500 MPa, and (i) 600 MPa

Figure 6.36(a) shows a sharp decrease in stress from one layer to the next. This implies that the inter-layer interface causes stress dissipation. This observation was made for all the experiments undertaken in this work, as can be seen in Figures 6.29(a), 6.32(a) and 6.36(a). Primarily the overlying layers; the wearing surface, base, and subbase, control the stress reductions [Figure 6.36(b)]. As shown in Figures 6.36(b) and 6.37, the highest stress reduction occurred from the wearing surface to the top of the subbase.

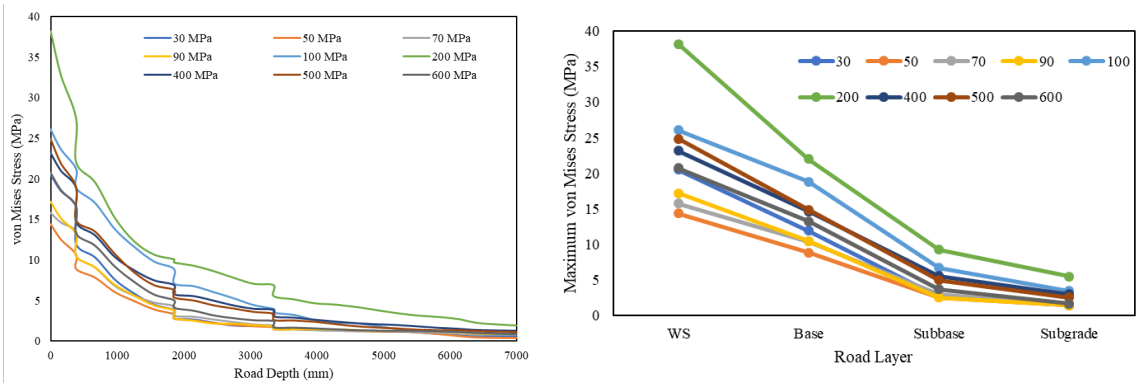

(a) (b)

Figure 6.36 Haul road (a) von Mises and (b) maximum layer von Mises stress at varying subgrade modulus

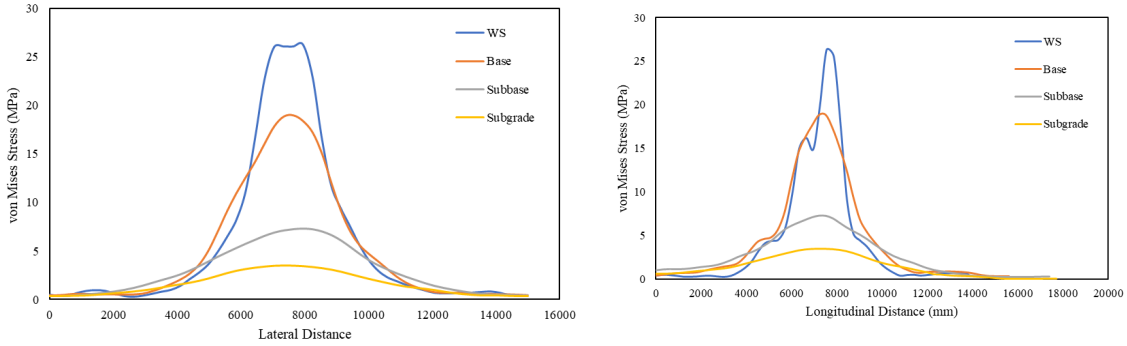

(a) (b)

Figure 6.37 Haul road surface (a) lateral and (b) longitudinal stress distributions at 100 MPa subgrade modulus

Though the strong subgrade roads had higher stress at the subgrade, they experienced a far lower deformation compared to the weak subgrade. The maximum deformation for the 600 MPa subgrade is -8.633 mm, while the maximum deformation for the 30 MPa subgrade is -156.4 mm, as shown in Figure 6.38 (a). The 30 MPa subgrade experienced a deformation that is 18.11 times the 600 MPa subgrade. The layers overlying the weak subgrades also experienced higher deformation compared to the layers overlaying the strong subgrades. The maximum deformation in the wearing surface was 240.2 mm for 30 MPa Subgrade modulus, while for the 600 MPa subgrade, the maximum wearing surface deformation was 138.6 mm. A similar trend exists for the base and subbase deformation; it was higher for weak subgrades and lower for strong subgrades. Thus, designing the overlying layers is very critical in weak formations to reduce the high deformations to near zero at the surface of the subgrade. This will ensure long term road structural integrity, reduced road maintenance and improved truck performance. The strong subgrade could have no overlying layers or minimum thickness of layers placed on it.

The equivalent plastic strains reduced from a maximum of 2.943 at the wearing surface to 0.1 at the surface of the competent subgrade as shown in Figure 6.38. The weak subgrade experienced a maximum strain of 0.2602 (2.6 times the strong subgrade strains). This reinforces the assertion that competent subgrade layers could have no overlying layers since they have very low plastic strains. Very weak subgrade materials present difficult challenges for haul road design. Thus, incorporating ultra-large dynamic forces in designing haul roads for operations involving weak subgrades is critical and should never be ignored as the consequences could greatly impact operations efficiency, safety, health and economics.

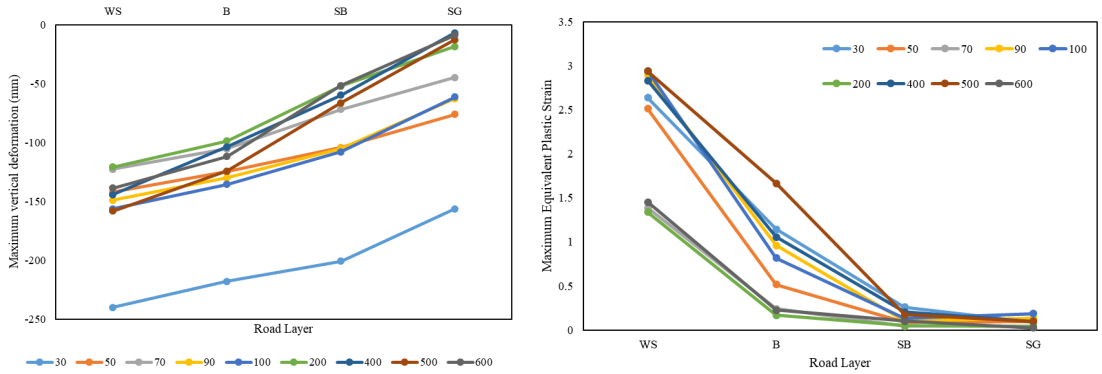

(a) (b)

Figure 6.38 Maximum (a) vertical deformation and (b) equivalent plastic strain at varying subgrade modulus

6.4.2. Impact of Truckloads. Figures 6.39 and 6.40 show the stress distribution through the road for a CAT 797F truck loaded at 80% and 100% payloads, respectively. Figure 6.39 shows a maximum von Mises stress of 13.23 MPa and major principal stress (compressive) of -17.35 MPa for the 80% loaded truck. Figure 6.40 shows a maximum von Mises stress of 15.99 MPa and major principal stress of -20.02 MPa for the 100% (rated payload) loaded truck. For the payload increase of 20%, the maximum von Mises and major principal stresses increased by 20.86% and 22.96%, respectively. Thus, higher payloads induce higher stresses on the road.

This analysis is useful in evaluating the benefits and negative impacts of over-loading trucks. Over-loaded trucks can cause hastened road deterioration due to the higher induced stresses, which will require expensive and frequent maintenance programs and interrupt the production process. Ultimately, the truck cycle times, fuel consumption and component damage can increase due to the over-loading of the truck. This will lead to reduced operations efficiency, increased operating and maintenance costs and reduced

truck availability and utilization. The intended benefits of over-loading the trucks, which is to increase productivity, can be eluded due to these issues.

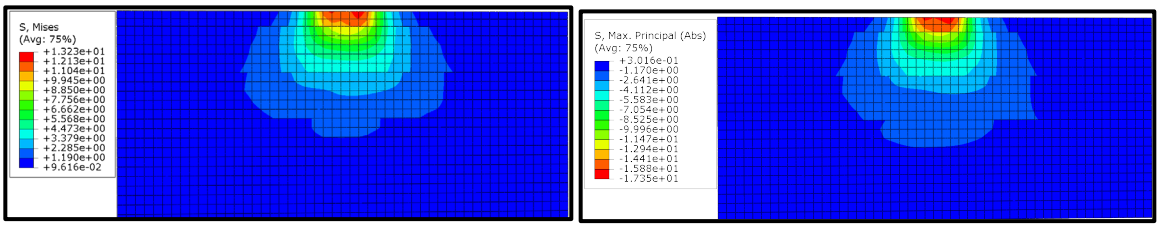

(a) (b)

Figure 6.39 Haul road (a) von Mises and (b) major principal stress distributions at 80% payload

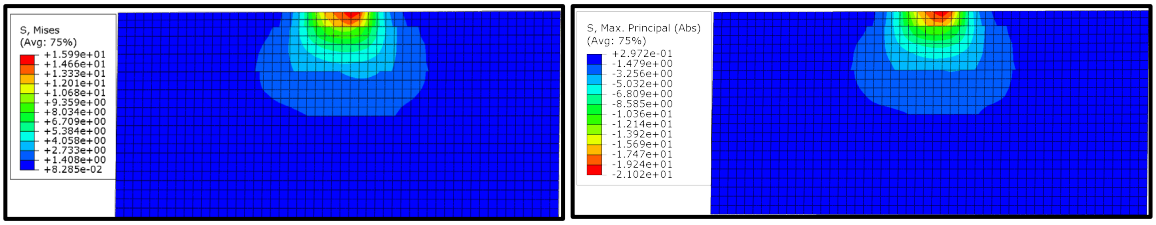

(a) (b)

Figure 6.40 Haul road (a) von Mises and (b) major principal stress distributions at 100% payload

Figure 6.41 gives a summary of the impact of increasing payload on maximum stresses in the road layers. The impact is significant as the maximum von Mises stresses increased from 10.54 MPa for an empty truck to 38.7 MPa for a 20% over-loaded truck. The maximum principal stresses increased from -15 MPa for an empty truck to -39.88 MPa for a 20% over-loaded truck. Thus, before deciding to over-load a truck, the impact on the road structural response has to be established using appropriate models as presented in this work. This is usually overlooked in practice and can cause operational inefficiencies as discussed previously.

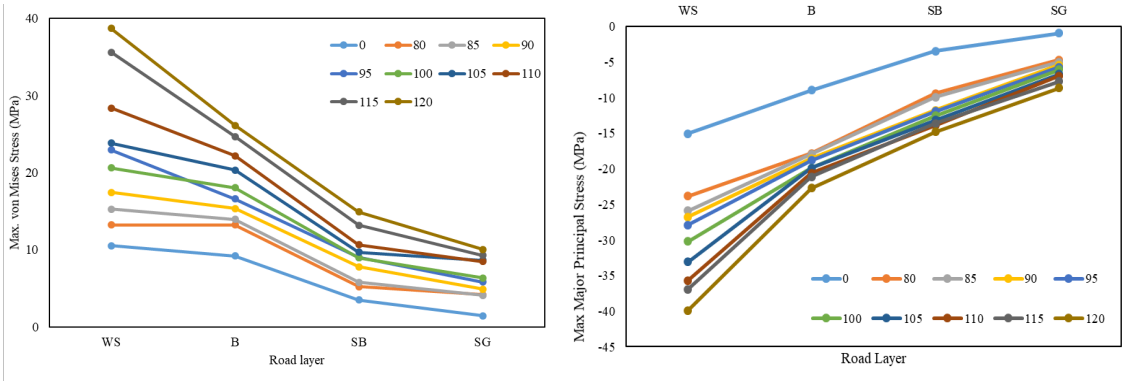

(a) (b)

Figure 6.41 Maximum (a) von Mises (b) major principal stresses at varying payloads

The road deformation and strain due to increasing payload are highlighted using Figure 6.42. The road under the empty truck showed a relatively lower deformation (131.27 mm for wearing surface and 35.42 mm for subgrade), while a 20% over-loaded truck caused a maximum road deformation of 215.49 mm on the wearing surface and 145.68 mm on the subgrade.

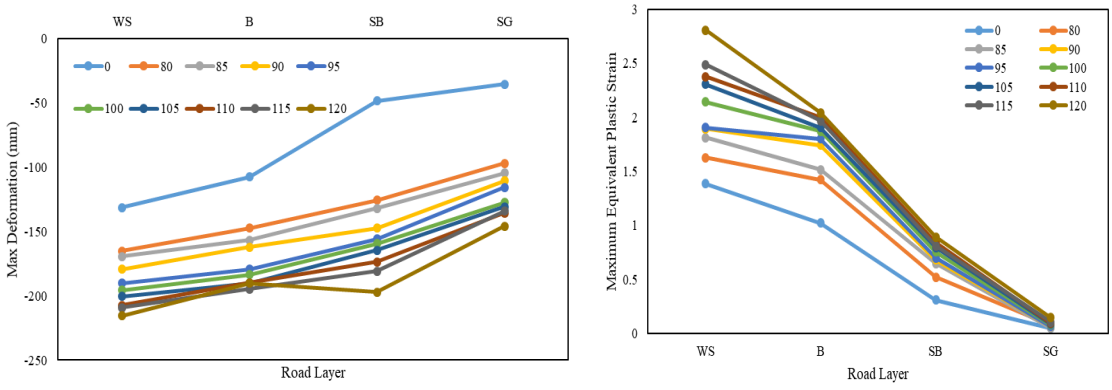

(a) (b)

Figure 6.42 Maximum road (a) deformation and (b) equivalent plastic strains at varying truck payloads

The corresponding plastic strains imposed by the empty truck were 1.387 on the wearing surface and 0.0502 on the subgrade. The 20% over-loaded truck-imposed strains of 2.809 on the wearing surface and 0.1472 on the subgrade. This further highlights the effects of ultra-large truck over-loading on haul road structural response. Thus, the optimal truck payload should be determined considering the strength of the haul road to prevent premature road deterioration and its attendant inefficiencies.

6.5. SUMMARY

This section presented the results and discussions of the study. The results and discussions centered on the dynamic force mathematical model, rigid MBD model in MSC.ADAMS, truck health and MLR analysis and road response model in ABAQUS. The results discussed in this section provide insights into the effect of haul road surface roughness and truck payload on the magnitude of dynamic forces generated by ultra-large truck tires during haulage operations. The results also highlighted the impact of truck payload imbalance on truck health during haulage. Models have been proposed for use with existing empirical haul road structural design models for improving road structural design. MLR models have also been formulated for predicting truck strut pressures, which can be used to determine optimal truck operating parameters for truck health and longevity.

The section also used virtual experimentation in ABAQUS to highlight the impact of varying haul road layer elastic modulus on the road structural performance. These results provide valuable data for haul road design engineers to be able to design structurally sustainable haul roads. The results are aimed at improving road structural design to improve truck performance and health and reduce maintenance costs.

The results from the mathematical and MSC.ADAMS models indicated that truck dynamic forces generated during haulage are significantly higher than the static forces, which are used in current road design techniques. Dynamic forces generated due to road surface roughness reached a maximum of 1,800 kN (1.78 times the maximum static force) for 10% over-loaded trucks. The MSC.ADAMS virtual model results showed that dynamic forces are significantly influenced by the truck payload. As the payload increased from 80% to 120% of the rated payload, the maximum truck tire dynamic forces increased from 2,589.81 kN to 3,096.24 kN. The average dynamic tire forces increased from 942.88 kN at 80% payload to 1,176.75 kN at 120% payload.

The field results indicated that unbalanced payloads significantly increased the rack, roll, and pitch stresses on the truck. Thus, the trucks were exposed to torsional stresses that were up to 2.9 times the recommended safe thresholds. Even balanced payloads still subjected trucks to high torsional stresses, probably due to the road surface roughness. This can reduce truck component health, resulting in reduced truck availability, productivity and component life. It can also subject operators to higher WBV, which can cause operator discomfort and health issues.

The FE model of road response to truck dynamic loads showed the significant impact of base, subbase and subgrade elastic modulus on road durability. It also showed the impact of truck over-loading on road structural performance. As the base modulus increased from 100 MPa to 450 MPa, the maximum deformation on the road wearing surface decreased from 258.26 mm to 61.67 mm. The roads with weak base layers experienced a maximum deformation of 39.38 mm below the base layer, while the roads with strong base layers experienced a maximum deformation of 15.94 mm below the base.

As the subbase elastic modulus increased from 100 MPa to 500 MPa, the maximum deformation occurring on the wearing surface decreased from 159.563 mm to 84.375 mm. Similarly, as the subgrade elastic modulus increased from 30 MPa (very weak) to 600 MPa (strong), its maximum subgrade deformation decreased from 156.4 mm to 8.633 mm. As the truck payload increased from 0 to 120% of rated payload, the maximum wearing surface deformation increased from 131.27 mm to 215.49 mm, while the maximum subgrade deformation increased from 35.42 mm to 145.68 mm. These results are critical for improving haul road performance, which directly impacts truck productivity, health and component longevity.

7. SUMMARY, CONCLUSIONS AND RECOMMENDATIONS

7.1. SUMMARY

Ultra-large trucks have been deployed for achieving bulk production targets due to their economies of scale and operational efficiency. Dynamic forces generated by these ultra-large trucks during haulage are very high and can affect machine component health, operator health and comfort, and haul road structural performance. These problems are exacerbated by rough haul road surfaces, imbalanced payloads and the desire of mining companies to over-load the trucks to achieve optimistic production targets. Current haul road structural design methods assume static truckloads, which are significantly lower than the dynamic forces generated during haulage. In addition, the existing methods cannot be used for ultra-large trucks, which have static tire loads up to 276,375 lbs, as the current methods are limited to maximum tire loads of 120,000 lbs. To ensure truck health and haulage efficiency, the dynamic forces imposed by ultra-large trucks on the haul roads must be quantified and incorporated into haul road structural design methods. This will result in designing roads of sufficient structural integrity to sustain the dynamic loads and reduce road stresses and deformation to levels that are non-destructive to the road subgrade.

This study quantified these dynamic truck forces using multi-body dynamic theories implemented in MATLAB/SIMULINK® and MSC.ADAMS. The road response was modeled using explicit dynamic analysis in ABAQUS for varying truckloads and road mechanical properties. Field data was used to establish the impact of imbalanced truck payloads on truck health and to formulate multiple linear regression models for predicting truck strut pressures during haulage operations. The dynamic force virtual prototype model

in MSC.ADAMS was used for experimenting the impact of truck over-loading on dynamic forces generated during haulage. The output from this model was used as loading conditions in the finite element model of ultra-large truck-haul road interaction in ABAQUS to study haul road stress, strain and deformation under the high impact loads from ultra-large trucks. This work presents the first attempt to incorporate dynamic ultra-large truck forces into haul road structural design. The models were made for CAT 797F truck, which has a rated GMW of 623 metric tons and is currently the largest mining truck. However, they can be used, with little modification of the input data, for other truck models. The results from this study provide a basis for modifying current haul road structural design methods to incorporate truck dynamics and ensure sustainable haul roads. They also present verified and validated models for predicting truck strut pressures, which are critical for ensuring truck health and component longevity, operator health and comfort and monitoring haul road surface conditions for real-time haul road maintenance decisions.

7.2. CONCLUSIONS

This study established the limitations of the existing haul road design methods by extensively reviewing relevant literature. The literature review revealed that existing haul road structural design methods ignore the dynamic effects of the tire-road interaction during haulage and assume static truck tire loads. It also revealed that existing road response models are 2D and only apply a constant tire pressure on an elliptical, circular or rectangular contact area to compute road responses. These assumptions in existing literature do not capture the significant dynamic forces generated during haulage and result in poor design and construction of haul roads which cannot sustain the high dynamic forces.

The research objectives set out in Section 1.3 have been achieved within the defined scope. Mathematical models, based on Lagrangian mechanics, have been presented in Section 3 for understanding the ultra-large truck-haul road load transfer mechanics during haulage. These models captured the road surface roughness, which was modeled using the ISO 8608 road roughness model [67]–[69], [190]. A virtual rigid multi-body dynamic model was also created and solved in MSC.ADAMS for estimating truck dynamic forces imposed on the haul road during haulage. These models were verified and validated using truck dynamic forces derived from truck strut pressure data obtained from an open-pit mine employing ultra-large trucks. The data obtained from an open-pit mine was used to formulate MLR models, based on the least-square fitting, for predicting dynamic truck strut pressures. An FEM was built, verified and validated in ABAQUS for modeling road response to ultra-large truck dynamic forces under varying operational conditions and road layer properties. These models provide a basis for improving haul road structural design and truck health towards improved truck availability and productivity.

Experiments were conducted for quantifying the impact of payload variation and road roughness on truck dynamic forces. From the virtual multi-body dynamic model in MSC.ADAMS and the mathematical model in MATLAB/SIMULINK®, the following conclusions can be drawn:

1. On higher (positive) road profiles, the tire impact forces reduced due to reduced tire vertical acceleration. As the tire runs over depressions, the tire vertical velocity increased, resulting in positive vertical acceleration and increased tire vertical dynamic impact forces.

2. The vertical dynamic forces caused by haul road surface roughness were 1.76 times the maximum rated static tire forces.
3. As the truck payload increased from 80% to 120% of the rated payload, the maximum dynamic tire impact forces increased from 2.53 to 3.02 times the maximum static tire forces.

From the field data, truck health analysis and multiple linear regression analysis, the following conclusions can be drawn:

1. The maximum loaded strut pressure was 4.22 times the empty strut pressure. This subjected the trucks to higher torsional stresses that can reduce truck component and tire life.
2. The maximum loaded rack, roll, and pitch experienced by the truck were up to 2.9 times the threshold values. These high torsional stresses occurred very frequently during operations and were primarily caused by truck over-loading, road surfaces roughness, and payload imbalance.
3. Unbalanced payloads caused more frequent occurrence of above-threshold torsional stresses compared to balanced payloads.
4. The multiple linear regression models for truck strut pressure had MPE ranging from 7% to 19% and R^2 ranging from 0.8% to 45.7%. The models for the loaded trucks showed superior performance compared to the models for the empty trucks.
5. The key significant parameters affecting truck strut pressure were identified as truck speed, payload and service hours (age). The interaction between these parameters also significantly affected the truck strut pressure, and hence, the truck health.

6. The low R^2 values indicate that there could be other factors affecting strut pressures that are not captured in the proposed models.

The FE model for road response focused on studying the road stress, deformation, and strain propagation through the haul road. It also focused on establishing and quantifying the response dissipation abilities of the road layers. From the results of the experimentation on the virtual FE model, the following conclusions can be derived:

1. Increasing the base and subbase elastic modulus reduced the stresses, strains, and deformation of the underlying layers. A competent base and subbase dissipate road responses significantly, resulting in improved road structural integrity.
2. A competent base protected the underlying layers from extreme stresses, strains, and deformation and supported the wearing surface against excessive deformation. A competent subbase only protected the subgrade but did not provide significant support for the wearing surface and base.
3. Stronger layers should be placed closer to the road surface to protect the underlying layers and support the wearing surface. Thus, the base should be the most competent road layer, followed by the subbase. This is more critical when the subgrade is weak.
4. The equivalent plastic strains at the wearing surface were very high in all cases tested, but reduced significantly before reaching the subgrade, the reduction being dependent on the elastic modulus of the base and subbase. However, since this study simulated a single tire pass, repeated high dynamic loading can cause rapid road deterioration due to accumulated plastic strains.

5. Strong subgrade layers can withstand high tire loads as they showed significantly lower deformation and strains compared to the weak subgrades. Weak subgrades require competent overlying layers to minimize road deterioration.
6. Truck over-loading imposed higher road stresses, resulting in higher road deformation and strains. A 20% truck over-loading caused the von Mises and major principal stresses to increase by 20.86% and 22.96%, respectively. As the payload increased from 0% (empty truck) to 120% (20% above rated payload), the maximum wearing surface deformation increased from -131.27 mm to -215.49 mm. Over the same range, the subgrade deformation increased from -35.42 to -145.68 mm.
7. Detailed analysis of road response is required in weak formations to determine the optimal truck payload. This will help to minimize road deterioration and prevent truck haulage inefficiencies that can result from road defects.

7.3. RESEARCH CONTRIBUTIONS

This research is a pioneering effort to understand and quantify the impact of ultra-large truck dynamic forces on haul roads and to model the truck dynamic strut pressure during haulage. It advances knowledge in haul road structural design and truck health. The specific contributions of this research are outlined as follows:

1. The Lagrange formulations for ultra-large truck-haul road interactions presented in this work are the most comprehensive mathematical models for understanding ultra-large truck load transfer during haulage.

2. The 3D virtual FE road response developed in this work is a pioneering contribution towards understanding haul road stress-strain-deformation propagation under ultra-large truck dynamic loading. Earlier attempts were limited to 2D models under static truck loading on circular, elliptical or rectangular contact areas.
3. The proposed mathematical models for incorporating truck dynamic loading in empirical haul road design methods are a significant scientific contribution towards the design of structurally competent haul roads for ultra-large truck haulage applications.
4. This research presents the first known real-time data-driven multivariate statistical models for predicting ultra-large truck dynamic strut pressures during haulage operations.
5. The methods, models and results presented in this work have significant industrial applications for improving haul road structural design and performance, and truck component health and durability.

7.4. RECOMMENDATIONS FOR FUTURE WORK

To continuously advance knowledge in haul road structural design and truck health, the following are recommended:

1. A haul road surface roughness classification system should be developed for mining environments. The ISO 8608 system was designed for commercial roads and light vehicles, and thus, is limited for applications in mining environments. Measured truck strut pressure from different mines and roads of varying roughness can be used to develop a system for classifying haul road surface roughness. Other factors

should be controlled to allow a distinct evaluation of the impact of road roughness on the measured strut pressures.

2. Equations 6.1 to 6.5 require experimental and field validation to confirm their accuracy or improve their predictability for use in road structural design. They can be validated using measured truck tire dynamic force data.
3. A comprehensive numerical and experimental investigation of the impacts of truck dynamic torsional stresses on truck component and tire durability. This is necessary for determining operational thresholds for ensuring healthy truck operations.
4. The model developed in this research should be advanced to study the impact of the rear dual tire set on haul road response.
5. The stress distributions show the occasional occurrence of dual peaks at the tire-road contact. It is tentatively believed that these dual peaks are caused by the irregular tire surface due to the tire treads. Further investigation of the dual peaks is recommended to ascertain the mechanism of their occurrence.
6. Experimental testing of haul road response to truckloads and laboratory and/or field characterization of haul road materials. This will provide accurate input data for the road response models and for validating the models.

APPENDIX

DETAILED MLR RESULTS

CAT 793C Loaded: MLR Model Parameter test

Term	Estimate	Std Error	Wald ChiSquare	Prob > ChiSquare	Lower 95%	Upper 95%
Intercept	1948.41	27.0461	5189.7844	<.0001*	1895.4001	2001.4191
sh	0.1473	0.0056	698.40258	<.0001*	0.1363315	0.1581733
p	19.4255	0.0508	145982.91	<.0001*	19.325898	19.525195
(sh-4050.3)*(p-257.256)	-0.016	0.0002	6206.5626	<.0001*	-0.016348	-0.015554
gs	35.4246	0.2225	25353.195	<.0001*	34.988518	35.860618
(sh-4050.3)*(gs-10.1621)	0.0137	0.00046	871.68289	<.0001*	0.0127477	0.0145606
(p-257.256)*(gs-10.1621)	0.106	0.00598	313.8913	<.0001*	0.0942259	0.1176668
(sh-4050.3)*(p-257.256)*(gs-10.1621)	0.0008	1.5967e-5	2262.2366	<.0001*	0.0007281	0.0007907

CAT 793C Empty: MLR Model Parameter test

Term	Estimate	Std Error	Wald ChiSquare	Prob > ChiSquare	Lower 95%	Upper 95%
Intercept	2358.06	7.29529	104478	<.0001*	2343.7617	2372.3587
sh	-0.0025	0.00154	2.5663	0.1092	-0.005486	0.0005513
gs	1.4535	0.06039	579.29	<.0001*	1.3351809	1.5719149
(sh-4065.83)*(gs-19.899)	0.00145	0.00016	80.7506	<.0001*	0.0011375	0.0017722

CAT 793D Empty: MLR Model Parameter test

Term	Estimate	Std Error	Wald ChiSquare	Prob > ChiSquare	Lower 95%	Upper 95%
Intercept	5157.845	207.57	617.45801	<.0001*	4751.0161	5564.6756
sh	-0.0324	0.0023	193.37788	<.0001*	-0.03705	-0.027897
gs	5.00129	0.0585	7298.7249	<.0001*	4.8865548	5.1160306
(sh-88895.8)*(gs-15.9643)	-0.0084	0.00027	983.83693	<.0001*	-0.008951	-0.007898

CAT 793D Loaded: MLR Model Parameter test

Term	Estimate	Std Error	Wald ChiSquare	Prob > ChiSquare	Lower 95%	Upper 95%
Intercept	11964.03	372.757	1030.1574	<.0001*	11233.436	12694.616
sh	-0.10014	0.00419	568.73441	<.0001*	-0.108379	-0.091918
p	17.0805	0.03678	216549.8	<.0001*	17.008607	17.152487
(sh-88916)*(p-259.862)	0.00761	0.00016	2170.5386	<.0001*	0.0072886	0.0079288
gs	35.5441	0.18696	36144.685	<.0001*	35.177701	35.910566
(sh-88916)*(gs-9.19461)	-0.00296	0.00082	13.021156	0.0003*	-0.004565	-0.001352
(p-259.862)*(gs-9.19461)	0.1758	0.00562	978.88427	<.0001*	0.1648515	0.1868858
(sh-88916)*(p-259.862)*(gs-9.19461)	0.00077	2.9144e-5	705.36909	<.0001*	0.0007169	0.0008312

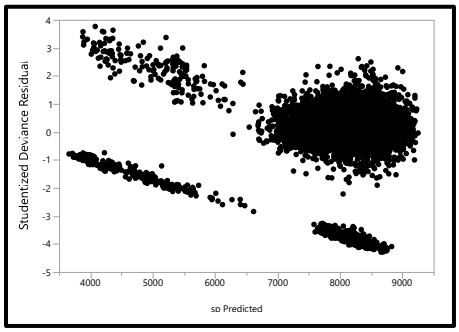

CAT 793B Loaded: Studentized Deviance Residual by Predicted

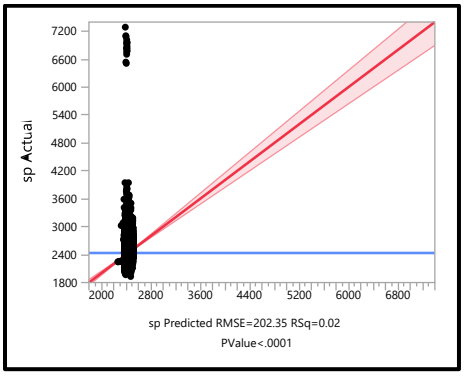

CAT 793B Empty: Actual by Predicted Plot

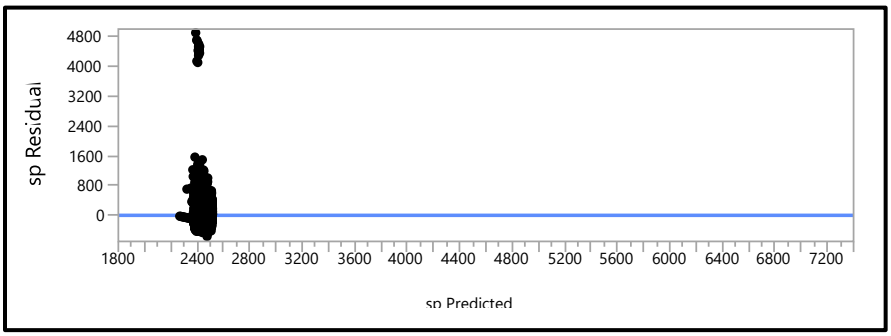

CAT 793B Empty: Residual by Predicted Plot

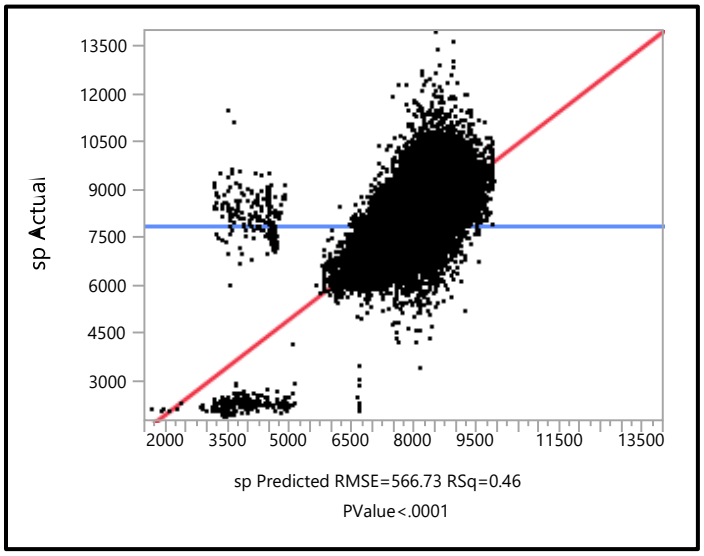

CAT 793C Loaded: Actual by Predicted Plot

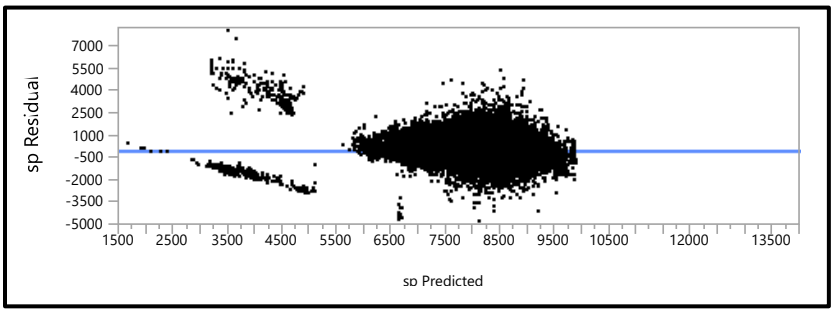

CAT 793C Loaded: Residual by Predicted Plot

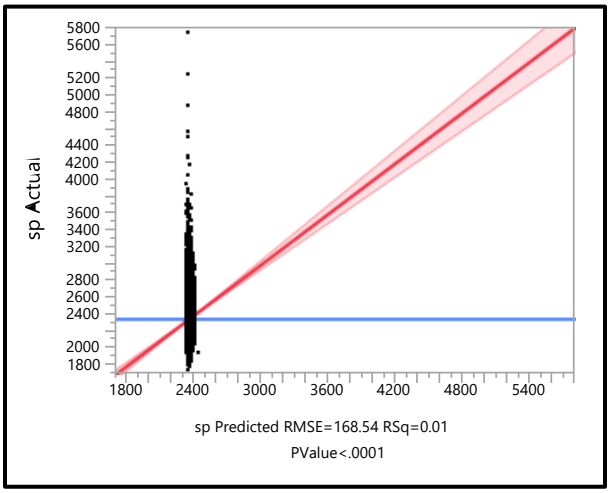

CAT 793C Empty: Actual by Predicted Plot

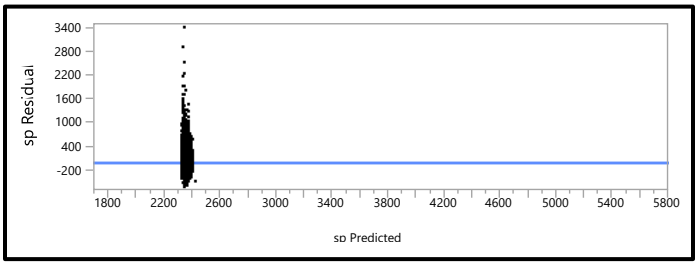

CAT 793C Empty: Residual by Predicted Plot

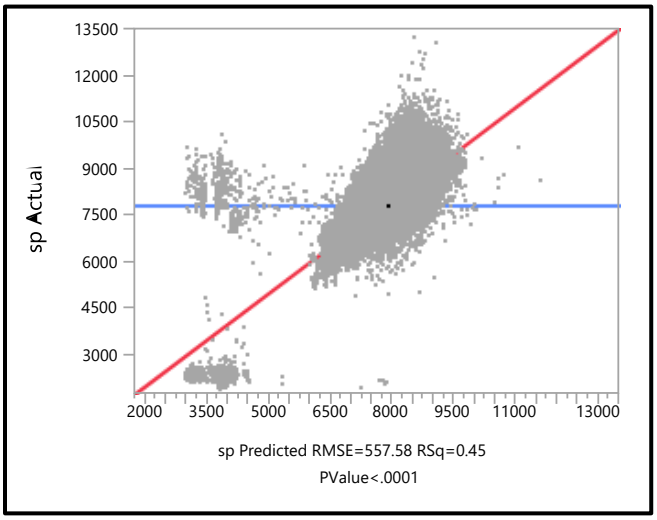

CAT 793D Loaded: Actual by Predicted Plot

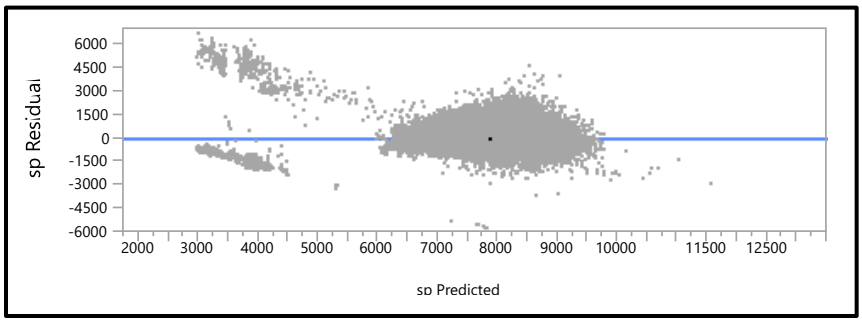

CAT 793D Loaded: Residual by Predicted Plot

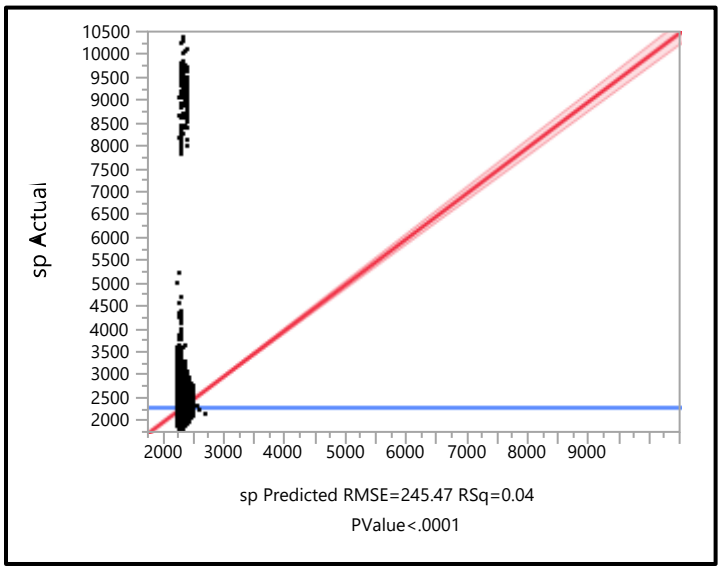

CAT 793D Empty: Actual by Predicted Plot

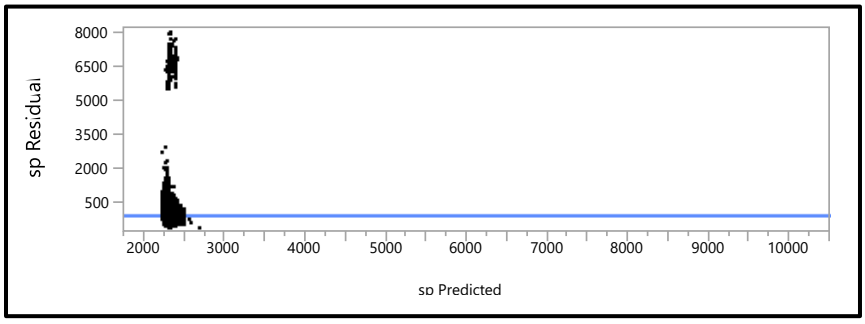

CAT 793D Empty: Residual by Predicted Plot

BIBLIOGRAPHY

[1] NMA, “Facts About Coal and Minerals,” 2016.

[2] F. Holmes, “Top 10 Gold Producing Countries - U.S. Global Investors,” *Frank Talk, a CEO Blog by Frank Holmes*, 2019. [Online]. Available: http://www.usfunds.com/investor-library/frank-talk/top-10-gold-producing-countries/#.XZOpAUZKiM8. [Accessed: 01-Oct-2019].

[3] U.S.G.S., “Mineral Commodity Summaries 2019,” 2019.

[4] B.P., “BP Energy Outlook,” 2018.

[5] U.S.G.S., “MINERAL COMMODITY SUMMARIES 2017,” 2017.

[6] US EIA, “Frequently Asked Questions What is U . S . electricity generation by energy source ?,” 2017. [Online]. Available: https://www.eia.gov/tools/faqs/faq.php?id=427&t=3.

[7] NMA, “Enhancing National Security Authorities,” 2018. [Online]. Available: https://nma.org/category/national-security/. [Accessed: 03-Aug-2018].

[8] DOE, “Mining Inustry Energy Bandwidth Study,” 2007.

[9] B. A. Kansake and S. Frimpong, “Analytical modelling of dump truck tire dynamic response to haul road surface excitations,” *Int. J. Mining, Reclam. Environ.*, pp. 1–18, 2018.

[10] W. G. Koellner, G. M. Brown, J. Rodríguez, J. Pontt, P. Cortés, and H. Miranda, “Recent advances in mining haul trucks,” *IEEE Trans. Ind. Electron.*, vol. 51, no. 2, pp. 321–329, Apr. 2004.

[11] J. Baucom, “The evolution of mining trucks is changing interactions and productivity at mine sites,” 2011.

[12] R. J. Thompson, “Principles of Mine Haul Road Design and Construction,” 2015.

[13] R. Widdifield, L., Riggle, “The Big Picture; An overview approach to surface mining,” 2016.

[14] Vermeer, “A new approach to haul roads,” 2015.

[15] V. Kecojevic, D. Komljenovic, W. Groves, and M. Radomsky, “An analysis of equipment-related fatal accidents in U.S. mining operations: 1995-2005,” *Saf. Sci.*, vol. 45, no. 8, pp. 864–874, Oct. 2007.

[16] M. Zhang, V. Kecojevic, and D. Komljenovic, “Investigation of haul truck-related fatal accidents in surface mining using fault tree analysis,” *Saf. Sci.*, vol. 65, pp. 106–117, Jun. 2014.

[17] A. T. Visser, “Haul roads can make money!,” *J. South. African Inst. Min. Metall.*, vol. 115, no. 11, pp. 993–999, Nov. 2015.

[18] D. Ali, “Mechanics of impulse force reduction for mitigating dump truck vibrations under HISLO conditions,” Missouri University of Science and Technology, 2016.

[19] D. Ali and S. Frimpong, “Artificial intelligence models for predicting the performance of hydro-pneumatic suspension struts in large capacity dump trucks,” *Int. J. Ind. Ergon.*, vol. 67, no. May, pp. 283–295, 2018.

[20] D. Ali and S. Frimpong, “Impulse force reductions and their effects on WBV exposures in high impact shovel loading operations,” *Int. J. Min. Sci. Technol.*, vol. 28, no. 3, pp. 423–435, 2018.

[21] D. Ali and S. Frimpong, “Virtual Simulation of High Impact Shovel Loading Operation for Optimum Dumping Characterization,” *J. Powder Metall. Min.*, vol. 06, no. 01, pp. 1–9, 2017.

[22] M. P. H. Smets, T. R. Eger, and S. G. Grenier, “Whole-body vibration experienced by haulage truck operators in surface mining operations: A comparison of various analysis methods utilized in the prediction of health risks,” *Appl. Ergon.*, vol. 41, no. 6, pp. 763–770, 2010.

[23] S. Kumar, “Vibration in operating heavy haul trucks in overburden mining,” *Appl. Ergon.*, vol. 35, no. 6, pp. 509–520, 2004.

[24] R. Wolfgang and R. Burgess-Limerick, “Whole-body vibration exposure of haul truck drivers at a surface coal mine,” *Appl. Ergon.*, vol. 45, no. 6, pp. 1700–1704, 2014.

[25] D. Tannant, B. Regensburg, “Guidelines for Mine Haul Road Design,” 2001.

[26] A. G. Mayton, W. L. Porter, X. S. Xu, E. B. Weston, and E. N. Rubenstein, “Investigation of human body vibration exposures on haul trucks operating at U.S. surface mines/quarries relative to haul truck activity,” *Int. J. Ind. Ergon.*, vol. 64, pp. 188–198, Mar. 2018.

[27] L. Burström, V. Hyvärinen, M. Johnsen, and H. Pettersson, “Exposure to whole-body vibration in open-cast mines in the barents region,” *Int. J. Circumpolar Health*, vol. 75, Feb. 2016.

[28] M. J. Rahimdel, M. Mirzaei, J. Sattarvand, and S. H. Hoseinie, “Health risk of whole body vibration in mining trucks during various operational conditions,” *J. Cent. South Univ.*, vol. 24, no. 8, pp. 1808–1816, Aug. 2017.

[29] R. Burgess-Limerick, “Measuring and Managing Workplace Whole-Body Vibration Exposures,” *Acoust. Aust.*, vol. 44, no. 1, pp. 129–135, Apr. 2016.

[30] A. Chamanara, “Enhancing mine haul truck KPIs via payload balance,” University of Alberta, 2013.

[31] R. J. Thompson and A. T. Visser, “An overview of the structural design of mine haulage roads,” *Journal of The South African Institute of Mining and Metallurgy*, vol. 96, no. 1. pp. 29–37, Jan-1996.

[32] R. J. Thompson and A. T. Visser, “A mechanistic structural design procedure for surface mine haul roads,” *Int. J. Surf. Mining, Reclam. Environ.*, vol. 11, no. 3, pp. 121–128, 1997.

[33] R. J. Thompson and A. T. Visser, “An introduction to the integrated design of surface mine haul roads,” *Int. J. Surf. Mining, Reclam. Environ.*, vol. 11, no. 3, pp. 115–120, 1997.

[34] R. J. Thompson and A. T. Visser, “Selection and maintenance of mine haul road wearing course materials,” *Inst. Min. Metall. Trans. Sect. A Min. Technol.*, vol. 115, no. 4, pp. 140–153, 2006.

[35] C. R. Maree, J. H., Van Zyl, N. J. W., Freeme, “Effective moduli and stress dependence of pavement materials as measured in some heavy-vehicle simulator tests,” *Transp. Res. Rec.*, no. 0361–1981, pp. 52–60, 1982.

[36] R. J. Thompson and A. T. Visser, “Designing and maintaining opencast mine hal roads for optimum performance,” in *SME Annual Meeting and Exhibit 2010*, 1999, p. 9.

[37] W. Nyaaba, “Thermomechanical fatigue life investigation of an ultra-large mining dump truck tire,” Rolla, MO, 2017.

[38] Y. Li and S. Frimpong, “Dynamic modelling and virtual prototype simulation of dump truck-haul road interactions,” *Int. J. Heavy Veh. Syst.*, vol. 15, no. 2–4, pp. 416–432, 2008.

[39] P. M. Siegrist and P. R. Mcaree, “Sensor Requirements for Tyre Force Estimation; Applications to Off-Highway Mining Trucks,” China China Machinery Press.

[40] N. Aouad, “Mechanics of dump truck vibrations in high-impact shovel loading operations,” Missouri S&T, Rolla, MO 2008.

[41] W. W. Kaufman and J. C. Ault, “DESIGN OF SURFACE MINE HAULAGE ROADS - A MANUAL.,” 1977.

[42] K. Douglas, Robert A., Lawrence, “Optimizing haul road design – a challenge for resource development in Northern Canada Optimizing haul road design – a challenge for resource development in Northern Canada,” in *Conference of the Transportation Association of Canada Montreal, Quebec*, 2014.

[43] S. Frimpong, “Truck Haulage Engineering Lecture Notes: Haul Road Design,” Rolla, 2017.

[44] V. Kumar, “Design and Construction of Haul Roads Using Fly Ash,” University of Alberta, 2000.

[45] A. T. Thompson, Roger J., Visser, “Selection, performance and economic evaluation of dust palliatives on surface mine haul roads,” *J. South African Inst. Min. Metall.*, vol. 107, pp. 435–450, 2007.

[46] Y. H. Huang, *Pavement Analysis and Design*, Second Edi. Upper Saddle River, NJ: Pearson Prentice Hall, 2004.

[47] C. S. Desai, “Unified DSC constitutive model for pavement materials with numerical implementation,” *Int. J. Geomech.*, vol. 7, no. 2, pp. 83–101, Mar. 2007.

[48] R. J. Thompson, “Mine haul road design and management best practices for safe and cost-efficient truck haulage,” in *SME Annual Meeting and Exhibit 2010*, 2010, pp. 140–146.

[49] R. J. Thompson, “Mine haul will road design, construction,” 2014.

[50] A. B. Cecala *et al.*, “Dust Control Handbook for Industrial Minerals Mining and Processing (RI 9689),” 2012.

[51] D. M. Burmister, “The general theory of stresses and displacements in layered soil systems. II,” *J. Appl. Phys.*, vol. 16, no. 3, pp. 126–127, 1945.

[52] D. M. Burmister, “The General Theory of Stresses and Displacements in Layered Soil Systems. III,” *J. Appl. Phys.*, vol. 16, no. 5, pp. 296–302, May 1945.

[53] C. C. Quinn, B. E., Wilson, “Can dynamic tire forces be used as a criterion of pavement condition,” Lafayette, Indiana, 1963.

[54] L. Sun, “Simulation of pavement roughness and IRI based on power spectral density,” *Math. Comput. Simul.*, vol. 61, no. 2, pp. 77–88, Jan. 2002.

[55] M. W. Sayers, T. D. Gillespie, and W. D. O. Paterson, *Guidelines for conducting and calibrating road roughness measurements*. World Bank, 1986.

[56] M. W. Sayers, T. D. Gillespie & C. A. V. Queiroz, *The international road roughness experiment : establishing correlation and a calibration standard for measurements*. University of Michigan. Transportation Research Institute. World Bank, 1986.

[57] C. J. Dodds and J. D. Robson, “The description of road surface roughness,” *Top. Catal.*, vol. 31, no. 2, pp. 175–183, 1973.

[58] P. Andren, “Power spectral density approximations of longitudinal road profiles,” *Int. J. Veh. Des.*, vol. 40, no. 1/2/3, pp. 2–14, 2006.

[59] K. M. A. Kamash and J. D. Robson, “Implications of isotropy in random surfaces,” *J. Sound Vib.*, vol. 54, no. 1, pp. 131–145, Sep. 1977.

[60] K. M. A. Kamash and J. D. Robson, “The application of isotropy in road surface modelling,” *J. Sound Vib.*, vol. 57, no. 1, pp. 89–100, Mar. 1978.

[61] S. Kondo, “Relation between haul road and damage of off-highway dump trucks,” in *Earthmoving Industry Conference*, 1984.

[62] L. Sun and T. W. Kennedy, “Spectral analysis and parametric study of stochastic pavement loads,” *J. Eng. Mech.*, vol. 128, no. 3, pp. 318–327, Mar. 2002.

[63] S. S. Law and X. Q. Zhu, “Bridge dynamic responses due to road surface roughness and braking of vehicle,” *J. Sound Vib.*, vol. 282, no. 3–5, pp. 805–830, Apr. 2005.

[64] C. W. Kim, M. Kawatani, and K. B. Kim, “Three-dimensional dynamic analysis for bridge-vehicle interaction with roadway roughness,” *Comput. Struct.*, vol. 83, no. 19–20, pp. 1627–1645, Jul. 2005.

[65] L. Ding, H. Hao, and X. Zhu, “Evaluation of dynamic vehicle axle loads on bridges with different surface conditions,” *J. Sound Vib.*, vol. 323, no. 3–5, pp. 826–848, Jun. 2009.

[66] X. Yin, Z. Fang, C. S. Cai, and L. Deng, “Non-stationary random vibration of bridges under vehicles with variable speed,” *Eng. Struct.*, vol. 32, no. 8, pp. 2166–2174, Aug. 2010.

[67] J. Oliva, J. M. Goicolea, M. Á. Astiz, and P. Antolín, "Fully three-dimensional vehicle dynamics over rough pavement," *Proc. Inst. Civ. Eng. Transp.*, vol. 166, no. 3, pp. 144–157, Jun. 2013.

[68] J. Oliva, J. M. Goicolea, P. Antolín, and M. Á. Astiz, "Relevance of a complete road surface description in vehicle-bridge interaction dynamics," *Eng. Struct.*, vol. 56, pp. 466–476, Nov. 2013.

[69] M. Oliva, J., Goicolea, J. M., Antolín, P., Astiz, "Dynamic behavior of underspanned suspension road bridges under traffic loads," *J. South African Inst. Civ. Eng.*, vol. 56, no. 3, pp. 77–87, 2014.

[70] C. Gorges, K. Öztürk, and R. Liebich, "Road classification for two-wheeled vehicles," *Veh. Syst. Dyn.*, vol. 56, no. 8, pp. 1289–1314, Aug. 2018.

[71] H. Prem, "Off-highway mine haul truck dynamics simulation," in *SAE Technical Papers*, 1998, p. 12.

[72] D. Hugo, "Haul road defect identification and condition assessment using measured truck response," University of Pretoria, 2005.

[73] D. Hugo, P. S. Heyns, R. J. Thompson, and A. T. Visser, "Haul road defect identification using measured truck response," *J. Terramechanics*, vol. 45, no. 3, pp. 79–88, 2008.

[74] H. M. Ngwangwa, P. S. Heyns, F. J. J. Labuschagne, and G. K. Kululanga, "Reconstruction of road defects and road roughness classification using vehicle responses with artificial neural networks simulation," *J. Terramechanics*, vol. 47, no. 2, pp. 97–111, Apr. 2010.

[75] H. M. Ngwangwa and P. S. Heyns, "Application of an ANN-based methodology for road surface condition identification on mining vehicles and roads," *J. Terramechanics*, vol. 53, no. 1, pp. 59–74, 2014.

[76] H. M. Ngwangwa, P. S. Heyns, H. G. A. Breytenbach, and P. S. Els, "Reconstruction of road defects and road roughness classification using Artificial Neural Networks simulation and vehicle dynamic responses: Application to experimental data," *J. Terramechanics*, vol. 53, no. 1, pp. 1–18, 2014.

[77] P. Yap, "Truck tire types and road contact pressures," 1989.

[78] L. Bakker, E., Nyborg, H. B. Pacejka, "Tyre modelling for use in vehicle dynamics studies," *Soc. Automot. Eng. Inc.*, no. 1, 1987.

[79] H. B. Pacejka and I. J. M. Besselink, "Magic Formula Tyre Model with Transient Properties," *Veh. Syst. Dyn.*, vol. 27, pp. 234–249, 1997.

[80] A. Higuchi and H. B. Pacejka, “Relaxation length concept at large wheel slip and camber,” *Veh. Syst. Dyn.*, vol. 27, no. Suppl, 1997.

[81] A. Ružinskas and H. Sivilevičius, “Magic Formula Tyre Model Application for a Tyre-Ice Interaction,” *Procedia Eng.*, vol. 187, pp. 335–341, 2017.

[82] J. A. Cabrera, A. Ortiz, E. Carabias, and A. Simon, “An Alternative Method to Determine the Magic Tyre Model Parameters Using Genetic Algorithms,” *Veh. Syst. Dyn.*, vol. 41, no. 2, pp. 109–127, Feb. 2004.

[83] J. A. Cabrera, A. Ortiz, B. Estebanez, F. Nadal, and A. Simon, “A coevolutionary algorithm for tyre model parameters identification,” *Struct. Multidiscip. Optim.*, vol. 41, no. 5, pp. 749–763, 2010.

[84] G. Smith and M. Blundell, “A new efficient free-rolling tyre-testing procedure for the parameterisation of vehicle dynamics tyre models,” *Proc. Inst. Mech. Eng. Part D J. Automob. Eng.*, vol. 231, no. 10, pp. 1435–1448, 2017.

[85] M. D. Van Gennip and J. McPhee, “Parameter Identification for Combined Slip Tire Models using Vehicle Measurement System,” *SAE Tech. Pap.*, vol. 2018-April, pp. 1–7, 2018.

[86] H. B. Pacejka, *Tyre and vehicle dynamics*, 2nd Editio. 2006.

[87] K. Popp and W. Schiehlen, *Ground Vehicle Dynamics*. Springer-Verlag Berlin Heidelberg, 2010.

[88] J. Svendenius and B. Wittenmark, “Brush tire model with increased flexibility,” in *European Control Conference, ECC 2003*, 2003, pp. 1863–1868.

[89] C. Li, Hao, Schindler, “Application of analytical and finite element method in tyre-soil modelling,” *Int. J. Heavy Veh. Syst.*, vol. 19, no. 4, pp. 333–354, 2012.

[90] H. Li and C. Schindler, “Investigation of tire-soil interaction with analytical and finite element method,” *Mech. Based Des. Struct. Mach.*, vol. 41, no. 3, pp. 293–315, 2013.

[91] C. W. Fervers, “Improved FEM simulation model for tire-soil interaction,” in *Journal of Terramechanics*, 2004, vol. 41, no. 2–3, pp. 87–100.

[92] M. G. Bekker, *Off-the-road locomotion: research and development in terramechanics*. University of Michigan Press, Ann Arbor, 1960.

[93] M. G. Bekker, *INTRODUCTION TO TERRAIN-VEHICLE SYSTEMS. PART I: THE TERRAIN. PART II: THE VEHICLE,*. University of Michigan Press, Ann Arbor, 1969.

[94] J. Y. Wong, *Theory of ground vehicles*, 3rd Editio. John Wiley and Sons, Inc., 2001.

[95] S. Frimpong, G. Galecki, Y. Li, and R. Suglo, "Dump truck tire stress simulation for extended service life," in *SOCIETY FOR MINING, METALLURGY, AND EXPLORATION*, 2012, vol. 332, pp. 422–429.

[96] N. Aouad, S., Frimpong, "Virtual Prototype Simulation of Truck Vibrations in High-Impact Shovel Loading Operations," *J. Powder Metall. Min.*, vol. 01, no. S1, pp. 1–5, 2013.

[97] S. Frimpong and M. Thiruvengadam, "Multi-Body Dynamic Modeling and Simulation of Crawler-Formation Interactions in Surface Mining Operations – Crawler Kinematics," vol. 15, no. 5, 2015.

[98] S. Frimpong and M. Thiruvengadam, "Rigid multi-body kinematics of shovel crawler-formation interactions," *Int. J. Mining, Reclam. Environ.*, vol. 30, no. 4, pp. 347–369, 2016.

[99] S. Frimpong, M. Thiruvengadem, "Contact and Joint Forces Modeling and Simulation of Crawler-formation Interactions," *J. Powder Metall. Min.*, vol. 04, no. 02, 2015.

[100] P. M. Siegrist, "A method for monitoring tyire-forces on off-highway mining trucks," The University of Queensland, 2004.

[101] Y. Lu, S. Yang, S. Li, and L. Chen, "Numerical and experimental investigation on stochastic dynamic load of a heavy duty vehicle," *Appl. Math. Model.*, vol. 34, no. 10, pp. 2698–2710, 2010.

[102] L. C. A. Silva, J. J. Eckert, F. G. Dedini, and F. C. Corrêa, "Development of a Tire Modeling with Adams/Simulink to study the vehicle control," *Proc. 23rd ABCM Int. Congr. Mech. Eng.*, no. 2006, 2015.

[103] D. Rubinstein and R. Hitron, "A detailed multi-body model for dynamic simulation of off-road tracked vehicles," in *Journal of Terramechanics*, 2004, vol. 41, no. 2–3, pp. 163–173.

[104] S. Taheri, C. Sandu, S. Taheri, E. Pinto, and D. Gorsich, "A technical survey on Terramechanics models for tire-terrain interaction used in modeling and simulation of wheeled vehicles," *Journal of Terramechanics*, vol. 57. Elsevier Ltd, pp. 1–22, 2015.

[105] N. D. Beskou and D. D. Theodorakopoulos, "Dynamic effects of moving loads on road pavements: A review," *Soil Dynamics and Earthquake Engineering*, vol. 31, no. 4. pp. 547–567, Apr-2011.

[106] E. Kausel, “Can a discrete dynamic model ever perfectly simulate a continuum?,” *Soil Dyn. Earthq. Eng.*, vol. 112, pp. 53–57, Sep. 2018.

[107] H. Bufler, “Theory of elasticity of a multilayered medium,” *J. Elast.*, vol. 1, no. 2, pp. 125–143, Dec. 1971.

[108] I. L. Al-Qadi, H. Wang, P. J. Yoo, and S. H. Dessouky, “Dynamic analysis and in situ validation of perpetual pavement response to vehicular loading,” *Transp. Res. Rec.*, no. 2087, pp. 29–39, 2008.

[109] H. Wang and I. L. Al-Qadi, “Combined effect of moving wheel loading and three-dimensional contact stresses on perpetual pavement responses,” *Transp. Res. Rec.*, no. 2095, pp. 53–61, 2009.

[110] V. L. Green, “Investigation of Structural Responses for Flexible Pavement Sections at the Ohio-SHRP,” Ohio University, 2008.

[111] B. Picoux, A. El Ayadi, and C. Petit, “Dynamic response of a flexible pavement submitted by impulsive loading,” *Soil Dyn. Earthq. Eng.*, vol. 29, no. 5, pp. 845–854, May 2009.

[112] Y.-R. Kim, H. Ban, and S. Im, “Impact of Truck Loading on Design and Analysis of Asphaltic Pavement Structures,” 2010.

[113] Z. Wu, X. Chen, and X. Yang, “Finite Element Simulation of Structural Performance on Flexible Pavements with Stabilized Base/Treated Subbase Materials under Accelerated Loading,” 2011.

[114] C. W. Huang, R. K. Abu Al-Rub, E. A. Masad, and D. N. Little, “Three-Dimensional Simulations of Asphalt Pavement Permanent Deformation Using a Nonlinear Viscoelastic and Viscoplastic Model,” *J. Mater. Civ. Eng.*, vol. 23, no. 1, pp. 56–68, Feb. 2011.

[115] L. Zheng, Y. Hai-lin, W. Wan-ping, and C. Ping, “Dynamic stress and deformation of a layered road structure under vehicle traffic loads: Experimental measurements and numerical calculations,” *Soil Dyn. Earthq. Eng.*, vol. 39, pp. 100–112, Aug. 2012.

[116] X. Cui, N. Zhang, J. Zhang, and Z. Gao, “In situ tests simulating traffic-load-induced settlement of alluvial silt subsoil,” *Soil Dyn. Earthq. Eng.*, vol. 58, pp. 10–20, Mar. 2014.

[117] L. S. Tang, H. K. Chen, H. T. Sang, S. Y. Zhang, and J. Y. Zhang, “Determination of traffic-load-influenced depths in clayey subsoil based on the shakedown concept,” *Soil Dyn. Earthq. Eng.*, vol. 77, pp. 182–191, Oct. 2015.

[118] Z. Lu, Z. Hu, H. Yao, J. Liu, and Y. Zhan, "An analytical method for evaluating highway embankment responses with consideration of dynamic wheel-pavement interactions," *Soil Dyn. Earthq. Eng.*, vol. 83, pp. 135–147, Apr. 2016.

[119] N. D. Beskou, G. D. Hatzigeorgiou, and D. D. Theodorakopoulos, "Dynamic inelastic analysis of 3-D flexible pavements under moving vehicles: A unified FEM treatment," *Soil Dyn. Earthq. Eng.*, vol. 90, pp. 420–431, Nov. 2016.

[120] P. Liu, D. Wang, and M. Oeser, "Application of semi-analytical finite element method to analyze asphalt pavement response under heavy traffic loads," *J. Traffic Transp. Eng. (English Ed.*, vol. 4, no. 2, pp. 206–214, Apr. 2017.

[121] J. Chen and Y. Zhou, "Dynamic responses of subgrade under double-line high-speed railway," *Soil Dyn. Earthq. Eng.*, vol. 110, pp. 1–12, Jul. 2018.

[122] D. Sheng Ling, Y. Zhao, B. Huang, F. Zhang, and Y. Zhou, "Analysis of dynamic stress path in inhomogenous subgrade under moving aircraft load," *Soil Dyn. Earthq. Eng.*, vol. 111, pp. 65–76, Aug. 2018.

[123] F. Lekarp, U. Isacsson, and A. Dawson, "State of the art. I: Resilient response of unbound aggregates," *J. Transp. Eng.*, vol. 126, no. 1, pp. 66–75, 2000.

[124] A. Roscoe, K. H., Schofield, A. N., Thurairajah, "Yielding of clays in states wetter than critical," *Geotechnique*, vol. 13, no. 3, pp. 211–240, 1963.

[125] J. B. Roscoe, K. H., Burland, *ON THE GENERALIZED STRESS-STRAIN BEHAVIOUR OF WET CLAY*. 1968.

[126] P. Schofield, Andrew, Wroth, *Critical state soil mechanics*. 1968.

[127] M. D. Liu and J. P. Carter, "A structured Cam Clay model," *Can. Geotech. J.*, vol. 39, no. 6, pp. 1313–1332, Dec. 2002.

[128] M. D. Liu, J. P. Carter, and F. Masce, "A structured Cam Clay Model," 2006.

[129] C. Callari, F. Auricchio, and E. Sacco, "A finite-strain cam-clay model in the framework of multiplicative elasto-plasticity," *Int. J. Plast.*, vol. 14, no. 12, pp. 1155–1187, 1998.

[130] T. D. White, S. M. Zaghloul, G. L. Anderton, and D. M. Smith, "Pavement analysis for moving aircraft load," *J. Transp. Eng.*, vol. 123, no. 6, pp. 436–446, 1997.

[131] Takeuchi, "Pavements Unbound," PROCEEDINGS OF THE 6th INTERNATIONAL SYMPOSIUM ON PAVEMENTS
UNBOUND (UNBAR 6), 6–8 JULY 2004, NOTTINGHAM, ENGLAND

[132] N. Chai, J;Miura, "Traffic-Load-Induced Permanent Deformation of Road on Soft Subsoil," *J. Geotech. Geoenvironmental Eng.*, vol. 128, no. 11, pp. 907–916, 2002.

[133] B. Sukumaran, M. Willis, and N. Chamala, "Three dimensional finite element modeling of flexible pavements," in *Geotechnical Special Publication*, 2005, no. 130–142, pp. 87–98.

[134] B. Saad, H. Mitri, and H. Poorooshasb, "Three-dimensional dynamic analysis of flexible conventional pavement foundation," *J. Transp. Eng.*, vol. 131, no. 6, pp. 460–469, Jun. 2005.

[135] B. Saad, H. Mitri, and H. Poorooshasb, "3D FE analysis of flexible pavement with geosynthetic reinforcement," *J. Transp. Eng.*, vol. 132, no. 5, pp. 402–415, May 2006.

[136] L. Ševelová and A. Florian"Comparison of Material Constitutive Models Used in FEA of Low Volume Roads," World Academy of Science, Engineering and Technology International Journal of Civil and Environmental Engineering Vol:7, No:10, 2013

[137] J. Uzan, "Permanent deformation of a granular base materials," *Transp. Res. Rec.*, pp. 89–94, 1999.

[138] L. R. Alejano and A. Bobet, "Drucker-Prager criterion," *Rock Mech. Rock Eng.*, vol. 45, no. 6, pp. 995–999, Nov. 2012.

[139] T. S. Vepa and K. P. George, "Deflection response models for cracked rigid pavements," *J. Transp. Eng.*, vol. 123, no. 5, pp. 377–384, 1997.

[140] A. C. Seibi, M. G. Sharma, G. A. Ali, and W. J. Kenis, "Constitutive relations for asphalt concrete under high rates of loading," *Transp. Res. Rec.*, no. 1767, pp. 111–119, 2001.

[141] M. Huang, B., Mohammad, L. N., Rasoulian, "Three-dimensional numerical simulation of asphalt pavement at Louisiana Accelerated Loading Facility," *Transp. Res. Rec.*, pp. 44–58, 2001.

[142] M. F. Saleh, B. Steven, and D. Alabaster, "Three-Dimensional Nonlinear Finite Element Model for Simulating Pavement Response: Study at Canterbury Accelerated Pavement Testing Indoor Facility, New Zealand," in *Transportation Research Record*, 2003, no. 1823, pp. 153–162.

[143] Y. Zhang, M. Bernhardt, G. Biscontin, R. Luo, and R. L. Lytton, "A generalized Drucker–Prager viscoplastic yield surface model for asphalt concrete," *Mater. Struct. Constr.*, vol. 48, no. 11, pp. 3585–3601, 2015.

[144] D. W. Park, A. E. Martin, and E. Masad, "Effects of nonuniform tire contact stresses on pavement response," *J. Transp. Eng.*, vol. 131, no. 11, pp. 873–879, Nov. 2005.

[145] L. Tashman, E. Masad, H. Zbib, D. Little, and K. Kaloush, "Microstructural viscoplastic continuum model for permanent deformation in asphalt pavements," *J. Eng. Mech.*, vol. 131, no. 1, pp. 48–57, Jan. 2005.

[146] E. Masad, S. Dessouky, and D. Little, "Development of an elastoviscoplastic microstructural-based continuum model to predict permanent deformation in hot mix asphalt," *Int. J. Geomech.*, vol. 7, no. 2, pp. 119–130, Mar. 2007.

[147] B. M. Luccioni and M. Luege, "Concrete pavement slab under blast loads," *Int. J. Impact Eng.*, vol. 32, no. 8, pp. 1248–1266, 2006.

[148] S. Ivorra, R. Irles, L. Estevan, J. M. Adam, F. J. Pallarés, and B. Ferrer, "Drucker-Prager yield criterion application to study the behavior of CFRP confined concrete under compression," 2010.

[149] C. Chazallon, P. Hornych, and S. Mouhoubi, "Elastoplastic model for the long-term behavior modeling of unbound granular materials in flexible pavements," *Int. J. Geomech.*, vol. 6, no. 4, pp. 279–289, Jul. 2006.

[150] L. A. Al-Khateeb, A. Saoud, and M. F. Al-Msouti, "Rutting prediction of flexible pavements using finite element modeling," *Jordan J. Civ. Eng.*, vol. 5, no. 2, pp. 173–190, 2011.

[151] F. Gu, X. Luo, Y. Zhang, R. Lytton, and H. Sahin, "Modeling of unsaturated granular materials in flexible pavements," in *E3S Web of Conferences*, 2016, vol. 9.

[152] J. H. Keyak and S. A. Rossi, "Prediction of femoral fracture load using finite element models: An examination of stress- and strain-based failure theories," *J. Biomech.*, vol. 33, no. 2, pp. 209–214, 2000.

[153] X. Wang, M. R. Allen, D. B. Burr, E. J. Lavernia, B. Jeremić, and D. P. Fyhrie, "Identification of material parameters based on Mohr-Coulomb failure criterion for bisphosphonate treated canine vertebral cancellous bone," *Bone*, vol. 43, no. 4, pp. 775–780, Oct. 2008.

[154] Y. Bai and T. Wierzbicki, "Application of extended Mohr-Coulomb criterion to ductile fracture," *Int. J. Fract.*, vol. 161, no. 1, pp. 1–20, 2010.

[155] J. F. Labuz and A. Zang, "Mohr-Coulomb failure criterion," *Rock Mech. Rock Eng.*, vol. 45, no. 6, pp. 975–979, Nov. 2012.

[156] A. P. W. Rowe, “The stress-dilatancy relation for static equilibrium of an assembly of particles in contact,” *Proc. R. Soc. London. Ser. A. Math. Phys. Sci.*, vol. 269, no. 1339, pp. 500–527, 1962.

[157] E. Gbadam and S. Frimpong, “Bench Structural Integrity Modeling of Oil Sands for Optimum Cable Shovel Performance,” *J. Powder Metall. Min.*, vol. 03, no. 01, pp. 1–7, 2014.

[158] M. Fahey and J. P. Carter, “A finite element study of the pressuremeter test in sand using a nonlinear elastic plastic model,” *Can. Geotech. J.*, vol. 30, no. 2, pp. 348–362, 1993.

[159] S. W. Sloan, “INTERNATIONAL KNIRNAL FOR NUMERICAL AND ANALYTICAL METHODS IN LOWER BOUND LIMIT ANALYSIS USING FINITE ELEMENTS A N D LINEAR PROGRAMMING,” 1988.

[160] I. F. Collins and M. Boulbibane, “Geomechanical analysis of unbound pavements based on shakedown theory,” *J. Geotech. Geoenvironmental Eng.*, vol. 126, no. 1, pp. 50–59, Jan. 2000.

[161] A. D. Nguyen, A. Hachemi, and D. Weichert, “Application of the interior-point method to shakedown analysis of pavements,” *Int. J. Numer. Methods Eng.*, vol. 75, no. 4, pp. 414–439, Jul. 2008.

[162] H. Ling, Hoe I.; Liu, “Finite element studies of asphalt concrete pavement reinforced with geogrid,” *J. Enginee*, vol. 129, no. 7, pp. 801–811, 2003.

[163] I. L. Howard and K. A. Warren, “Finite-element modeling of instrumented flexible pavements under stationary transient loading,” *J. Transp. Eng.*, vol. 135, no. 2, pp. 53–61, 2009.

[164] B. Ghadimi, H. Nikraz, and M. Rosano, “Dynamic simulation of a flexible pavement layers considering shakedown effects and soil-asphalt interaction,” *Transp. Geotech.*, vol. 7, pp. 40–58, Jun. 2016.

[165] B. Ghadimi and H. Nikraz, “A comparison of implementation of linear and nonlinear constitutive models in numerical analysis of layered flexible pavement,” *Road Mater. Pavement Des.*, vol. 18, no. 3, pp. 550–572, May 2017.

[166] Caterpillar, “797F Mining Truck,” 2012.

[167] H. P. Gavin, “Numerical Integration in Structural Dynamics,” 2016.

[168] S. Jin, Xing; Qiang, M.A., Li, “Comparison of four numerical methods for calculating seismic dynamic response of SDOF system,” in *13th World Conference on Earthquake Engineering*, 2004.

[169] P. J. Lu, Y., Wright, “Lu and Wright, 1998,” *Comput. Struct.*, vol. 69, pp. 139–147, 1998.

[170] S. P. Newmark, N. M., Chan, “r:~qA A COMPARISON OF NUMERICAL METHODS FOR ANAL YllNG THE DYNAMIC RESPONSE OF STRUCTURES Ket. le~erenee Roem OFFICE OF NAY Al RESEARCH Contract N6onr-71, Task Order VI CO:MPARISON OF NUMERICAL METHODS FOR ANALYSING THE DYNAMIC RESPONSE OF STRUCTURES A Te,” 1952.

[171] K. J. Bathe, “Conserving energy and momentum in nonlinear dynamics: A simple implicit time integration scheme,” *Comput. Struct.*, vol. 85, no. 7–8, pp. 437–445, 2007.

[172] F. Tyan, Y.-F. Hong, S.-H. Tu, and W. S. Jeng, “Generation of Random Road Profiles,” 2009.

[173] Caterpillar, “Caterpillar Performance Handbook,” 2015.

[174] MSC.ADAMS, “About Adams / Solver,” 2016.

[175] M. Kertész and F. Palčák, “The role of the stiffly stable integrators in nonlinear dynamic simulations,” in *APLIMAT 2015 - 14th Conference on Applied Mathematics, Proceedings*, 2015, no. February 2015, pp. 446–455.

[176] D. Negrut, R. Rampalli, G. Ottarsson, and A. Sajdak, “On an implementation of the Hilber-Hughes-Taylor method in the context of index 3 differential-algebraic equations of multibody dynamics (DETC2005-85096),” *J. Comput. Nonlinear Dyn.*, vol. 2, no. 1, pp. 73–85, Jan. 2007.

[177] J. Krzyzanowska, “The impact of mixed fleet hauling on mining operations at Venetia mine,” *J. South. African Inst. Min. Metall.*, vol. 107, no. 4, pp. 215–224, 2007.

[178] Caterpilllar Inc., “Large Mining Truck - Truck Overload Policy ‘10/10/20’ (Revision #4),” 2019. [Online]. Available: https://caterpillarinformation.blogspot.com/2011/03/gross-machine-operating-weights-have.html. [Accessed: 01-Oct-2019].

[179] ANSYS, “ANSYS Explicit: The Solution Strategy,” 2019. [Online]. Available: https://www.sharcnet.ca/Software/Ansys/17.0/en-us/help/exd_ag/exp_dyn_theory_whatis.html.

[180] ABAQUS, “ABAQUS Theory Guide (2016),” 2016. [Online]. Available: http://130.149.89.49:2080/v2016/books/stm/default.htm.

[181] M. Sasso, G. Palmieri, G. Chiappini, and D. Amodio, "Characterization of hyperelastic rubber-like materials by biaxial and uniaxial stretching tests based on optical methods," *Polym. Test.*, vol. 27, no. 8, pp. 995–1004, 2008.

[182] R. W. Ogden, G. Saccomandi, and I. Sgura, "Fitting hyperelastic models to experimental data," *Comput. Mech.*, vol. 34, no. 6, pp. 484–502, 2004.

[183] W. Nyaaba, S. Frimpong, and A. Anani, "Fatigue damage investigation of ultra-large tire components," *Int. J. Fatigue*, vol. 119, no. July 2018, pp. 247–260, 2019.

[184] D. D. Tannant and V. Kumar, "Properties of fly ash stabilized haul road construction materials," *Int. J. Surf. Mining, Reclam. Environ.*, vol. 14, no. 2, pp. 121–135, 2000.

[185] SANRAL, *South African Pavement Engineering Manual - Materials Testing*, no. November. 2011.

[186] D. G. Abraha, D. C. Sego, K. W. Biggar, and R. Donahue, "Sulfur concrete for haul road construction at Suncor oil sands mines," *Can. Geotech. J.*, vol. 44, no. 5, pp. 564–578, May 2007.

[187] A. Al-Jawadi, "Some Useful Numbers on the Engineering Properties of Materials (Geologic and Otherwise)," 2019.

[188] Viewpoint, "Scale studies help mining companies maximize payload, increase production," *Viewpoint Mining Magazine*, 2019. [Online]. Available: http://viewpointmining.com/article/scale-studies-help-mining-companies-maximize-payload.

[189] B. T. Schexnayder, C., Weber, S. L., Brooks, "T Ruck & T Railer S Ize & W Eight," *J. Constr. Eng. Manag.*, vol. 125, no. 1, pp. 1–7, 1999.

[190] J. Q. Oliva, "PRPgenerator User's Manual," 2014.

VITA

Bruno Ayaga Kansake was born in the Upper East Region of Ghana. He obtained his BS and MPhil degrees in Mining Engineering from the University of Mines and Technology (UMaT), Tarkwa, Ghana in 2013 and 2016, respectively. He worked as a mining engineering intern at Ghana Manganese Company Limited (GMC). He also served as a Teaching Assistant and Demonstrator in the Mining Engineering Department at UMaT from 2013 to 2016. Bruno worked with Safety and Environmental Research and Consultancy Limited in Ghana, where he was part of a team that offered consultancy services to mining companies in Ghana on blast impact prediction and modeling.

He joined Missouri S&T in Fall 2016 to pursue a Ph.D. program in Mining Engineering under the mentorship of Dr. Samuel Frimpong, Director of the Heavy Mining Machinery Research Group at Missouri S&T. During his time at Missouri S&T, he worked as a Research and Teaching Assistant and served as the African Students' Association Diversity Leadership Council (DLC) representative. He worked as an Academic Industry Mining (AIM) Fellow at Freeport-McMoRan in Phoenix during the summer of 2019. He received his Ph.D. in Mining Engineering from the Missouri University of Science and Technology in December 2019.